Multipole Analysis of the Δ^0 in ^{3}He

Joseph Donnelly

Presented as a Thesis for the Degree of Doctor of Philosophy

Nuclear Physics Experimental
Department of Physics & Astronomy
University of Glasgow

Glasgow, Scotland

ABSTRACT

The "shape" of the Δ^+ has been previously measured to be deformed. Many studies have looked at the multipole ratios R_{EM} and R_{SM} finding small but non-zero values broadly in line with the theories. By studying the angular distribution of the decay products from a Δ excitation, the multipole ratios can be measured. Little data for Δ^0 production exists. By looking at the angular distributions of the decay products from the reaction $^3\mathrm{He}(e, e'p\pi^-)\,2p$, we have studied the multipole transitions of the quasi-free neutron excited to a Δ^0 and extracted information on its shape from measuring the dominant magnetic dipole (M1) and the interference from the electric quadrupole (E2) and Coulomb quadrupole (C2). We will report that over the Q^2 range 0.1-0.4 $(GeV/c)^2$, we measured values that are in the range of $+3.5\% < R_{EM} < +6.5\%$ and $-0.5\% < R_{SM} < -1.9\%$. These are very different from the results obtained in previous Δ^+ measurements. Values for the multipole ratios R_{EM} and R_{SM} were determined for the first time on a quasi-free neutron target in a ^{3}He nucleus and comparisons with existing "free" neutron theoretical models indicate large differences between the current models and the data.

ACKNOWLEDGEMENTS

I would like to firstly thank my mum and dad, Margaret and Terry Donnelly. My dad, for instilling in me a passion for science and a desire for learning from an early age. That early seed of curiosity has driven me through the years to things I would not have ventured towards in its absence. My mum, for going above and beyond the call of duty in looking after me. I have never been found wanting for support or means with my parents unshakeable faith in me and for this I will always cherish them.

I would like to thank my siblings Keli, Terence and Nicky for many reasons, particularly for not acting on the impulse to strangle me over the years. I must give praise to my friends, including Karen Mann who has always provided an ear for listening, Roger Henderson who has never yet fallen out with me despite frequent provocation, Iain Hannah who never bothered to mention me in his thesis, and Damian "Crabbe-boy" Crabbe whose incessant insistence that he be mentioned paid off.

I would like to thank my supervisor, Dave Ireland for all the help and guidance he has provided, perhaps most importantly his input to this thesis that might have been incomprehensible otherwise. I would like to thank the members of the Nuclear Physics group who over the years have aided me in various ways, including Günther Rosner, Jim Kelly, Ken Livingston, Dan Protopopescu and Derek Glazier. Thanks are due to my various office and neighbouring office mates over the years who have endured my frequent conversations with great tenacity; most recently Bryan McKinnon, Craig Patterson, Andrew Osborne and others. I must thank the Multi-hadron group and others at Jefferson Lab for providing support and knowledge, including but not limited to Stepan Stepanyan, Larry Weinstein, Maurik Holtrop and Kyunseon Joo. My project would not have happened without the funding from the Engineering and Physical Sciences Research Council, so a substantial thanks to them.

And of course thanks to Homer for setting the tone for the ensuing document and Douglas Adams for stating so clearly what many physicists often feel.

"Facts are meaningless. You could use facts to prove anything that's even remotely true !" - Homer Simpson

"In the beginning the Universe was created. This has made a lot of people very angry and been widely regarded as a bad move." - Hitchhikers Guide to the Galaxy

DECLARATION

The data presented in this thesis were obtained as part of the e2b run group for the CLAS Collaboration at Jefferson Laboratory, Virginia, USA. I participated fully in the execution of the experiment. The analysis of the experimental data is entirely my own work. I composed this thesis myself.

TABLE OF CONTENTS

LIST OF TABLES

LIST OF FIGURES

CHAPTER I
INTRODUCTION

The standard model which has served particle and nuclear physics extremely well since the 1970s is known to be incomplete. Some aspects of fundamental nuclear physics are simply not understood. The strong force and how it affects particles in the nuclear environment is one of these poorly understood areas and much research has been performed over the years to help complete the picture. The underlying theory of strong interactions is Quantum ChromoDynamics (QCD), yet there are no ab initio calculations of nuclei available. Nuclei are effectively and well described as clusters of protons and neutrons held together by a strong, long-range force mediated by meson exchange, whereas the saturation properties of nuclear matter arise from the short-range, repulsive part of the strong interaction [1]. Whether the nucleon bound in the nuclear medium changes structure has been a long-standing issue in nuclear physics.

Quantum Chromodynamics (QCD) is the theory that governs all strong physics interactions. The Δ resonance is the first excited state of the nucleon and interacts via the strong force which is described by QCD. QCD is not solvable in the low energy limit, and different models for various length scales describe interactions that take place [2, 3]. In the quark model, the nucleon is made of three quarks with gluons being the force carriers. In this picture the Δ is created by flipping the spin of a quark leaving the three quarks spin aligned (spin $\frac{3}{2}$, isospin $\frac{3}{2}$). The contribution of the Δ in the nucleus is estimated to be 1%-2% of the total wave function in three nucleon systems [4].

1.1 Previous Studies

Many studies have been previously performed looking at the properties of the Δ. These have been restricted for the most part to production of the Δ^+ state, as this can be excited from a proton target. The "shape" of the resonance can be determined by studying the multipole transitions of the resonant state and this has been the focus of past experiments. The object of these studies was to identify whether the Δ was simply spherical as some QCD models suggested, or "deformed".

Deformation of the Δ was first examined in the context of the constituent quark model [5]. In this case where one gluon is exchanged, a colour magnetic dipole-dipole interaction causes a d-wave admixture in the nucleon and Δ wave function which leads to deformation. Other models that lead to deformation include cloudy bag models where asymmetric pion clouds cause deformation [6,7], or the constituent quark model [8] where it has been proposed that deformation is due to eliminating gluonic and quark-antiquark degrees of freedom. Looking for a quadrupole strength in the $\gamma^* N \to \Delta$ transition, spin-parity selection rules allow a magnetic dipole (M1), an electric quadrupole (E2) or a Coulomb quadrupole (C2) amplitude. The electric quadrupole is important for studying nuclear deformations and in many models, a tensor force in the hyperfine interaction [9] arises from one gluon exchange between the quarks leading to a d-state admixture in the ground state. This is similar to the tensor force in nucleon-nucleon interactions which makes the deuteron prolate. If E2 and C2 are zero then the shape of the particle is spherical. Experimental evidence shows that the Δ has non-zero E2 and C2 contributions [10, 11] (figure 1.1) and is therefore not purely spherical. This is in line with constituent quark models that predict values of the range $-3.5\% < R_{EM} < 0\%$ [5, 12–15] while relativized quark models [16,17] give small values of about -0.1%. The cloudy bag model [6,7] produces results in the range $-3.0\% < R_{EM} < -2.0\%$ while Skyrme models [18] give larger values at between -2.5 and -5%. There are at present QCD lattice calculations [19] that give R_{EM} to be $(+3 \pm 8)\,\%$.

Many multipole analyses have been carried out in facilities including MAMI[1] [20–22], LEGS[2] [23], ELSA[3] [24], BATES[4] [10] and Jefferson Laboratory [25–27] in the last fifteen years. Data extending back to 1969 also exists (CEA/Harvard [28], DESY [29–31], NINA/Daresbury [32–35] and Bonn [36]). Substantial variations in these data leading to large distributions of values for the multipole ratios have been measured (figure 1.1). It is clear from figure 1.1 that whilst there exists large variation in the measurements of the multipole ratios, in almost all cases non-zero R_{EM} and R_{SM} values were measured showing the resonance to be deformed. The data taken at Jlab [37] were the most recent and precise measurements and show the best consistent trend over a large Q^2 range. Large variation in the R_{EM} measurements around zero meant the sign of the ratio was uncertain; equal amounts of data points were positive and negative. The more recent experiments however seem to indicate a negative sign of this ratio at a few percent, which is consistent with several of the theoretical models mentioned. All results for the Δ^+ studies agree that the ratio R_{SM} has a negative sign and most of the more recent experiments (including the Jlab data) place its

[1]Mainz Microtron.

[2]Laser Electron Gamma-ray Source, Brookhaven National Laboratory.

[3]Electron Stretcher and Accelerator, Bonn.

[4]Bates Linear Accelerator Center, M.I.T.

magnitude around $-10\% < R_{SM} < -5\%$.

The previous experimental measurements of multipoles and the various models give small but non-zero values for the multipole interference terms. By studying these quadrupoles in the context of a ^{3}He nucleus we can look at these properties for the Δ^0. Little previous work exists for Δ-production on a quasi-free neutron. One previous analysis performed cross-section calculations for π^0 production on the bound neutron in deuterium [38]. No multipole study has been performed on a neutron in a ^{3}He target. By studying the Δ^0 we can add a great deal of knowledge where there is almost a complete lack of previous measurements for this resonance. We will be able to compare our findings to existing theoretical models and highlight where they succesfully describe our results and where they fail.

1.2 Additional Study

In addition to looking at the multipole values for our transition, we can expand on a previous study looking for medium modification of the Δ. Some of the first indications of the medium influencing deep inelastic scattering processes were studied at the European Muon collaboration [39] in the early 1980s. The study looked at the cross-section ratio σ^{Fe}/σ^{D} (the ratio for the measured cross-section per nucleon for iron (Fe) and deuterium (D)) and showed non-unity values which couldn't be accounted for solely by Fermi-motion. Successive experiments at SLAC (Stanford Linear Accelerator) [40,41] and CERN [42] confirmed these results. More recent polarisation transfer measurements of the $^4\text{He}(e,e'p)^3\text{H}$ reaction [43–46] indicate medium modification of the nucleon electromagnetic form factors. It is the case that previous studies often have had limited statistics for their distributions over relevant kinematic variables.

We used electrons as our probe particle since the interaction is electromagnetic and governed by the well known QED (Quantum Electrodynamics) theory and the weakness of the interaction allows the whole nucleus to be probed. Also, a virtual photon is exchanged in the interaction allowing energy and momentum transfer to be varied independently of each other.

1.3 Inclusive Studies

This additional study follows on from previous work performed [47–49] that found the invariant mass of the Δ to vary in the nuclear environment. In those studies, inclusive measurements (where only the scattered electron is detected) showed a Q^2

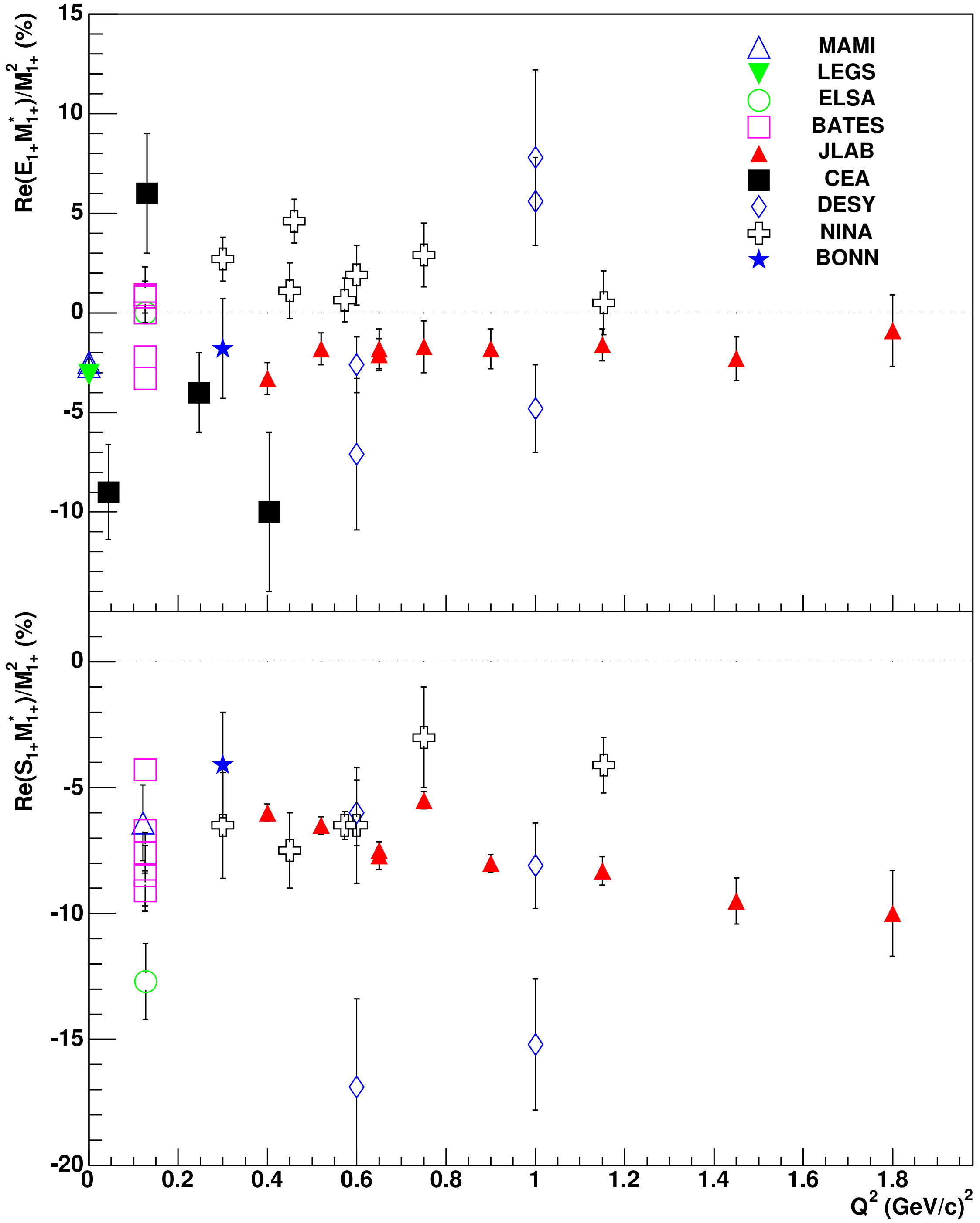

Figure 1.1: Previous measurements of multipole ratios R_{EM} and R_{SM}.

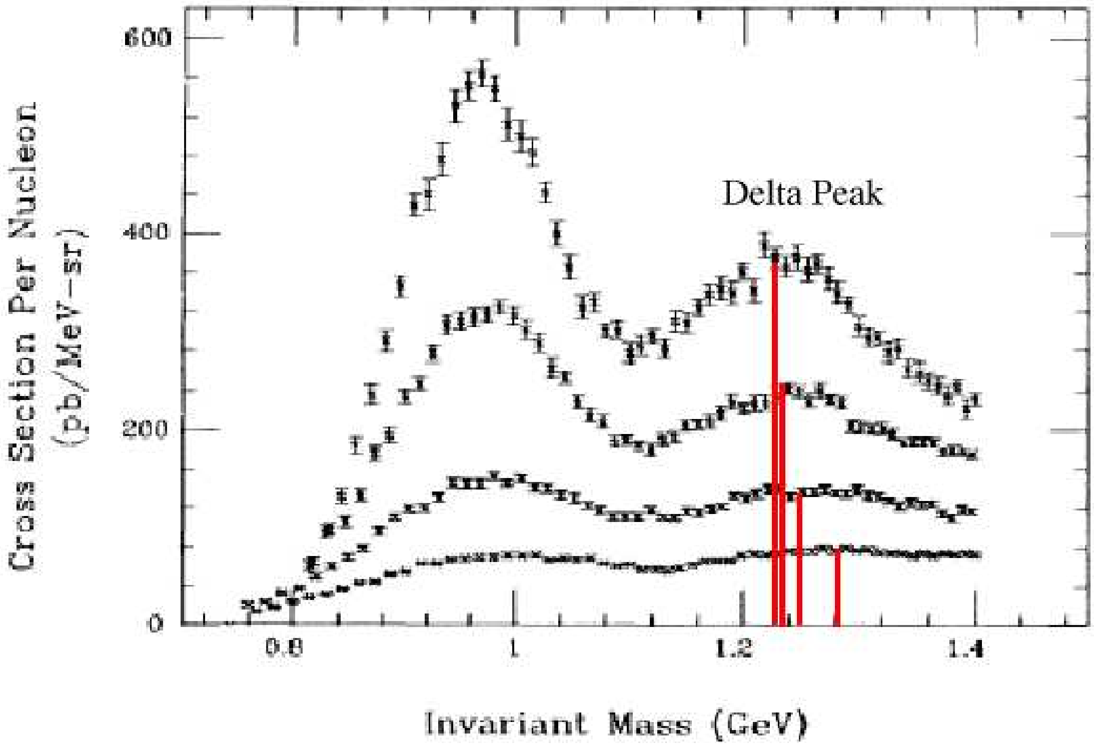

Figure 1.2: Doubly differential cross-sections divided by atomic mass for inclusive electron scattering from carbon. From top to bottom, the electron energies were 0.96, 1.1, 1.3 and 1.5 GeV giving Q^2 values at the Δ of around 0.2, 0.3, 0.4 and 0.5 $(\text{GeV/c})^2$.

(figures 1.2 and 1.3) dependence[5] of the invariant mass where Q^2 gives us information about the virtual photon that was transferred [50] in the interaction (in fact it is the invariant mass squared of the virtual photon and a measure of resolution). The implication of this result was that the potential the Δ experiences in the nucleus is dependent on its momentum. For the nucleons (protons and neutrons) no such dependence has been observed [51]. An inclusive study where only the scattered electron is detected "includes" contributions from all reactions making unambiguous extraction of the Δ cross-section from background processes impossible. This severely limits what conclusions can be drawn from such studies.

The analysis performed in [48] was an inclusive measurement. Many inclusive studies have been performed at low energies [52–55], high energies [56, 57] and intermediate energies [48]. Due to competing reaction mechanisms, each one of which

[5]Where $Q^2 = \mathbf{q}^2 - \omega^2$ and $\mathbf{q}$ and ω are the differences between the beam and scattered electron momenta and energies. (section 2.2)

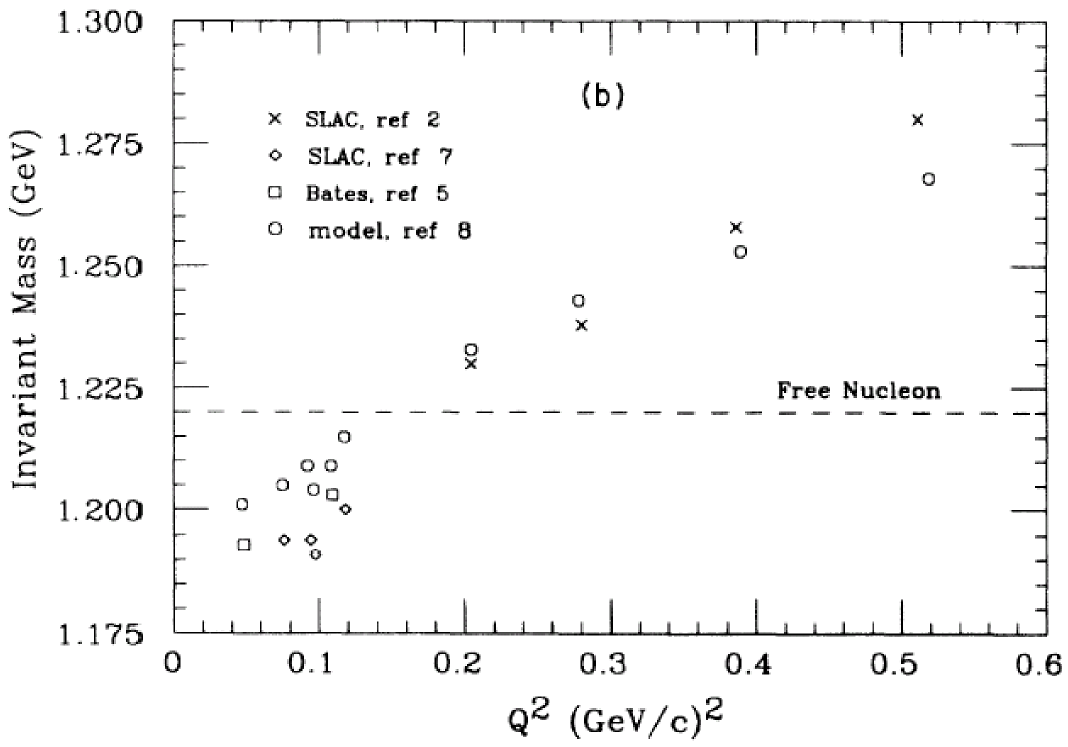

Figure 1.3: Invariant mass peak positions vs Q^2 for cross-sections as shown in figure 1.2 for the Δ electroproduction peak.

contributes to the cross-section and has a poorly known energy and Q^2 dependence, an inclusive measurement is insufficient. To access the Δ "cleanly", an exclusive measurement where all particles in the final state are detected and measured must be made. Such a measurement is "exclusive" to the reaction channel being studied and allows a clean separation of the Δ signal from other processes.

1.4 Exclusive Measurements

If all the particles in the final state of an interaction are measured then the reaction can be completely described kinematically using the particle's four-momenta. The detector system used in this study (section 3.2) has a large solid-angle detection capability and was ideal for the purpose of measuring all particles in the final state of a reaction. The ability to make exclusive measurements allows us to separate the competing reaction mechanisms' cross-sections and identify the Δ peak cleanly.

Some exclusive measurements have been made looking for a Q^2 dependence of the Δ mass in carbon [58] and ^{3}He [59] [60]. These also studied the peak position of the Δ-resonance. In our target the possible reaction mechanisms for Δ production and decay are,

$$\gamma^* + n \rightarrow \Delta^0 \rightarrow \begin{cases} n + \pi^0 \rightarrow n + \gamma + \gamma \\ p + \pi^- \end{cases} \tag{1.1}$$

$$\gamma^* + p \rightarrow \Delta^+ \rightarrow \begin{cases} p + \pi^0 \rightarrow p + \gamma + \gamma \\ n + \pi^+ \end{cases} \tag{1.2}$$

The circled decay products are preferential in our analysis due to better detection efficiencies of charged particles in our detector system. The pπ^- channel provides the greatest statistics and will be the focus of the analysis. The nπ^0 channel would provide cleaner results for reasons explained in section 7.1, but is not covered in this thesis.

CHAPTER II
THEORY

2.1 Δ Resonance

The Δ is the first excited state of the nucleon and is the most prominent and isolated resonance [61]. Both the proton and neutron can be thought of as a charge substate of the nucleon where the isospin is I=$\frac{1}{2}$ for both, and the difference is in the third component of isospin $I_3=\pm\frac{1}{2}$. Isospin is useful in that it is conserved in strong interactions [62, 63].

This study aims to look at the properties of the Δ^0 generated from a quasi-free neutron in a ^{3}He target. Deformations of particles are usually seen through electric multipole moments [64] and the lowest order moment would be a dipole moment. However, static electric moments of odd order are forbidden due to parity conservation, leaving the lowest allowed order to be a quadrupole moment(L=2) (section 2.3.1). Due to the Wigner-Eckart theorem [65], any multipole moment with L $>$ 2I (where I is the spin state) vanishes. It is therefore impossible to measure the dipole moment of the nucleon since it has spin $\frac{1}{2}$.

The Δ has a spin of $\frac{3}{2}$ and so can in principle allow measurement of its quadrupole moment. The resonance is generated through the spins of all three constituent quarks aligning. A list of the various ways in which the nucleon can be excited to a resonance are given in table 2.1. The excitation can be due to an incident magnetic dipole photon (M1) which produces a magnetic transition where one quark spin-flips to align with the other quarks. (The convention is that the M1 refers to the Magnetic transition due to a photon with angular momentum equal to 1). This excitation is the dominant one and only through interference with it can the others be accessed. Another way to create a Δ is to have an incident electric quadrupole photon (E2). If either the nucleon or Δ wave function have an admixture of an L=2 component, the excitation can occur on a single quark. A different way an E2 photon can interact is by coupling with the exchange currents between two quarks (figure 2.1). The scalar transition can occur in similar way to the electric transition.

There exist four sub-states of the delta: $\Delta^-, \Delta^0, \Delta^+$ and Δ^{++}. With a nuclear target the only major contribution is from the $\Delta^0$and Δ^+ produced from the neutron and proton. This is because with an electron scattering experiment, no charge is exchanged. An example plot of W for the reaction $^3\mathrm{He}(e, e'p\pi^-)\,2p$ is shown in figure 2.2 where W is the invariant mass of the multi-particle final state. The free Δ has a

Resonance	J^P	Multipolarities	
		γN $\rightarrow N^*$	$N^* \rightarrow$ Nπ
P_{33} $\Delta(1232)$	$\frac{3}{2}^+$	$E2, C2, M1$	E_{1+}, S_{1+}, M_{1+}
P_{11} $N^*(1440)$	$\frac{1}{2}^+$	$C0, M1$	S_{1-}, M_{1-}
D_{13} $N^*(1520)$	$\frac{3}{2}^-$	$E1, C1, M2$	E_{2-}, S_{2-}, M_{2-}
S_{11} $N^*(1535)$	$\frac{1}{2}^-$	$E1, C1$	E_{0+}, S_{0+}
S_{31} $\Delta(1620)$	$\frac{1}{2}^-$	$E1, C1$	E_{0+}, S_{0+}
S_{11} $N^*(1650)$	$\frac{1}{2}^-$	$E1, C1$	E_{0+}, S_{0+}
D_{15} $N^*(1675)$	$\frac{5}{2}^+$	$E3, C3, M2$	E_{2+}, S_{2+}, M_{2+}
F_{15} $N^*(1680)$	$\frac{5}{2}^+$	$E2, C2, M3$	E_{3-}, S_{3-}, M_{3-}

Table 2.1: The resonances of the nucleon in the reaction $\gamma_\nu N \rightarrow N^*$,$N^* \rightarrow N\pi$ with their angular momentum/parity J^P. The states are given by either A_{l_γ} or $A_{l_\pi \pm}$ denoting the initial and final states respectively. These denote the transverse electric (E), magnetic (M) and longitudinal Coulomb/Scalar (C,S) excitations . The subscripts refer to the incident photon angular momentum l_γ and decay pion angular momentum l_π and how it couples to the nucleon spin to get total angular momentum $J = l_\pi \pm \frac{1}{2}$.

mass of 1230-1234 MeV/c^2 and a width of 115-125 MeV/c^2 [66]. It decays through the strong interaction in around 10^{-24} s with a branching ratio of $> 99\%$ into a nucleon and a pion [66]. The alternative reaction is the Δ decaying to a nucleon and photon. However, with such a low branching ratio and the kinematic discrimination that will be discussed later, the contribution from this can be disregarded. It is already known that the properties of the Δ created in the nuclear environment differs from those of the free particle [67, 68]. The width of the resonance is increased as a result of the Fermi motion of the bound nucleons. When the resonance decays, if it has an energy below the Fermi level, Pauli blocking increases the lifetime of the Δ thus reducing the width of the resonance [69]. Also an alternative decay channel for the resonance has to be considered where N + $\Delta \rightarrow$ N + N. This increases the width of the resonance [69] and is a much larger effect than the Pauli blocking. It is evident that the nuclear environment does alter the properties of the resonance and by looking at the shape of the Δ through the multipoles, the mechanisms and characteristics of these differences can be studied.

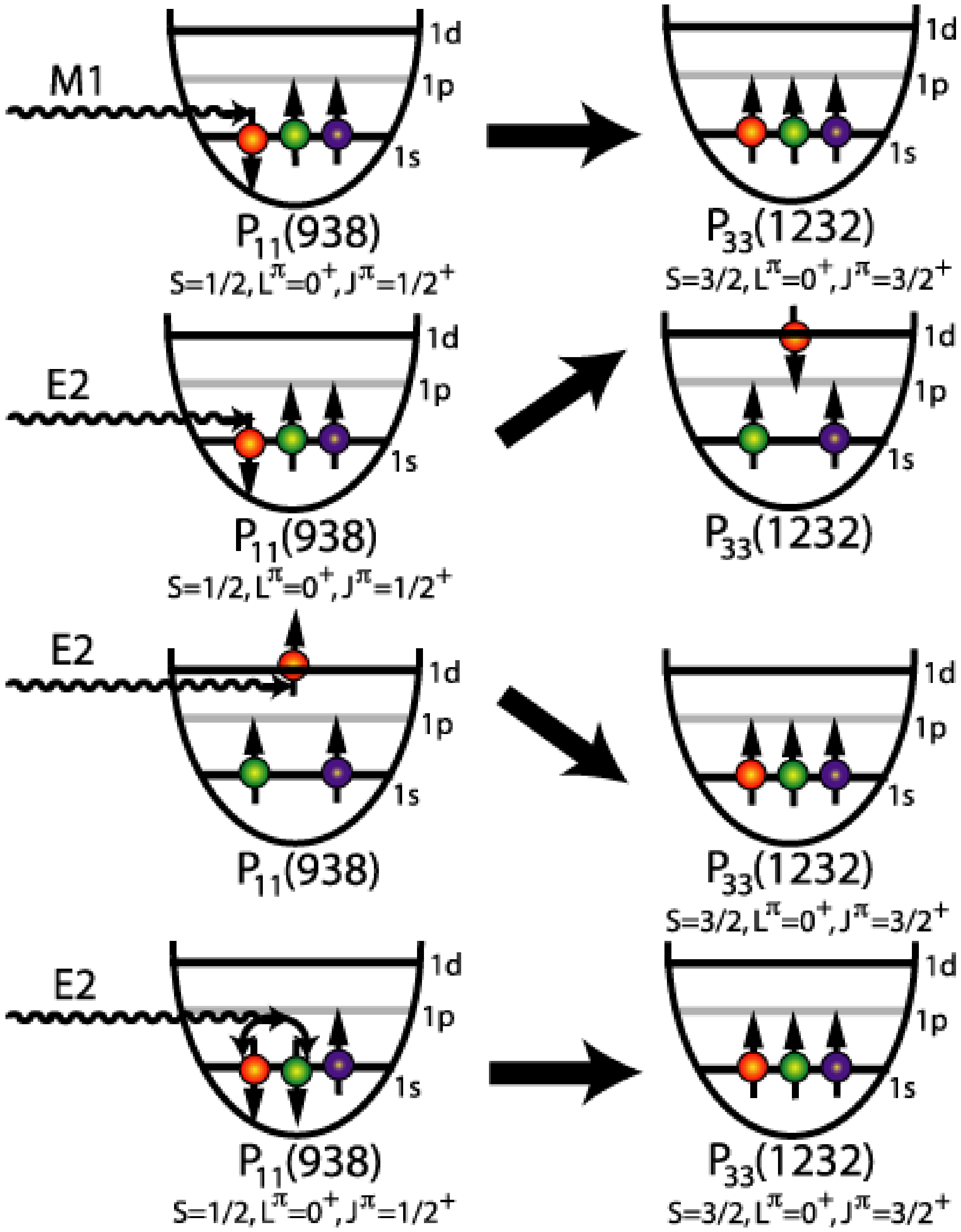

Figure 2.1: From [64]. The different ways to create a Δ in descending order: M1, photon incident on a nucleon spin-flips a single quark; E2 absorption where the Δ wave-function has admixture of L=2 component; E2 photon incident on nucleon wave-function with admixture of L=2 component; E2 photon incident on nucleon couples to exchange currents between two quarks spin-flipping both.

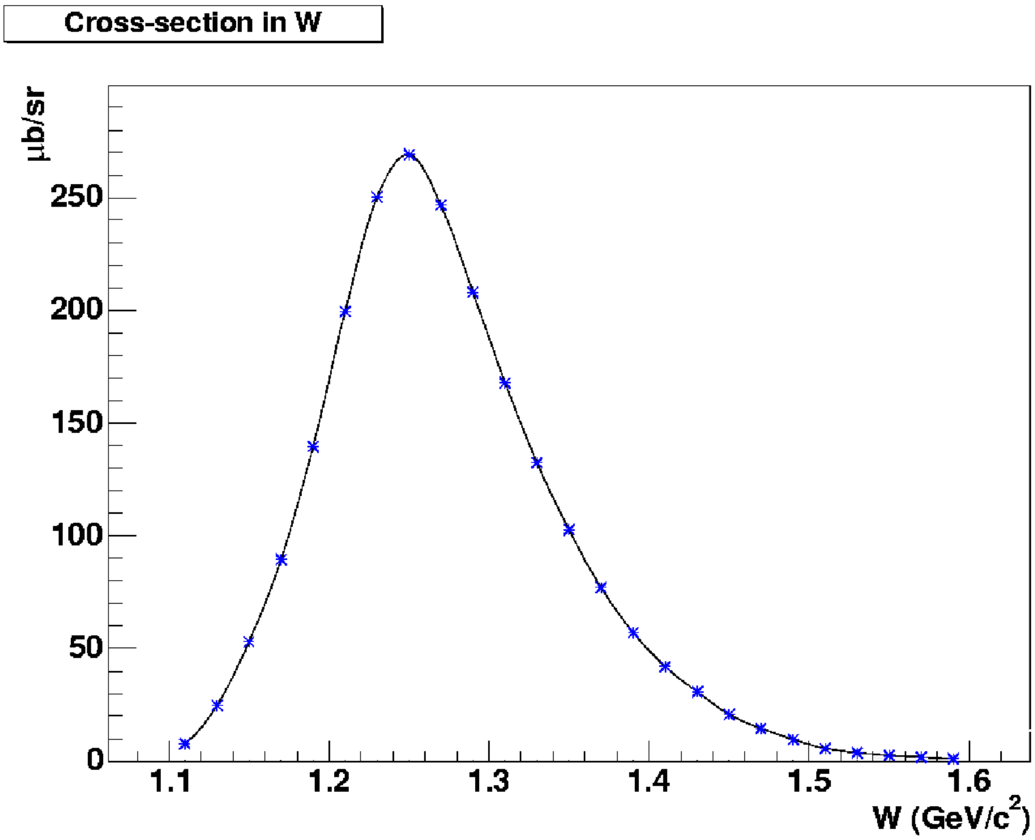

Figure 2.2: An example W spectrum for the channel $^3\mathrm{He}(e, e'p\pi^-)2p$.

2.2 Kinematics of Electron Scattering

The four-momentum of a particle can be expressed as $p^\mu = (E, \mathbf{p})$, where the three-momentum is given by $\mathbf{p}$ and the energy is E. For light target nuclei where $\mathrm{Z}\alpha \ll 1$ (Z is the proton number and α is the fine structure constant), the electron wave distortion is not very large in an electron scattering process and so to a good approximation, only one photon is exchanged. This one photon exchange approximation is easily justified by QED, where it can be shown that in successive photon exchanges the probability is diminished by a factor of $\mathrm{Z}\alpha$.

In electron scattering, a virtual photon is exchanged between the incident electron and the target nucleon. To generate a Δ, around 300 MeV of energy has to be transferred to the target nucleon. However, by using an electron probe the momentum transfer can be varied independently of the energy transfer. The virtual photon's energy ω (GeV), and momentum $\mathbf{q}$ (GeV/c) are defined as follows:

$$\omega = E_e - E_{e'} \tag{2.1}$$

$$\mathbf{q} = \mathbf{k}_e - \mathbf{k}_{e'} \tag{2.2}$$

Where $k^\mu = (E_e, \mathbf{k}_e)$ is the four vector of the incoming electron and $k'^\mu = (E_{e'}, \mathbf{k}_{e'})$ is the four vector of the scattered electron.

In the reaction (e,e$'$pπ^-), the three-momenta of the protons and pions are measured in coincidence with the scattered electrons. The missing momentum, missing energy and missing mass of the reactions are given thus:

$$\mathbf{p}_m = \mathbf{q} - \mathbf{p_p} - \mathbf{p}_\pi \tag{2.3}$$

$$E_m = \omega - E_p - E_\pi \tag{2.4}$$

$$M_m = \sqrt{E_m^2 - p_m^2} \tag{2.5}$$

These quantities combined represent the four-vector of the residual system; the two spectator protons in the case of a ^{3}He target. Also, as is the convention in nuclear physics, units are used where it is taken that $\hbar$=c=1.

In electron scattering experiments, the invariant mass squared of the exchanged virtual photon,

$$Q^2 = \mathbf{q}^2 - \omega^2 \tag{2.6}$$

is a measure of the momentum transferred to the nucleon. As Q^2 is invariant it is a good quantity for investigation. Another invariant quantity is the mass of the recoiling hadronic system, W (GeV/c^2). It can be calculated as,

$$W^2 = m_N^2 + 2m_N\omega - Q^2 \tag{2.7}$$

where m_N is the mass of the struck nucleon. Both these quantities are used to define the kinematic bins of the calculated cross-sections seen later.

2.3 Multipoles

2.3.1 Multipole Theory

Under the SU(6) symmetric quark models, the $\gamma N \Delta$ transition is mediated by a single quark spin flip in the ground state of the nucleon leading to M_{1+} dominance and E_{1+}=S_{1+}=0 [70]. For QCD-motivated constituent quark models this is not the case. Tensor forces from the interquark hyperfine interaction lead to a d-state admixture in the baryon ground state leading to M_{1+} dominance and small but non-negligible E_{1+} and S_{1+} contributions as discussed in section 2.1.

In the CQM, 3 "heavy" valence quarks are present each with spin-parity $S^p = \frac{1}{2}^+$. We know how the orbital angular momentum of a particle (L) couples to the spin (S) to give the total angular momentum of the system (J),

$$J = L \otimes S \tag{2.8}$$

With the proton spin=$\frac{1}{2}$ and the Δ spin=$\frac{3}{2}$ we can determine that L can take the values 0 or 1 for the proton and 0, 1 or 2 for the Δ. But using parity conservation,

$$P = (P_{q-1})(P_{q-2})(P_{q-3})(-1)^L \;= (+)(+)(+)(-1)^L \;=\; (-1)^L \tag{2.9}$$

Where P is the parity of the system and $P_{q-1..3}$ the constituent quark parities. Thus L must be 0, or 2. In the case that L is 0 we get a spherical distribution.

$$J = \frac{1}{2} = 0 \otimes \frac{1}{2} \quad \text{proton} \leftarrow spherical \rightarrow \Delta \quad J = \frac{3}{2} = 0 \otimes \frac{3}{2} \tag{2.10}$$

And with L = 2 we get a deformed particle.

$$J = \frac{1}{2} = 2 \otimes \frac{3}{2} \quad \text{proton} \leftarrow deformed \rightarrow \Delta \quad J = \frac{3}{2} = 2 \otimes \left(\frac{1}{2}, \frac{3}{2}\right) \tag{2.11}$$

It is the L=2 component that corresponds to deformation from the simple spherical shape.

Due to reasons outlined in section 2.1 the quadrupole in the case of the nucleon can not be measured. Instead you must excite it to its first resonance state, the Δ. If we use "quadrupole photons" (photons involved in a reaction where an L=2 admixture exists) we can study quadrupole transitions. The type of photons that can create the $\Delta(1232)$ can be determined.

Let us take the case of scattering from a proton as an example. The reaction would be,

$$\gamma^* \;+\; p \;\rightarrow\; \Delta(1232)$$

$$So, \tag{2.12}$$

$$L_\gamma^P \otimes \tfrac{1}{2}^+ \;=\; \tfrac{3}{2}^+$$

Where L_γ^P is the photon angular momentum and parity and $\frac{1}{2}^+$ and $\frac{3}{2}^+$ the values for the proton and Δ. Therefore the photon must have even parity due to parity conservation. The parity of the multipoles are as follows [71],

$$\begin{aligned} Electric\ EL &= (-1)^L \\ Magnetic\ ML &= (-1)^{L+1} \\ Scalar\ CL &= (-1)^L \end{aligned} \tag{2.13}$$

Combining the fact that the photon parity must be even with the above multipolarity parities we se that,

$$\begin{aligned} L_\gamma^P &= 1^+ \ \Leftrightarrow M1\ \ (magnetic\ dipole) \\ L_\gamma^P &= 2^+ \ \Leftrightarrow E2, C2\ \ (quadrupole) \end{aligned} \tag{2.14}$$

More than the photon's M1, E2 and C2 properties are needed. There exist constraints on l (the relative angular momentum of the pπ pair in the final state). When after the reaction in equation 2.12 the Δ proceeds to decay to a proton and pion we have,

$$\begin{aligned} \Delta\,(1232) &\rightarrow\ p\ +\ \pi \\ J^P\ =\ \tfrac{3}{2}^+ &\rightarrow\ \left[\left(\tfrac{1}{2}^+ \otimes 0^-\right)_{spin} \otimes l\right] \end{aligned} \tag{2.15}$$

Therefore we have either,

$$\begin{aligned} l\ +\ \frac{1}{2}\ &=\ \frac{3}{2}\ \ (i.e.\ l\ =\ 1) \\ &or \\ l\ -\ \frac{1}{2}\ &=\ \frac{3}{2}\ \ (i.e.\ l\ =\ 2\ ) \end{aligned} \tag{2.16}$$

Again with parity conservation the final parity must be positive.

$$\begin{aligned} P_{final}\ &=\ (P_\pi)\,(P_{proton})\,(-1)^l\ =\ (+)\,(-)\,(-1)^l \\ +\ &=\ (-1)^{l+1}\ \ so\ \ l\ =\ ODD \end{aligned} \tag{2.17}$$

From equations 2.16 and 2.17 it is obvious that $l = 1$.

So we see that in the case of the $\Delta(1232)$ the dominant "spherical" transition is the M_{1+} with a magnetic photon M1 and the smaller "deformed" quadrupole transitions E_{1+} and S_{1+} created by an electric and scalar photon respectively. It is through the way these smaller transitions interfere with the dominant magnetic transitions that we measure the ratios,

$$R_{EM} = E_{1+}/M_{1+} \tag{2.18}$$

and,

$$R_{SM} = S_{1+}/M_{1+} \tag{2.19}$$

These ratios give us information on the shape of the Δ exposing any deformations.

2.3.2 Multipole Analysis

For electron scattering in the one-photon exchange approximation, figure 2.3 shows the reaction schematically. An electron of initial energy E_e scatters through an angle of θ_e to a final energy E_e'. The scattering and reaction planes are shown in figure 2.4. Deriving the relevant cross-sections for the experiment requires that some assumptions are made about the hadron currents since they are not completely known or understood. A full description of the derivation of the cross-section can be found in Appendix A where the calculation is worked from the basic scattering from a point-like Dirac particle, to the complicated virtual photon cross-section involving scattering from a particle with internal structure.

Under the one photon-exchange approximation, the electroproduction cross-section factorises as follows:

$$\frac{d^4\sigma}{dQ^2 dW d\Omega_\pi^*} = J\Gamma \frac{d^2\sigma}{d\Omega_\pi^*} \tag{2.20}$$

where Γ is the flux of virtual photons (equation A.30) and the Jacobian,

$$|J| = \left| \frac{\partial(Q^2, W)}{\partial(e', cos\theta_e)} \right| \tag{2.21}$$

This relates the binning variables of the analysis dQ^2dW to the electron kinematics $de^{'}dcos\theta_e$. For an unpolarised beam and target the centre-of-mass differential cross-section $d^2\sigma$ depends on the transverse (ϵ) and longitudinal (ϵ_L) polarisation of the virtual photon through four structure functions: σ_T, σ_L and their interference

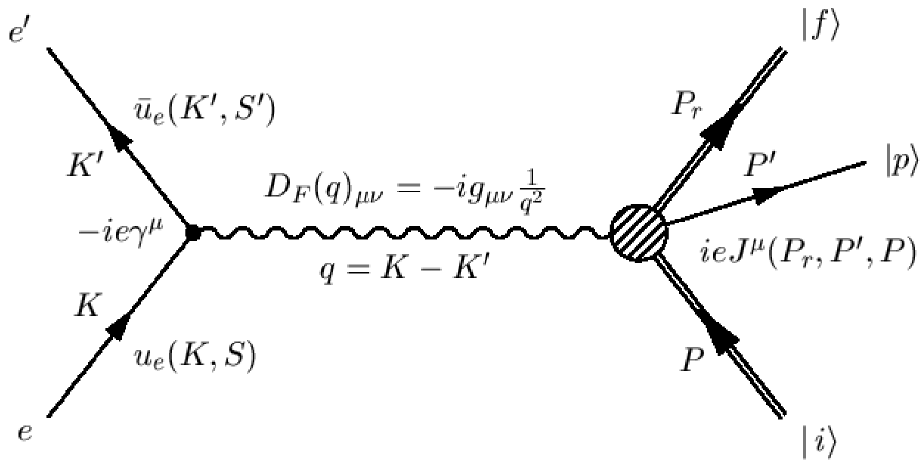

Figure 2.3: Lowest order graph for the exclusive (e,e'X) electron scattering process.

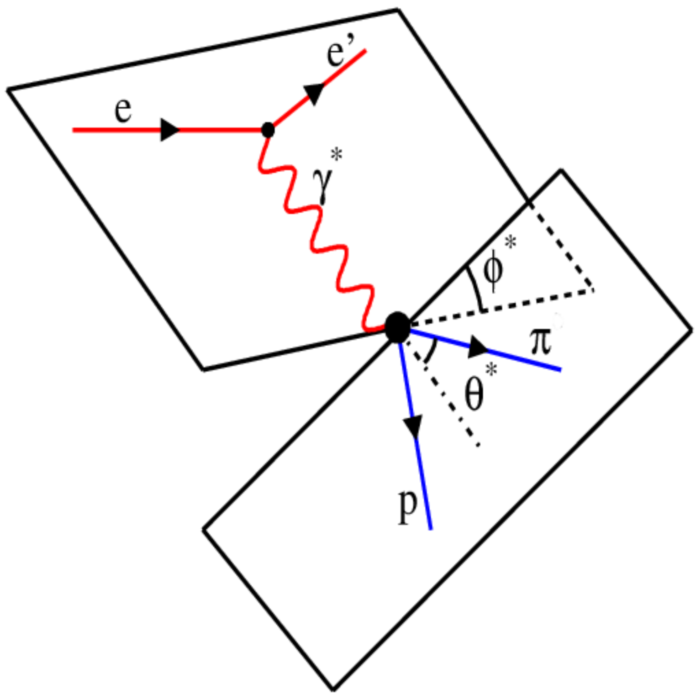

Figure 2.4: The exclusive reaction where all particles in the final state are detected.

terms σ_{LT} and σ_{TT}.

$$\frac{d^2\sigma}{d\Omega^*_\pi} = \frac{P^*_\pi}{k^*_\gamma}(\sigma_T + \epsilon_L\sigma_L + \epsilon\sigma_{TT} sin^2\theta^*_\pi cos2\phi^*_\pi + [2\epsilon_L(\epsilon+1)]^{\frac{1}{2}}\sigma_{LT} sin\theta^*_\pi cos\phi^*_\pi) \quad (2.22)$$

Where P^*_π and θ^*_π are the c.m. momentum and polar angle and ϕ^*_π is the azimuthal rotation of the πp plane with respect to the electron scattering plane $(e, e^{'})$. For invariant masses less than 2 GeV/c^2 (which includes the Δ), the structure functions can be expanded into partial waves which represent states of definite angular momentum/parity J^P. Table 2.1 shows that the $\Delta(1232)$ is excited through three p-wave multipoles, the dominant magnetic dipole M_{1+} and weak transverse electric quadrupole E_{1+} and longitudinal Coulomb quadrupole S_{1+}.

The Coulomb/Scalar multipoles C_n and $S_{l\pm}$ are accessible only though measurement of the longitudinal structure functions σ_L or σ_{LT}. For σ_L, multiple beam energies are needed to perform a Rosenbluth-type separation [72] where ϵ_L is varied. But σ_{LT} can be measured if the entire ϕ^*_π coverage is available, which is the case with our detector system. In the case of the $\Delta(1232)$ where the longitudinal excitations are very weak relative to the the transverse excitations the latter method is preferable.

2.3.3 Obtaining R_{EM} and R_{SM}

By accumulating the data into bins of (Q^2,W,cosθ^*_π,ϕ^*_π) the structure functions can be extracted by fitting the ϕ^*_π distributions with the form of equation 2.22. That is of the form $A + Ccos2\phi^*_\pi + Dcos\phi^*_\pi$. The extracted functions can be expanded into a partial wave series using Legendre polynomials in cosθ^*_π [73]. Previous analyses have shown that it is only necessary to fit the final pπ final state up to l_π=1 [37].

$$\begin{aligned} \sigma_T + \epsilon_L\sigma_L &= A_0 + A_1 cos\theta^*_\pi + A_2 P_2\left(cos\theta^*_\pi\right) \\ \sigma_{TT} &= C_0 \\ \sigma_{LT} &= D_0 + D_1 cos\theta^*_\pi \end{aligned} \quad (2.23)$$

So by limiting the series at l_π=1, the s-wave and p-wave multipoles M_{1+}, E_{1+}, S_{1+}, M_{1-}, E_{0+}, S_{0+} and S_{1-} are given in terms of the partial wave coefficients as in [74]. We can include higher terms to check for d-wave strength. But previous analyses have found no indication of this (chapter 7).

$$
\begin{aligned}
A_0 &= 2|M_{1+}|^2 + 6|E_{1+}|^2 + |M_{1-}|^2 + |E_{0+}|^2 + \epsilon_L(8|S_{1+}|^2 + |S_{0+}|^2 + |S_{1-}|^2) \\
A_1 &= 2Re(E_{0+}^*(M_{1+} - M_{1-} + 3E_{1+})) + 2\epsilon_L(Re(S_{0+}^*(S_{1-} + 4S_{1+}))) \\
A_2 &= 3|E_{1+}|^2 - |M_{1+}|^2 - 2Re(M_{1+}^*(M_{1-} - 3E_{1+}) + 3E_{1+}^* M_{1-}) \\
&\quad +8\epsilon_L(|S_{1+}|^2 + Re(S_{1+}^* S_{1-})) \\
C_0 &= -\tfrac{3}{2}|M_{1+}|^2 + \tfrac{6}{2}|E_{1+}|^2 - 3Re(M_{1+}^*(M_{1-} + E_{1+}) - E_{1+}^* M_{1-}) \\
D_0 &= -Re(S_{0+}^*(M_{1-} - M_{1+} + 3E_{1+})) - Re((S_{1-} - 2S_{1+})E_{0+}^*) \\
D_1 &= -6Re(S_{1+}^*(M_{1-} - M_{1+} + 3E_{1+})) - 6Re((S_{1-} - 2S_{1+})E_{1+}^*)
\end{aligned} \tag{2.24}
$$

There exists a problem in that with the seven multipoles in general being complex, excluding an overall phase we must determine 13 quantities with only 6 partial wave coefficients. We then have to apply additional assumptions to simplify the analysis in the absence of extra observables or restrictions.

Using the fact as mentioned previously (section 2.3.1) that the M_{1+} transition is dominant, we can approximate the equations 2.24 by dropping all terms not involving M_{1+} i.e. removing anything that does not directly interfere with the dominant transition. Thus we obtain $|M_{1+}|^2$ and its projection onto five other s-wave and p-wave multipoles,

$$
\begin{aligned}
&|M_{1+}|^2 = A_0/2 \\
&Re(E_{1+}M_{1+}^*) = (A_2 - 2C_0/3)/8 \\
&Re(M_{1-}M_{1+}^*) = -(A_2 + 2(A_0 + C_0))/8 \\
&Re(E_{0+}M_{1+}^*) = A_1/2 \\
&Re(S_{0+}M_{1+}^*) = D_0 \\
&Re(S_{1+}M_{1+}^*) = D_1/6
\end{aligned} \tag{2.25}
$$

It is the relationships in equations 2.25 that show how the smaller quadrupoles E_{1+} and S_{1+} can be accessed through how they interfere with the much larger M_{1+}. The charge multipoles are related to the isospin multipoles in the following way.

$$
\begin{aligned}
&A\left(\gamma^* p \to n\pi^+\right) = \sqrt{2}\left[A^{(0)} + \tfrac{1}{3}A^{\left(\frac{1}{2}\right)} - \tfrac{1}{3}A^{\left(\frac{3}{2}\right)}\right] \\
&A\left(\gamma^* p \to p\pi^0\right) = A^{(0)} + \tfrac{1}{3}A^{\left(\frac{1}{2}\right)} + \tfrac{2}{3}A^{\left(\frac{3}{2}\right)} \\
&A\left(\gamma^* n \to p\pi^-\right) = \sqrt{2}\left[A^{(0)} - \tfrac{1}{3}A^{\left(\frac{1}{2}\right)} + \tfrac{1}{3}A^{\left(\frac{3}{2}\right)}\right] \\
&A\left(\gamma^* n \to n\pi^0\right) = -A^{(0)} + \tfrac{1}{3}A^{\left(\frac{1}{2}\right)} + \tfrac{2}{3}A^{\left(\frac{3}{2}\right)}
\end{aligned} \tag{2.26}
$$

Using the assumption that $M_{1+}^{\left(\frac{1}{2}\right)} \ll M_{1+}^{\left(\frac{3}{2}\right)}$ and that the I=$\frac{1}{2}$ channel is mostly real for M_{1+} [20] we have at the $\Delta(1232)$ resonance peak:

$$Re\left(E_{1+}M_{1+}^{*}\right) \approx Im\left(E_{1+}^{\left(\frac{3}{2}\right)}\right) Im\left(M_{1+}^{\left(\frac{3}{2}\right)}\right) \tag{2.27}$$

By the Fermi-Watson theorem [75], $M_{1+}^{\left(\frac{3}{2}\right)}$ follows the πN phase shift δ_{33} for which the real part vanishes at W=1.232 GeV/c^2. Thus we use,

$$R_{EM} = \frac{Re\left(E_{1+}M_{1+}^{*}\right)}{|M_{1+}|^2} \approx \frac{Im\left(E_{1+}^{\left(\frac{3}{2}\right)}\right)}{Im\left(M_{1+}^{\left(\frac{3}{2}\right)}\right)} \tag{2.28}$$

$$R_{SM} = \frac{Re\left(S_{1+}M_{1+}^{*}\right)}{|M_{1+}|^2} \approx \frac{Im\left(S_{1+}^{\left(\frac{3}{2}\right)}\right)}{Im\left(M_{1+}^{\left(\frac{3}{2}\right)}\right)} \tag{2.29}$$

CHAPTER III
EXPERIMENTAL SETUP

The analysis and results presented were performed on data taken as part of an experimental run at the Thomas Jefferson National Accelerator Facility, in Newport News, Virginia, USA. The experiment was run during May and June of 2002 and the data were taken in Hall B of the facility using the CEBAF[1] Large Acceptance Spectrometer (CLAS) which has $\sim 4\pi$ sr coverage.

3.1 Accelerator

The CEBAF accelerator is a superconducting radio frequency (RF) circuit that propels electrons to energies up to approximately 6 GeV. It provides a beam which is simultaneously supplied to three experimental halls A, B and C (figure 3.1). A fourth hall (Hall D) will be built when the facility receives an upgrade to 12 GeV capability.

The electrons are supplied using a gallium-arsenide (GaAs) cathode injector. A circularly polarised laser beam incident on the injector produces photo-electrons which are accelerated to 67 MeV and sent into the first linear accelerator (LINAC). These electrons are then accelerated around the circuit which is made up of two parallel linacs connected by guiding arcs with a radius of 80 m. On each passage the electron is boosted in energy by roughly 1 GeV with a maximum of five circuits. Only one circuit was necessary for the data in this run providing a beam at 0.984 GeV. Twenty cryomodules line the linacs and each of these contain eight superconducting niobium cavities. The cavities are maintained at 2 K by liquid helium produced at the Central Helium Liquefier (CHL). The linac energies are set to be identical and the RF cavities are phased to provide maximum acceleration. Subsequent passes through the accelerator are phased to maximise energy gain by adjusting the length of travel in the preceding arc.

As was mentioned, the accelerator is capable of supplying all halls simultaneously. It does this by using an RF chopping system operating at 499 MHz to develop a 3-beam 1.4971 GHz bunch train at 100 keV. The beam is then longitudinally compressed and provides bunches to each hall 2 ns apart. The maximum current that can be supplied is about 200 μA with a beam spot at the target of 0.5 mm. Hall B needs only a small fraction of this capability because of its large solid angle detection abilities, with the typical current during this run period being around 10 nA.

[1] Continuous Electron Beam Accelerator Facility

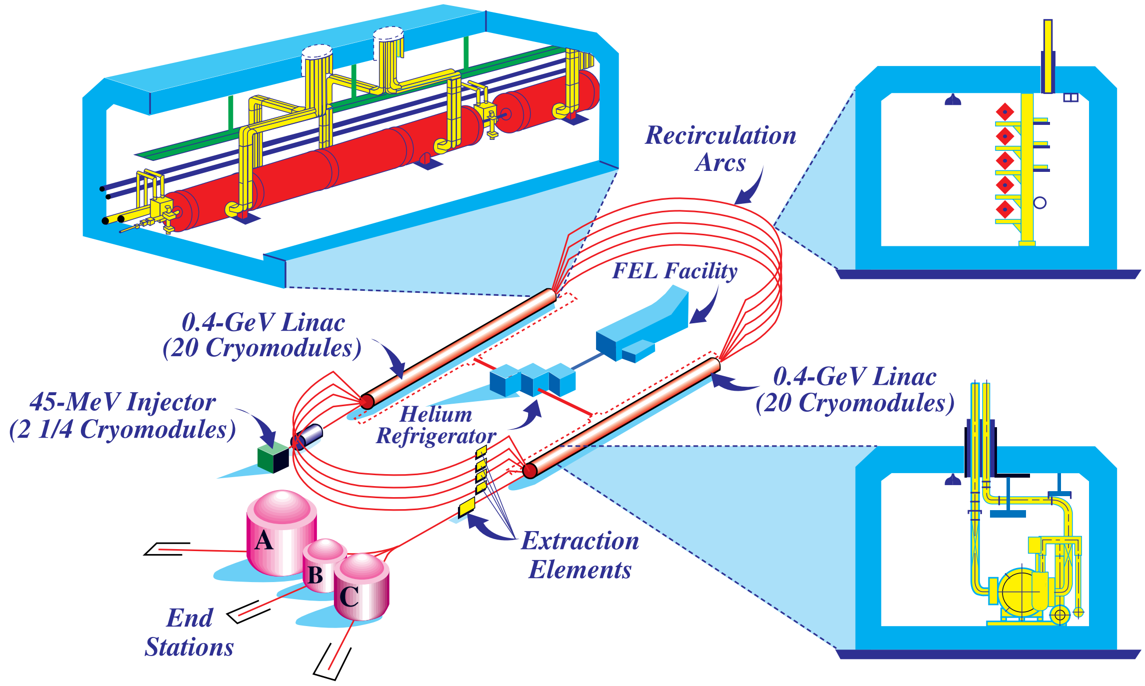

Figure 3.1: The CEBAF accelerator. The three blowup boxes show (clockwise from top left): one of the LINAC cryomodules; a cross-section of the tunnel with five recirculating arcs; a cross-section of a cryomodule.

3.2 The CLAS (CEBAF Large Acceptance Spectrometer) Detector

The CLAS detector has roughly 4π sr coverage arranged in a layered structure (figure 3.2) consisting of drift chambers, Čerenkov counters, scintillation counters and electromagnetic calorimeters. The drift chambers are used for determining particle trajectories and momenta. The Čerenkov counters are used for particle identification, primarily separating electrons from negatively charged pions. The scintillation counters provide time-of-flight (TOF) information and the electromagnetic calorimeters are used to detect showering particles like electrons and photons. CLAS is arranged in six sectors defined by the six toroidal iron-free superconducting coils. These are positioned around the beam axis and produce a circular field with a maximum strength of 2 T. The field is at maximum in the forward direction dropping off by a factor of five at larger angles. The core of CLAS is field-free, to allow polarised target operation.

The mini torus is a small toroidal coil inserted into the cavity of the large superconducting magnet and generates a magnetic field to remove low energy electrons which are part of the background. This field is small compared to the main field but is extremely efficient at removing Møller electrons (a factor of 100 background rejection in region 1 of the drift chambers).

3.2.1 Drift Chambers

The drift chambers (DC) [76] in CLAS are used to determine particle tracks and momenta. The DCs are arranged in three regions in each of the six sectors covering a range of 8^o to 140^o in polar angle and about 80% of the azimuthal range (2π). Three regions serve different functions measuring different aspects of the charged particles progress through the magnetic field and are arranged at specific locations to allow this (figure 3.4). Region 1, the innermost and closest to the target, is in the nearly field free part of CLAS inside the Torus bore and determines the initial direction of charged particle tracks. Region 2 [77] is located where the field strength is greatest and thus where the charged particles achieve their maximum curvature. This allows good momentum resolution. The final set of DCs, region 3, are outside of the field coils and in a position where the magnetic field is low. They are used to measure the final direction of the charged particles as they head outwards to the time-of-flight counters, Čerenkov counters and electromagnetic calorimeters.

Each region of the DC comprises one axial superlayer with up to 1200 sense wires in six layers (four layers in the case of region 1) and one stereo superlayer with wires in six layers at an angle of 6^o with respect to the axial wires.

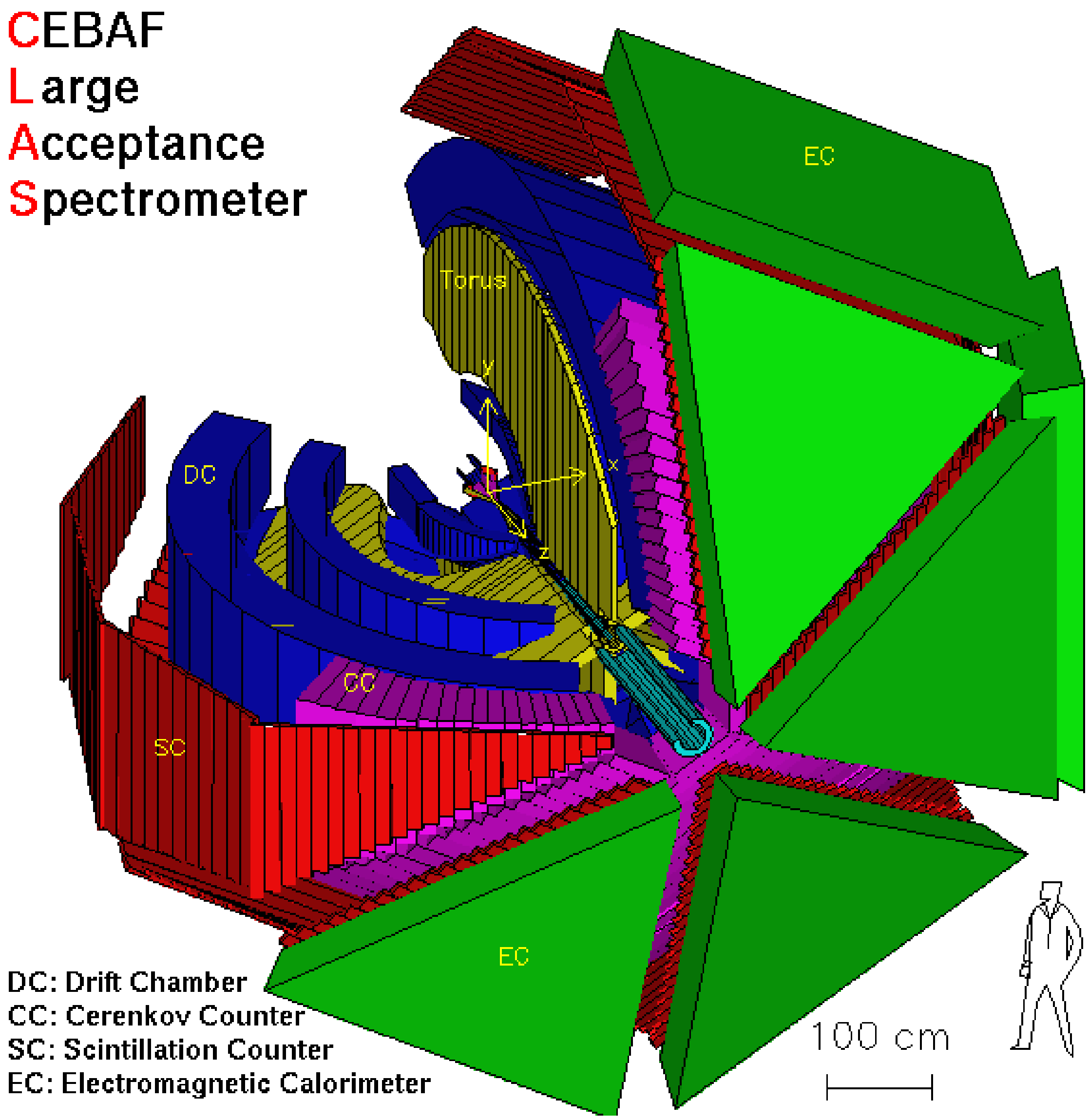

Figure 3.2: The CLAS detector (produced with GSIM). The calorimeter is in green in the most forward position upstream of the beam. The red is the time-of-flight (scintillation) detectors and the purple are the Čerenkov counters. The drift chambers are dark blue with the target located at the centre of the detector in the beam line.

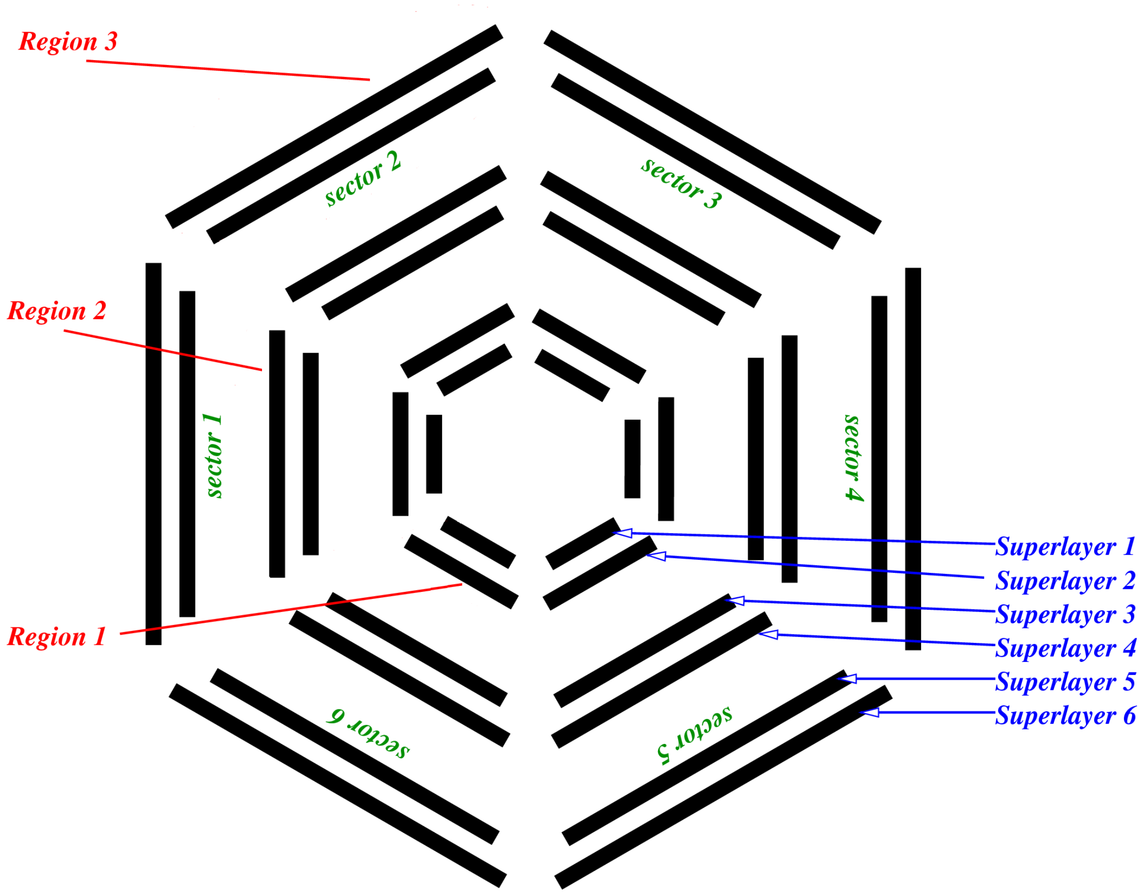

Figure 3.3: The drift chambers arranged in three regions in each of the six sectors. Each region also consist of two superlayers. The schematic is viewed in the direction of the beam.

This allows measurement of both polar angle θ and azimuthal angle ϕ of the track. A hexagonal pattern for the wires has been used as a good approximation of the ideal circular cell in which the drift/time relation is independent of the entrance angle. In this configuration each wire is surrounded by six shared field wires. Edge effects are minimised with a row of guard wires surrounding the superlayers that smooth the electric field.

The gas mixture within the drift chambers is 90% argon and 10% CO_2. When a charged particle travels through this gas, ionisation takes place and the electrons and positive ions released drift in opposite directions due to the electric field created by the wires. The electrons and ions are collected by the anode and cathode wires respectively. Close to the anode wires where the electric field strength is great, the liberated electrons can collide with the gas molecules causing secondary ionisation and providing an amplification effect. The average layer efficiency of the DC is greater than 98%.

The hits within each superlayer are formed to provide a track segment. These are then linked between superlayers to form a track giving the momentum within 5% of true value. The DC drift time resolution is only 1 ns while proton/pion discrimination for momenta up to 2.5 GeV/c requires 300 ps resolution. By combining the drift chamber and time-of-flight information, this can be achieved.

3.2.2 Čerenkov Counters

The Čerenkov counters (CC) [78] are used to identify electrons and separate them from pions and other charged particles. Čerenkov light is produced when a particle enters a medium at a velocity greater than that of the speed of light in the medium. Pions may be misidentified by producing knock-on electrons with velocities greater than the Čerenkov threshold. These are produced in the radiator gas, in the entrance window or in the material of the last layer of the DC. The efficiency for detecting these however is lower than for the primary particles since a large fraction is produced at unfavourable angles.

The gas used in the detectors is perfluorobutane (C_4F_{10}) and was chosen for its high refractive index (1.00153), which results in a high photon yield and an acceptably high pion momentum threshold of $P_\pi \sim 2.5$ GeV/c. In addition it has excellent light transmission properties. The energy threshold for producing Čerenkov light is 9.24 MeV for electrons and 2.51 GeV for pions [79].

The detectors consist of a three-mirror system that focuses light from particles

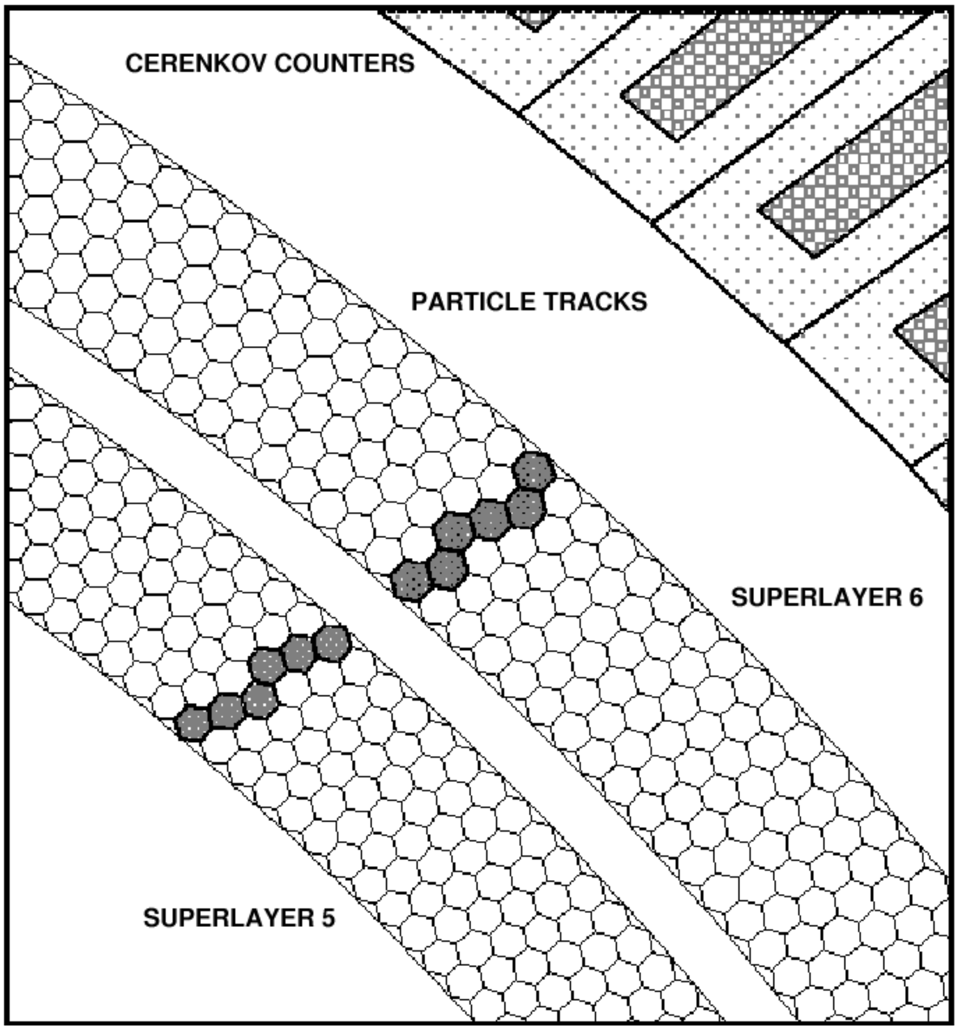

Figure 3.4: Each hexagon represents a drift cell, with sense wires at the centre and field wires at the vertices. The shaded cells are a track from a charged particle crossing the drift chamber.

with different azimuthal angles to a point near the coil where the photomultiplier is located. Since the CC are upstream from the time-of-flight detectors and electromagnetic calorimeters it is necessary to minimize the amount of material used in the CC to reduce electron and hadron absorption and secondary particle production. This means the photomultipliers and light collecting cones are positioned in the region of ϕ which is obscured by the magnetic coils. Each of the six sectors are divided into 18 regions of θ, with each θ segment divided into two modules about the symmetry plane bisecting each sector. This gives 12 subsectors around the ϕ direction for each θ interval resulting in a total of 216 light collection modules (figure 3.5).

The light of each θ module was designed to focus the light onto a photomultiplier tube (PMT) associated with that module and located in the region obscured by the coils. Figure 3.6 shows the optical arrangement of one module. The optical element of each module consist of two focussing mirrors, a "Winston" light collection cone, and a cylindrical mirror at the base of the cone.

3.2.3 Scintillation (TOF) Detectors

Particle identification is done using the time-of-flight (TOF) systems [80]. The scintillators are located between the Čerenkov detectors and electromagnetic calorimeters. They are positioned outside of the DC region 3 and Čerenkov detectors to reduce multiple scattering and production of knockout electrons (figure 3.2). The counters are mounted in four panels (figure 3.7) in each of the six sectors. Scintillators 1-23 are mounted in panel 1 and are referred to as the "forward-angle" counters. They correspond to scattering angles less than 45^o. Panels 2, 3 and 4 are called "large angle". Each scintillator paddle is placed perpendicular to the incident beam direction, so each counter subtends $\sim 2^o$ of the scattering angle. The counters are parallel to the normal drift chamber wires and span the azimuthal angular range of one sector. There are 57 scintillators per sector all possessing PMTs at both ends. The final 18 which cover the backward angles are paired into 9 logical counters. This gives 48 logical counters (or paddles) per sector. The lengths of these counters vary from 445 cm in the centre region, to 32 cm at the forward and backward edges. The forward-angle counters and the last four paddles of panel 4 are 15 cm wide, whilst the rest are 22 cm wide. The SC subsystem sums a total area of $\sim 206\ m^2$.

The maximum counting rate in the scintillators occurs in the forward direction. At small angles the timing resolution is better due to the smaller paddle lengths and the velocity resolution better due to the greater distance between the target and scintillators in this direction. The average time resolution for electrons is 163 ps [80].

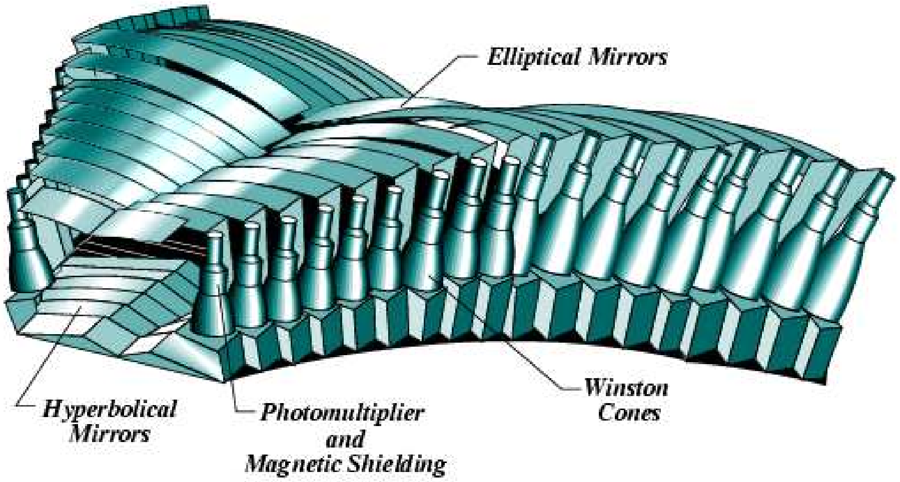

Figure 3.5: A schematic diagram of the array of optical modules in one of the six sectors.

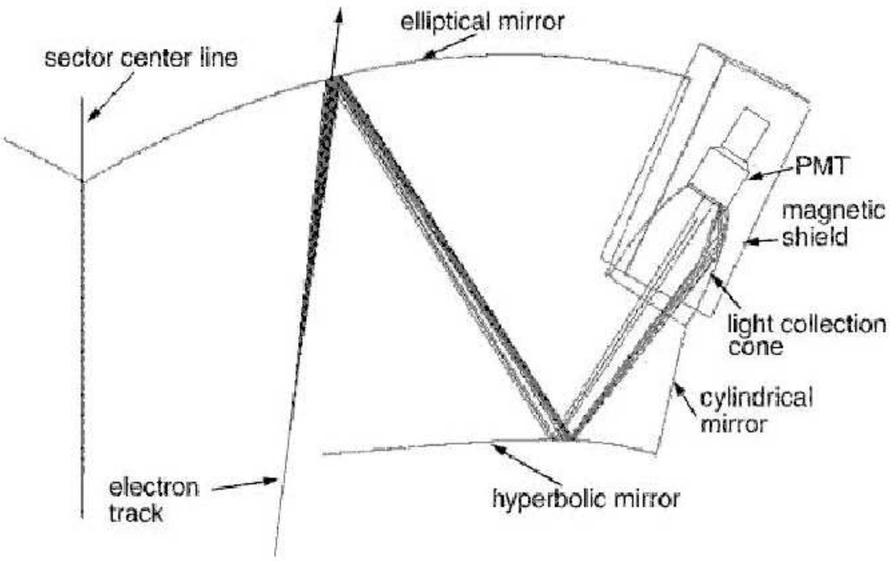

Figure 3.6: Optical arrangement of one of the 216 optical modules of the CLAS Čerenkov detector, showing the optical and light collection components.

3.2.4 Electromagnetic Calorimeters

The electromagnetic calorimeter (EC) [81] is used to both discriminate between electrons and pions, and to detect photons and other neutral particles. It covers the polar angles from 8^o to 45^o in all sectors with coverage extended in two sectors to 60^o with the large angle calorimeter (LAC). The design of the calorimeter was based on the following criteria:

- e and γ energy resolution $\frac{\sigma}{E} \leq \frac{0.1}{\sqrt{E(GeV)}}$;
- position resolution δr $\approx$ 2 cm at 1 GeV;
- $\frac{\pi}{e}$ rejection greater than 99% at $E \leq 1GeV$;
- fast ($<$ 100ns) total energy sum for the event trigger;
- mass resolution for two photon decays $\frac{\delta m}{m} \leq 0.15$;
- neutron detection efficiency $>$ 50% for $E_n > 0.5\ GeV$;
- time-of-flight resolution $\approx 1ns$.

As mentioned, the abilities of the EC include particle identification. In electron scattering, the information they gather along with that given by the CC can be used for pion and electron identification (for $E_e > 0.5$ GeV). The EC can also be used to reconstruct π^0s by identifying their 2γ decay products (for $E_\gamma > 0.2$ GeV) and for neutron identification, allowing discrimination between the photons and neutrons.

The EC is a sampling calorimeter where the energy deposited in the scintillators is less than that possesed by the particle. It features a lead-scintillator sandwich structure of alternating layers of scintillator strips and lead sheets with a total thickness of 16 radiation lengths. A lead/scintillator ratio of 0.21 is used, requiring 39 cm of scintillator and 8.4 cm of lead per module. With this ratio, approximately $\frac{1}{3}$ of the energy in an electromagnetic shower is deposited in the scintillator.

In order to match the hexagonal geometry of the CLAS detector, the lead-scintillator sandwich is in the shape of an equilateral triangle. There are 39 layers, each consisting of a 10 mm thick BC412 scintillator followed by a 2.2 mm thick lead sheet. The EC uses a "projective" geometry (figure 3.8) in which the area of each successive layer increases.

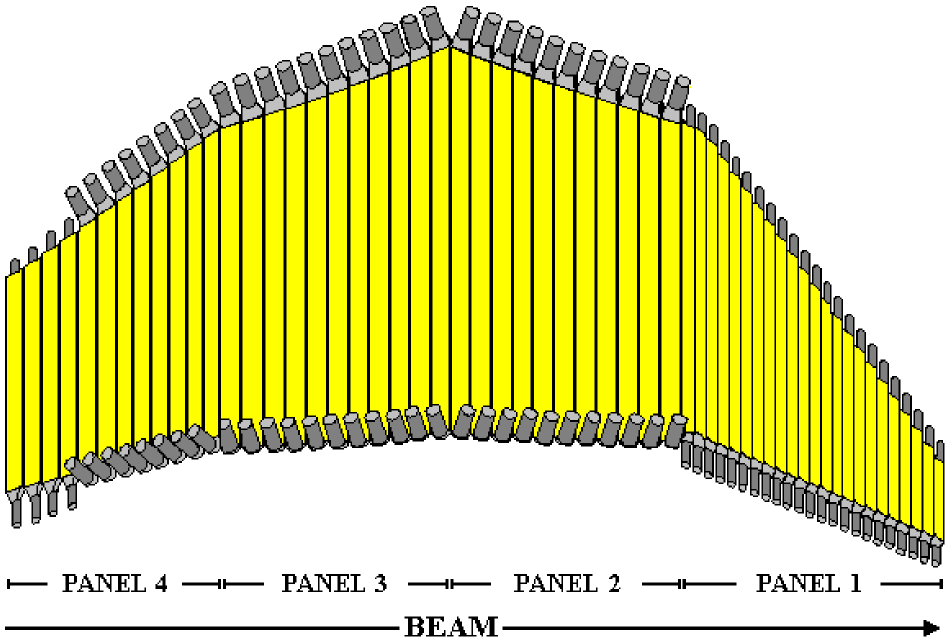

Figure 3.7: The four panels of scintillators that equip one sector. The forward-angle scintillators (panel 1) have short stubby light guides and 5 cm PMTs. The large-angle system has bent light guides coupled to $7\frac{1}{2}$ cm PMTs (except for the last four counters).

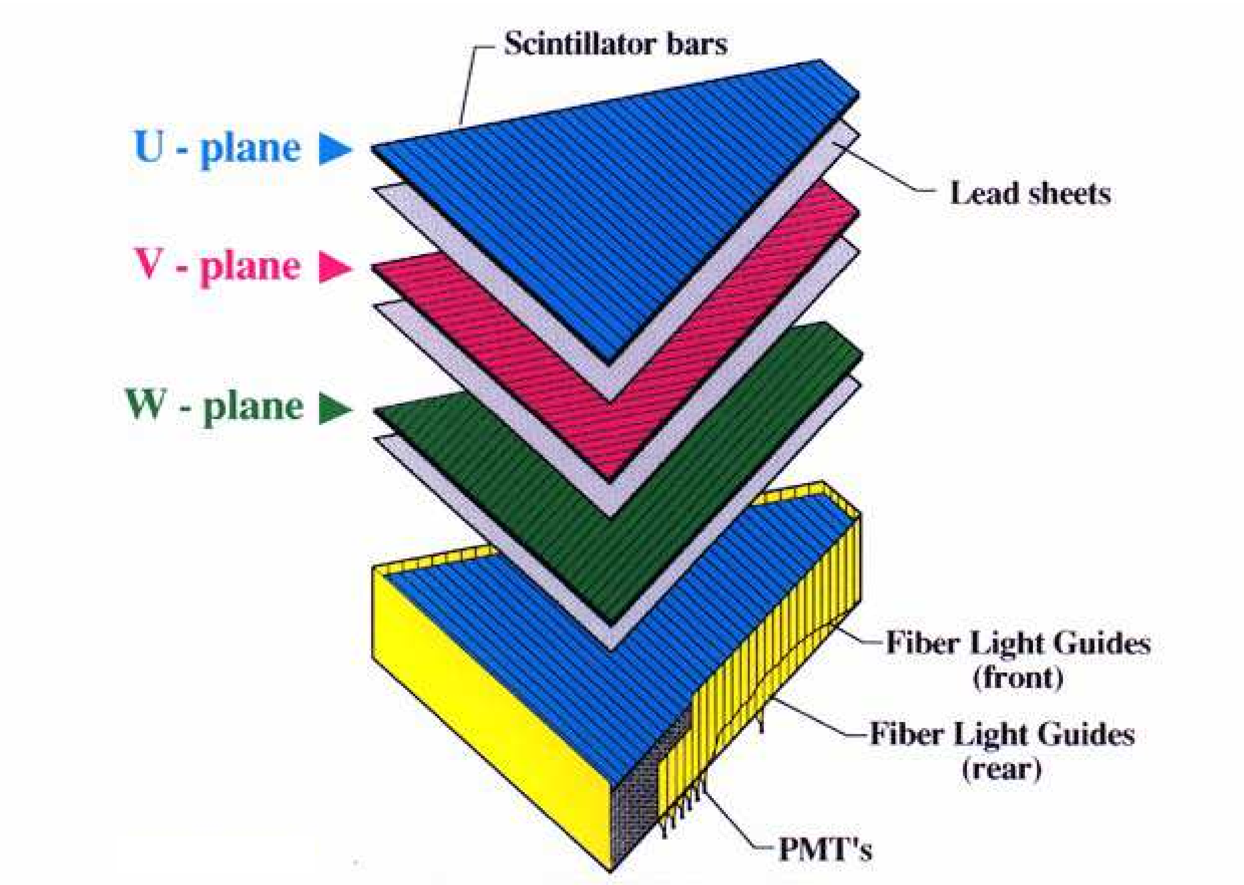

Figure 3.8: Exploded view of one of the modules for the electromagnetic calorimeter.

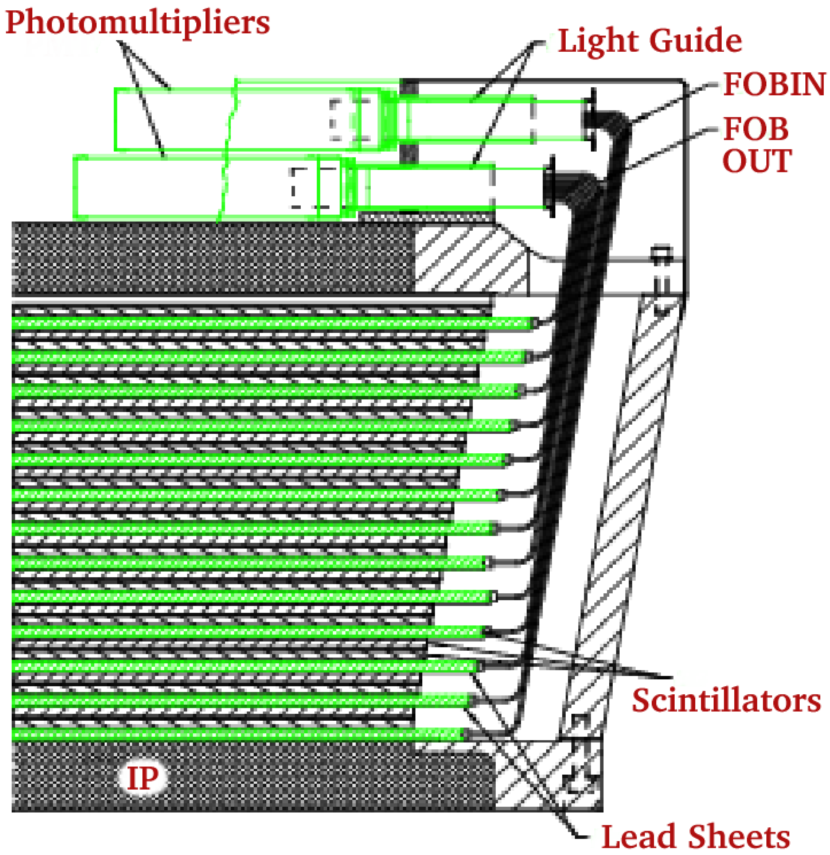

Figure 3.9: Schematic vertical cut of EC light readout system. PMT-photomultiplier, LG-light guide, FOBIN-fiber optic bundle inner, FOBOUT-fiber optic bundle outer, SC-scintillators, Pb-2.2 mm lead sheets, IP- inner plate(composite:two 1.905 mm stainless steel face sheets and 72.2 mm foam core plate).

This minimises shower leakage at the edges of the active volume and minimises the dispersion in arrival times of signals originating in different scintillator layers. Each layer is composed of 36 scintillator strips parallel with one side of the triangle, the orientation of the strips changing by 120^o between adjacent layers. This establishes three orientations labelled U, V and W which provide stereo information on the hit position. Each orientation contains 13 layers (figure 3.9) which are divided in to an inner and outer region containing 5 and 8 layers respectively. This allows improved hadron identification by longitudinal sampling of the shower.

3.3 Cryo-target

In the experimental run from which the data used in this analysis were taken, six targets were employed, two liquid (^{3}He and H_2) and four solid targets (CH_2, carbon, iron and lead). Of these, only two, the ^{3}He and hydrogen targets, were used in the data taking presented in this thesis. The liquid target was a cryogenic liquid which was filled into the conic kapton cell (figure 3.10). The cell had two aluminium windows in the forward and backward end and was surrounded by insulation material. There was a 15 μm aluminium plate at the front of this insulation. The whole construction was placed into a scattering chamber which is a cylinder with a spherical front and exiting cone. The target cell specifications are given in table 3.1.

	'Z' location (cm)	Material	Thickness	Inside dia.
Target cell inlet window	-6.50	Aluminium	15.0 μm	4 mm flat disk
Target liquid	—	^{3}He or H_2	5.00 cm	1.2 cm upstream 0.7 cm downstream
Target cell exit window	-1.50	Aluminium	15.0 μm	4 mm flat disk
Insulating foil	0.25	Aluminium	15.0 μm	5 mm
Scattering chamber exit window	23.5	Aluminium	71.0 μm	2.54 cm

Table 3.1: Liquid target dimension.

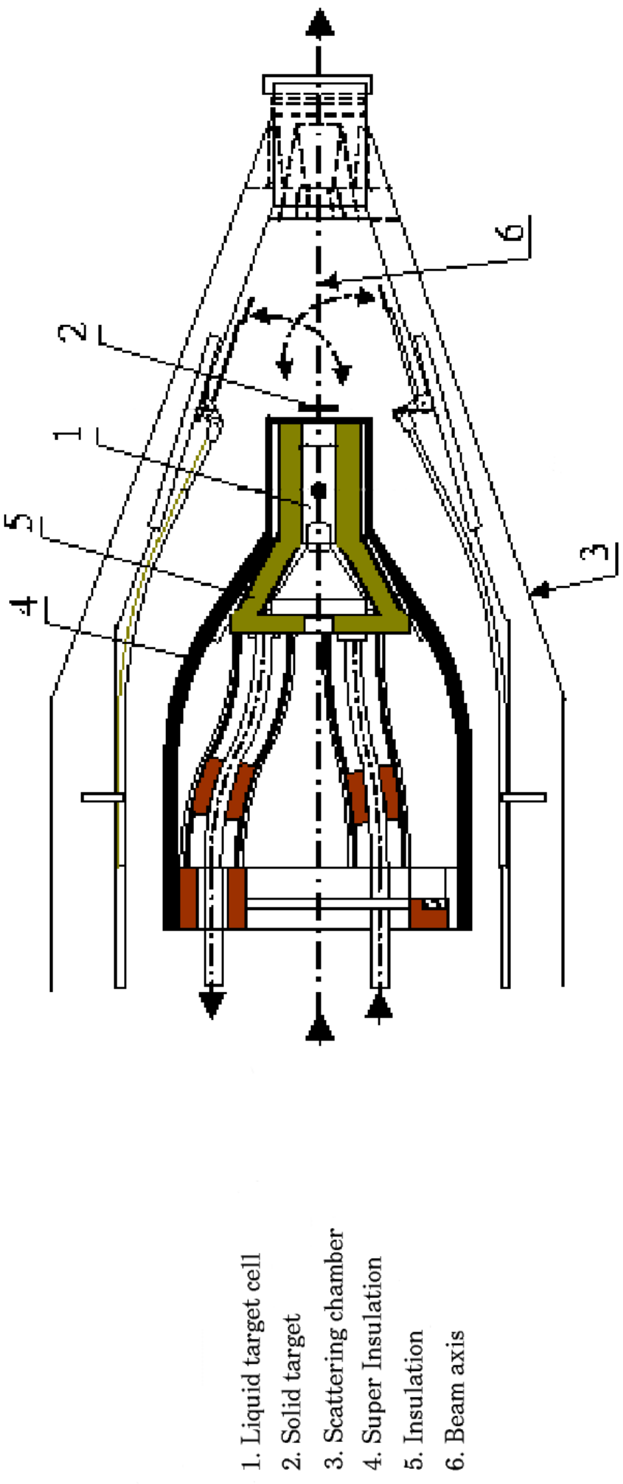

Figure 3.10: Schematic of the target used in the experimental run with the beam entering at the bottom of the diagram and exiting at the top. The two arrows in opposition, left and right of the beam line are the flow of the coolant for the cryo-targets.

3.4 Trigger and Data Acqusition

The trigger is designed to identify valid events for the data acquisition system (DAQ) for recording, and to separate these from background processes which are rejected. The trigger establishes the time bases for digitisation. It uses the hit pattern in the scintillator and Čerenkov layers and the energy deposited in the electromagnetic calorimeter. The specifications for the detector thresholds used during the run for the CC and EC are given in table 3.2. These values are tailored to the run specifications including the beam energy and torrus current. If the signal from an event is above threshold, the event is passed to the Level 1 trigger which requires a hit in the CC and EC in the same sector. Given electrons are all forward scattering, this condition indicates a potential electron and the event is stored through the data acquisition system.

Detector	Threshold (mV)	Threshold
Electromagnetic Calorimeter	100	0.250 GeV
Čerenkov Counter	20	$<$ 1 photo-electron

Table 3.2: CC and EC pretrigger thresholds.

The electronics of the DAQ are given schematically in figure 3.11. When a trigger is generated the signal proceeds to the Trigger Supervisor which commands the FASTBUS and VME controllers to read out. The data are digitised and transmitted through the Read Out Control memory to the network and Event Builder. From here, the data are given to the Event Recorder that stores them locally until they are transferred to the tape silo of Jefferson Laboratory.

After the events reach the Event Builder and subsequently the Event Recorder, they are passed to monitoring software (at about 20 Hz) that continuously monitors the status of the detector, and the beam and data quality. Mostly the monitoring involved occupancy plots of the various detector sub-systems, but an event viewer called CLAS Event Display (CED) is also used to show the detector hit patterns in the sub-systems. The primary run characteristics such as total number of triggers, integrated beam charge, average live time of the DAQ and the magnetic settings are stored in the CLAS online database.

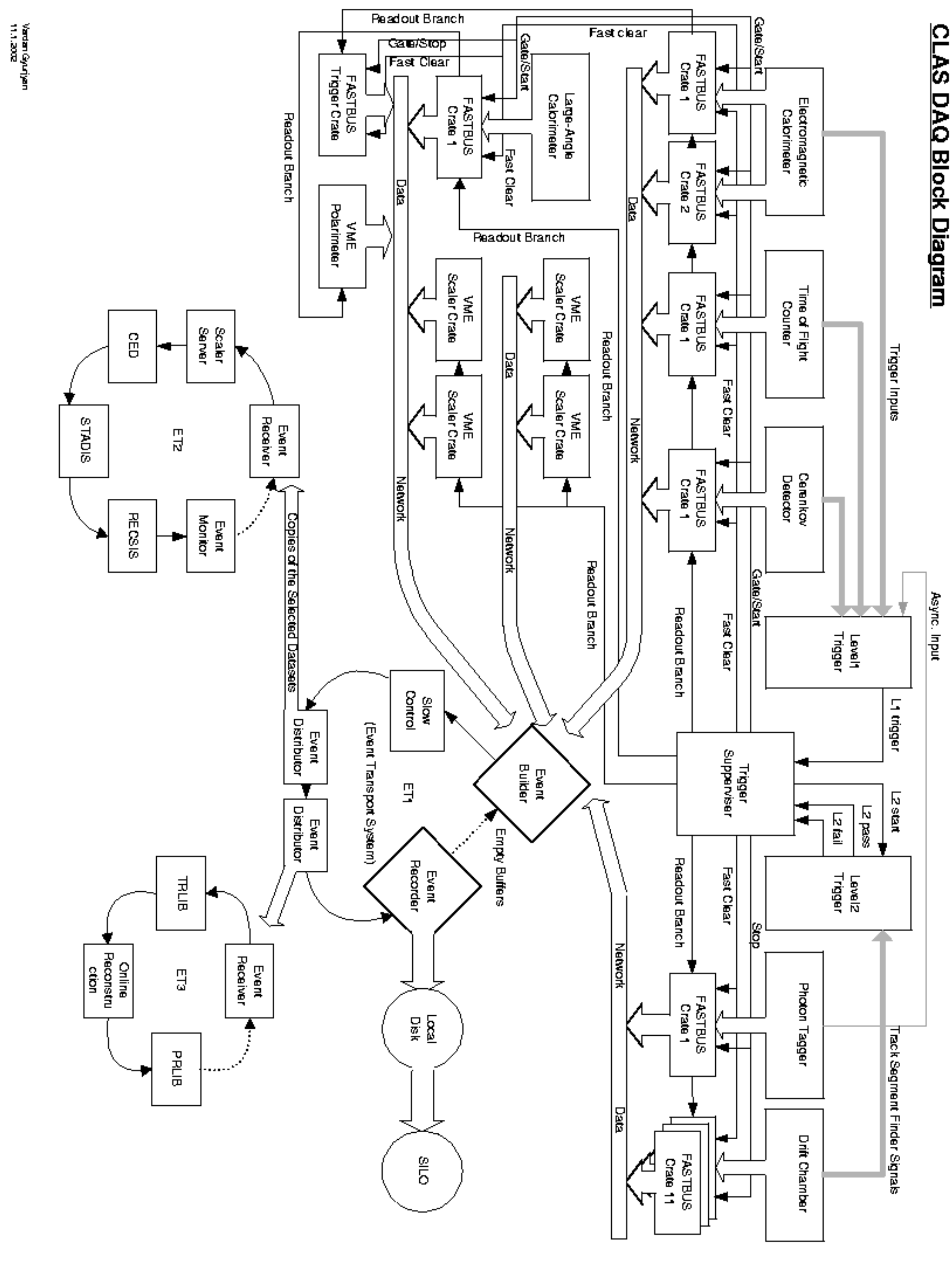

Figure 3.11: CLAS DAQ [82].

CHAPTER IV
COOKING AND CALIBRATIONS

Once a data run is complete and the data acquisition system (DAQ) has stored all triggered events in the data silo at Jefferson Laboratory, it is necessary, if any physics analysis is to be performed to convert the data from what is raw information provided by the many detector sub-systems to usable physics information such as momenta and particle identity. The process of the conversion is called "cooking" and requires calibration constants for each sub-system. The work was split amongst several people involved in the analysis of the experimental data. The "cooking" was performed by Gagik Gavalian[1], the drift chamber calibration by Alexei Klimenko[2], the time-of-flight detectors by Hovannes Bagdasaryan[1] and the calibration of the electromagnetic calorimeter was performed by myself.

4.1 Cooking

Processing the data, or "cooking", involves taking the output produced by the DAQ and converting the data into higher level information such as four-vectors [83]. The procedure is specific for each detector system and performed using a program called RECSIS (REConstruction and analySIS package). RECSIS takes the raw data files from the detector and obtains the necessary calibration constants to process the raw event information and generates an output file containing various reconstructed data areas that are the cooked file. This output is then used as input for monitoring and calibration programs. Some of the detector systems require the prior calibration of others and so a sequence of calibrations are performed (referred to as passes).

After all sub-system calibrations were completed, more cooking was performed in what was called the pass1 production. Only the specific data areas that are relevant for physics analyses for our working group were selected and put into a format called rootDst (root Data Summary Tape), where ROOT is the collection of Cern C++ libraries utilised in our analysis. The cooked data files were then stored back on the data silo as rootDSTs. These files were also copied to the Glasgow Nuclear Group work disks to allow analysis of the data to be performed at Glasgow instead of remotely.

[1] JLab, Newport News, Virginia

[2] Old Dominion University, Norfolk, Virginia

4.2 Calibration of Drift Chambers

The purpose of the Drift Chambers (DC) calibration is to refine the position measurements from time based tracking (TBT). By using a selection of runs evenly spaced throughout the run period the calibration constants for the time-to-distance function can be obtained. The time-to-distance function is the relationship between the closest distance from the track to the sense wire and the time it takes the electrons created by the particle to drift from the track to the sense wire. The frequency of the check depends on the run period.

When a charged particle passes through the drift chambers, in an ideal case each of the 34 layers record a hit. However, due to inefficiencies such as "holes" (dead wires in the chamber), the average turns out to be about 30 [79, 84]. These hits are used to reconstruct the particle tracks using a least squares fit, where a minimisation of the sum of squares of the closest distance from each hit wire to the track candidate is performed. The calibration is done by parameterising the drift velocity function for every superlayer in every sector [85,86]. The drift velocity function is the relationship between the calculated distance of closest approach of a particle track to the drift time. The drift time is defined to be the time needed for the ions created by the particle to drift to the sense wire. The TDCs attached to each wire measured the drift time. The initial function for drift velocity was parameterised using a trial function based on prior calibration. Using the aforementioned least square fit method the particle tracks were reconstructed and then used to geometrically calculate the closest distances which were then fitted against the drift time to improve the trial function. This improved function was used to reconstruct the tracks in an iterative process until the drift velocity function converged to the best parameterisation. [85,86]

4.3 TOF Calibration

The scintillator counters (SC) are essential for charged hadron identification. Without this, the determination of complex final states comprising protons, pions etc. would be impossible. The SC are essential since particle masses are obtained by combining the results from the Time of Flight (TOF) and momentum measurements. Additionally, as mentioned before, the calibration of some systems is dependent on that of others. This is true for the DC and EC time calibrations (described later) which require precise TOF measurements. The calibration of TOF [80,84,87] involves several steps that use not only time measurements, but also the energy deposited in the SC. The sequence of steps is; calibration of the individual TDC channels; left-right

PMT alignment and/or energy loss; attenuation length calibrations; effective velocity calibration; then counter-to-counter delay adjustment and after these, an overall RF (radio frequency) offset calibration.

TDC Calibration

The channel-to-time calibrations of all the CLAS TDCs, except those of the DC, were performed using a special pulser run for which the responses of each TDC for various delays between start and stop were analysed. A quadratic equation was used to convert the TDC channel number, T, to actual time t(ns):

$$t = c_0 + c_1 T + c_2 T^2 \tag{4.1}$$

The c_0 parameter was not relevant since a left-right calibration was performed later on.

Time-Walk Correction

Time-walk is an instrumental shift in the time measured using a leading-edge discriminator that is due to different time-rise in the analogue pulse for different pulse heights. The time-walk correction is implemented in the software using the function

$$t_\omega = t - f_\omega \left(\frac{A_P}{\tau} \right) + f_\omega \left(\frac{600}{\tau} \right) \tag{4.2}$$

where A_P is the pedestal-corrected ADC channel number, τ is the channel corresponding to the leading-edge discriminator threshold of 20 mV ($\approx$ 35 channels) and $f_\omega(x)$ is the time-walk correction function. The figure 600 corresponds to the minimum ionizing particle (MIP) channel setting, where $t_\omega \to t$. The correction function $f_\omega(x)$ is obtained for each PMT separately using laser calibration data. This is further described in [80, 84, 87].

Left-Right PMT Alignment

As described in section 3.2.3, each TOF scintillation counter has one PMT attached to each of the two ends. Each end measures the arrival time of the leading edge of the pulse generated by the PMT and the differences between the time measured at each end indicates the position along the length of the scintillation bar where the particle hit. Therefore, if the x coordinate is chosen such that 0 sits at the centre of the bar, the hit position x is

$$x = \frac{v\,(t_r - r_l)}{2} \tag{4.3}$$

where $t_{r(l)}$ is the time measured by the right (left) TDC and v is the velocity of light in scintillator (16 cm/ns). If the particle hits the centre of the scintillator bar, the time measured by the left end and the right end should be the same. However, cable length delays and PMT delays for the left and right ends are different so an offset adjustment was required. A description of this is given in [79].

A more detailed description of all steps is found in [80, 84, 88].

4.4 Electromagnetic Calorimeters

The calibration of the Electromagnetic Calorimeter was performed by me. The Electromagnetic Calorimeter (EC) in CLAS is essential to neutral particle identification. It is used to detect photons and neutrons and to distinguish between them the EC time measurement is used. This is because they can be separated only through their velocities. This means the neutron's time-of-flight is the only measurement of its energy since it doesn't deposit all of its energy in the calorimeter making the time measurement vital. The hardware design of the EC leads to some problems in making a simple calibration of the particle arrival time. As described in section 3.2.4, the scintillation bars have PMTs attached to one end only. Additionally, the EC is subdivided into inner and outer layers and in each layer five or eight scintillation bars share a single PMT for readout. These make determination of hit position very difficult and therefore make the determination of the time it takes for the light to travel from the hit position to the readout end difficult as well.

The Time-of-Flight electron times are used to calibrate the EC time. Since there is no magnetic field between the scintillator counters and the EC, the track of an electron is straight. If we assume that t_{sc} is correctly calibrated, the EC time measured should be:

$$t_{ec} = t_{sc} + \frac{d_{ecsc} cos\alpha}{v} \tag{4.4}$$

where d_{ecsc} is the distance between the EC and SC layers, v is the electron velocity and α is the impact angle to the EC plane (figure 4.2).

We use the following formula to reconstruct particle arrival time measured by the EC:

$$t_{EC} = p_0 + p_1 tdc + \frac{p_2}{\sqrt{adc}} + p_3 l^2 + p_4 l^3 - \frac{l}{v_{eff}} \tag{4.5}$$

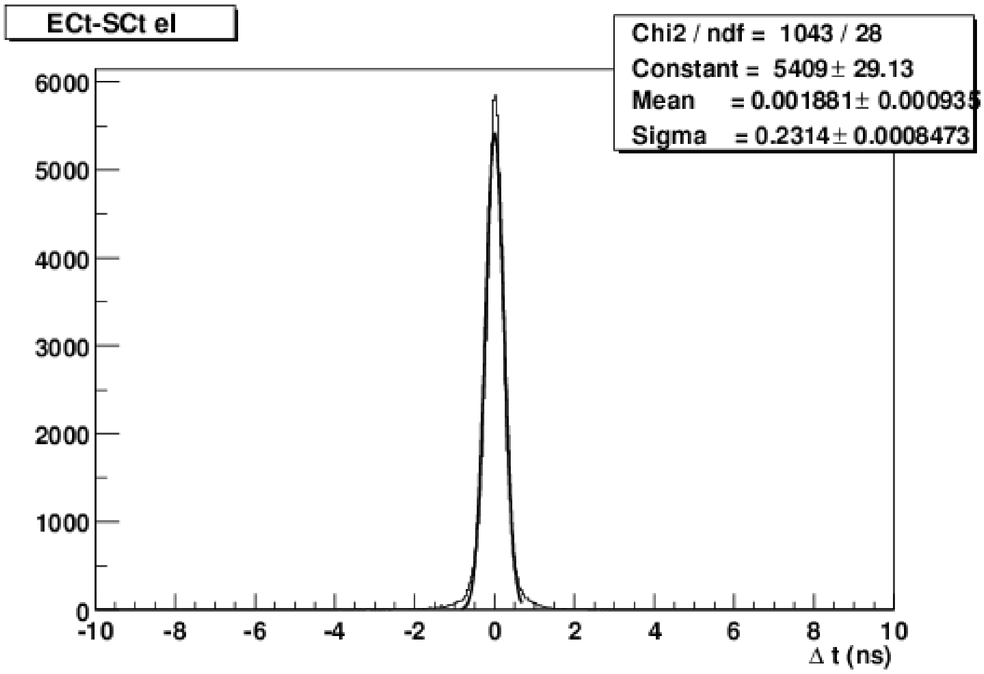

Figure 4.1: The distribution of the difference between the electron arrival time measured by the EC and that extrapolated from the SC measurement for the EC sector one.

where p_i are five fit parameters, tdc and adc are the TDC and ADC values, l is the length from the hit point to the EC readout edge and v_{eff} is the speed of light in the scintillator material. The first two terms $(p_0 + p_1 tdc)$ represent the simple linear TDC response. The third term $\left(p_2/\sqrt{adc}\right)$ is the correction to the time-walk effect of the signal pulse. The fourth and fifth terms $(p_3 l^2 + p_4 l^3)$ are small corrections for the fact that signals arrive at the readout edge at slightly different times for the scintillation bars connected to the same PMT. The last term (l/v_{eff}) is the compensation to the time for the scintillation light to travel from the hit position to the readout edge.

Because the arrival times of the electrons are measured by both the EC and SC, the calibration can be done by comparing these measurements with the assumption that the SC figures are accurate. After the calibration, the calibration constants are only used for neutral particles arrival time reconstruction. For electrons, the time measurements from the SC are used, since these are regarded as more accurate. The difference between the reconstructed EC time and the Time-of-Flight value defines the time resolution for the electrons (figure 4.1). The time resolution for electrons was found to be approximately 200 ps [79]. A more detailed description of the EC calibration procedure is found in [79].

4.5 Particle Identification

In our study electron identification is essential to CLAS electro-production data analysis since the electrons are the trigger particles. Also, the identification of other particles is strongly dependent on identifying the electrons correctly along with their precise timing information. Mainly it is negative pions that can be misidentified as electrons and must be accounted for. The way this is done is by looking at how the two have different behaviours in the CLAS detectors.

During the cooking process, certain criteria are applied in the identification [79]. Firstly, an event is recorded only when there was at least one negative track which geometrically matched hits in the Electromagnetic Calorimeter and Čerenkov Counters. This requirement was of a hit in the EC and CC was mentioned previously as the trigger condition. If an event had only one negative track, it was considered to be an electron. If there were several, the one which matched the electrons characteristics best such as matching hits in the EC, SC, CC and so on, was taken as the electron candidate. Finally, after the identification was made, time of flight and momentum analysis was used to identify other particles.

Whilst the above criteria match the particle track to the trigger condition, they aren't very good at rejecting pions matching the same condition. To do, this more precise methods of discrimination must be applied.

4.5.1 Cut on Total Energy Deposited in the Calorimeter

One of the discriminations that can be made between the electron and the pion is how it deposits energy in the electromagnetic calorimeter. Pions only deposit a small amount of energy in the EC compared to electrons and during data taking a hardware threshold for the EC is set to minimise pion contamination. Some pions could however pass the threshold and still register as a trigger. We therefore put an additional software threshold to reject these pions which typically deposit small amounts of energy. Figure 4.3 shows the distribution of the total energy deposited in the EC for electron candidates. The threshold is set at 0.08 GeV.

4.5.2 Cut on Inner Layer of Calorimeter

As described in section 3.2.4, the EC is split into an outer and inner layer. The amount of energy a minimum ionising pion deposits in the inner layer of the

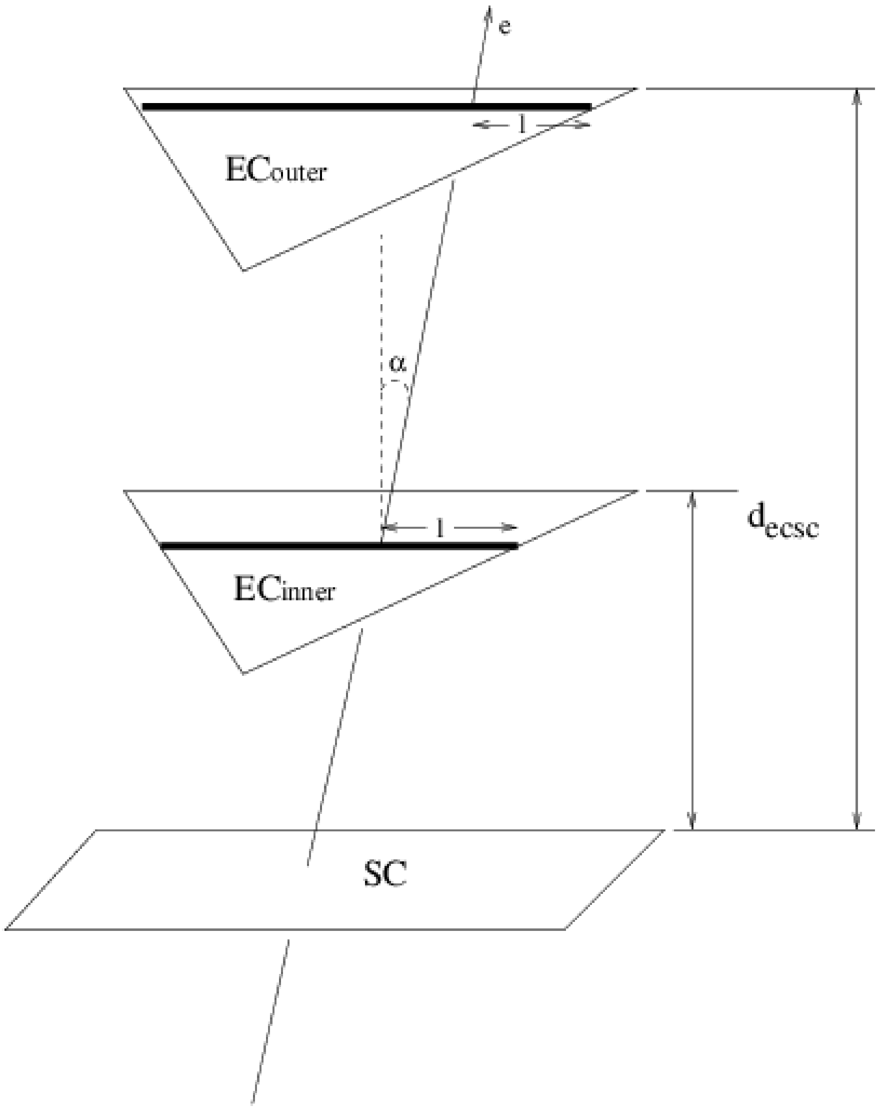

Figure 4.2: EC time extrapolation from SC time. d_{ecsc} is the distance between the EC layer (inner or outer) and the SC layer, α is the electron impact angle to the EC plane and l is the length from the hit point to readout edge along the scintillation bar.

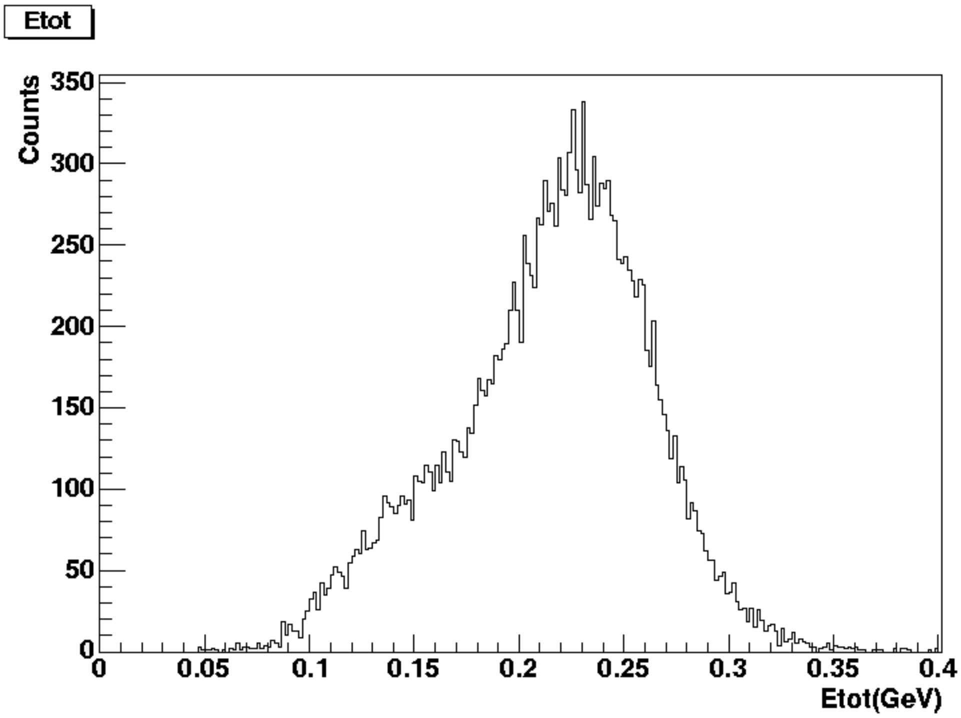

Figure 4.3: Total energy deposited in electromagnetic calorimeter for electron canditates. A software threshold is put at 0.08 GeV.

calorimeter depends only on the material and the thickness of the calorimeter layer. This is independent of the pion's momentum and is small compared to the electron case. Figure 4.4 shows the energy deposited in the inner layer of the EC for electron candidates. The small bump at low energy corresponds to pions. A cut is placed at 0.055 GeV to remove these pions.

4.5.3 EC Sampling Fraction

The total energy deposited in the scintillators is measured as a fraction of the incident particle's energy. This fraction, which is called the EC sampling fraction is about 0.3 [81]. Figure 4.5 shows the scatter plot of the total deposited energies vs. the momenta (since the electrons are travelling at almost the speed of light, the energy and momentum are equivalent). There is a band with the sampling fraction centering at about 0.3 showing the good electrons. By slicing along the y-axis and performing a Gaussian fit of each slice, the centre and width of the band at the slice can be determined [89]. Cuts are placed at three times the standard deviation above and below.

Using the above procedures accurate identification of the electron can be performed and general particle identification can be made with good accuracy.

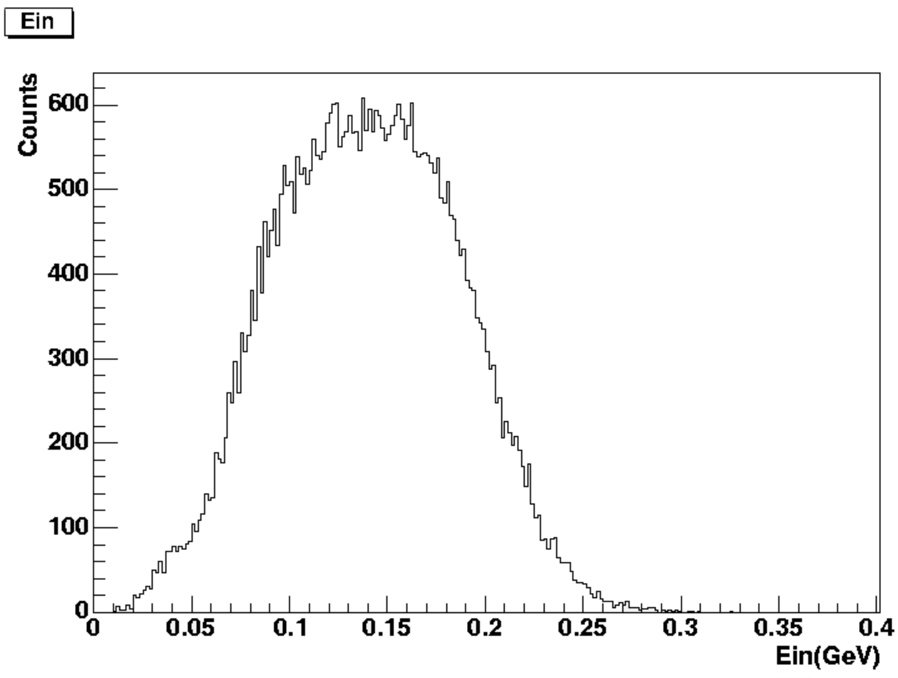

Figure 4.4: Energy deposited in the inner layer of the electromagnetic calorimeter for electron candidates. The small bulge on the left corresponds to minimum ionising pions. A cut is placed at 0.055 GeV for these.

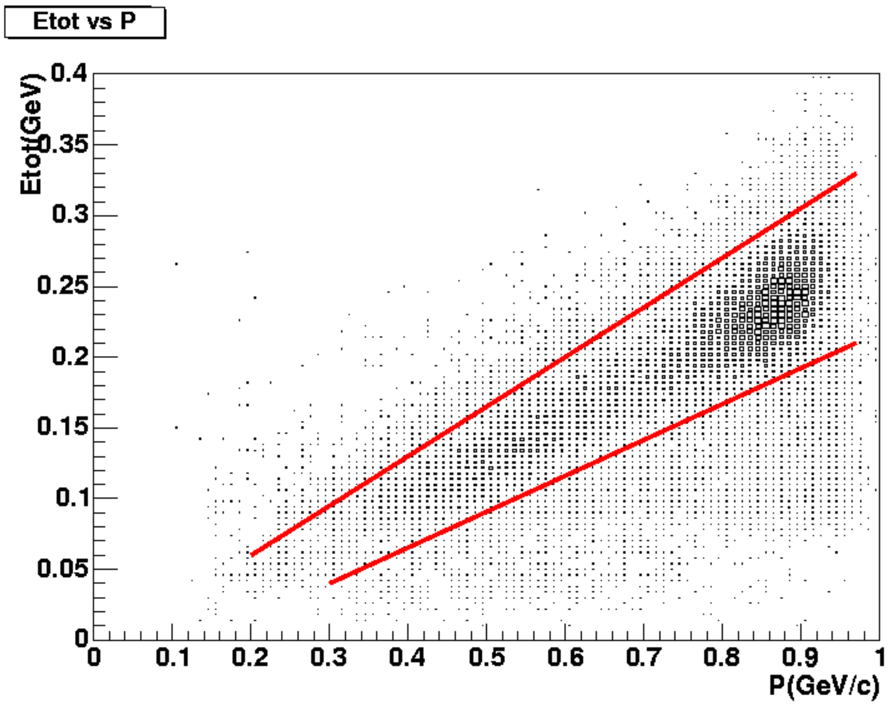

Figure 4.5: Total energy deposited in calorimeter vs. the momentum for electron candidates. The two lines indicate the 3σ cut around the centre of the electron band.

CHAPTER V
DATA CUTS AND CORRECTIONS

In order to perform cross-section calculations and extract meaningful information, it is necessary to ensure the data being analysed is "clean". In addition to cutting data whose validity is lacking or suspect, an account must be made for the fact that the map of the magnetic field of CLAS has altered since its construction and measurements and adjustments have to be made to account for this. After the detector cuts and corrections, as a final guarantee that the data are "good", kinematic cuts are applied. All of these mean that not only are we confident about the measured particle IDs and four vectors, we are also certain that the particles in an event originated from the decay channel specific to our analysis. The various stages of corrections and cuts to provide this quality are outlined in the subsequent sections of this chapter and the next. They include,

- Detector cuts and corrections; vertex cuts, electron momentum correction and fiducial cuts.

- Kinematic cuts for channel selection; missing energy cuts and opening angle cuts.

The various stages are shown diagrammatically in figure 5.1.

5.1 Vertex Cuts

The helium target is contained within a liquid target cell. It is necessary to ensure that the particles detected in the final state originated in the target. Therefore empty target data taken with the target cell was used to identify the contribution from the cell material and the spatial boundaries of the cell edges. From the plot of Event Vertices (figure 5.2), both cell windows can be seen (where the x-axis is the beam line) as peaks. The origin corresponds to the centre of CLAS so that the plot shows our target cell to be positioned with its rear window at this location. The double peak at the back of the target cell corresponds to the target window for the first peak and aluminium foil on the insulation after. Fitting these peaks with a Gaussian, or double Gaussian in the case of the second peak where the aluminium foil is contributing, the centroid is used with a 1.5σ reach to define the perimeter of the target cell. These parameters are used to cut on events ensuring all particles being analysed originated within the target cell.

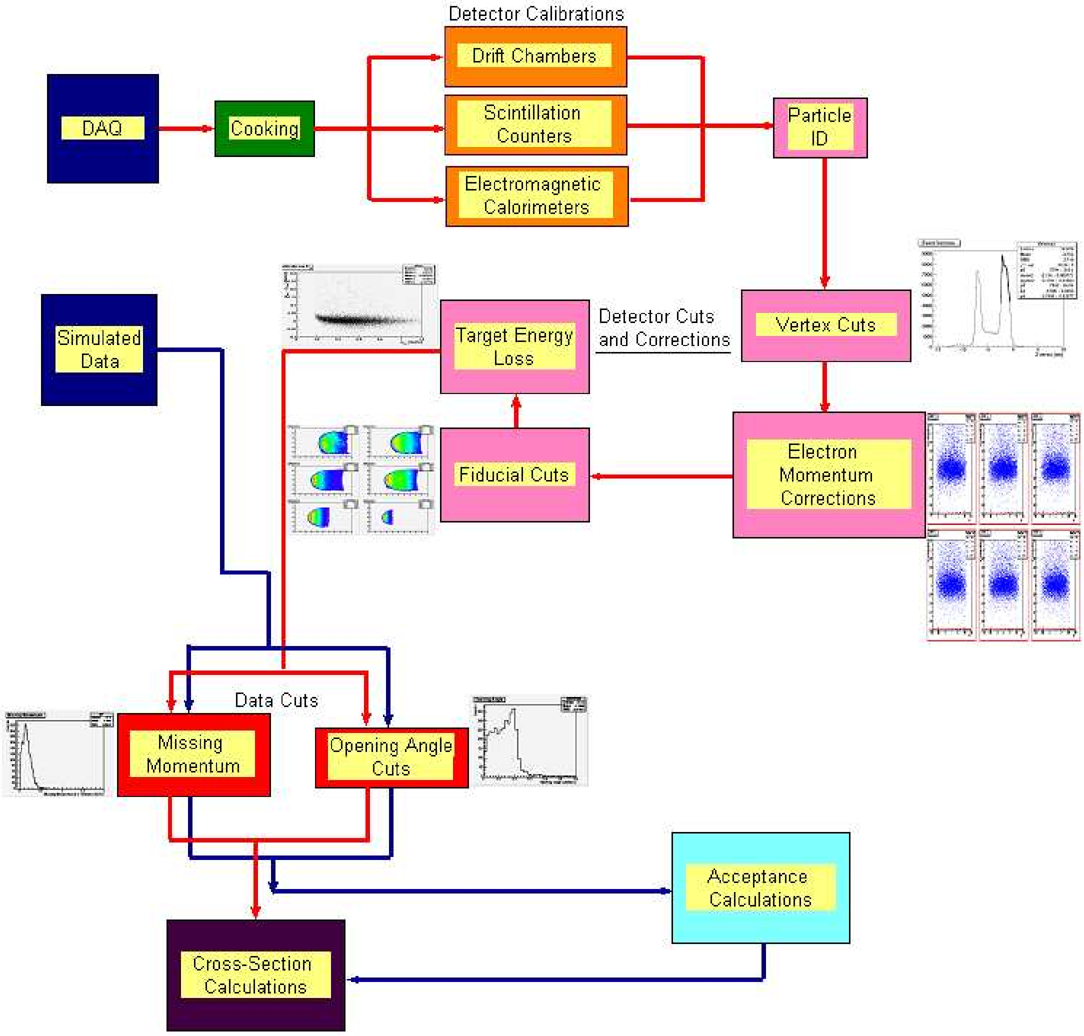

Figure 5.1: The various stages of cuts and corrections to prepare the data for the analysis. The simulations included fiducial cuts, but no other cuts or corrections.

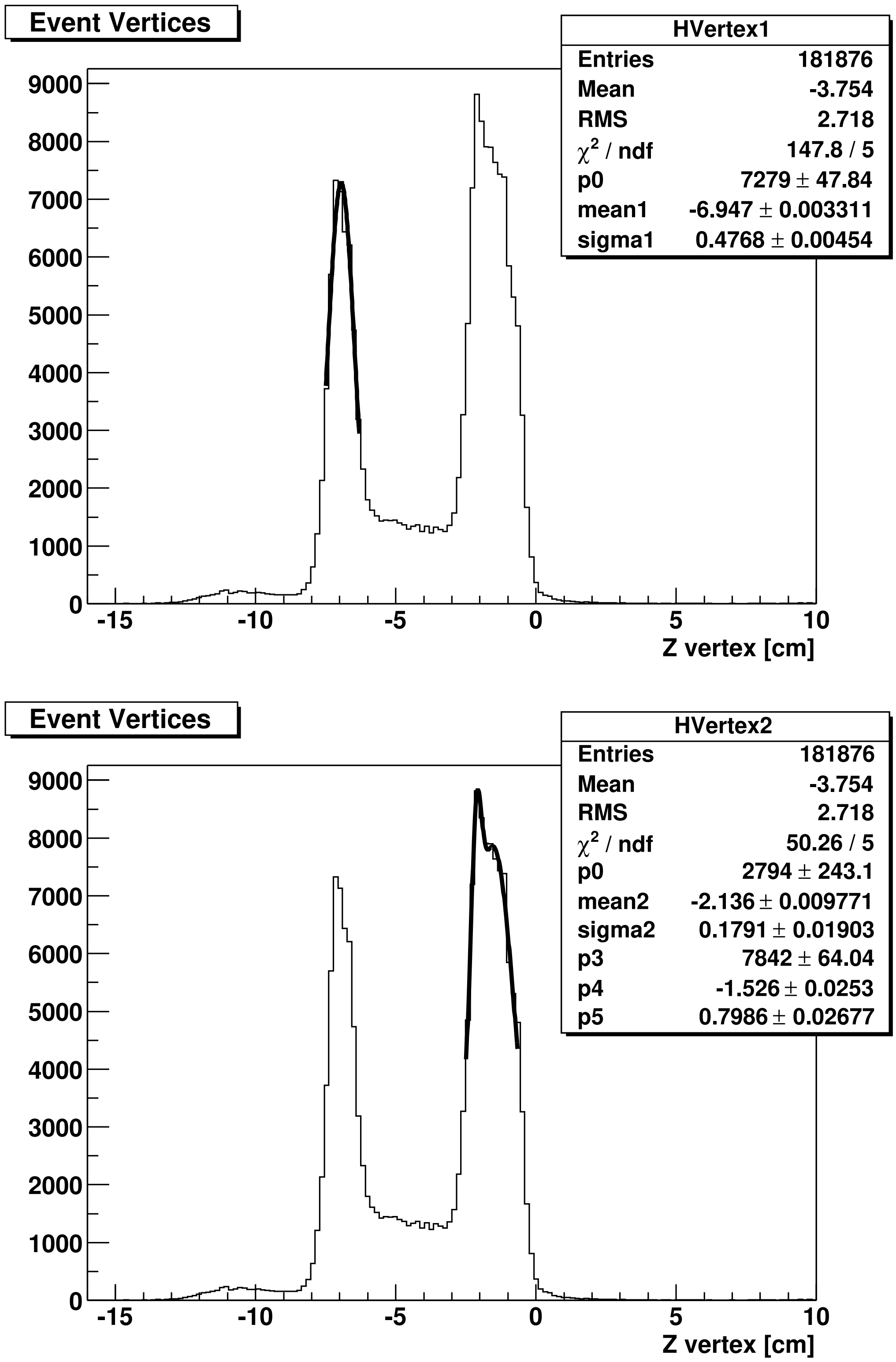

Figure 5.2: The event vertices on an empty target run provide the positions of the target cell edges.

5.2 Electron Momentum Corrections

The CLAS detectors toroidal magnetic field is complicated and our knowledge of the field mapping is incomplete. This leaves uncertainty in the measurements of the momentum vectors [90]. To address this difficulty, a correction function must be introduced to correct the momentum as a function of its orientation. This correction function is obtained using as a reference a well known process.

The well known process used is the elastic scattering of an e^- from a free proton (hydrogen target). From the invariant mass spectrum the range for W around the proton mass is selected from 0.85 to 1.1 GeV/c^2 (figure 5.5). We filter out data with $\theta < 16^o$ since this corresponds to the hole at the front of CLAS. The assumption is that the correction determined in the elastic region holds for the whole spectrum.

5.2.1 Method

The function employed depends on the momentum of the electron, p, as well as its angles θ and ϕ. Variations from sector to sector also have to be factored into the function. So we end up with the corrected momentum being a function of all these variables; $p_{corr} = f(p, \theta, \phi, s)$ where p_{corr} will be the true value of the momentum.

Since the main uncertainties are due to the distribution of the torus field and angles mainly defined by DC geometry, we assume that the angles are measured correctly and the magnitude of the momentum needs to be corrected. There exists in the detector a correlation between the range of ϕ and θ of a detected particle due to the detector geometry. At large θ, the majority of particles detected are far from the edges of the sectors and well within the fiducial region. However, at smaller values of the polar angle where the sector edges take more of the azimuthal range, effects from the magnetic coils proximity are more significant. Whilst these effects must be kept in mind, the fiducial cuts (section 5.3) will almost completely eliminate them. We can separate out the θ and ϕ dependence into two different functions (f_1 and f_2) for each sector. We can now derive the angular dependences separately to get an overall correction function.

5.2.2 Correction Functions

The correction functions used are the ratios between the calculated electron momentum and the measured momentum for individual sectors.

$$f_i(\alpha_i, s) = \frac{p_{calc}(\alpha_i, s)}{p_{exp}} \quad \alpha_1 = \phi, \alpha_2 = \theta \tag{5.1}$$

Where p_{exp} is the measured momentum. We obtain the calculated momentum p_{calc} as follows:

$$p_{calc} = \frac{E_{beam}}{1 + E_{beam}(1 - cos\theta)/m_p} \tag{5.2}$$

E_{beam} is the energy of the electron beam and m_p the proton mass. There are no ϕ terms in this equation and we therefore calculate the function f_1 with the assumption of isotropy in ϕ.

If we plot the calculated ratios for each event against ϕ (figure 5.3), we can then take strips in ϕ and fit these with a Gaussian. The means are plotted for these fits against ϕ again and the distribution of these can be fitted with a polynomial function. This polynomial function is used as the correction function $f_1(\phi, s)$.

As stated, the ϕ and θ dependence are separate. Now that the correction for ϕ is done the same method can be repeated for parameterising $f_2(\theta)$ (figure 5.4). For both cases, it has to be decided which algebraic functions are best, and it has been found [84, 90] that the most suitable are,

$$f_1(\phi, s) = P_2(\phi, s) \quad f_2(\theta, s) = a_s + P_2(\theta, s).e^{-\theta} \tag{5.3}$$

P_2 is a second degree polynomial and a_s is a fit parameter.

In ϕ the correction is parabolic and fits very well in the region of interest. If at the extremities something goes awry, it isn't important as the fiducial cuts will deal with these.

The correction in θ is more complex where at larger values of θ the function $f_2(\theta)$ reaches a plateau. To get around this, we insert the offset a_s and the inverse exponential $e^{-\theta}$ which forces the polynomial into a flat horizontal curve in the region roughly above 25^o (figure 5.4). In the region $\theta < 16^o$, the function is not guaranteed to hold, however, we are not interested in θ in this range.

5.2.3 Momentum Correction Results

The process of the fitting procedures and parameterisation produces a set of 42 parameters corresponding to the properties of the fit functions which are used to correct the measured momentum from our data. The effect of this correction can be seen in comparing figures 5.5 and 5.6. Notice that the quasi-elastic peak before the correction, was centered on ~940 MeV/c^2. This isn't greatly different from the

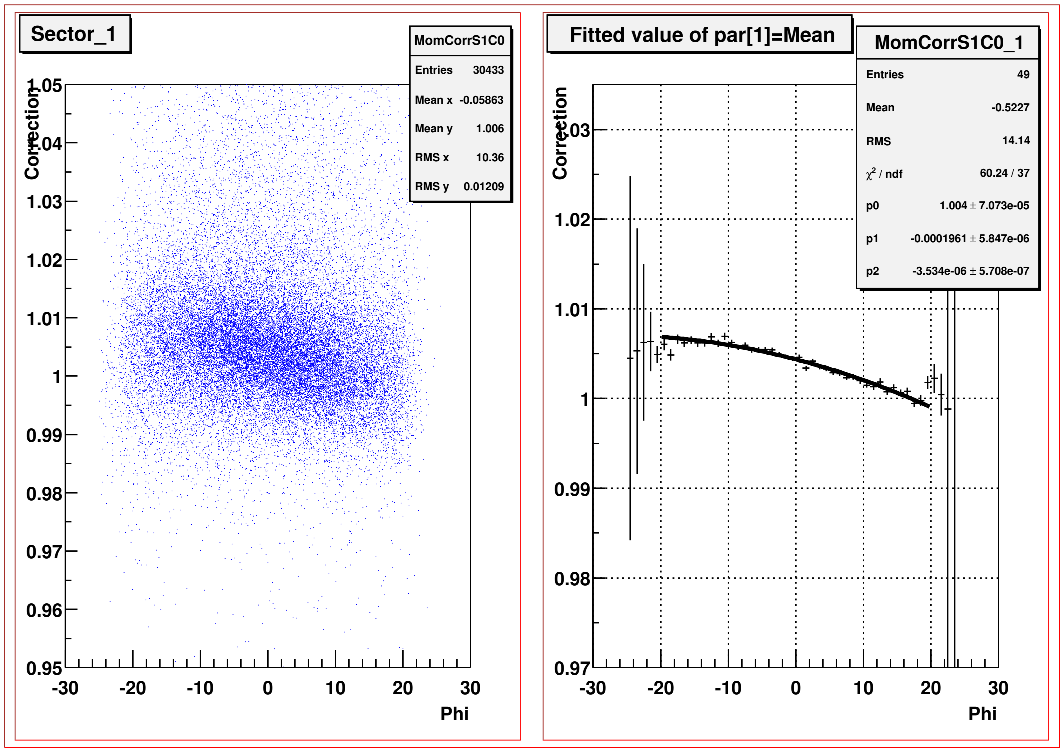

Figure 5.3: The correction function f_1 is derived by fitting slices in ϕ with Gaussians and using the means to obtain the second function used for the ϕ dependence.

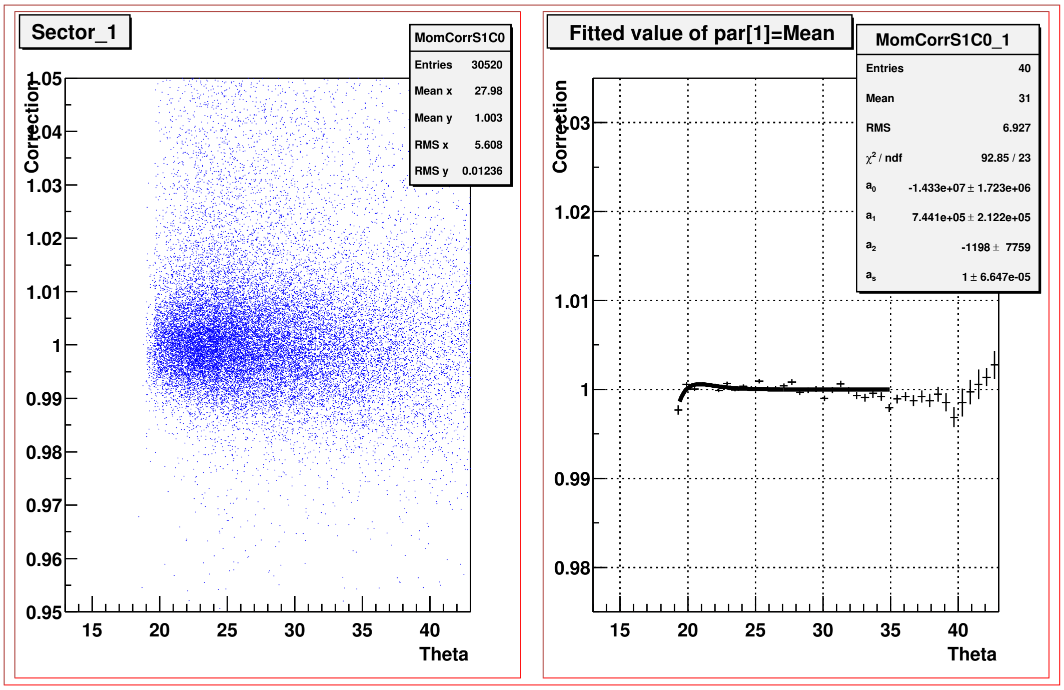

Figure 5.4: The correction function f_2 is derived in the same fashion as f_1 using θ.

proton mass (938 MeV) but still it is necessary to account for this discrepancy for completeness. After the corrections are calculated and applied we obtain figure 5.6 which now has the quasi-elastic peak centered where it should ideally be, on 938 MeV/c^2. The corrected momentum now gives what would be expected if the magnetic mapping were known in detail. What must be remembered is the assumption that the ϕ and θ dependences are independent. This assumption can be verified by observing the ϕ distributions of the correction function for different ranges of θ. As can be seen in figures 5.7 and 5.8, the distribution in ϕ is unaffected by selecting different ranges of θ. We chose to correct the modulus rather than the orientation of the electron momentum vector.

5.3 Fiducial Cuts

5.3.1 Electron Fiducial Cuts

The CLAS detector systems arrangement of six super conducting coils are designed to generate a toroidal magnetic field. This field bends particles towards or away from the beam line depending upon their electric charge. Electron detection efficiency around the mid-plane of each sector (furthest from the field coils) is reproducible in the GEANT (GSIM) simulation package. Due to the complicated readout structures of the EC and CC, detection and reconstruction efficiencies are not well understood in the regions closest to the field coils. For this reason, only events that are within what is defined as the fiducial regions are used for analysis and those outside are discarded.

Fiducial cuts for electrons define a region in the production (θ,ϕ) space for a given momentum where detection efficiency is almost constant in the azimuthal angle (ϕ) and can be reproduced in simulations. The region is enveloped by a doubly-curved surface passing through the three-dimensional (p,θ,ϕ) space. We define the uniform acceptance region to be the plateau contained between the two drop-off's observed in a Counts vs. ϕ plot (figure 5.11) at a given p and θ, the drop-off corresponding to the sector edges.

For this analysis a fiducial region was defined by performing two steps:

I Select "good" electrons with cuts on the forward electromagnetic calorimeter (EC).

II Select flat acceptance regions for small bins of momenta in θ and ϕ space.

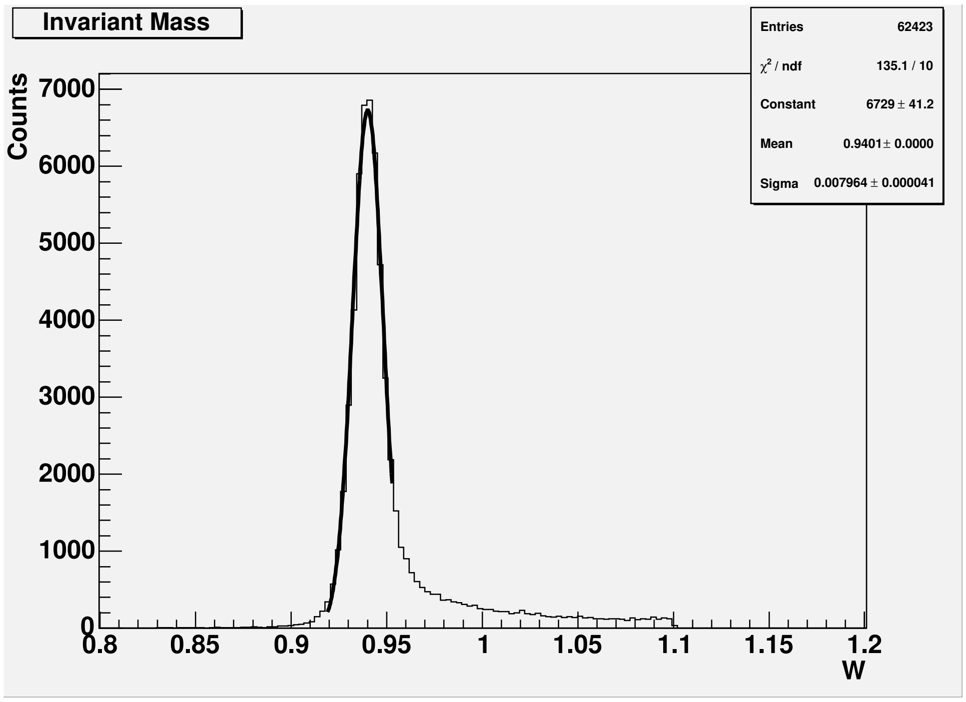

Figure 5.5: Before corrections are applied, the quasi-elastic peak is centered on ∼940 MeV/c^2.

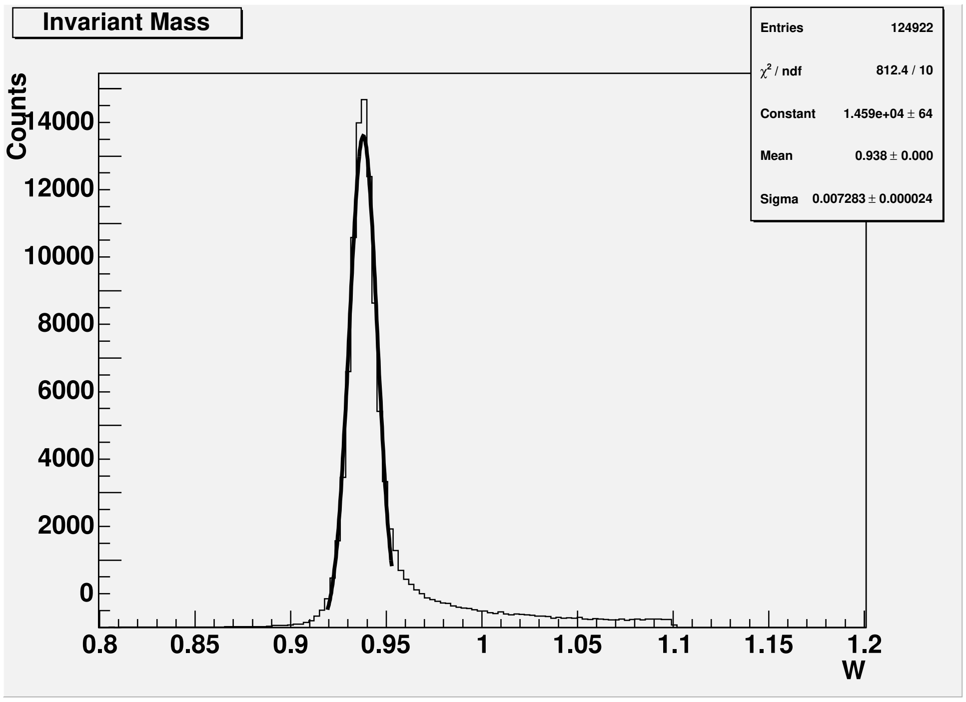

Figure 5.6: After corrections, the quasi-elastic peak is now centred on ∼938 MeV/c^2.

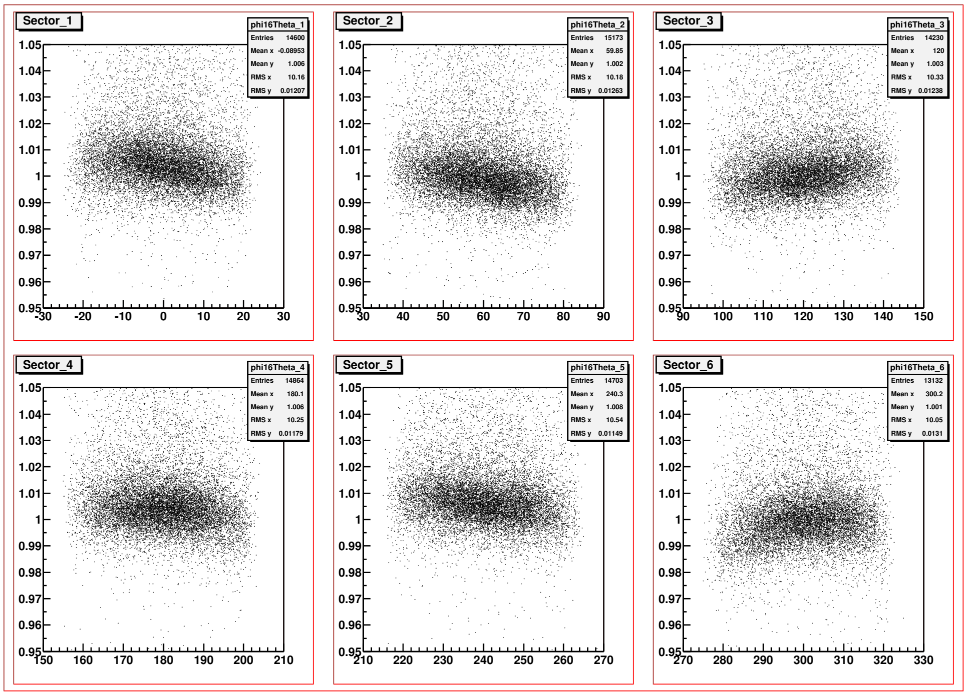

Figure 5.7: ϕ distribution of correction function for $\theta < 25^o$.

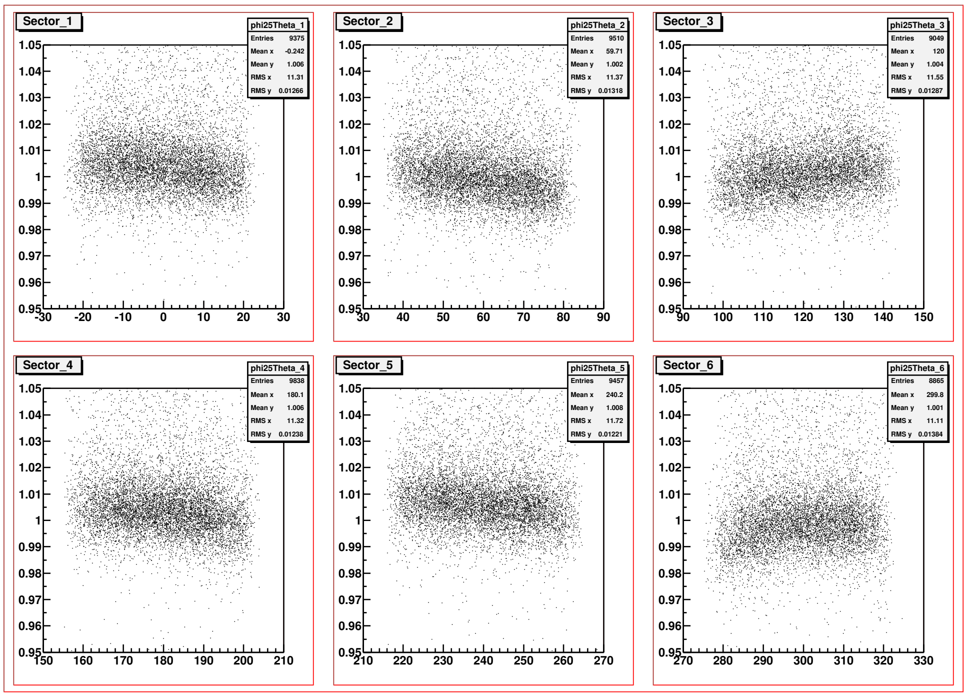

Figure 5.8: ϕ distribution of correction function for $\theta > 25^o$. Compare to 5.7 to see that the ϕ and θ dependence are independent i.e. the ϕ distribution is the same in different ranges of θ.

Forward Calorimeter Cut

The first of the cuts is purely a geometric one, eliminating angular locations where problems exist. Since the ratio of the deposited energy in the EC to the momentum measured in the DC is the main tool for π/e rejection, the fiducial region is where the electron distribution is constant in ϕ after a cut on deposited energy. In locations where the energy is not as it should be (due to shower leakage etc.), these regions are eliminated. As described previously, the EC is arranged in three planes denoted U, V, and W. The U plane scintillator bars are perpendicular to the beam axis, while the bars of the remaining planes are rotated by 120^o. In figure 5.9 the distributions of electrons on the calorimeter views are shown. This defines the natural system of coordinates that are used for defining the geometric cuts.

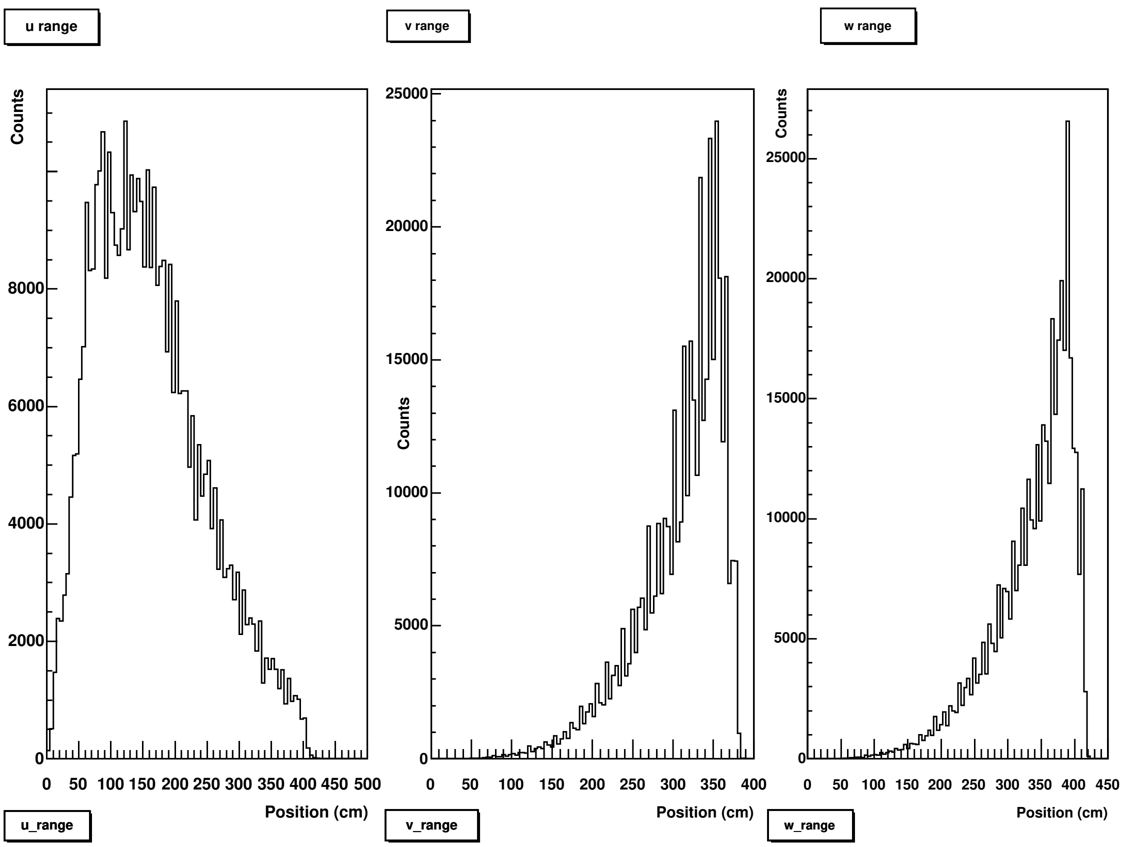

Figure 5.9: The energy deposition distributions of the three views of the EC system.

As a first step in this cut, only electrons with a ratio of deposited energy to momentum greater than 0.2 are selected ($E_{EC}/p > 0.2$). This ratio is called the sampling fraction (figure 5.10) and the design of the detector fixes this value to about

0.3. It is clear from figure 5.10 that near the edges of the detector there is a drop as energy is lost from shower leakage. By setting a limit at these drop-off's, the values of the cuts were determined to be:

$$u > 60cm, v < 360cm, w < 396cm, E_{EC}/p > 0.2 \tag{5.4}$$

Uniform Acceptance Region

Figure 5.12 shows some typical (ϕ,θ) plots after the forward calorimeter cut has been applied. The energy range was divided into small bins and then for each energy bin and each sector two-dimensional distributions of events in the θ and ϕ plane were studied. The plots in figure 5.12 show a well contoured semicircle with the edges showing a low number of events. The solid region inside this is where we wish our events to come from, this is the flat acceptance region and we discard all events outside of this. To do this, we fit the contour with a function ϕ (θ,E_n,s), where E_n is the energy bin, s the sector and θ the angle. To define this "flat" region, we slice the two-dimensional plots into θ bins and fit these with a trapezoidal function.

$$y = \begin{cases} 0 & if \quad x \leq p_0 \\ p_4(x-p_0)/(p_1-p_0) & if \quad p_0 < x \leq p_1 \\ p_4 & if \quad p_1 < x \leq p_2 \\ p_4(x-p_3)/(p_2-p_3) & if \quad p_2 < x \leq p_3 \\ 0 & if \quad x > p_3 \end{cases} \tag{5.5}$$

Some examples of the trapezoidal fits can be seen in figure 5.11 showing the top horizontal part of the trapezoid to be our "flat" acceptance region. The points at which the distributions drop away are logged and their values used in the analysis software to create an array of coordinates where each event being analysed is passed or cut according to where it is detected.

These points can be defined with a function used to define the fiducial region. The function ϕ=ϕ(θ,E$_n$,s) is dependent on the polar angle θ of the particle, the sector and the energy bin. The function can be well described with the form:

$$\phi(\theta) = \begin{cases} b(1-((\theta-t_0)a/b+1)^{-1}) & if \quad t_0 < \theta < t_1 \\ 0 & otherwise \end{cases} \tag{5.6}$$

where the coefficients a, b, t_i contain the dependency on E_n and s. The actual angle ϕ is obtained by scaling this formula for each sector thus:

$$f_{0,1}(\theta, E_n, s) = 60(s-1) \mp \phi(\theta) \tag{5.7}$$

where the + is used for the upper region (using a_1, b_1, t_0, t_1) and the - is for the lower region (using a_0, b_0, t_0, t_1).

A fuller description of this procedure with additional plots can be found in [91].

Summary

Figure 5.13 shows the effect the cuts have on the data. Where there was a blurred and ill-defined edge near the sides of each sector, there is now a well defined region from where we can be confident in the events being analysed. About one third of electrons are removed by the fiducial cuts, the majority of which come from the higher momentum region. This is because higher momentum electrons are directed at small $\theta_{e'}$ where the $\phi_{e'}$ acceptance is small.

To implement the fiducial cuts, the fit parameters derived above are loaded into our analysis code. Equation 5.7 was used to select the regions where particles are regarded as "safe" and beyond which the fiducial cuts were applied.

5.3.2 Proton Fiducial Cuts

As with the electrons, we must apply a similar treatment to define a fiducial region for the protons where there is a flat efficiency. The same technique as in the electrons case can be applied making adjustments for different kinematics and the variation due to these from the magnetic field. Figure 5.14 shows the distribution of the protons before any cut is applied to them (top plot) and the selection of a flat acceptance region after the cut parameters have been determined and applied to the data distribution (bottom plot).

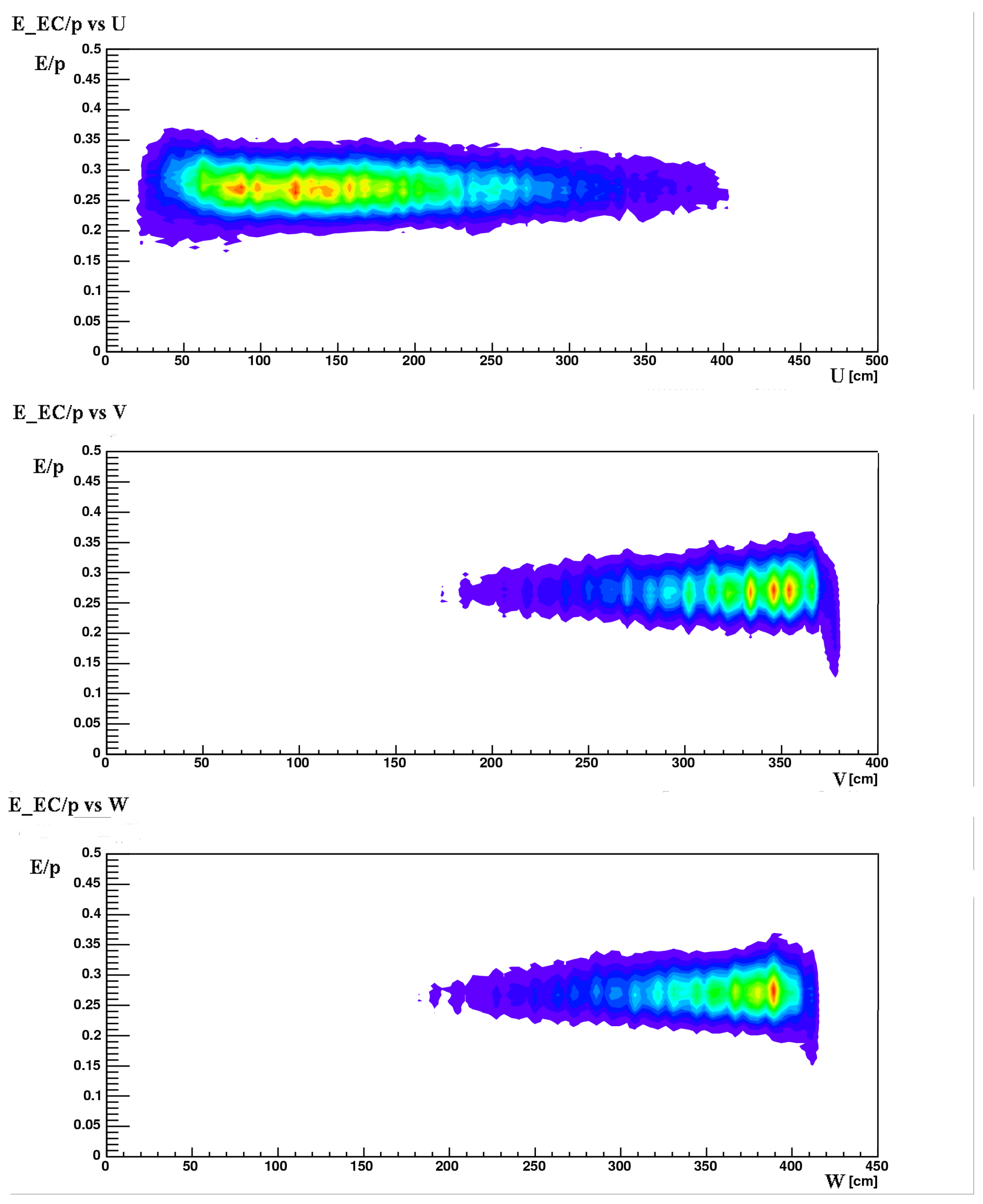

Figure 5.10: The sampling fraction for the EC.

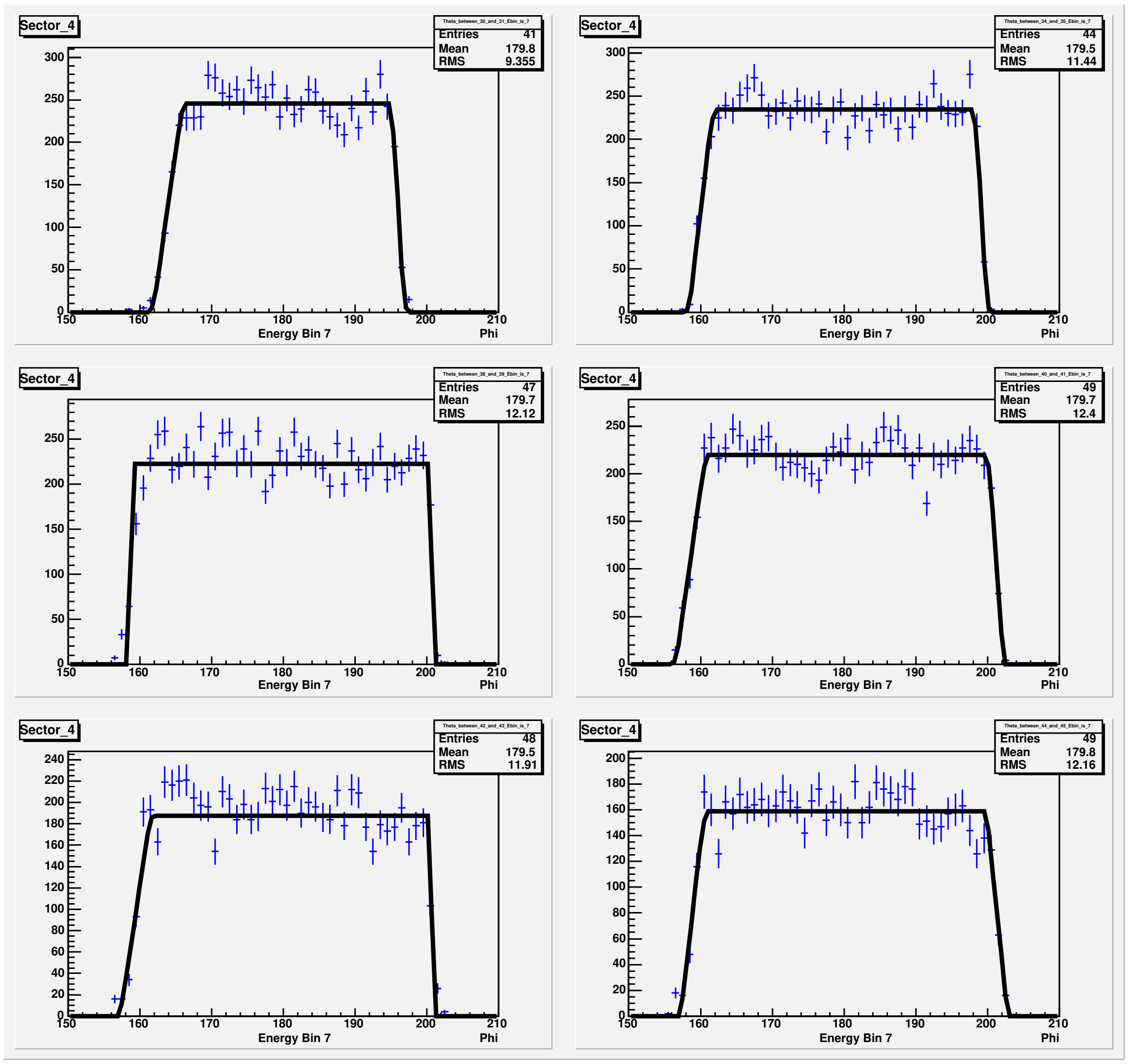

Figure 5.11: Distributions in ϕ showing the regions of flat acceptance and the drop-off where the fiducial region ends.

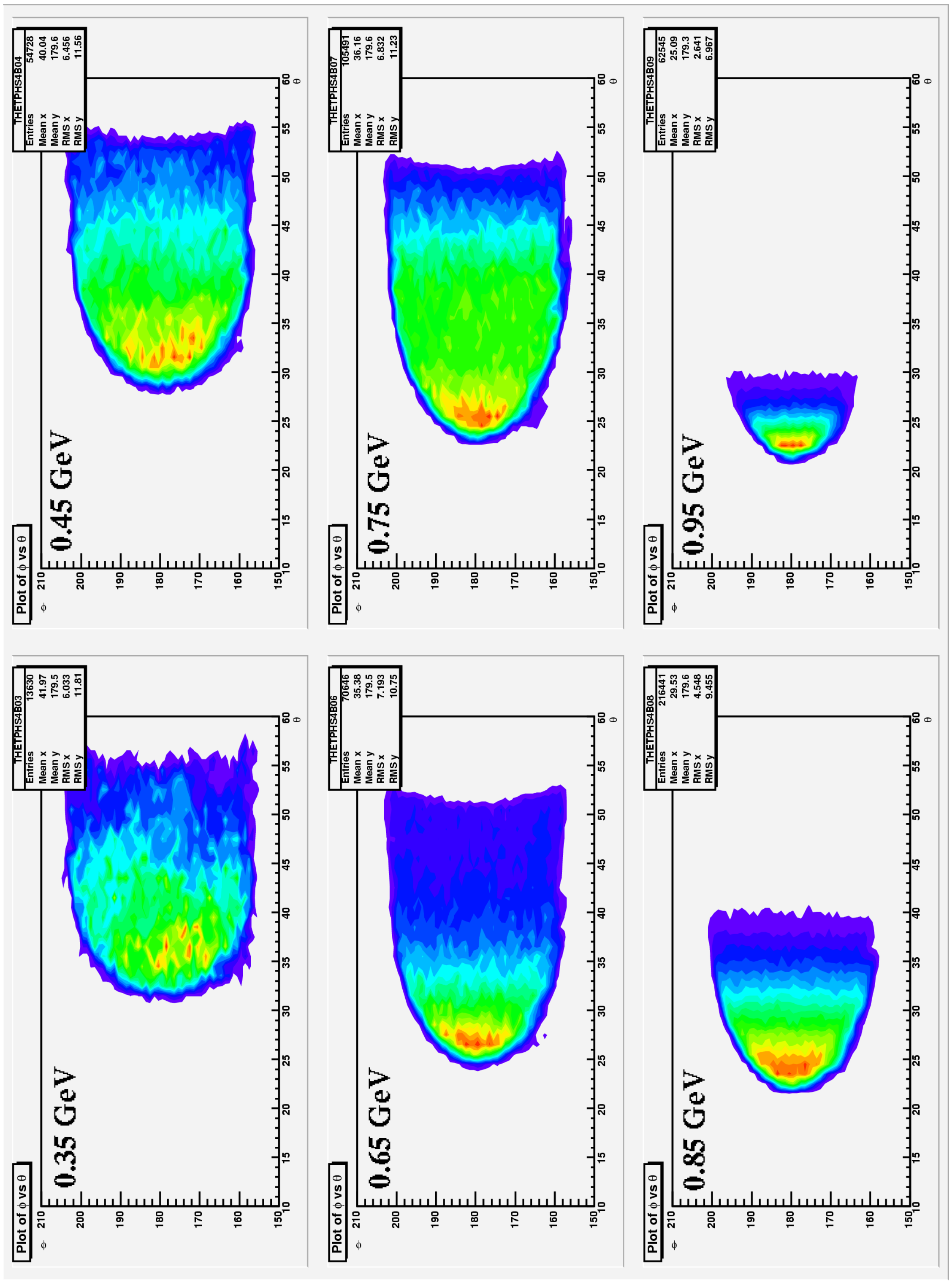

Figure 5.12: The data distribution in ϕ vs. θ showing the fiducial regions. The fiducial region is defined in θ and ϕ for different energy bins. The plots show the various energy bins used running from 0.35 GeV to 0.95 GeV with a width of 0.1 GeV.

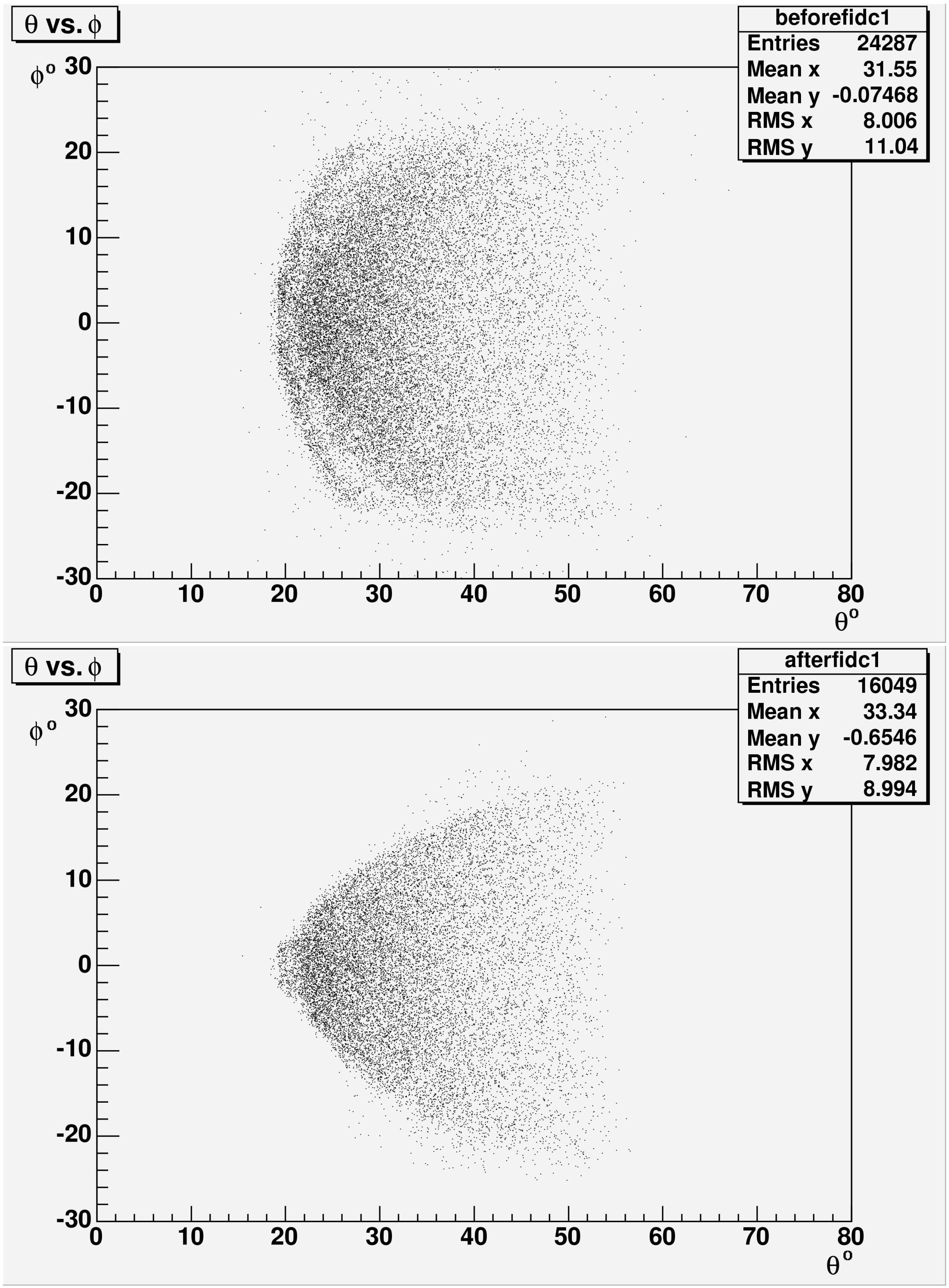

Figure 5.13: The before fiducial cut (top) and after (bottom) plots of data distributions for electrons.

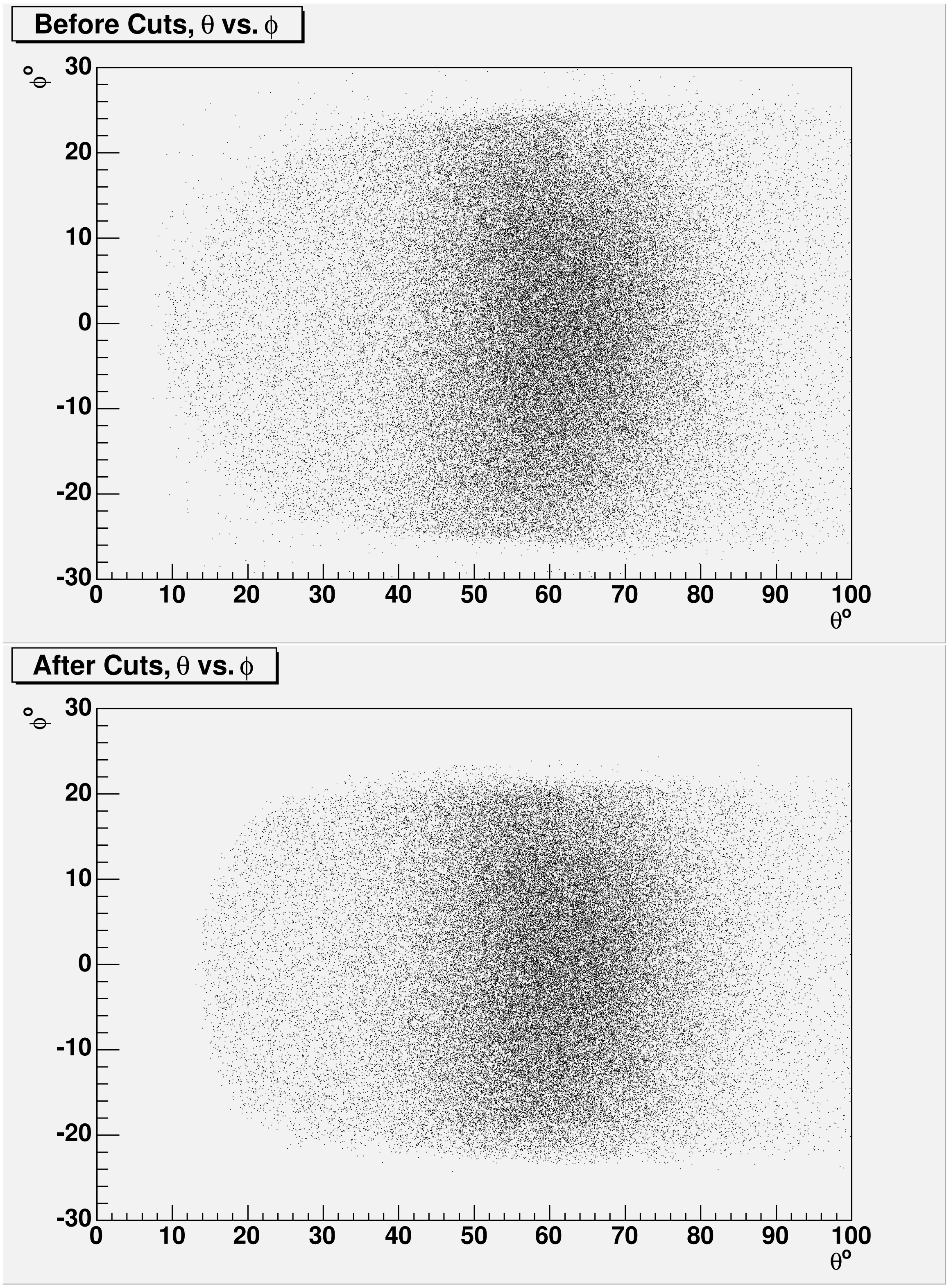

Figure 5.14: Proton distribution before fiducial cut (top) and after fiducial cut (bottom).

5.4 Proton Energy Loss Correction

When protons are exiting from the target in the CLAS detector, they can lose some of their kinetic energy when passing through the target material and detector material. This effect is greater when the momentum of the proton is relatively low. At lower momenta the amount of loss can be substantial. A correction factor has to be applied to ensure that the proton energy is what it was immediately post-reaction.

To determine how the target and detector materials can affect the proton's energy, simulations can be used. As will be described in the next section, an accurate simulation of the detector system and target cell is necessary to determine acceptances for cross-section calculations. These simulations can be used by first looking at a particle's energy as set using a phase-space generator and then comparing it to the energy of the same particle after it is detected. When the generated proton passes through the simulation, energy losses can be examined by generating a plot of the difference between the proton's generated and simulated momentum versus the simulated momentum (figure 5.16). It can be clearly seen at the lower momentum levels there is a rise corresponding to the generated momentum being greater than that after the simulation. This means the proton has lost some energy. We can fit this trend (figure 5.15) and generate a function that allows us to correct for the loss. Figure 5.17 shows the effect of applying the correction; the straight line shows that the momentum of the proton is as it was when generated.

5.5 Simulations

In order to obtain cross-sections from the data taken by CLAS, it is necessary to understand how the detector responds to different particles across the entire solid angle that is covered. The only way to do this is to accurately simulate the detector system and all of its components and look at how a particle is affected through detection. By looking at the efficiency of detection of particular particles across all angles and accounting for losses encountered post-detection, we can adjust our calculations and derive accurate total cross-sections.

5.5.1 Acceptance Correction

When determining the differential cross-sections, the angular coverage of the detector, along with any kinematic variables being considered are divided into bins. Each of these bins will have an acceptance associated with it due to processes such

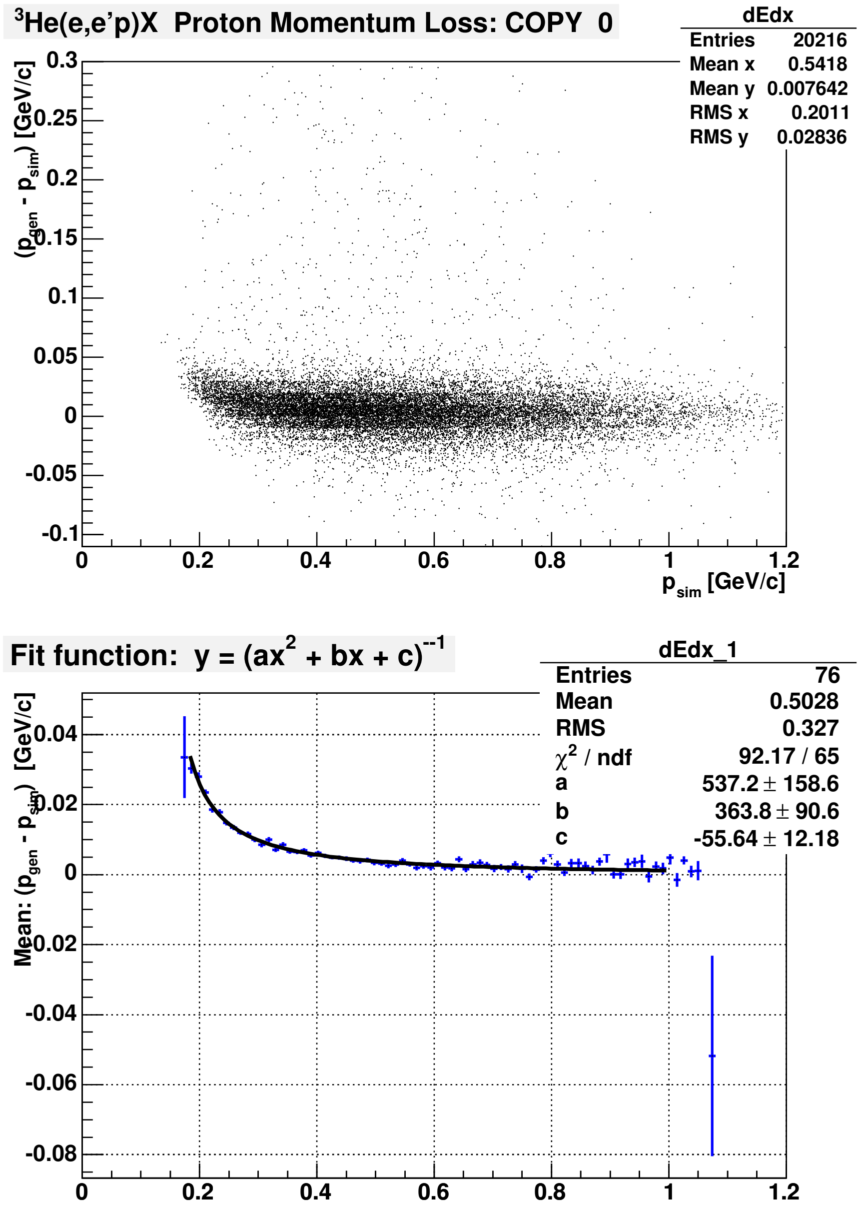

Figure 5.15: Fitting 5.16 to obtain a function that can be applied to correct for the energy loss.

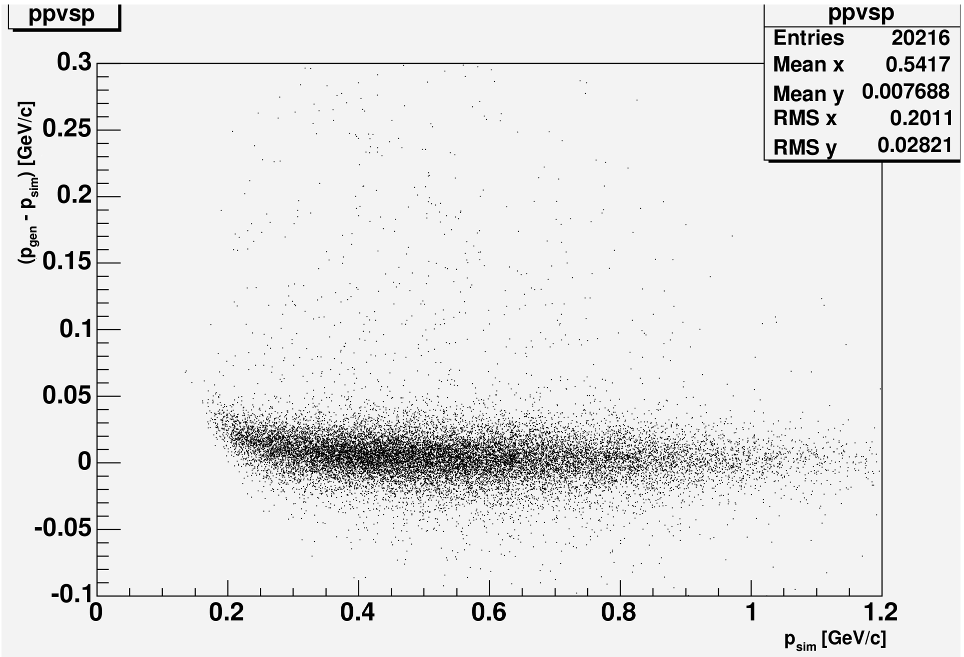

Figure 5.16: Plot showing the difference in the proton's momentum before and after simulations versus the momentum after. Clearly there is a loss in the lower momentum region.

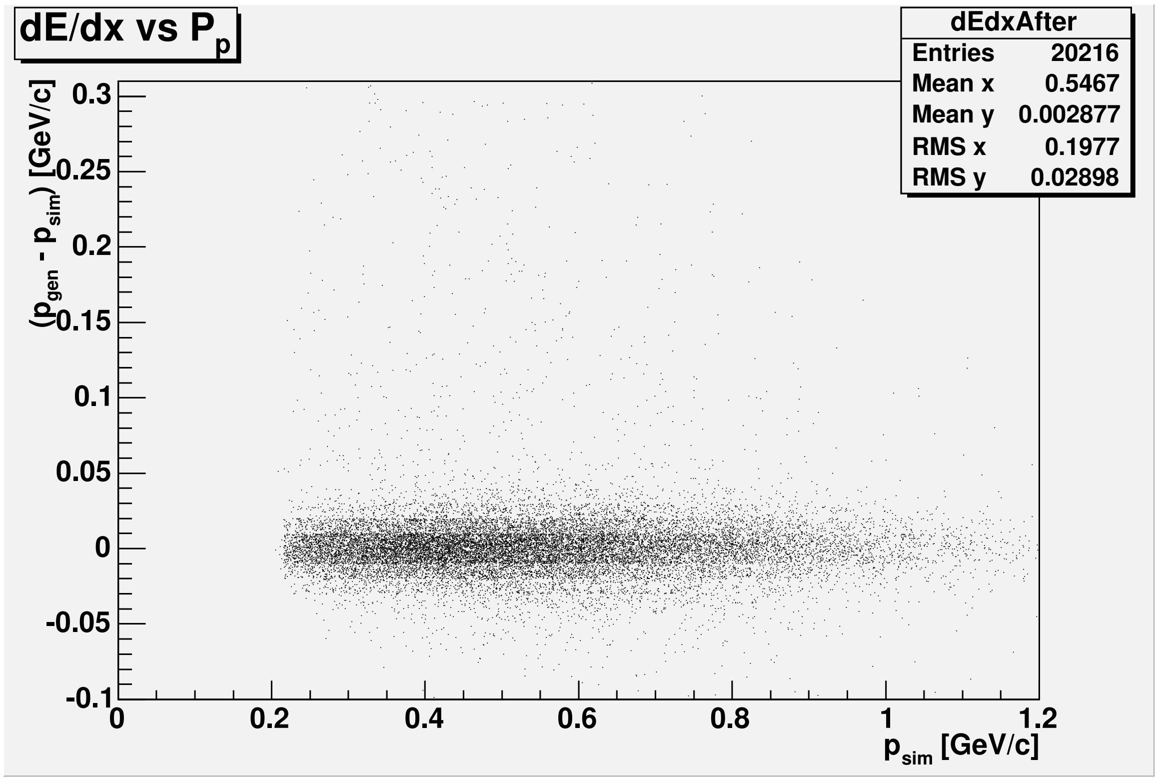

Figure 5.17: Plot showing the corrected proton momentum, corrected for energy loss.

as multiple scattering and energy loss which can move particles between bins in what is termed "migration" [92]. These effects are quantified through the acceptance calculations and used to correct the effects when calculating the cross-sections. The calculations for acceptance [93] can be thought in simple terms as the probability S_k that the detector accepts a particle thrown into bin k,

$$S_k = \frac{D_k}{N_k} \tag{5.8}$$

where D_k is the number of particles detected when N_k particles are thrown into bin k. The error on this is [94],

$$\sigma_k = \sqrt{\frac{S_k\,(1 - S_k)}{N_k - 1}} \tag{5.9}$$

The "thrown" events are taken from simulated data that has had exactly the same treatment of cuts and corrections as the real data. This ensures consistency and prevents the corrections from creating effects in the real data that aren't accounted for in the simulations.

5.5.2 Event Generator

The event generator employed [95] was designed to create a phase-space distribution of the channels of interest in this analysis. The generator simply takes the sum of the beam and target and decays these into a set of ($e'p\pi^-$). Since the target was ^{3}He the products shown are a couple of nucleon masses less than they should be. It was found however that generating the particles from a proton or neutron with Fermi-motion factored in made no difference in the phase-space distributions from those generated from a ^{3}He target. In the reaction we are dealing with a quasi-free nucleon with some random 3-momentum due to its motion within the nucleus, so the Fermi-momentum nucleon target was felt to be a better representation.

The production of a multiple particle final state can be thought of as a sequence of two particle decays of the total energy of the system defined by the incident electron and target [50]. The total energy of this system is defined as [58],

$$s^2 = (e + N)^2 \tag{5.10}$$

where e and N are the incident beam and target respectively (figure 5.18).

The angles are generated in the centre of mass frame and are distributed uniformly in (cos θ,ϕ) space given by,

$$\left.\begin{array}{rcl}\phi_i &=& 2\pi P_i \\ \cos\theta_i &=& 2Q_i - 1\end{array}\right\} \qquad i = 0, 1, ..., n \tag{5.11}$$

Where P_i and Q_i are random numbers between 0 and 1. The mass of the intermediate particle j is given by

$$M_j = \mu_j + R_j\left(M_{j+1} - \mu_{j+1}\right) \qquad j = 2, 3, ...n \tag{5.12}$$

where R_j is a random number between 0 and 1 and μ_j is

$$\mu_j = M_{p0} + M_{p1} + ... + M_{p_j-1} \tag{5.13}$$

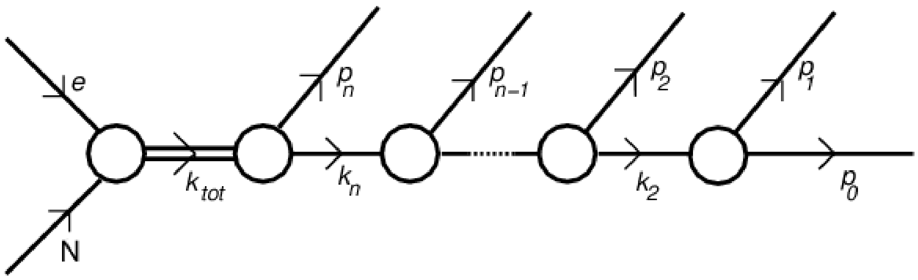

Figure 5.18: The generation of an n particle final state.

For the exclusive channels figure 5.18 reduces to figure 5.19. The masses produced in sequence are therefore

$$\begin{array}{rcl}M_\Delta &=& (M_p + M_{\pi^-}) + R_2\left[s - (M_p + M_{\pi^-} + M_{e'})\right] \\ M_X &=& M_{\pi^-} + R_1\left[M_\Delta - (M_p + M_{\pi^-})\right]\end{array} \tag{5.14}$$

This means,

$$\begin{array}{rcl}M_p + M_{\pi^-} &\leq M_\Delta \leq& s - M_{e'} \\ 0 &\leq M_X \leq& M_\Delta - M_p\end{array} \tag{5.15}$$

Naturally, in this system the recoil particle is simply the π^-.

Figure 5.20 shows the distribution of the mass of the Δ in the generator. The fi-

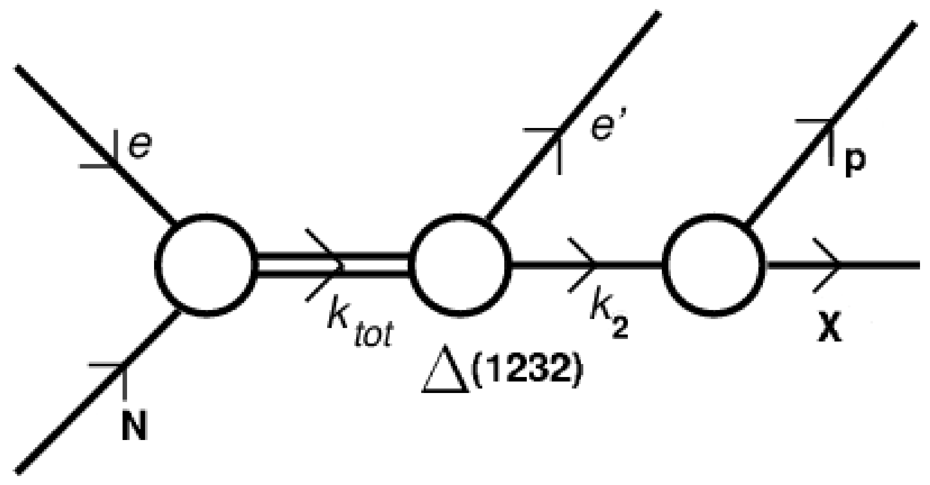

Figure 5.19: The exclusive channel representation of particle generation.

nal four vectors of the electron, proton and pion are stored and used for analysis.

5.5.3 Simulation Package

As stated previously, to obtain the acceptances an accurate simulation of the detector system and its components has to be performed. This is done using GSIM (GEANT Simulation) that is distributed as part of the CLAS software packages. GEANT (GEometry ANd Tracking) is a system developed in CERN and is a system of detector descriptions and simulation tools used to design and optimise detectors, develop and test reconstruction and analysis programs and interpret experimental data. The GEANT program simulates the passage of elementary particles through matter.

GSIM is GEANT with the specifications of the CLAS detector systems programmed into it. Thus we can fully simulate CLAS and its subsystems. Some documentation exists [96], but it is necessary to use specific run parameters such as the target cell and position, beam energies and torus currents. The output from the generator of the previous section is "fed" into GSIM which processes all the events as if they were passing through the detector itself. Specific to this data analysis was [97], the details of which were entered by a collaboration member.

The only differences between the output from GSIM and experimental measurements are [58]:

- there are no resolution effects;

- there is no trigger condition applied since we are generating our specific reaction channel;

- there is no accounting for dead detector channels.

To compensate for these, an additional piece of software, GPP (GSIM Post Processor), is used. This program "smears" the time-of-flight and momentum quantities to get a resolution comparable to CLAS. The trigger (section 3.4) was also applied. Additionally, dead detector channels were removed so the simulation matched the experimental conditions. After GPP is applied, cooking takes place to reconstruct particle tracks and make preliminary particle IDs. Figure 5.21 shows some plots of real data and figure 5.22 shows some simulated data. They compare quite well.

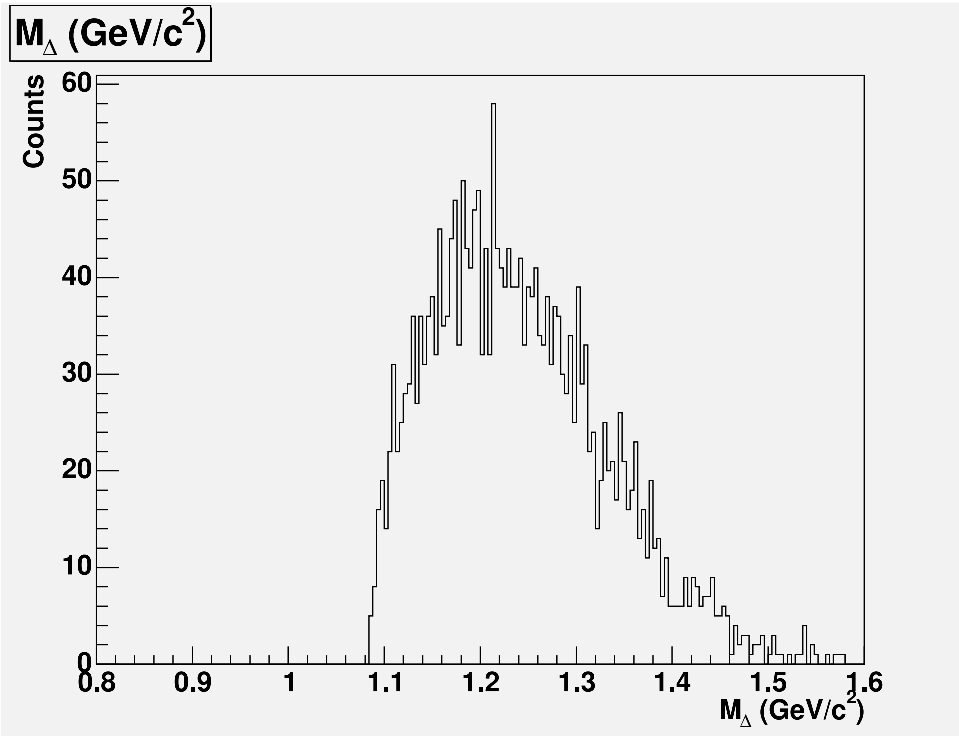

Figure 5.20: The mass distribution of the Δ as the intermediate particle in the exclusive channel generation. As can be seen, the lower limit corresponds to the sum of the proton and pion mass. The upper limit is the total energy of the system minus what the scattered electron takes with it.

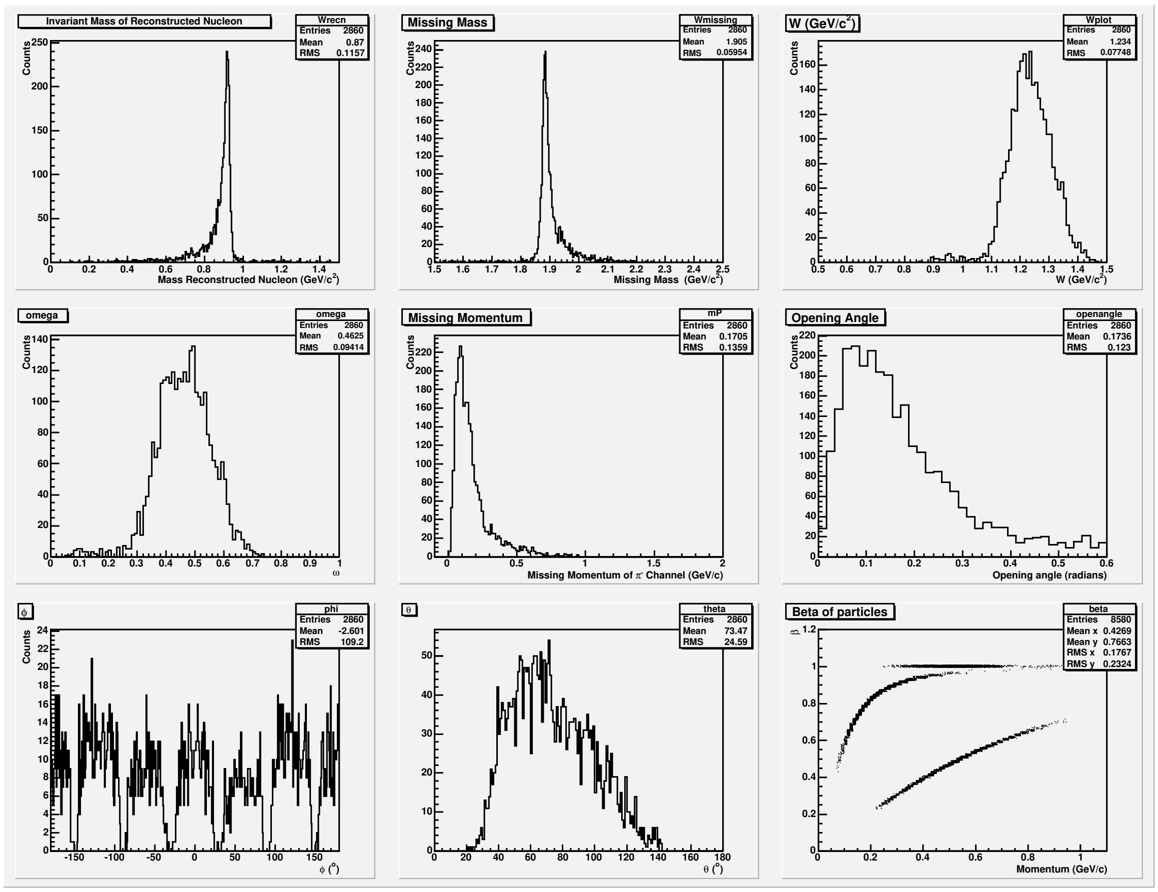

Figure 5.21: The various physical quantities measured from our data. The aim is to get the simulated distributions to match these as closely as possible.

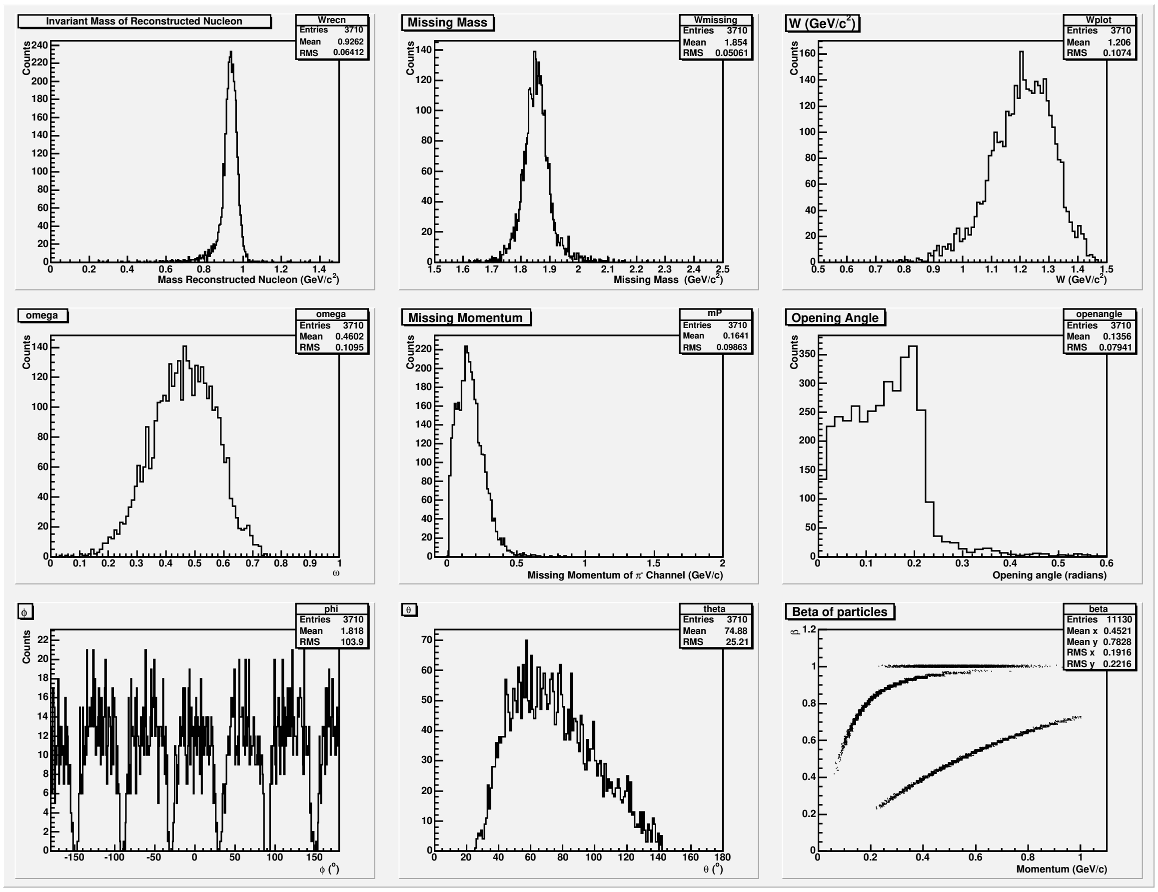

Figure 5.22: The distributions of various quantities for the simulated data. These should be as close matching as possible to figure 5.21.

CHAPTER VI

DATA SELECTION AND ANALYSIS

6.1 Data Selection

With the CLAS detector system having roughly 4π coverage, it is the case that a lot of events are recorded that have nothing to do with what we are looking to analyse. It is also the case that certain events that would seem to be valid are in fact unacceptable for various reasons. For example, if whilst analysing the $^3\text{He}(e, e'p\pi^-)2p$ channel we detect all the final state particles as desired. It is possible that the π^- is not from our reaction vertex and is recorded as part of the wrong event. These "errant" particles can be identified through a kinematic study looking at the missing momentum and opening angle of the event and applying the relevant cuts.

6.1.1 Missing Momentum Cuts

Using the fact that momentum is conserved combined with an exclusive measurement where all particles in a reaction can be accounted for, we can identify events where we are confident that each recorded particle is genuinely part of the event through the missing momentum. The missing momentum of a reaction can be found from the four-vectors:

$$M^\mu = \gamma^{*\mu} + T^\mu - (p^\mu + \pi^\mu) \tag{6.1}$$

Where $\gamma^{*\mu}$ is the virtual photon four-momentum, T^μ is the struck nucleon (proton or neutron) four-momentum, p^μ is the outgoing proton four-momentum(produced from the resonance decay) and π^μ is the π^- four-momentum for the reaction channel in our study. In an exclusive measurement, the missing momentum would ideally be zero. However, due to factors such as radiative losses and target motion the missing momenta are unlikely to be exactly zero. These effects are relatively small compared with the situation where a measured particle did not originate at the reaction vertex and cuts can be applied where an event has a large missing momentum. The plot in figure 6.1 show the missing momentum distributions of the π^- channel. To decide where the limit of the momentum cut should be placed, the opening angle cut explained below is used to define this.

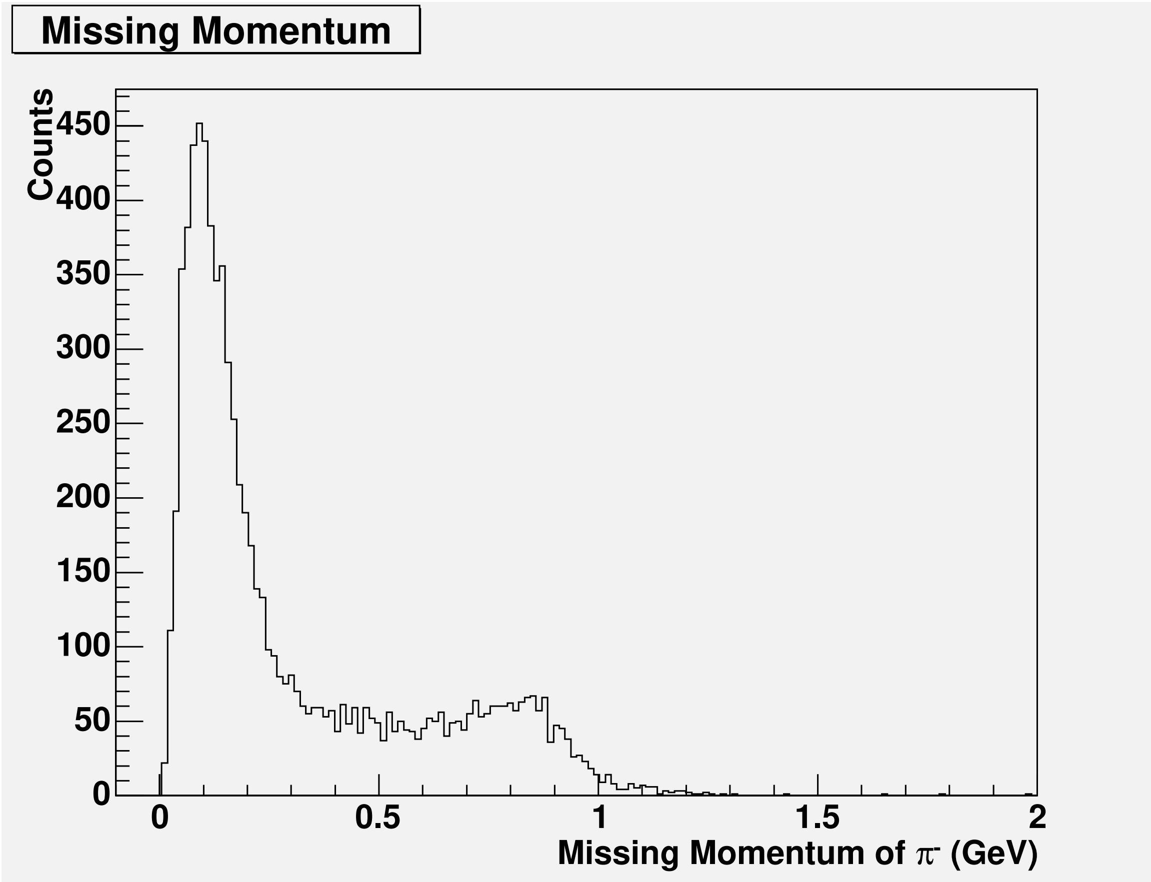

Figure 6.1: Missing momentum for the $p\pi^-$ channel before the opening angle cut.

6.1.2 *Opening Angle Cut*

If the struck nucleon is considered at rest then the angle between the reconstructed resonance and the virtual photon should be zero, that is the momentum of the virtual photon and the Δ should be identical. This angle is referred to as the opening angle. In the case of a ^{3}He target the struck nucleon is only quasi-free and not at rest, but has some random momentum due to Fermi-motion within the nucleus. Therefore we cannot cut all events whose opening angle is non-zero, since this will encompass most "good" events as well as unreliable ones. What we can do is declare a maximum opening angle outside which an event is defined to be unreliable and therefore is rejected. This cut should as much as possible deal with eliminating those events where the detected proton and pion do not both originate from the same decay. So for example, in the case where the proton from the resonance decay strikes another of the protons from the ^{3}He nucleus that goes on to be detected in the event bucket. It will be less probable that this secondary proton would carry on with the same momentum and direction of the original particle. So by cutting on the angle between the virtual photon four-vector and the combined four-vectors of the measured pion and proton, we can eliminate much of these undesirable events.

The opening angle distribution (figure 6.2) before the missing momentum cuts were applied show quite a large distribution over a broad angular range. Evidently there are many events where the pion and proton don't originate from the same source. The momentum cuts above were used to decide the optimal value for the opening angle limit.

6.1.3 *Results of Cuts*

As was said, the limit of the missing momentum cut was to be determined using the opening angle cut. Figure 6.3 shows how the missing momentum distribution alters with increasing cuts on the opening angle. From the right of the plot going left the coloured areas are the distributions corresponding to no opening angle cut, 0.4 radians, 0.3 radians, 0.2 radians and 0.1 radians respectively. It can be seen that the size of the main peak isn't affected until the cut at 0.1 radians. This means each of the other limits progressively remove more undesirable events until the cut of 0.2 radians, below which too many valid events are removed. Therefore it was decided to use an opening angle limit of 0.2 radians to define good events.

It can be seen from the plot in figure 6.4 the effect the missing momentum cut has on the opening angle distribution. Similar to the above process, using suc-

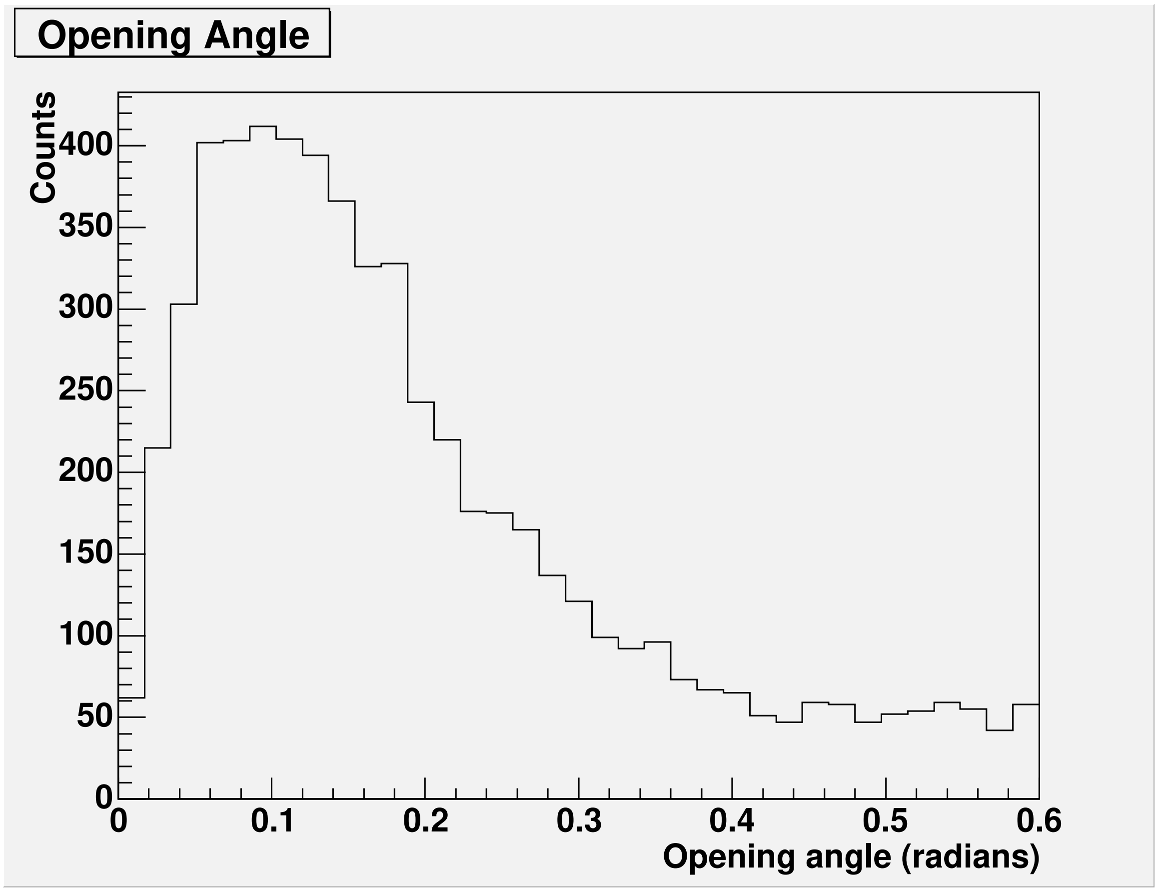

Figure 6.2: Opening angle distribution in the $p\pi^-$ channel before the momentum cut.

cessively more severe cuts on the missing momentum yielded various distributions of the opening angle. The distributions from right to left correspond to successive cuts on momentum of 0.5 GeV/c, 0.4 GeV/c, 0.3 GeV/c, and 0.2 GeV/c. We see that the main peak starts to drop slightly after reaching a cut of 0.2, so we take this to be our limit cutting all events with a missing momentum greater than 0.2 GeV/c. After the cuts of either were applied, the resulting distributions of opening angle and missing momentum for the $p\pi^-$ channel are shown in figures 6.1 and 6.2.

The cuts were to ensure that the events we were including in the analysis were from the reaction $^3\mathrm{He}(e, e'p\pi^-)2p$; all the particles detected in the final state were from the reaction. By restricting the allowed missing momentum and the opening angle to be 0.2 GeV/c and 0.2 radians respectively, we can be confident that we have identified the event and all its components accurately.

6.2 Struck Nucleon Rest-Frame

Previous analyses looking at multipole ratios involved studies where the struck nucleon is stationary. This is not appropriate however for our case where we are interacting with nucleons (either protons or neutrons) in a bound nuclear target (^{3}He). For our purposes, we must compensate for the fact that the bound nucleons possess momentum from their Fermi-motion.

To compensate for the nucleon motion (so we can make a valid comparison between ours and previous studies), we can adjust the four-vectors of all particles measured in an event so that they are described in the rest-frame of the struck nucleon. The energies and momenta of the particles are then the same as if they had been measured in a reaction where an electron interacts with a nucleon at rest. By doing this, we have a situation where our reaction is the same as those where the target nucleon is at rest. However, we no longer have the beam exclusively along the defined beam axis since the random motion of the struck nucleon in phase space can move the beam electrons four-vector off-axis after being boosted to the rest frame of the struck nucleon. This isn't a problem since the calculations we discuss later for the differential cross-sections depend on the relative angles between the reaction plane defined by the beam and scattered electron, and the scattering plane defined by the pion and proton (figure 2.4). Therefore an arbitrary beam direction is not a problem when you have measured all the particles in an event and their relative directions.

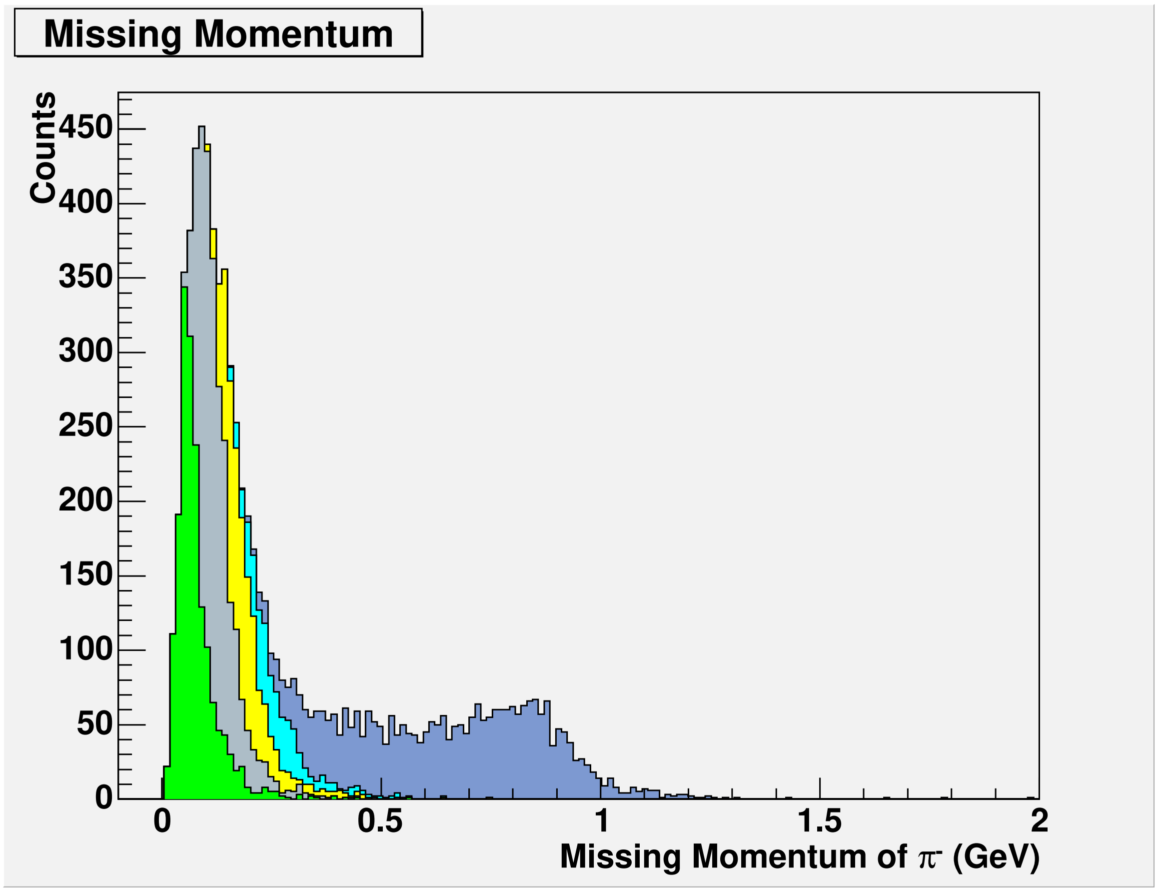

Figure 6.3: Plot of missing momentum distributions for various cuts in the opening angle; Dark blue, no cut; light blue, 0.4 radians; yellow, 0.3 radians; grey, 0.2 radians; green, 0.1 radians.

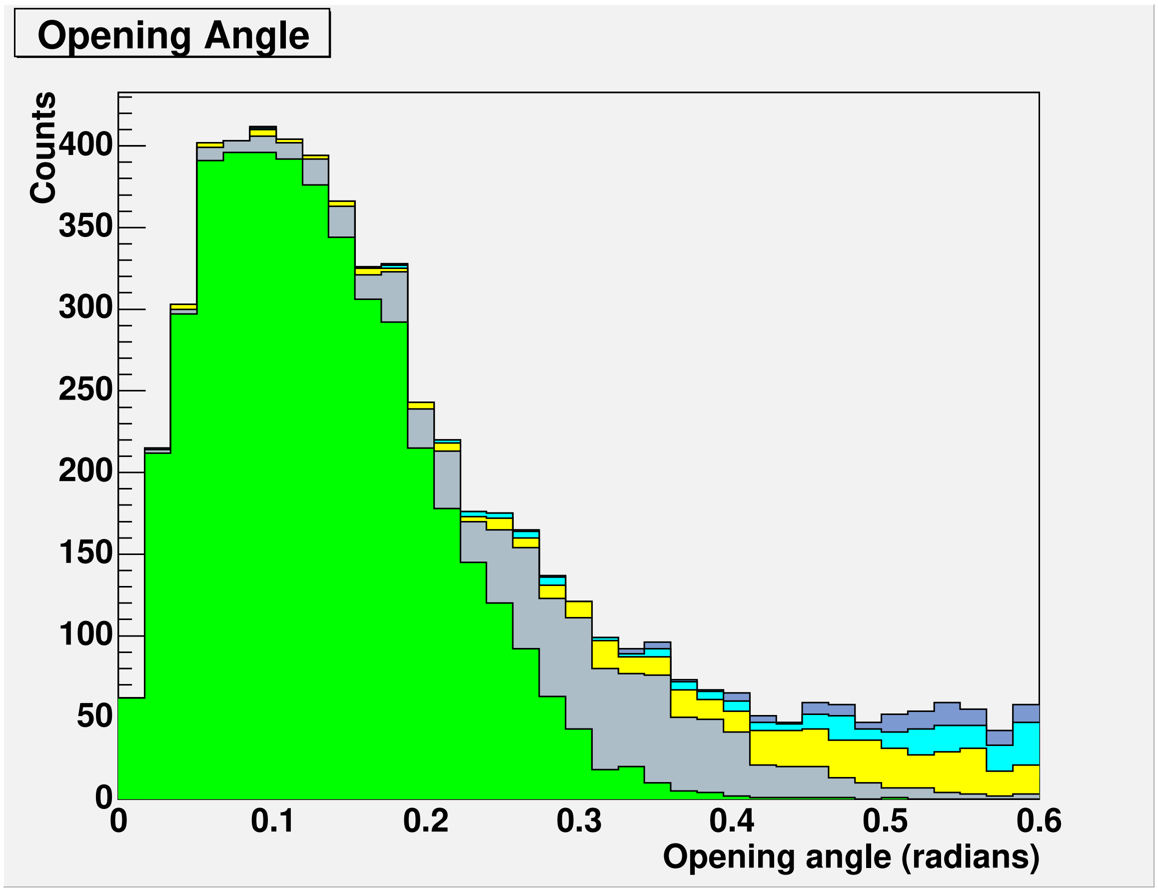

Figure 6.4: Plot of opening angle distributions for various cuts in missing momentum; Dark blue, no cut; light blue, 0.5 GeV/c; yellow, 0.4 GeV/c; grey, 0.3 GeV/c; green, 0.2 GeV/c.

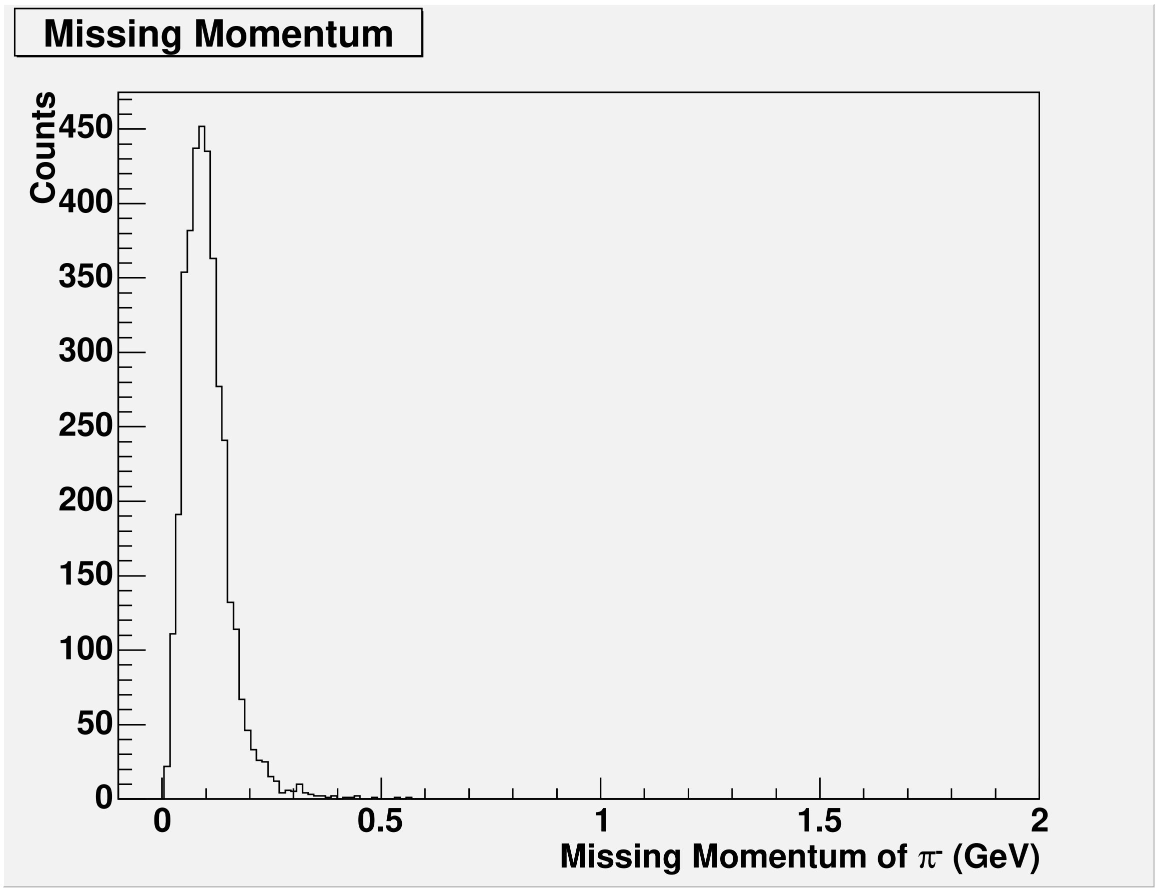

Figure 6.5: Missing momentum for the $p\pi^-$ channel after the opening angle cut.

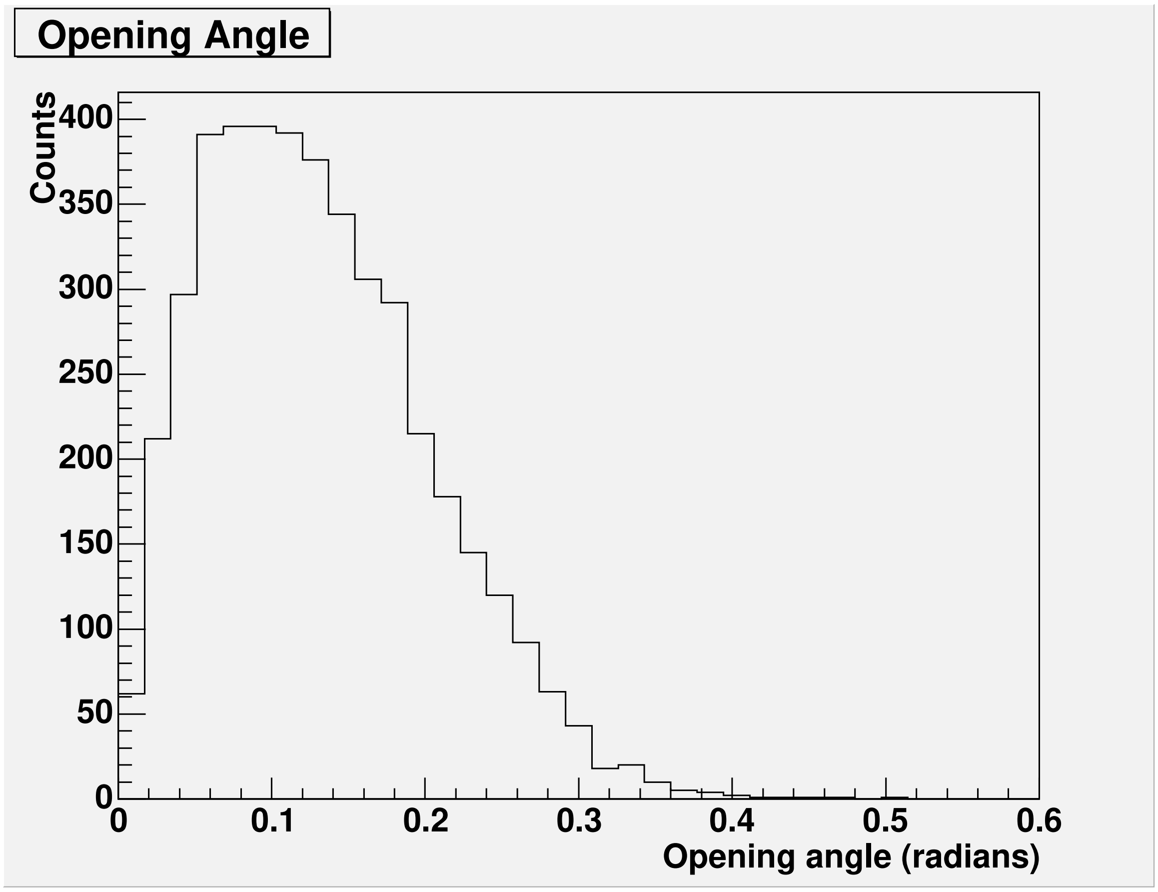

Figure 6.6: Opening angle distribution in the $p\pi^-$ channel after the momentum cut.

The transformation of each spatial component and energy component must be performed separately. The equations to do this are shown below.

In the case where the rest-frame of the target nucleon is moving only along a single axis, z for instance in the lab-frame, a matrix describing the relationship between the two is given by,

$$\begin{pmatrix} E' \\ P'_z \end{pmatrix} = \begin{pmatrix} \gamma & -\beta\gamma \\ -\beta\gamma & \gamma \end{pmatrix} \begin{pmatrix} E \\ P_z \end{pmatrix} \tag{6.2}$$

with $P'_x = P_x, P'_y = P_y$.

This yields the relationship of the energy and momentum between frames to be,

$$P'_z = \gamma \left(P_z - \beta_z E\right) \tag{6.3}$$

$$E' = \gamma \left(E - \beta_z P_z\right) \tag{6.4}$$

Where P_x, P_y and P_z are the spatial components of our particles four-momentum and E is the energy. The primed and unprimed variables differentiate the frames they are determined in. β is the velocity of the particle taken as a fraction of the speed of light i.e. $\beta = v/c$. The struck nucleon whose frame we are interested in has a random motion across all the axes. This means we have to extend the above relationships to include each spatial axes dependency on the others. We therefore use the matrix,

$$\begin{pmatrix} E' \\ P'_x \\ P'_y \\ P'_z \end{pmatrix} = \begin{pmatrix} \gamma & -\gamma\beta_x & -\gamma\beta_y & -\gamma\beta_z \\ -\gamma\beta_x & 1+\frac{(\gamma-1)}{\beta^2}\beta_x^2 & \frac{(\gamma-1)}{\beta^2}\beta_x\beta_y & \frac{(\gamma-1)}{\beta^2}\beta_x\beta_z \\ -\gamma\beta_y & \frac{(\gamma-1)}{\beta^2}\beta_x\beta_y & 1+\frac{(\gamma-1)}{\beta^2}\beta_y^2 & \frac{(\gamma-1)}{\beta^2}\beta_y\beta_z \\ -\gamma\beta_z & \frac{(\gamma-1)}{\beta^2}\beta_x\beta_z & \frac{(\gamma-1)}{\beta^2}\beta_y\beta_z & 1+\frac{(\gamma-1)}{\beta^2}\beta_z^2 \end{pmatrix} \begin{pmatrix} E \\ P_x \\ P_y \\ P_z \end{pmatrix} \tag{6.5}$$

Which provides the relationship of each momentum component and energy between the lab-frame and the rest-frame of the struck nucleon,

$$P'_\mu = P_\mu + \beta_\mu \left(\frac{\gamma - 1}{\beta^2}\left(\vec{\beta}.\vec{q}\right) - \gamma E\right) \tag{6.6}$$

$$E' = \gamma\left(E - \vec{\beta}.\vec{q}\right) \tag{6.7}$$

With all final-state particles now expressed in the rest-frame of the struck nucleon (and resonance state), we can make a comparison between the cross-sections calculated for our experiment and the previous analyses without being concerned about effects from our nucleon motion.

6.3 Radiative Effects

There is a non-negligible probability that an electron will emit a photon in the field of an atom or nucleus. Experimentally this means that the electron that interacted with the nucleus had less energy than the beam energy or the scattered electron had more energy than was detected. In either case the virtual photon transferred did not have the energy calculated using the detected electron. To compensate for this effect we drew on previous work done in [37] that had performed an extensive study of the radiative effects and calculated factors associated with the kinematic bins to compensate. We employed the corrections derived in that study and found that a small but non-negligble effect was present. Figure 6.7 shows how the cross-section plotted against W is altered by applying these radiative corrections. These correction factors were applied to the data during the cross-section calculations described in section 6.4.3.

6.4 Binning of the Data

In order to analyse the data in terms of the cross-sections as outlined in section 2.3.2, the experimental data is binned in the variables Q^2, W, $\cos(\theta^*_\pi)$ and ϕ^*_π. To relate these variables to the lab measured variables, a Jacobian factor has to be employed. The calculation of this is outlined in Appendix A. The number of bins in ϕ^*_π and $\cos(\theta^*_\pi)$ are set at 12 and 10 respectively. This has to be the minimum for each since the analysis is dependent on the distribution of the differential cross-sections in these variables.

6.4.1 Determination of J

The cross-section calculated in the kinematic bins of W, Q^2, $\cos\theta^*_\pi$, ϕ^*_π requires that a Jacobian factor be applied relating the measured lab variables such as the beam and scattered electron energy and the angle between them to the binning variables chosen. The Jacobian matrix we use is,

$$J = \frac{\partial\left(Q^2, W\right)}{\partial\left(e', cos\left(\theta_e\right)\right)} = \begin{vmatrix} \frac{\partial Q^2}{\partial e'} & \frac{\partial Q^2}{\partial cos(\theta_e)} \\ \frac{\partial W}{\partial e'} & \frac{\partial W}{\partial cos(\theta_e)} \end{vmatrix} \tag{6.8}$$

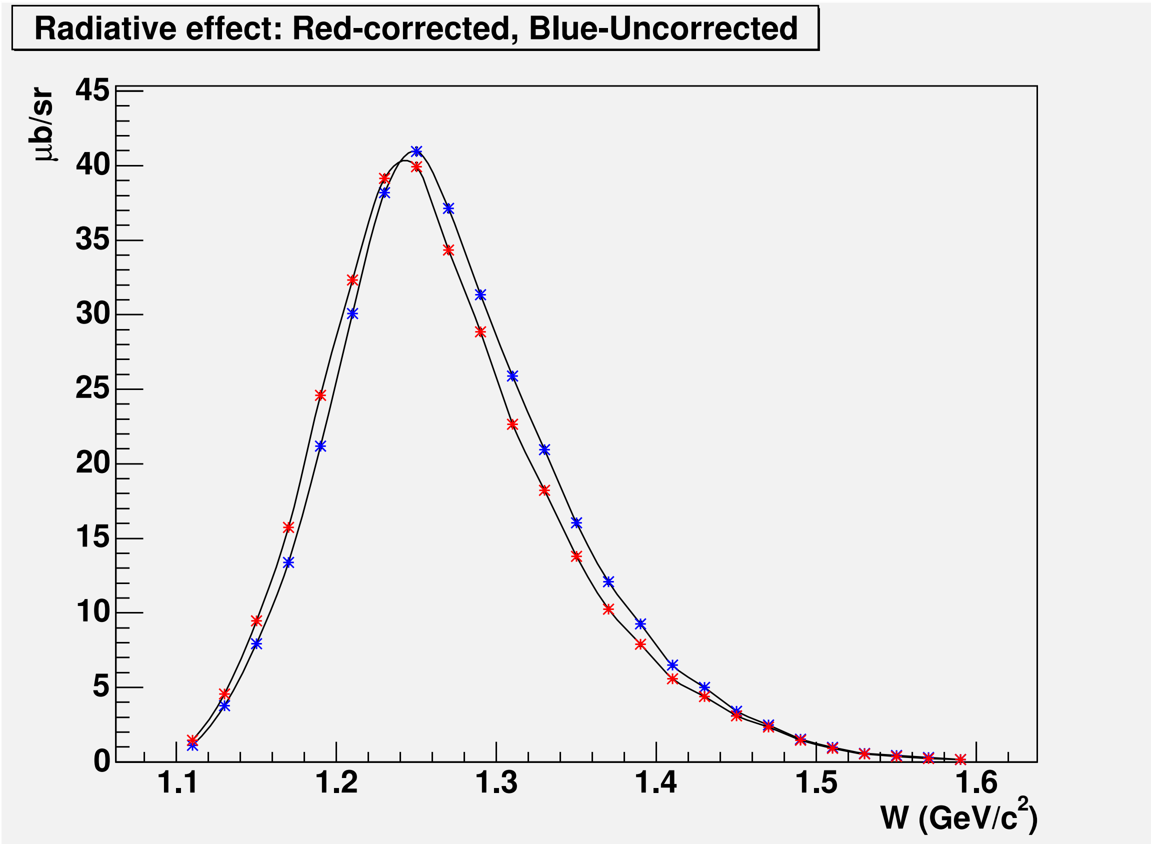

Figure 6.7: A plot showing the effect of applying radiative corrections to the data. The blue points are the uncorrected data and the red corrected data. The radiative tail to the right of the data distribution is "shifted" back to the peak.

where Q^2 and W are defined previously and e' is the scattered electron energy and θ_e is the angle between the scattered and beam electrons.

From this matrix, the Jacobian factor is calculated to be,

$$|J| = \frac{ee'm_N}{\pi W} \tag{6.9}$$

where e is the beam electron energy and m_N is the mass of the struck nucleon.

Given that each bin in W contains a range of e and $cos\,(\theta_e)$, an average Jacobian factor for a particular bin is used in the calculation of the differential cross-sections which relates the centres of the bins in each set of variables. As would be expected, there should exist no θ^*_π or ϕ^*_π dependence on the Jacobian, only a variation in W and Q^2.

A fuller description of the derivation of the Jacobian factor is provided in Appendix A.

6.4.2 Determination of Γ

The factor Γ outlined in section 2.3.2 is given by the equation,

$$\Gamma = \frac{\alpha}{2\pi^2 Q^2}\frac{E_{e'}}{E_e}\frac{k_\gamma}{Q^2}\frac{\omega^*}{1-\epsilon} \tag{6.10}$$

Where e' and e are the beam and scattered electron energies respectively, k_γ the equivalent real-photon energy exciting a nucleon, and ϵ a measure of the transverse linear polarisation of the virtual photon. Γ can be interpreted as the flux of virtual photons [73] i.e. the number of virtual photons per scattered electron in dΩ.

Like the Jacobian factor described above, experimentally the factor Γ can be calculated on an event-by-event basis. For a kinematic bin with multiple events, an average factor is calculated across all the events in the bin. There is no dependence on θ^*_π or ϕ^*_π in this factor.

6.4.3 Experimental Cross-section

The cross-section is measured for the bins W, Q^2, cos(θ^*_π) and ϕ^*_π. The differential cross-section dσ^ν for bin ν is obtained by:

$$d\sigma^\nu = N^\nu.\frac{1}{\omega}.\frac{1}{L} \tag{6.11}$$

Where N^{ν} is the number of events in bin ν, L is the total luminosity from the target and beam and ω is the product of the bin widths of W, Q^2, $\cos(\theta^*_\pi)$ and ϕ^*_π.

With the different experimental parameters the cross-section (equation 6.11) becomes,

$$\frac{d^4\sigma}{d\Omega^* dW dQ^2}_{experimental} = N_e . \frac{Q_e}{Q_{tot}} . \frac{1}{\epsilon} . \frac{A}{\rho_t l_t N_A} . \frac{1}{\Delta cos\left(\theta^*_\pi\right) \Delta\phi^*_\pi \Delta W \Delta Q^2} \tag{6.12}$$

$$\begin{aligned} N_e &= \text{Number of electrons in the } Q^2,\ W,\ \cos(\theta^*_\pi),\ \phi^*_\pi \text{ bin} \\ Q_e &= \text{Electronic charge } (1.602 \times 10^{-19}) \ [C] \\ Q_{tot} &= \text{Total charge incident on the target } [C] \\ \epsilon &= \text{Acceptance factor for the } Q^2,\ W,\ \cos(\theta^*_\pi),\ \phi^*_\pi \text{ bin} \\ A &= \text{Mass number of the target } [g/mol] \\ \rho_t &= \text{Target density } [g/cm^3] \\ l_t &= \text{Target length } [cm] \\ N_A &= \text{Avogadro's Number } (6.022 \times 10^{23}) \ [1/mol] \end{aligned}$$

In order to perform the analysis outlined in section 2.3.2, we have to relate the experimental cross-section (equation 6.12) to the theoretical cross-section (equation 2.22). This is achieved as outlined in equation 2.20 through the use of the Jacobian factor (J) and virtual photon flux (Γ).

CHAPTER VII
RESULTS

7.1 Previous Multipole Measurements

This study measured the multipoles of the neutron to Δ^0 transition. Most previous studies had only studied the Δ^+ through the production of a π^0. A recent study of this type was performed by K. Joo et al. [37] at Jefferson Lab in Virginia and much of the formalism established in previous work was used to study the Δ^0 through the production of a π^- in our study. For this analysis and others of a similar type, the π^0 decay channel is preferable as it is a much cleaner channel for analysis. In the case for the neutral pion, non-resonant background contributions are suppressed [71]. This is because the incident photon does not couple to the neutral pion so that only nucleon Born terms mix with the resonance excitation. In order to study the Δ^0 however, an analysis can look at the $n\pi^0$ or $p\pi^-$ channels (equations 1.1). The $p\pi^-$ channel was used since both product particles are charged and therefore the detection efficiency for the channel is much greater in our detector system. The results presented here are part of an extensive analysis with several stages of plots and fits. The flow diagram in figure 7.1, displays the various stages.

7.2 Extracting $\sigma_T, \sigma_L, \sigma_{TT}$ and σ_{LT}

As was described in section 2.3.2, the equation for the cross-section, equation 2.22, takes the form of A + C$\cos(2\phi_\pi^*)$ + D$\cos(\phi_\pi^*)$. If we then plot the experimental cross-sections and fit them with this form, the fit coefficients contain the structure functions σ_T, σ_L, σ_{TT} and σ_{LT}. Figure 7.2 shows an example distribution of the experimental cross-section in ϕ_π^* for the highest of the Q^2 bins of our data set. In Joo et al. [37], Q^2 bins ranging from 0.4 to 1.8 $(GeV/c)^2$ were analysed. Since the highest Q^2 bin achieved in our data set was 0.35 $(GeV/c)^2$ with a width of 0.05 $(GeV/c)^2$, our uppermost Q^2 bin is best for a comparison between the two analyses. Figure 7.5 shows the corresponding set of cross-sections distributed in ϕ_π^* taken from [37]. Clearly in both analyses the $\cos 2\phi$ form of the distribution and fitted function is evident. The ten distributions shown are for each bin in θ_π^*, W and Q^2. For our analysis there were fifteen W bins and three Q^2 bins so that we have 3x15x10 equivalent plots to fit and draw information from. The errors on the data points from experimental factors were dominated by the number of triggers in each bin with the periphery of the data ranges having substantial errors due to low statistics. Typically the data and acceptance should contribute similar errors since the number of simulated events created for the acceptance calculation matched those of the data set, though slight variations may occur were the simulated model does not perfectly describe the reality.

The plots in figures 7.3 and 7.4 show the set of ϕ^*_π distributions around the Δ mass peak position for the two Q^2 bins of 0.15 and 0.25 $(GeV/c)^2$ respectively. A range of Q^2 bins is not only useful for the purpose of comparison with [37] and other previous multipole analyses, it also allows us to look for any variation in the Δ peak position with varying Q^2 as described in [49].

7.3 Obtaining the partial-wave coefficients

The extracted structure functions from the ϕ^*_π distributions can be expanded into a partial wave series using Legendre polynomials as described in section 2.3.3. By plotting the extracted coefficients A, C and D against $\cos(\theta^*_\pi)$, the distributions can be fitted with the Legendre polynomial series yielding the partial wave coefficients. The black crosses seen in figure 7.6 are the data points extracted from the fits of the ϕ^*_π distributions. The blue solid line is the fit using the series described in section 7.2. In addition to the data distributions, theoretical calculations were performed using the MAID2003 Unitary Isobar Model for electroproduction of pions [98,99]. MAID's calculations draw on a large database of experimental points taken for various reaction channels and reaction kinematics. The red dashed line corresponds to calculations based on the model for the P_{33} resonance in the $(p\pi^-)$ channel. The green dotted line is also for the P_{33} resonance and the same channel but is altered by added Born contributions to the models. Born contributions arise through interactions where a pion is produced but not through the production and decay of a resonant state.

7.3.1 $A_0..A_4$

Figure 7.6 shows the plotted distribution of the A_i's from the ϕ^*_π fits corresponding to $\sigma_T + \epsilon\sigma_L$. Figure 7.6 is from our analysis and figure 7.9 from [37], both at the same Q^2 value of around 0.4 $(GeV/c)^2$. It is clear that whilst the fits to the data in either case are similar, very noticeable differences exist. The form of the symmetrical distributions in [37] aren't exactly replicated in our data where the distributions "lean" to the left. This bias seems to be more pronounced in the Q^2 bins around the resonance peak. The theoretical calculations with Born contributions (green dotted line) also show an enhancement to the cross-section in the negative region of $\cos(\theta^*_\pi)$. Whilst the enhancement is more pronounced in our plots, it is evident that Born contributions at least play a role in the asymmetric distribution shape. It is notable that the distributions in [37] have the same form as those from the calculated distributions without Born terms. This demonstrates how the non-resonant contributions are suppressed in the neutral pion channel but very much present in the case of our charged π^- channel complicating extracting information about the Δ.

The purpose of plotting the coefficients of the fits to the experimental cross-section in ϕ^*_π, is to extract the partial wave-coefficients which allow us to access the multipole information. As mentioned this can be done by using an expanded partial-wave series expressed using Legendre polynomials. Figure 7.13 shows the plots from [37] at Q^2=0.4 $(GeV/c)^2$ with the set of coefficients $A_0..A_4$. Joo et al. fitted a partial wave series up to l_π=2, this allowed them to cover the s- and p-wave contributions corresponding to l= 0, 1 as well as checking to see if any d-wave strength was present in the coefficients A_3 and A_4. The major contributions in the π^0 channel appear in the A_0 and A_2 coefficients. If we compare this to the plots from our analysis (figure 7.10), we see that similar large contributions occur in both of these coefficients. Considering Born contributions and the fact we are reacting on a quasi-free neutron and producing a Δ^0, we see features in the additional coefficients where no strength was found in the previous analyses.

The coefficients themselves are a complex mixing of the various multipoles, and it is not possible at this stage to infer anything concrete as many possible contributions can be in effect. Again the red dashed lines corresponds to theoretical calculations without Born terms, and the green dotted lines are the theoretical calculations with Born contributions. It is obvious from our data plots that the Born terms are contributing in the coefficients A_1, A_3 and A_4, where as in the π^0 case any contributions are insignificant. This is in agreement with the theoretical model which also shows no resonance contribution to these coefficients.

In our highest Q^2 bin, for the data distributions in A_0 and A_2, the experimental cross-section is less than the calculated cross-section with Born contributions in the A_0 coefficient. The A_0 coefficient contains no interference terms, only the sum of the absolute values of all multipoles and therefore is proportional to the total cross-section. A_1 is purely an interference between s- and p-waves and is dominated by $Re(E_{0+}M^*_{1+})$. A_2 contains a mixture of p-wave multipoles and their mutual products including the desired quadrupole interference $Re(E_{1+}M^*_{1+})$ (section 2.3.1). An interesting observation is seen in the last two coefficients between our Q^2 bins (figures 7.10, 7.11 and 7.12). As can be seen from figure 7.13 no significant d-wave strength is present and the last two coefficients were extracted merely as a check. Our plots show the calculated resonance with no Born contributions is zero in these coefficients. But since we already know there are contributions it isn't surprising that our data show features. It is also apparent that the theoretical model is inadequate for describing our data in these coefficients. This is interesting since the other coefficients are not drastically different from the model predictions. Another interesting feature is that there is a definite Q^2 dependence observed in the A_3 and A_4 coefficients, whatever is contributing to these two coefficients gets larger with increasing Q^2. This information should prove quite useful in refining the existing models where there is at present a limited database of previous measurements to draw on.

7.3.2 C_0 and C_1

In the same fashion that the set of partial wave coefficients for $A_0..A_4$ are obtained by fitting $\sigma_T + \epsilon_L \sigma_{LT}$ with a Legendre polynomial series, this can be done for σ_{TT}. The figures 7.14, 7.15 and 7.16 show the distributions for our data set corresponding to the Q^2 bins of 0.35, 0.25 and 0.15 $(GeV/c)^2$ respectively. It is clear from the plots that the fits to these distributions are not fully informed. The Legendre series applied was calculated on the conditions of a Δ^+ produced from a free-proton (section 2.3.3) and may have been truncated too early cutting out possible contributions in our experiment. We applied a higher order polynomial and found the linear component unaffected; there was little difference in the linear coefficents. It is clear from our data distributions that there is more structure in the data than is in the fit we are applying. We desired to see how the various coefficients compared to the Δ^+ measurements taken in [37] and so we applied the fit and series truncated at the levels of that study.

The final fit, whilst obviously not appropriate for the set, was employed to create a comparison between our data and that of the previous measurements (figure 7.17). It is possible that higher terms have to be included in the partial-wave series to reveal contributions not being considered in our truncated series, or that other effects are taking place which interfere with the multipole measurements. The purpose here however is to show that clear differences are being observed between the Δ^+ and Δ^0 case. Figure 7.17 shows the plots from [37] for this structure function and clearly display a substantial difference between their distributions and our own. Given the different target, resonance state and reaction channels, it is not unexpected that this is the case. It is more interesting to look at the partial wave coefficients plotted against W.

As with the first set of coefficients (A_x's) we plot C_0 and C_1 against W. Figure

7.18 is data at Q^2=0.35 $(GeV/c)^2$ where we see for C_0 a reasonable agreement between the theoretical model results (both Born and non-Born contributions) and our data distribution. If we look at the result from [37] for these coefficients (figure 7.21) there is good agreement between the C_0 coefficients for our data set and those from [37]. Magnitude differences could be attributed to the different experimental parameters. Again for [37], the differential cross-section for the C_1 coefficient is negligible. This is not so in our case where there are clear effects being observed and predicted from the models. At the lowest Q^2 bin (figure 7.20) the model fits our distribution quite well (it should be noted that the model predicts the Born and non-Born cross-sections to be the same for C_1). At the higher Q^2 bins, C_1 deviates completely and C_0 considerably from the model indicating that there is perhaps an effect dependent on Q^2 taking place that the model doesn't cover. Since we know from the A_x coefficients that there was a Q^2 dependent effect it is not unreasonable to consider that same contribution is appearing here.

7.3.3 $D_0..D_2$

As with the previous sets of plots, the final partial-wave coefficients are obtained by fitting the set of distributions produced from the σ_{LT} structure function. Figures 7.22, 7.23 and 7.24 are the distributions for each of our Q^2 bins. These coefficients have large errors making drawing conclusions difficult. Figure 7.25 shows the equivalent distributions from [37]. The theoretical model calculations with and without Born terms don't agree in any substantial way with our data. However, it is more useful to look for any features in the partial-wave fit to these distributions.

The set of coefficients $D_0..D_2$ are ambiguous (figure 7.26, 7.27 and 7.28). It is not clear if they show anything at all. As was stated above, the coefficient D (from the fit of A + Ccos($2\phi^*_\pi$) + Dcos(ϕ^*_π)) extracted from the ϕ^*_π distributions of cross-section has large statistical errors and poorly matches both variants of the theoretical predictions in most bins of W across all the Q^2 range. It is only in our highest Q^2 bin at 0.35 $(GeV/c)^2$ that some non-zero contribution might be present. The first coefficient in this bin is far smaller than the model-predicted Born contribution. The distribution in D_0 is similar to that observed in [37] (figure 7.29) although D_1 shows little if anything in our data where there is observed a most definite effect in [37] and both of our model predictions. For the parts where the errors on the data are not so substantial as to negate drawing conclusions, the distributions such as they are, do not mirror the Δ^+ case nor either $(p\pi^-)$ model predictions except in the case where the distributions might be said to be zero. From the equations 2.25 it can be seen it is the case that the D_1 coefficient is defining for the ratio $Re\left(S_{1+}M_{1+}^{*}\right)/M_{1+}^{*}$. Our results indicate that this coefficient across all of our Q^2 bins has a very small contribution if not zero. The effect on the multipoles will be seen in the next section.

7.4 Multipoles

The purpose of obtaining the partial-wave coefficients was to extract information on the multipoles M_{1+}, E_{1+} and S_{1+}. As was described in section 2.3.3, the E and S multipoles can only be accessed through their interference with the dominant magnetic multipole. The various equations for deriving the multipole values over W were given by the set of equations 2.25. Figure 7.30 shows the results for our highest Q^2 bin showing the extracted multipoles based on the M_{1+} dominance assumption. Again as with the previous stages of the analysis, the red dashed line is the corresponding theoretical calculations for the multipoles where only the resonance is considered, and the green dotted line where both the resonance and Born contributions are included. The theoretical calculations were used to obtain the the structure functions σ_T, σ_L, σ_{LT} and σ_{TT} as outlined earlier in the chapter. The coefficients A_x, C_x and D_x were obtained in the case of these calculations by fitting the structure functions in the exact same way as we fitted our data. The theoretical calculations for the multipoles were therefore performed by using the fits to the models and the set of equations 2.25 just as the data values were obtained.

In order to make a comparison of our data with that for the Δ^+ [37], the assumptions and truncation of the partial wave series applied may not take into account additional contributions that could be present. It has been clearly observed through the partial wave coefficients that effects not present in [37] are present in our own data set. It is possible where only s- and p-wave contributions are considered in the partial-wave series of the previous analysis, contribution from d-wave strength may have to be considered in our own data. Or it may be the case that some other unexplored contribution is present.

This study uses the procedure outlined in [37] to highlight the differences observed between the Δ^+ which has had extensive analysis and the Δ^0. The results for the various Q^2 bins are shown in figures 7.30, 7.31 and 7.32 for Q^2 of 0.35, 0.25 and 0.15 $(GeV/c)^2$ respectively. We immediately see by comparing with the result from [37] in figure 7.33 that once again major differences exist. Again we compare our highest Q^2 bin with the lowest of [37]. The value for M_{1+} in our 0.35 $(GeV/c)^2$ bin is quite well described by the model predictions. It is a considerably smaller cross-

Q^2 $(GeV/c)^2$	R_{EM}	R_{SM}
0.15	+3.1 $\pm$ 3.1 %	-1.9 $\pm$ 1.2 %
0.25	+4.3 $\pm$ 2.5 %	-0.5 $\pm$ 0.9 %
0.35	+6.5 $\pm$ 2.3 %	-1.2 $\pm$ 0.8 %

Table 7.1: Values for the multipole ratios R_{EM} and R_{SM}.

section than in the Δ^+ case. Possible reasons for this are final state interactions. The interference terms $Re\left(M_{1-}M_{1+}^*\right)$, $Re\left(E_{0+}M_{1+}^*\right)$ and $Re\left(S_{0+}M_{1+}^*\right)$ clearly show the only contribution to come in the theoretical models arise from the with-Born calculations. We find contributions which only mimic the model in the case of $Re\left(E_{0+}M_{1+}^*\right)$, even then not very closely. The model is not designed for our quasi-free target and therefore it is no surprise that differences occur. Looking at the transition in the two lower Q^2 bins there is no apparent consistency where in the 0.25 $(GeV/c)^2$ bin (figure 7.31) the data peak sits between the two theoretical models in terms of magnitude and has a peak position corresponding to neither. In the 0.15 $(GeV/c)^2$ bin (figure 7.32) the distribution is significantly below both model calculations and again has a peak position matching neither. Evidently something is contributing that may have a Q^2 dependence providing less effect at higher values, and is not accounted for in the models or seen in the $\Delta^+ \rightarrow p\pi^0$ analysis.

The important quantities we are seeking as outlined in chapter 2 are the interference terms $Re\left(E_{1+}M_{1+}^*\right)$ and $Re\left(S_{1+}M_{1+}^*\right)$. The model predictions for these quantities is small but non-zero as the theory suggests (section 1.1). We find small non-zero contributions in the data with a very definite distribution of the E_{1+} factor in the upper two Q^2 bins and a reduced but non-zero contribution in the lowest Q^2 bin. The S_{1+} factor however shows almost no features, with the contribution in this term close to zero. As was pointed out earlier, the value of the $Re\left(S_{1+}M_{1+}^*\right)$ is wholly dependent on the coefficient D_1, which our measurements had a great deal of uncertainty with. By dividing the distributions by the dominant magnetic dipole (section 2.3.3) it may be possible to discern more.

7.5 Multipole Ratios

It is through the non-dominant multipoles interference with the M_{1+} that measurements of properties such as the shape can be made (section 2.3.3). By measuring the quantities listed in equations 2.25 and dividing the interference terms through by $|M_{1+}|^2$ we can obtain R_{EM} and R_{SM} (as well as the various other multipole interferences). In our data plots (figure 7.34, 7.35 and 7.36) the model where no Born contributions are present indicate a small negative value for the ratio R_{SM} and a larger positive value for R_{EM} at the resonance peak position. At our highest Q^2 bin we find in the case of R_{EM} a value of $+6.5\pm2.3\%$. We also find R_{SM} for this bin to be $-1.2 \pm 0.8\%$. Figure 7.37 shows the ratios determined in [37]. In their experimental setup the values for R_{EM} and R_{SM} were about -4% and -5% respectively. Our distributions are very different from the model calculations demonstrating further that we are dealing with a situation not covered by the any of theoretical models. The remaining Q^2 bins show approximately the same distributions as the highest bin with little or no change in the strength of the various ratios. Table 7.1 shows the values for the Q^2 bins and our measured R_{EM} and R_{SM} at the resonance peak. It is clear that our data in the other ratios are very different from the theoretical calculations for the Δ^+ case.

Additionally we find useful results in the other three ratios for M_{1-}, E_{0+} and S_{0+}. The theoretical model shows no contribution in these ratios for the resonance, only the with-Born model has a non-zero distribution around the resonance region. Our data shows significant contributions in the ratios for M_{1-} and E_{0+} not closely corresponding to the model predictions. Since only the with-Born model shows strength in these quantities, the data we have produced should prove very useful in refining it. So we have produced results that give experimental distributions for the magnetic dipole and the interference terms from the other contributing multipoles for a Δ^0 produced from a quasi-free neutron target. These data should prove a great help in refining the theoretical models and add to the database that guides these models.

7.6 Resonance Peak Position

As an additional opportunity presented by our study, we could look for medium modifications of the Δ. The studies performed in [48] and [49] reported that in an inclusive measurement of the bound Δ, a shift in the resonance mass peak position was observed as Q^2 varied. It was thought that this was an indication of the medium effects being looked for and showed that the Δ mass peak increased with increasing Q^2. In this data set we have observed no such Q^2 dependence. Looking at the plots in figure 7.10 where the coefficient A_0 corresponds to the fit of the form A+C$\cos(2\phi^*_\pi)$+D$\cos(\phi^*_\pi)$ to the ϕ^*_π distributions of the differential cross-section. As was mentioned, A_0 is proportional to the total electroproduction cross-section and its peak position indicative of the Δ resonance peak position for the measured Q^2. We would expect to see any variations in peak value show up in this coefficient. We see in the plots of figures 7.10, 7.11 and 7.12 that the data peak position stays at around 1230 GeV/c^2 and no significant movement is observed that is beyond resolution limitations. We haven't observed any consistent movement of the peak over our measured Q^2 range. This does not mean that medium effects do not exist or are not present in our data. By studying the angular distribution of the decay products we have gone far beyond the simple study of peak positions through inclusive measurements of the cross-section.

7.7 Discussion

The analysis presented here uses the procedure outlined to study the angular distribution of the decay products in our experiment. We have applied exclusive measurements and derived differential cross-sections to achieve this. Much has been done and still more could be done to extend the study to even more useful research.

As was outlined in the theory sections and referred to throughout the analysis sections, the study was running in a similar vein with previous work performed on the Δ^+. Assumptions were made about the truncation of the partial-wave series to accommodate limited pion momentum, presumption of s- and p-wave contributions only (where any d-wave contributions were found to be roughly zero in Joo et al. [37]) and magnetic dipole dominance. These are all valid assertions and necessary as a first stage, but they also restrict the scope of our results, perhaps obscuring or removing effects that the study might otherwise find. The purpose of following these approximations was to create data distributions that could be compared to the previous works performed and expose the differences between the Δ^+ and Δ^0. The numerous plots of fits and multipole interferences and their ratios have shown us that there are substantial differences between the Δ^0 and Δ^+. It would prove useful to also see the equivalent distribution, using the $p\pi^0$ channel and observe the Δ^+ in the nuclear medium. This would greatly reduce the Born effects and allow the study of any differences between the free and bound Δ^+ that might be due to medium effects.

The difficulties with detecting the two-photon decay products of the π^0 make it necessary to have a larger data pool to obtain the required statistics to generate the large number of kinematic bins we used. A preliminary study of our data set indicated a factor of 10 fewer statistics in the π^0 channel to the π^- and it is likely a larger data set than our own is needed. A key advancement of the study, now that we have observed various and considerable differences would be to extend the partial-wave series to look for any higher contributions. It may also be possible to use data taken at the same time as our experiment but at higher energies. This would allow extending the analysis to higher Q^2 bins as a further check of the Δ peak position and a better look at any effects that may be dependent on Q^2. A combination of this, the extension of the partial-wave series and the π^0 channel would be an excellent next step to the work presented here.

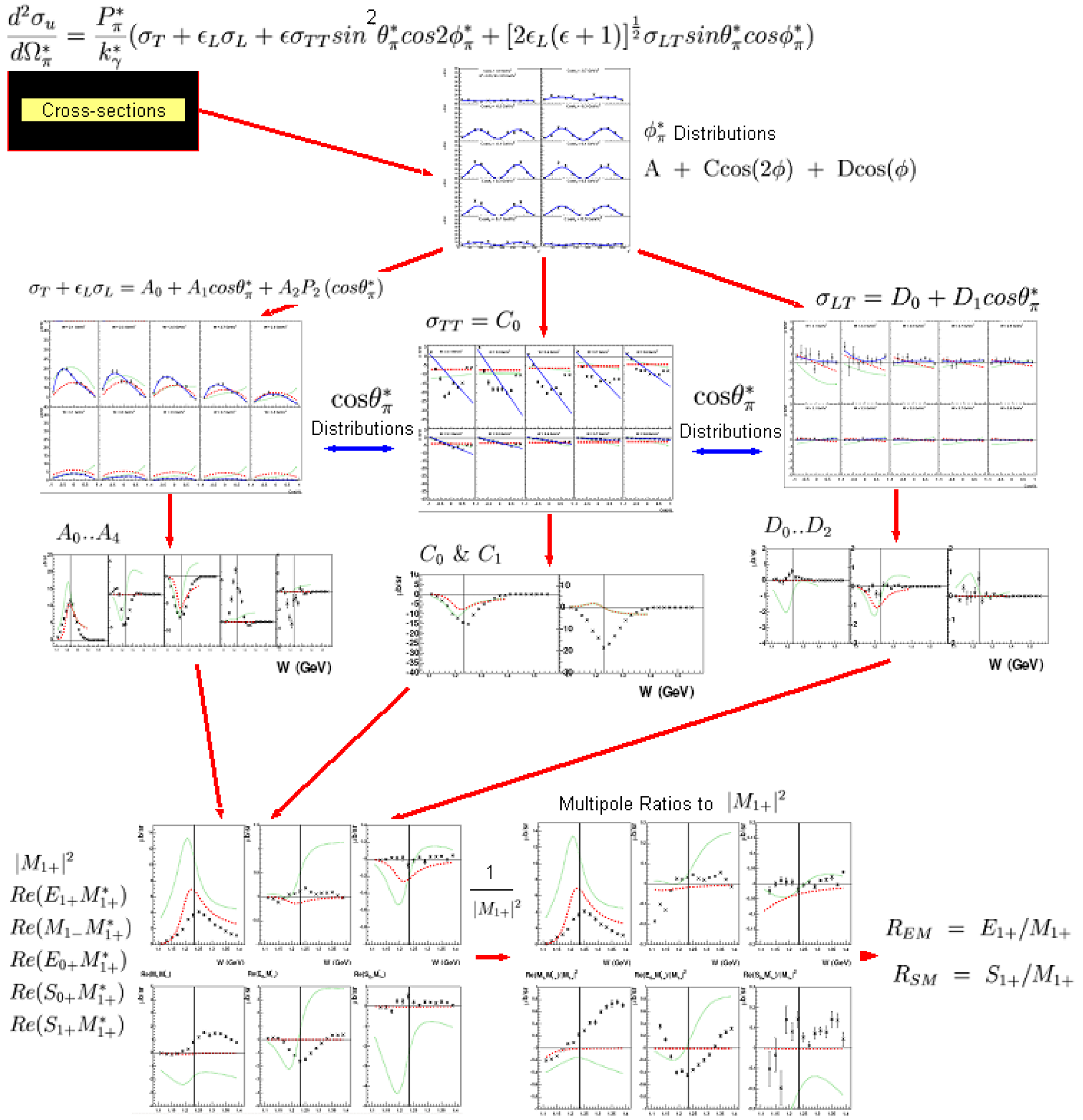

Figure 7.1: Flow chart for the various stages of the analysis and how the they progress to the final results.

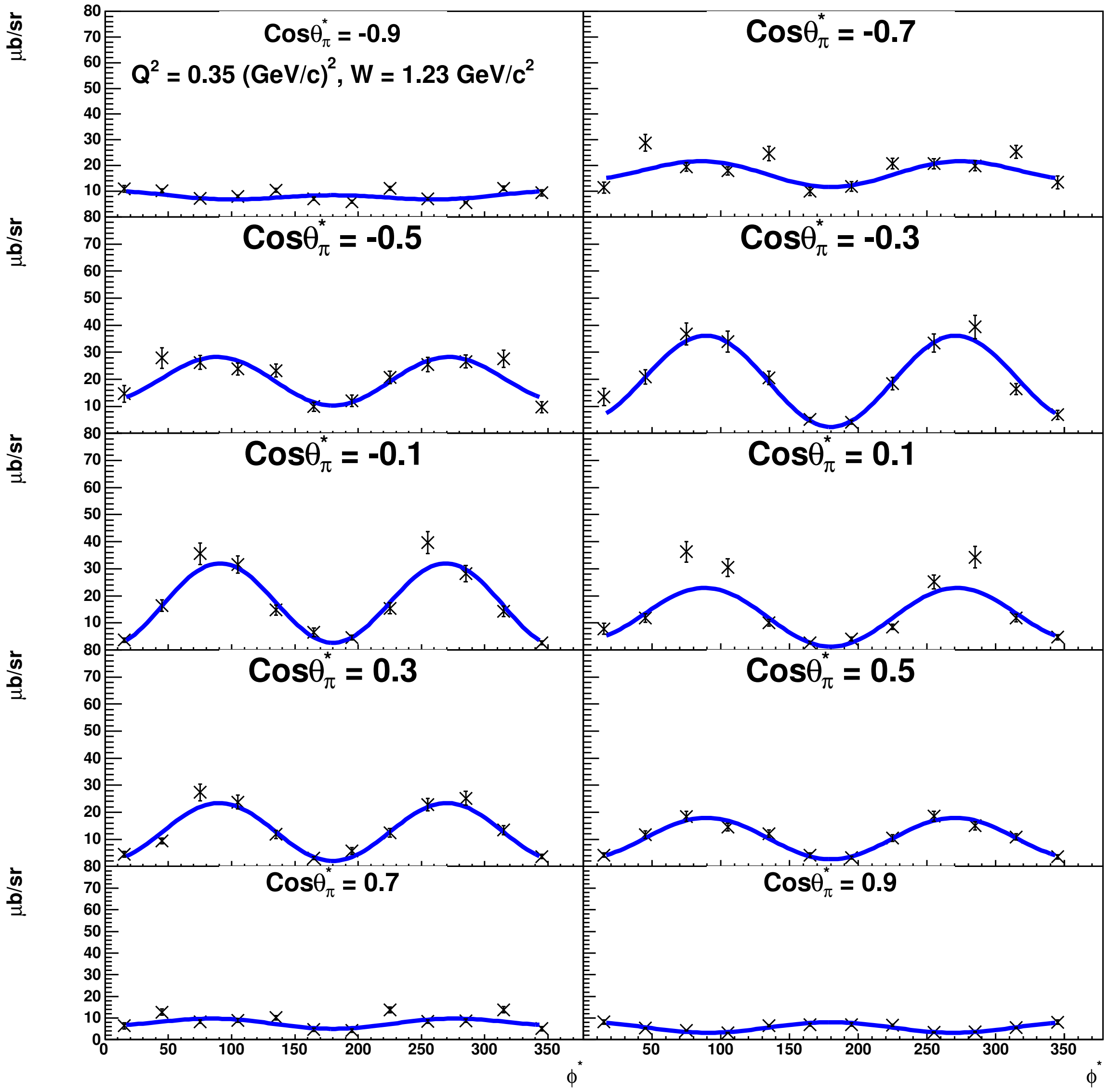

Figure 7.2: The differential cross-section plotted against ϕ_π^* at Q^2=0.35$(GeV/c)^2$. The characteristic of the distribution follows a A+Ccos(2ϕ)+Dcos(ϕ) form. The coefficients of this fit provide the structure functions.

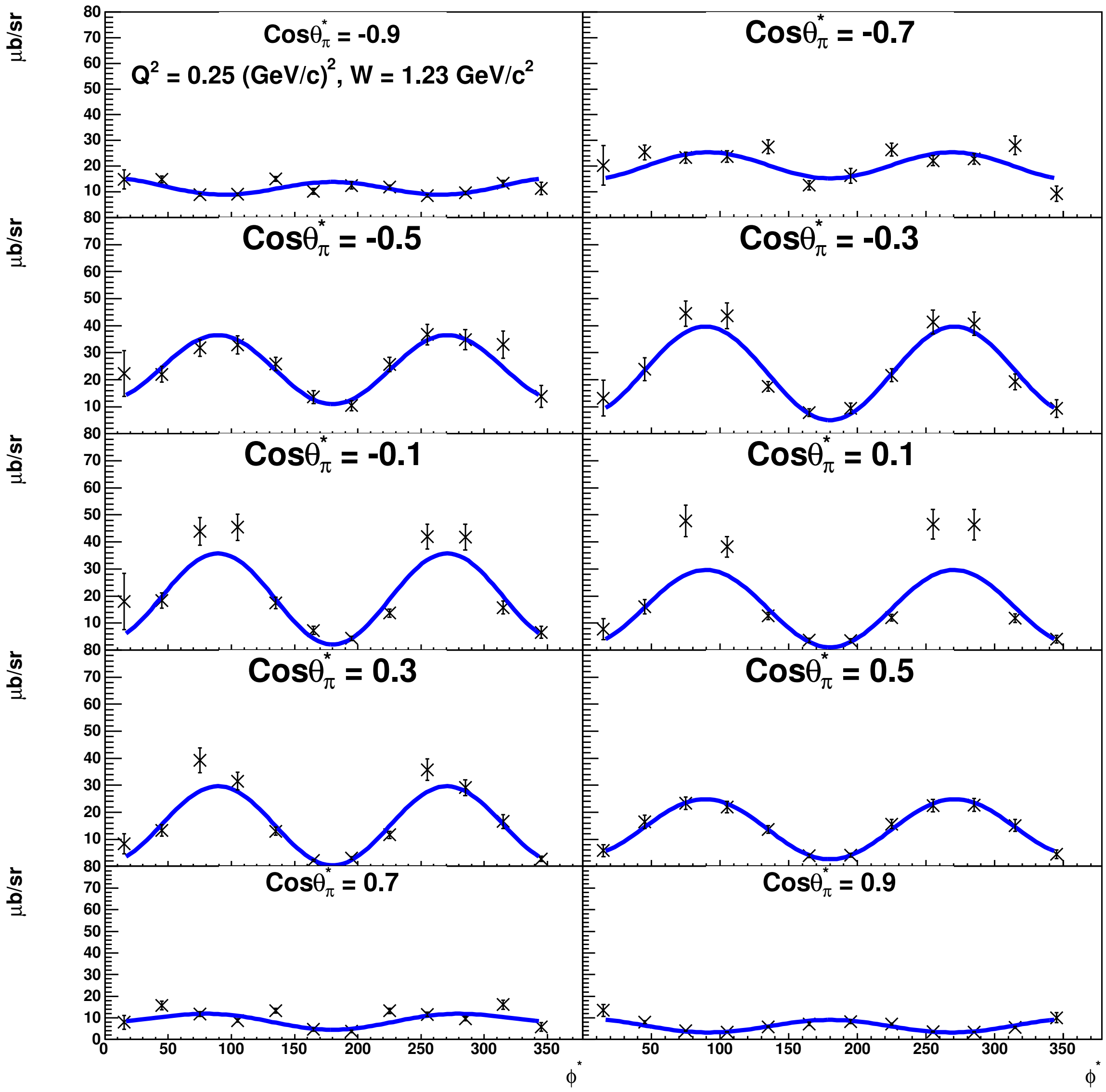

Figure 7.3: The differential cross-section plotted against ϕ_π^* at Q^2=0.25$(GeV/c)^2$. The characteristic of the distribution follows a A+Ccos(2ϕ)+Dcos(ϕ) form. The coefficients of this fit provide the structure functions.

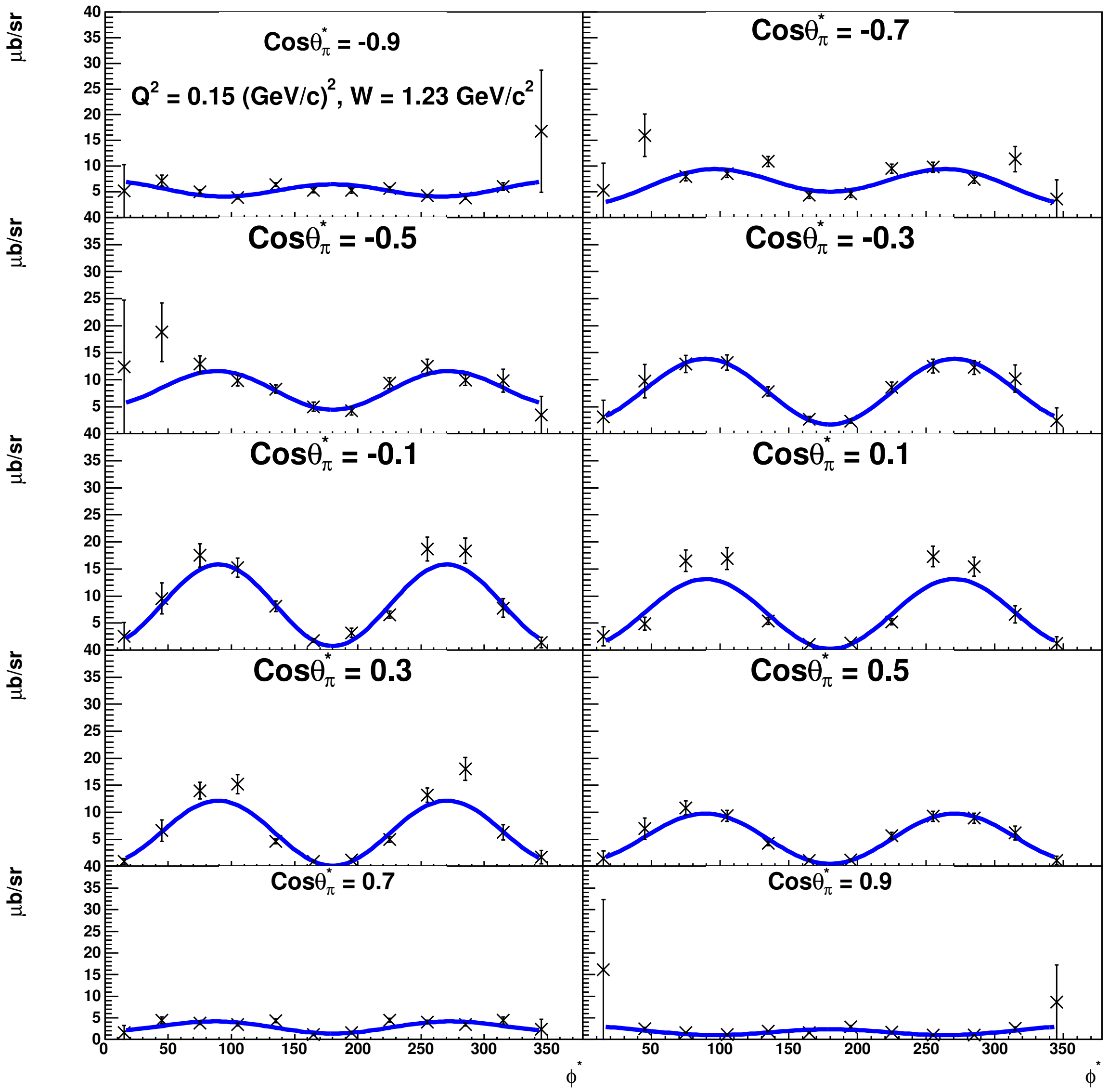

Figure 7.4: The differential cross-section plotted against ϕ_π^* at Q^2=0.15$(GeV/c)^2$. The characteristic of the distribution follows a A+Ccos(2ϕ)+Dcos(ϕ) form. The coefficients of this fit provide the structure functions.

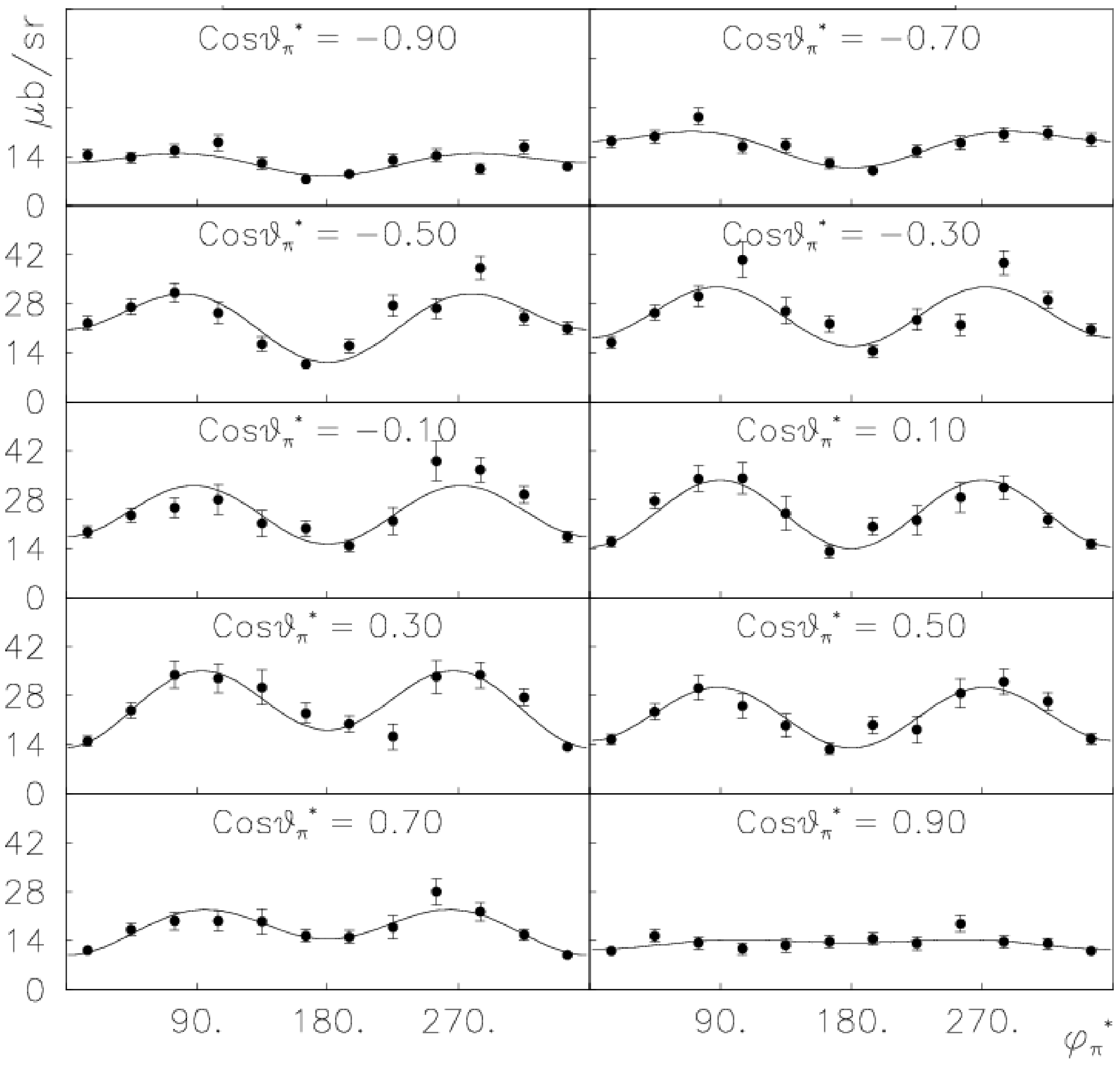

Figure 7.5: A typical ϕ^*_π dependence of the p(e,e'p)π^0 cross-sections measured at Q^2=0.4$(GeV/c)^2$ at the resonance peak position with CLAS. Taken from [37].

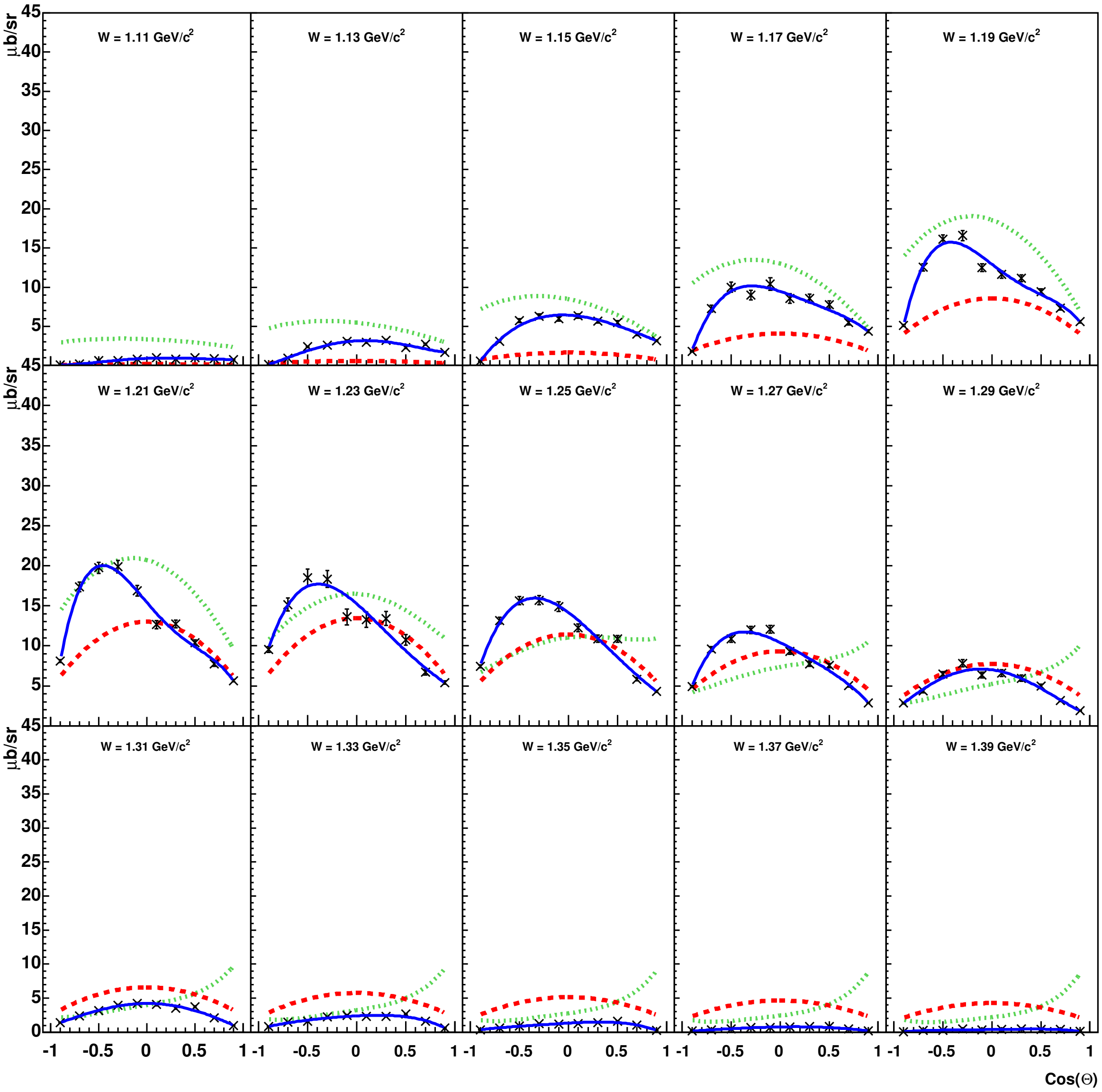

Figure 7.6: A plot of the fitted partial-wave series for the structure functions $\sigma_T + \epsilon_L \sigma_L$ on data at Q^2=0.35$(GeV/c)^2$. The blue curve is the fit to data, the red dashed line is a fit to theoretical calculations of the P33 resonance using MAID2003 and the green dotted line is the fit to theoretical calculations of the P33 + Born contributions.

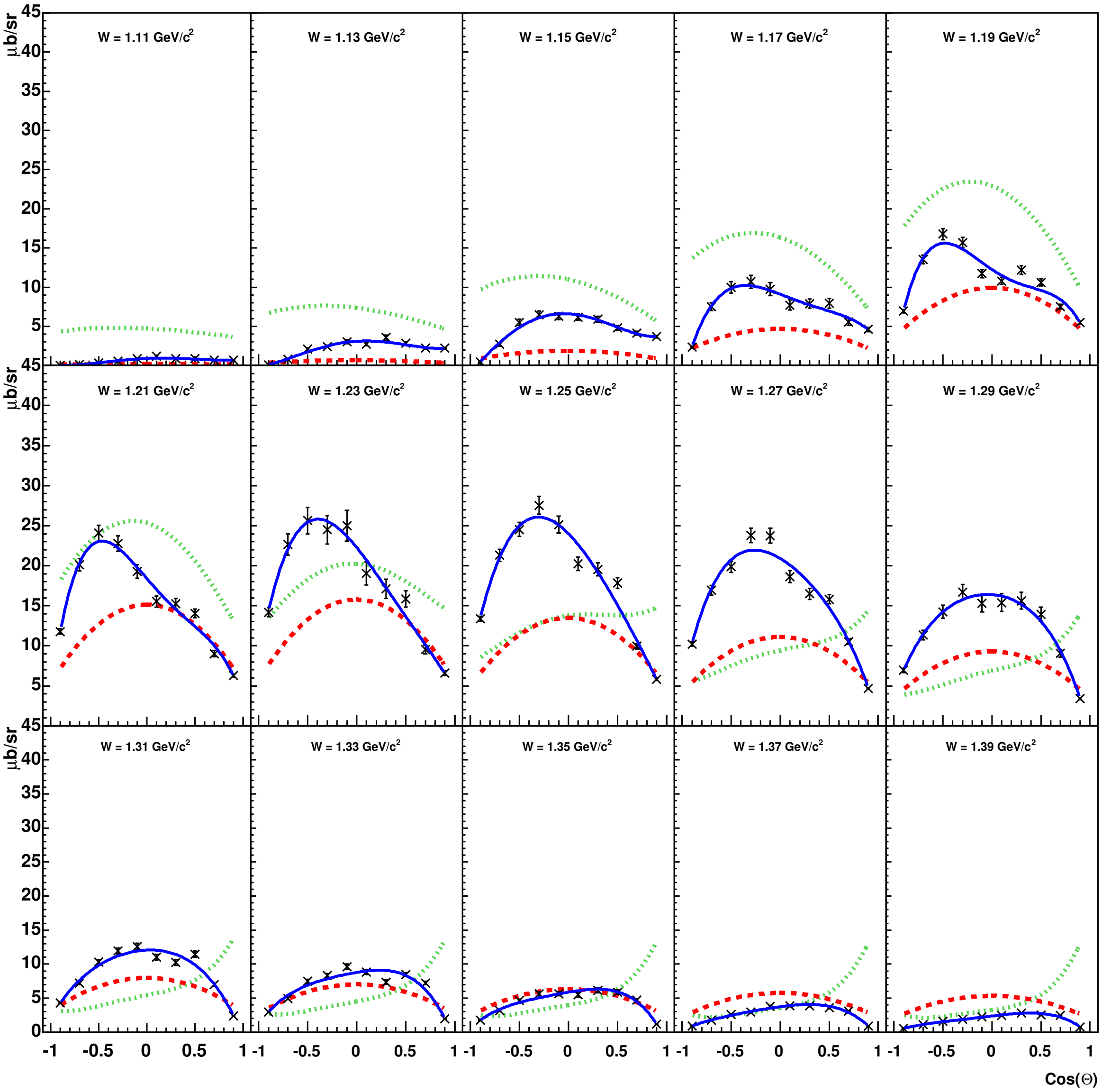

Figure 7.7: A plot of the fitted partial-wave series for the structure functions $\sigma_T + \epsilon_L \sigma_L$ on data at $Q^2{=}0.25(GeV/c)^2$. The blue curve is the fit to data, the red dashed line is a fit to theoretical calculations of the P33 resonance using MAID2003 and the green dotted line is the fit to theoretical calculations of the P33 + Born contributions.

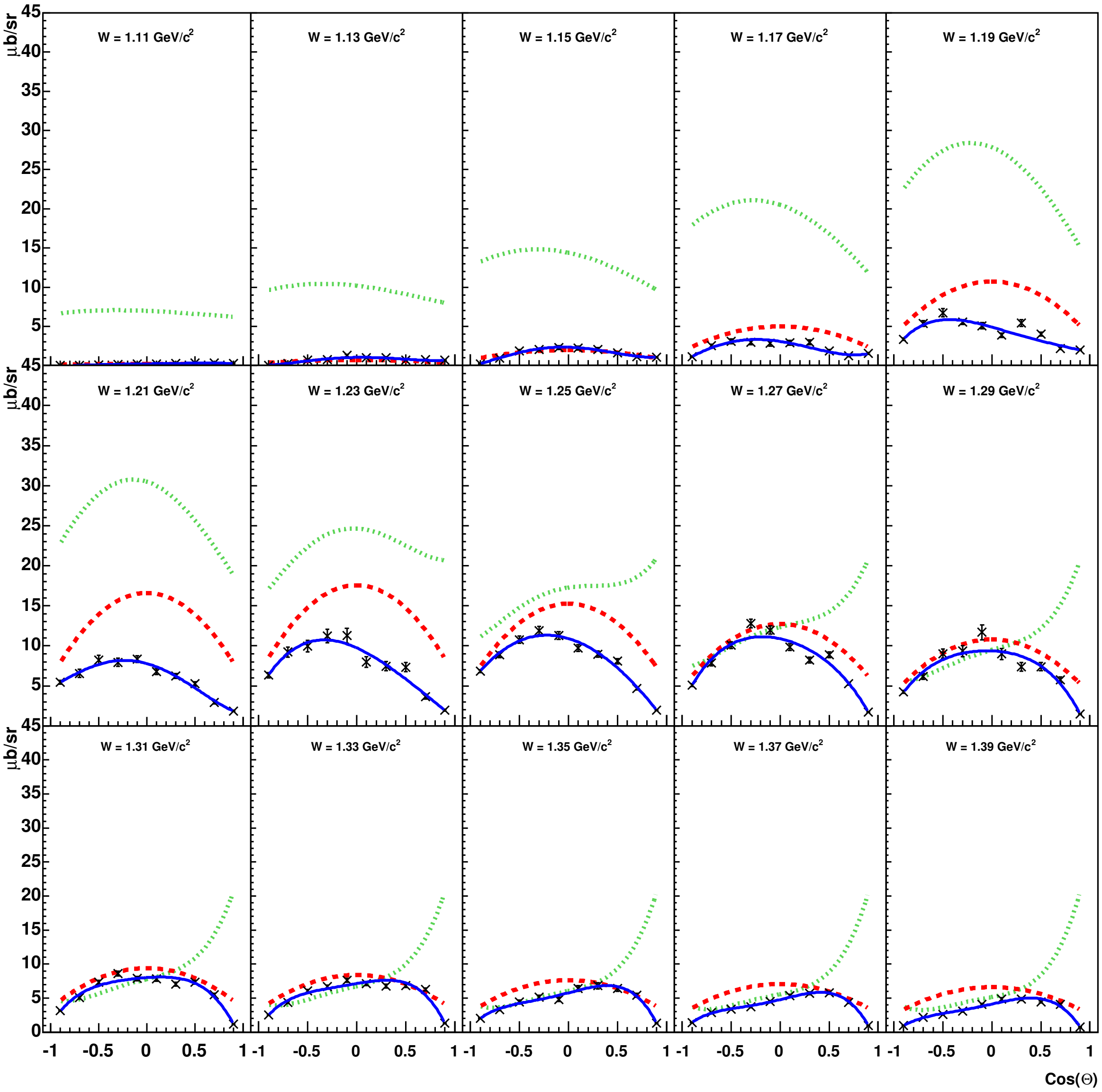

Figure 7.8: A plot of the fitted partial-wave series for the structure functions $\sigma_T + \epsilon_L \sigma_L$ on data at Q^2=0.15$(GeV/c)^2$. The blue curve is the fit to data, the red dashed line is a fit to theoretical calculations of the P33 resonance using MAID2003 and the green dotted line is the fit to theoretical calculations of the P33 + Born contributions.

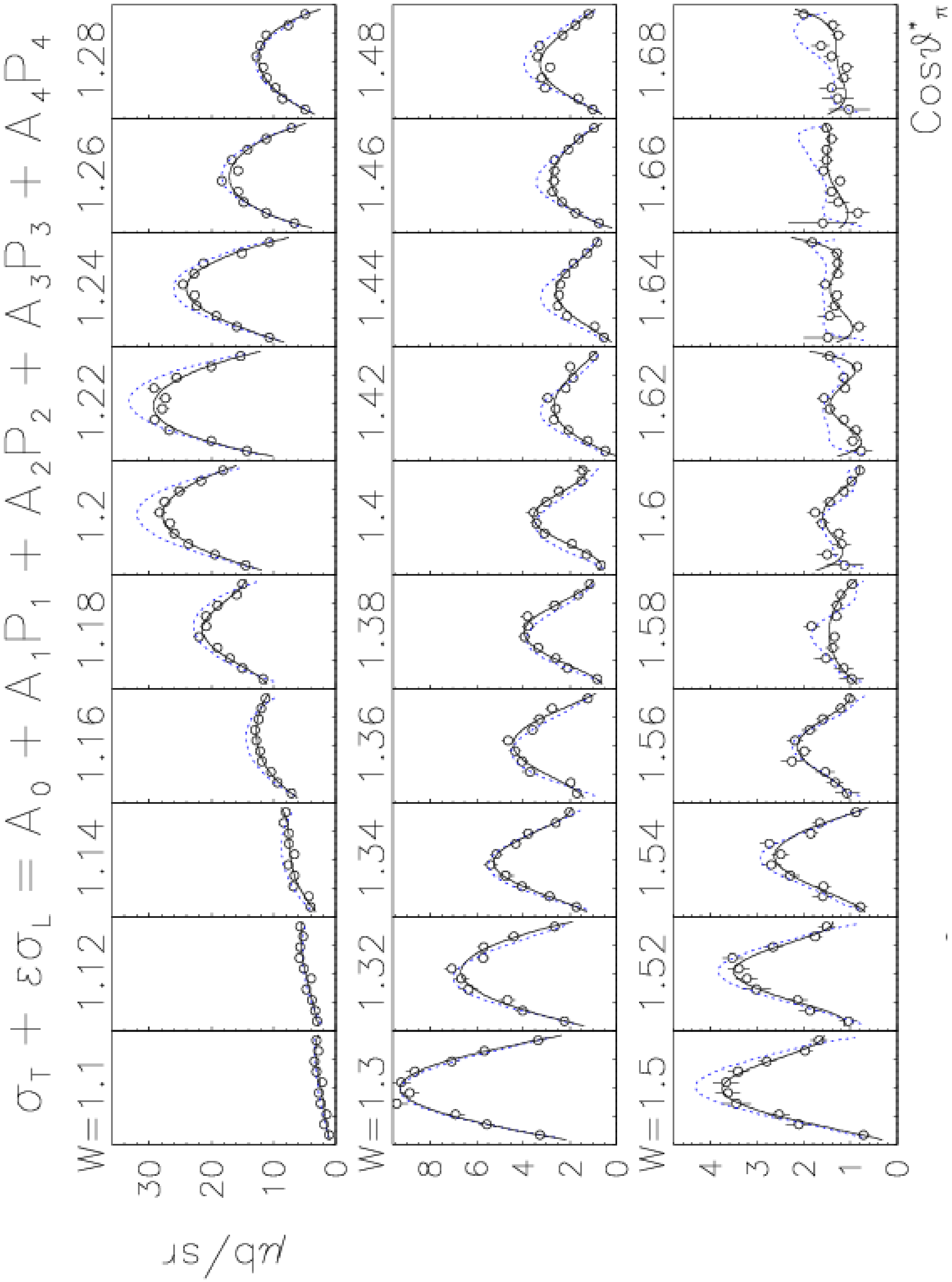

Figure 7.9: A plot of the fitted partial-wave series for the structure functions $\sigma_T + \epsilon_L \sigma_L$. The solid line is a fit to the data, the dashed line shows the MAID-98 theoretical calculations. Taken from [37].

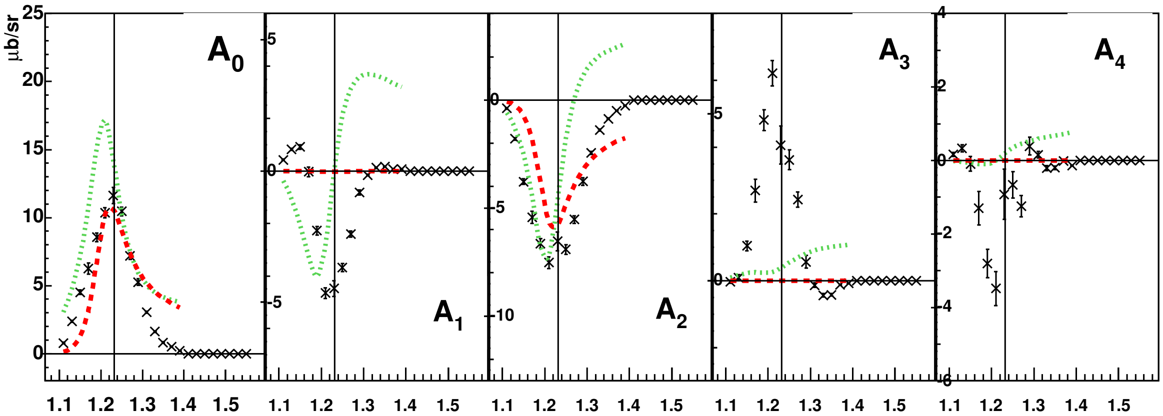

Figure 7.10: The set of partial-wave coefficients $A_0..A_4$ plotted against W for Q^2=0.35$(GeV/c)^2$. The red dashed line is a fit to theoretical calculations of the P33 resonance using MAID2003 and the green dotted line is the fit to theoretical calculations of the P33 + Born contributions. The black vertical line is the free-Δ mass (1232 GeV/c^2).

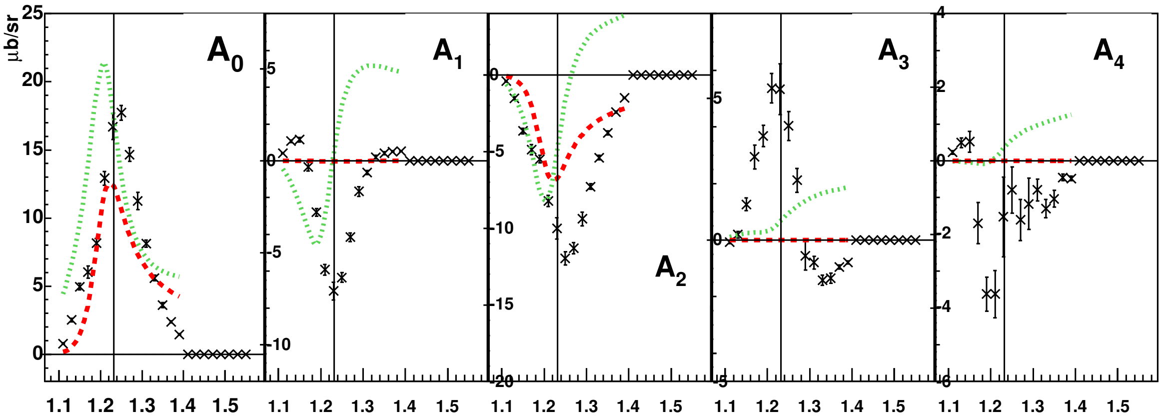

Figure 7.11: The set of partial-wave coefficients $A_0..A_4$ plotted against W for Q^2=0.25$(GeV/c)^2$. The red dashed line is a fit to theoretical calculations of the P33 resonance using MAID2003 and the green dotted line is the fit to theoretical calculations of the P33 + Born contributions. The black vertical line is the free-Δ mass (1232 GeV/c^2).

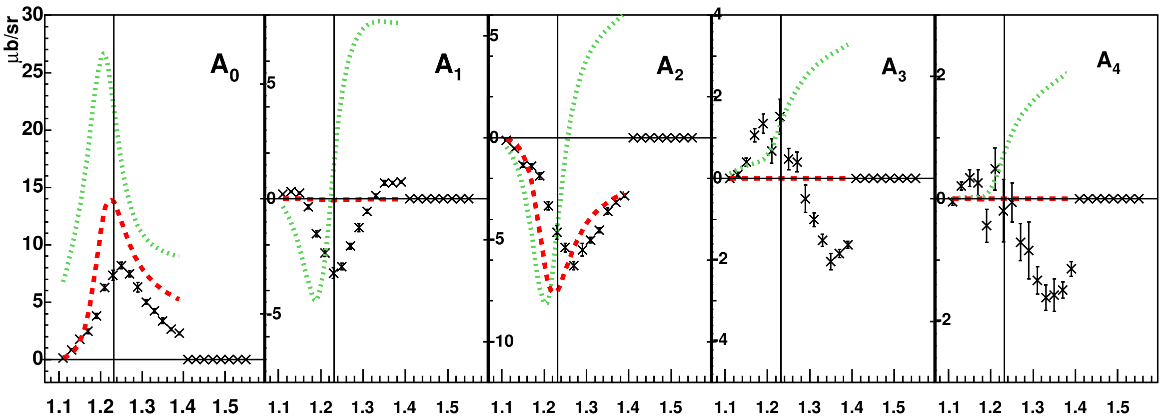

Figure 7.12: The set of partial-wave coefficients $A_0..A_4$ plotted against W for Q^2=0.15$(GeV/c)^2$. The red dashed line is a fit to theoretical calculations of the P33 resonance using MAID2003 and the green dotted line is the fit to theoretical calculations of the P33 + Born contributions. The black vertical line is the free-Δ mass (1232 GeV/c^2).

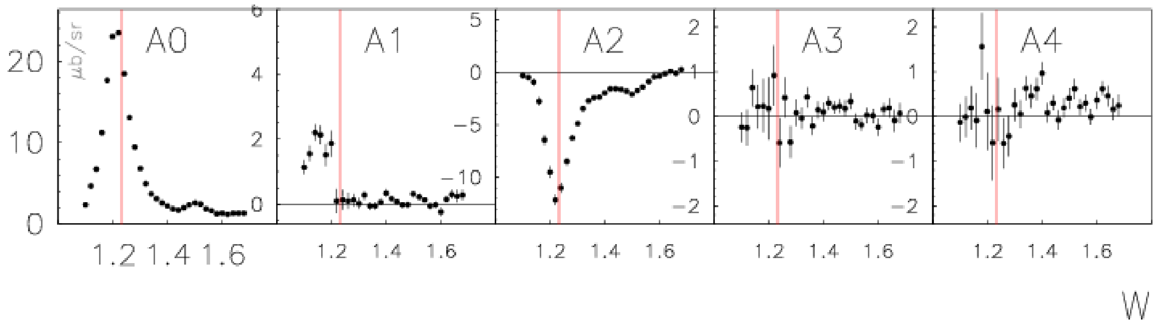

Figure 7.13: The set of partial-wave coefficients $A_0..A_4$ plotted against W. Taken from [37].

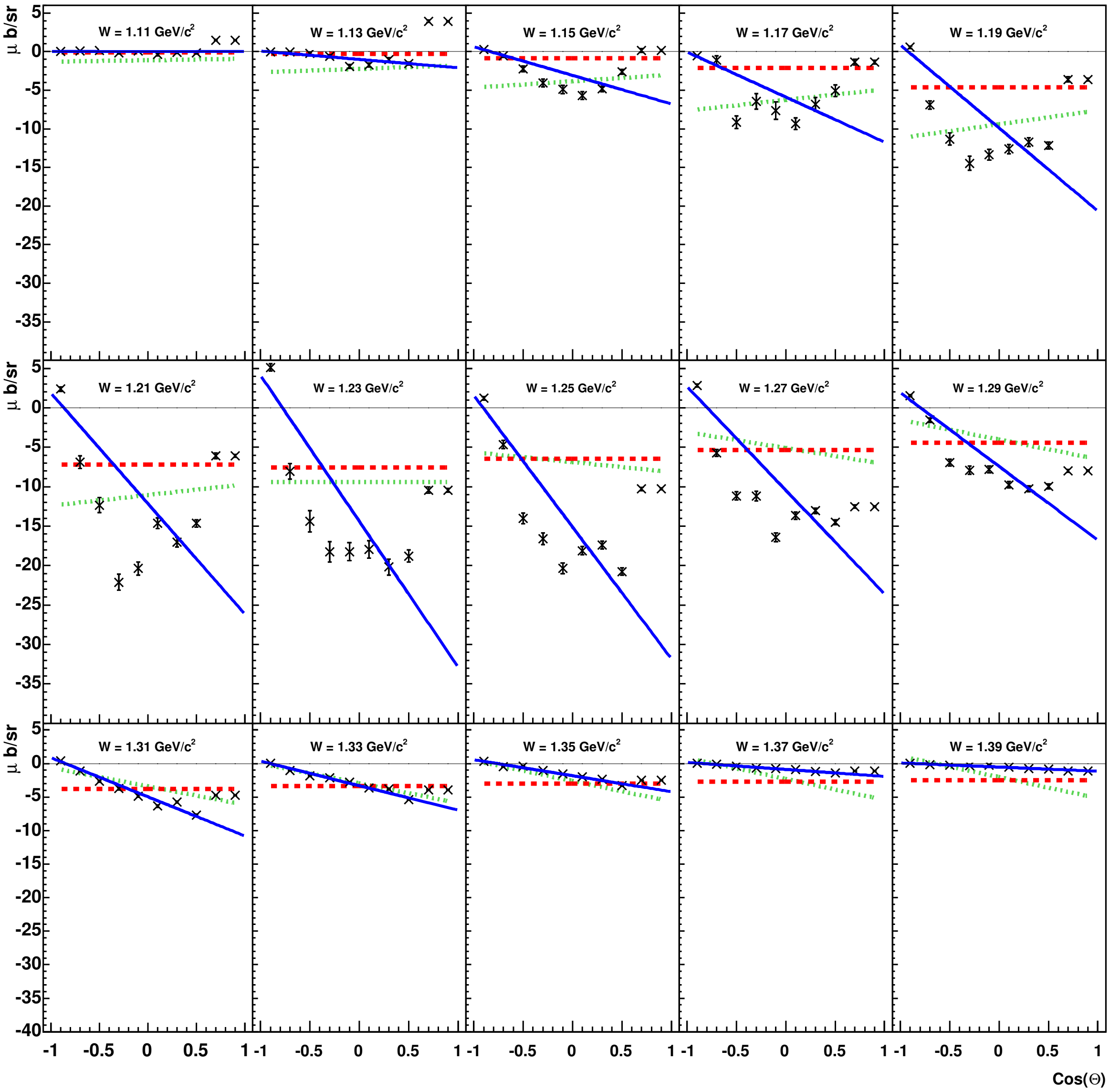

Figure 7.14: A plot of the fitted partial-wave series for the structure function σ_{TT} on data at Q^2=0.35$(GeV/c)^2$. The blue line is the fit to data, the red dashed line is a fit to theoretical calculations of the P33 resonance using MAID2003 and the green dotted line is the fit to theoretical calculations of the P33 + Born contributions.

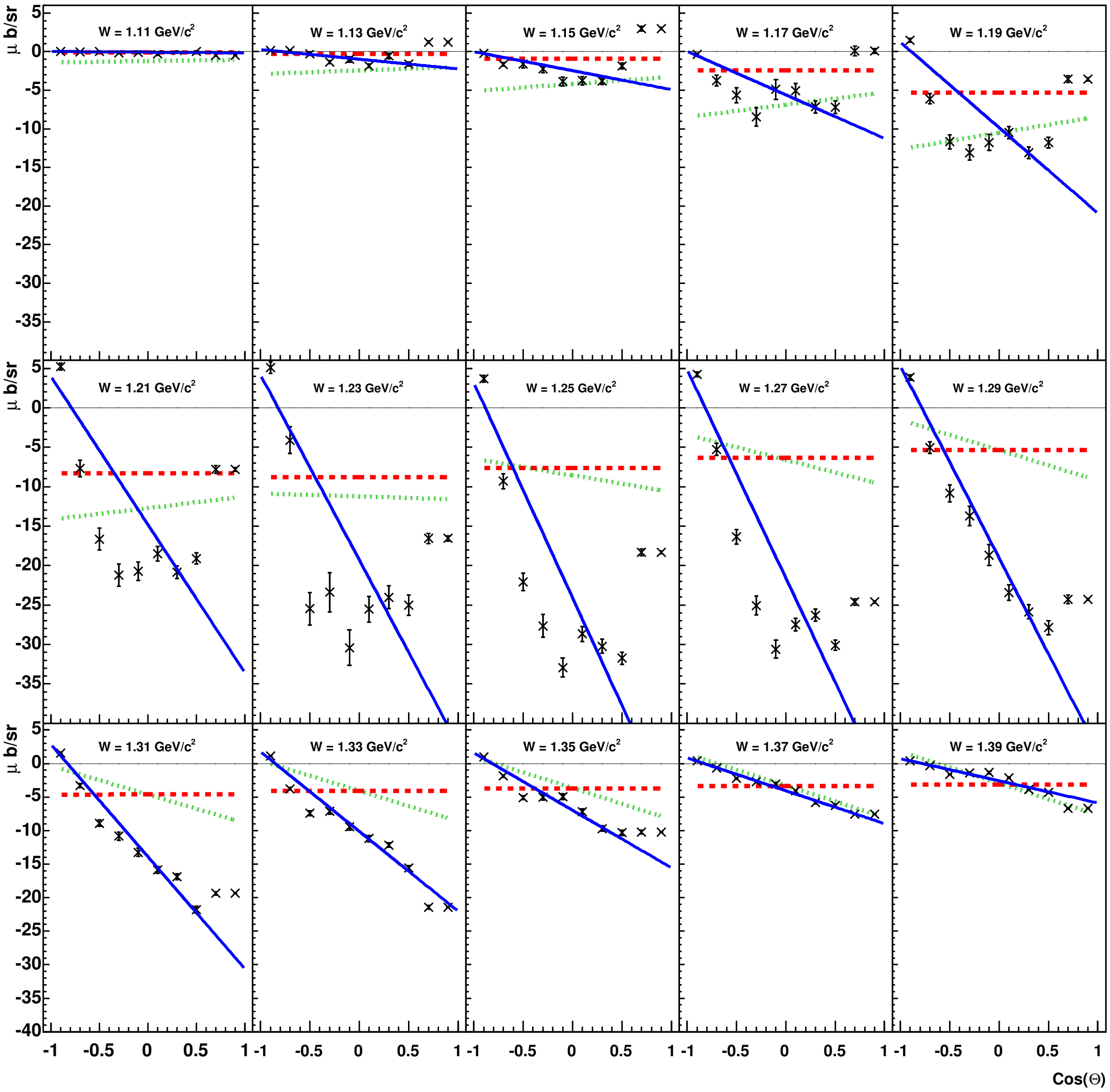

Figure 7.15: A plot of the fitted partial-wave series for the structure function σ_{TT} on data at Q^2=0.25$(GeV/c)^2$. The blue line is the fit to data, the red dashed line is a fit to theoretical calculations of the P33 resonance using MAID2003 and the green dotted line is the fit to theoretical calculations of the P33 + Born contributions.

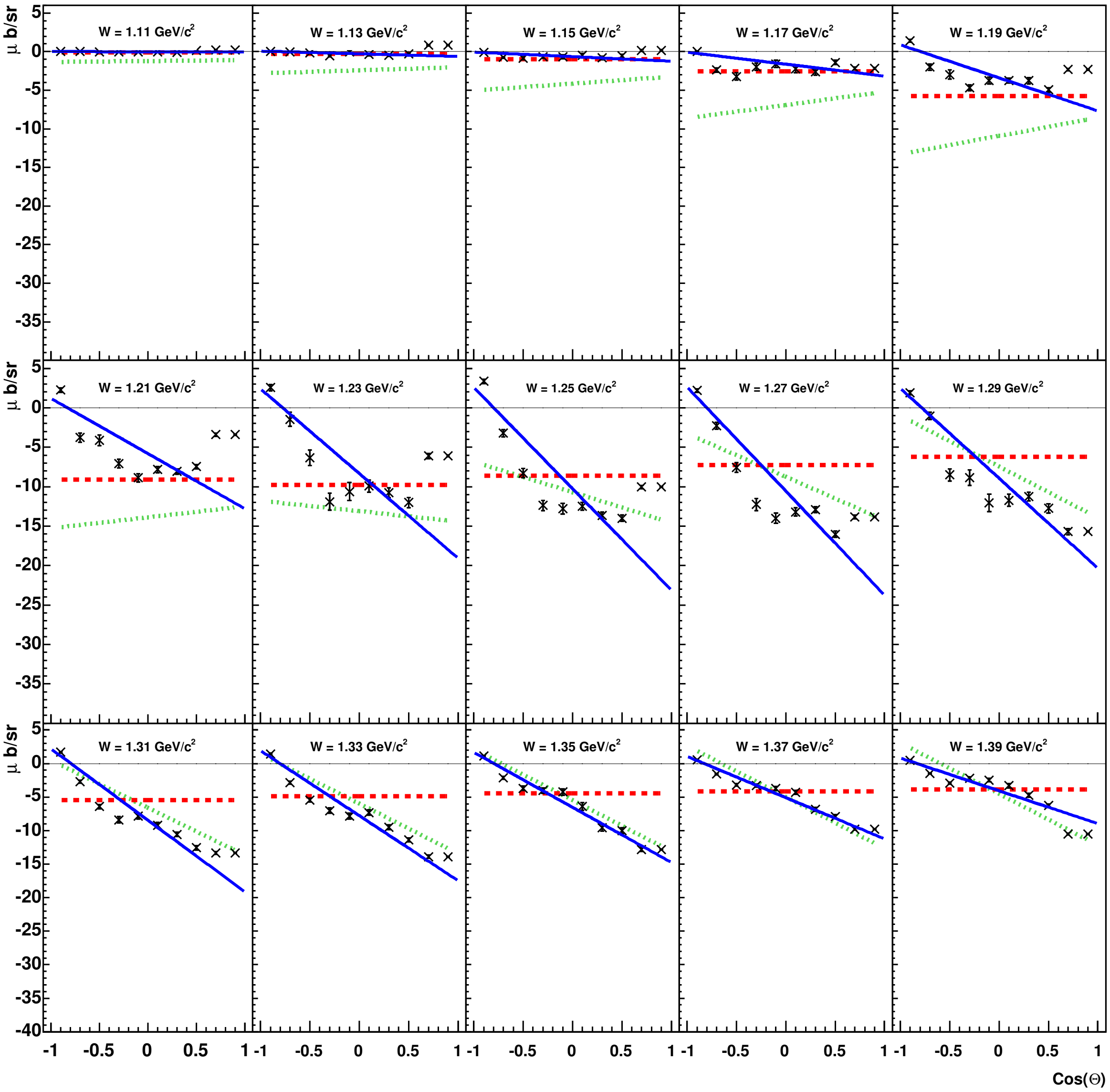

Figure 7.16: A plot of the fitted partial-wave series for the structure function σ_{TT} on data at Q^2=0.15$(GeV/c)^2$. The blue line is the fit to data, the red dashed line is a fit to theoretical calculations of the P33 resonance using MAID2003 and the green dotted line is the fit to theoretical calculations of the P33 + Born contributions.

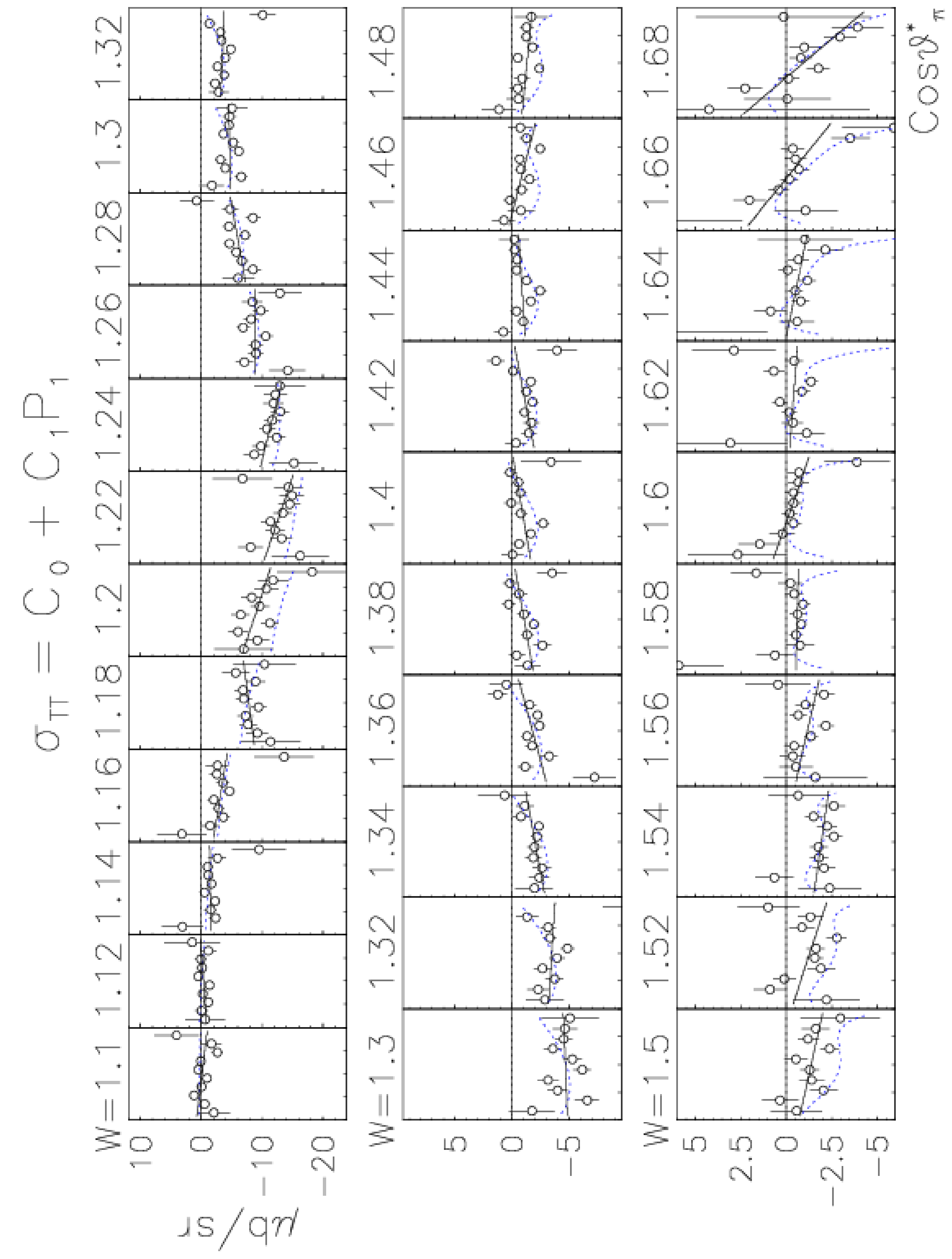

Figure 7.17: A plot of the fitted partial-wave series for the structure function σ_{TT}. The solid line is a fit to the data, the dashed line shows the MAID-98 theoretical calculations. Taken from [37].

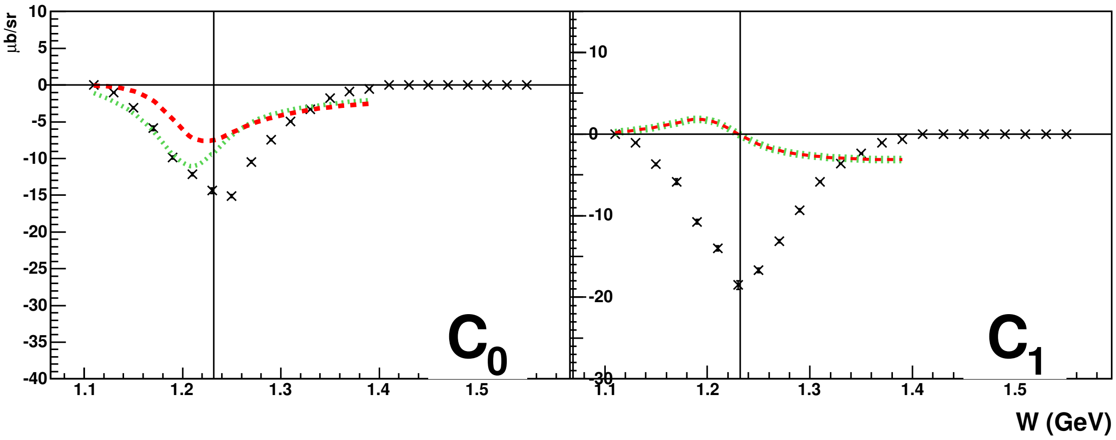

Figure 7.18: The set of partial-wave coefficients C_0 and C_1 plotted against W for Q^2=0.35$(GeV/c)^2$. The red dashed line is a fit to theoretical calculations of the P33 resonance using MAID2003 and the green dotted line is the fit to theoretical calculations of the P33 + Born contributions. The black vertical line is the free-Δ mass (1232 GeV/c^2).

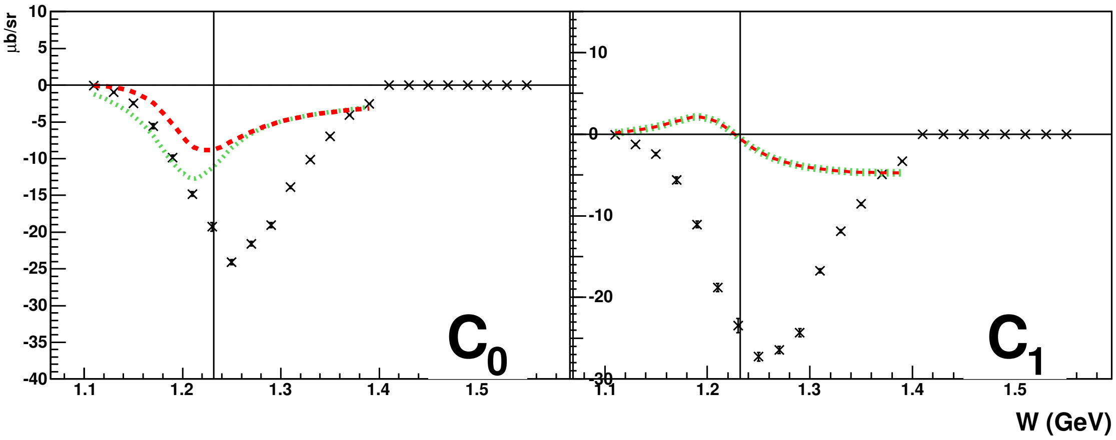

Figure 7.19: The set of partial-wave coefficients C_0 and C_1 plotted against W for Q^2=0.25$(GeV/c)^2$. The red dashed line is a fit to theoretical calculations of the P33 resonance using MAID2003 and the green dotted line is the fit to theoretical calculations of the P33 + Born contributions. The black vertical line is the free-Δ mass (1232 GeV/c^2).

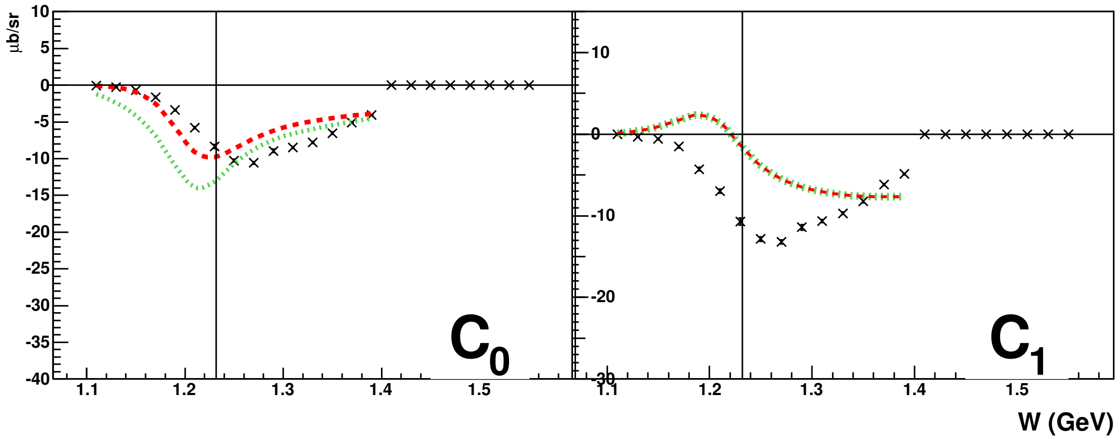

Figure 7.20: The set of partial-wave coefficients C_0 and C_1 plotted against W for Q^2=0.15$(GeV/c)^2$. The red dashed line is a fit to theoretical calculations of the P33 resonance using MAID2003 and the green dotted line is the fit to theoretical calculations of the P33 + Born contributions. The black vertical line is the free-Δ mass (1232 GeV/c^2).

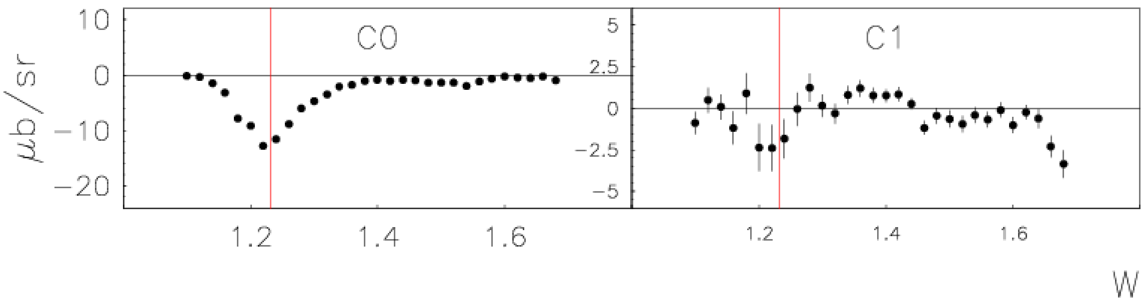

Figure 7.21: The set of partial-wave coefficients C_0 and C_1 plotted against W. Taken from [37].

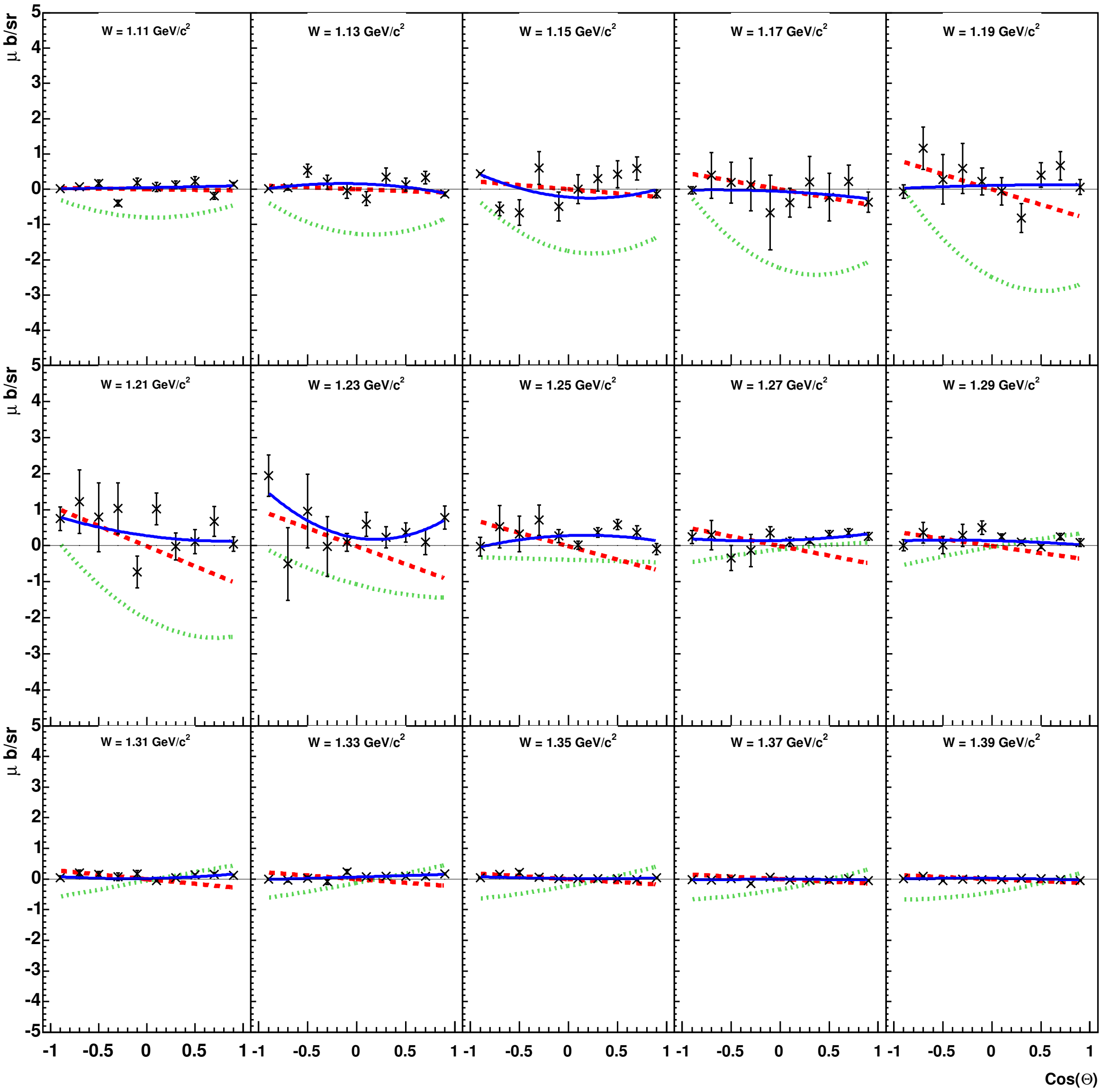

Figure 7.22: A plot of the fitted partial-wave series for the structure function σ_{LT} on data at Q^2=0.35$(GeV/c)^2$. The blue curve is the fit to data, the red dashed line is a fit to theoretical calculations of the P33 resonance using MAID2003 and the green dotted line is the fit to theoretical calculations of the P33 + Born contributions.

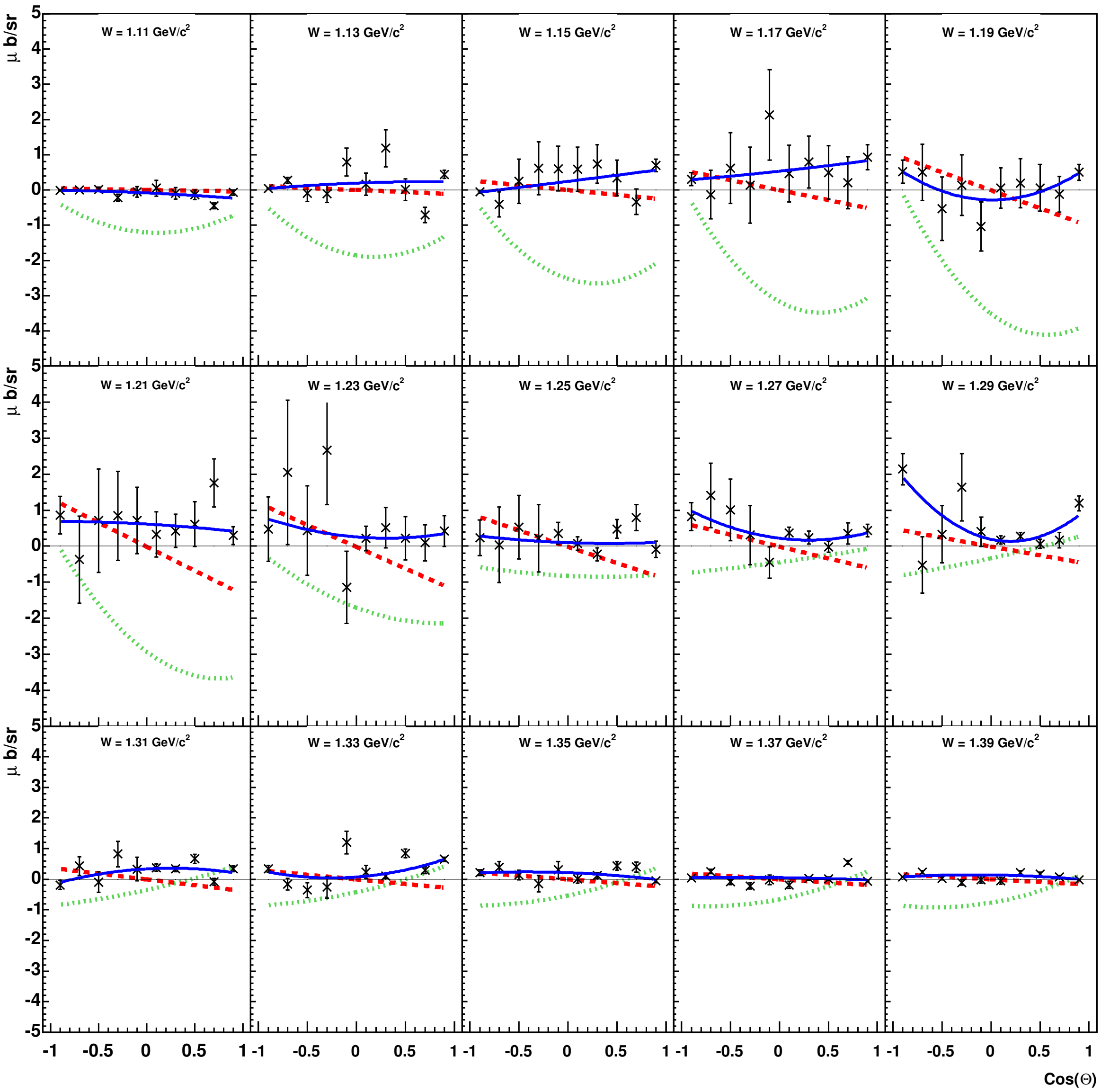

Figure 7.23: A plot of the fitted partial-wave series for the structure function σ_{LT} on data at Q^2=0.25$(GeV/c)^2$. The blue curve is the fit to data, the red dashed line is a fit to theoretical calculations of the P33 resonance using MAID2003 and the green dotted line is the fit to theoretical calculations of the P33 + Born contributions.

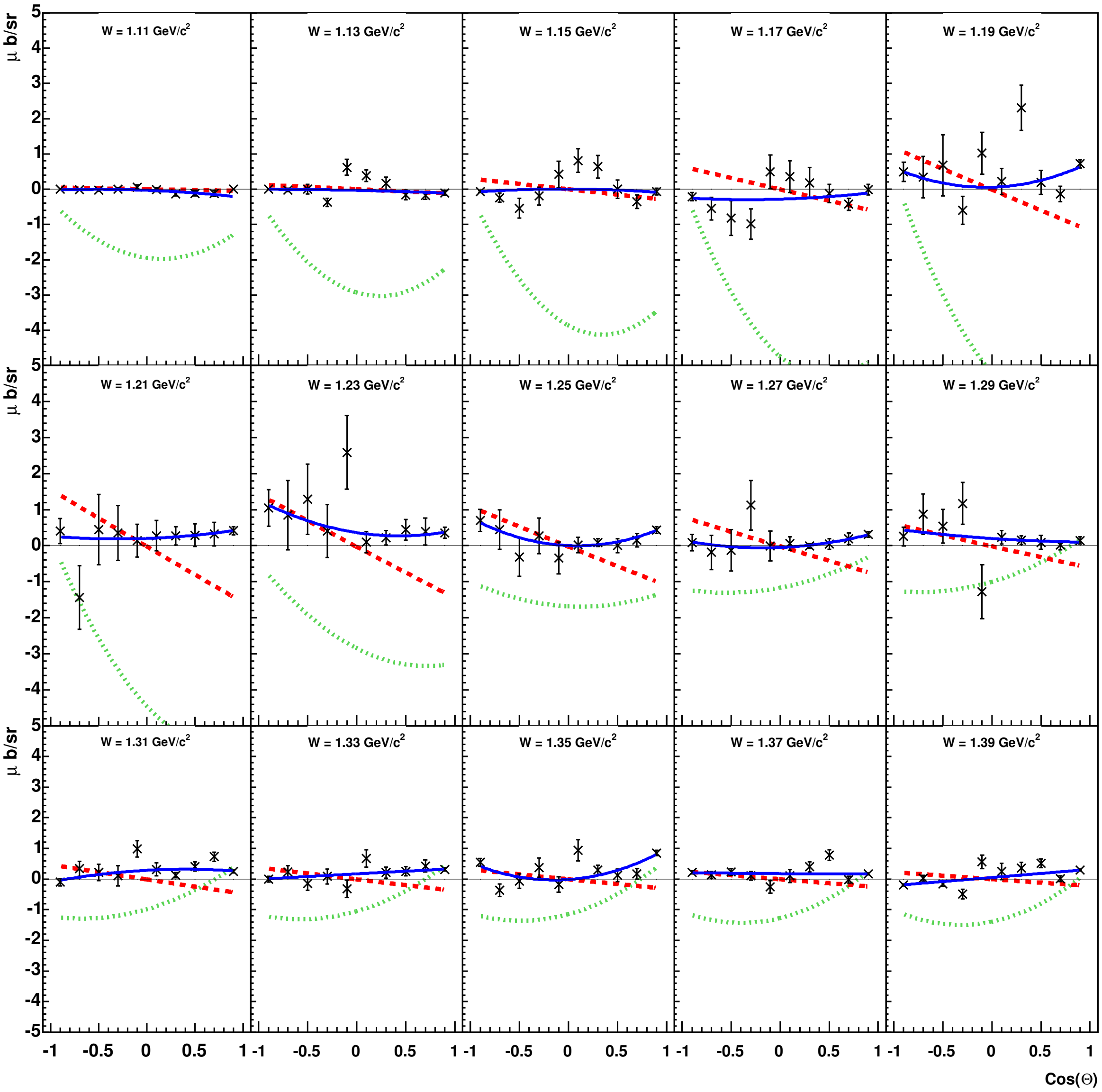

Figure 7.24: A plot of the fitted partial-wave series for the structure function σ_{LT} on data at Q^2=0.15$(GeV/c)^2$. The blue curve is the fit to data, the red dashed line is a fit to theoretical calculations of the P33 resonance using MAID2003 and the green dotted line is the fit to theoretical calculations of the P33 + Born contributions.

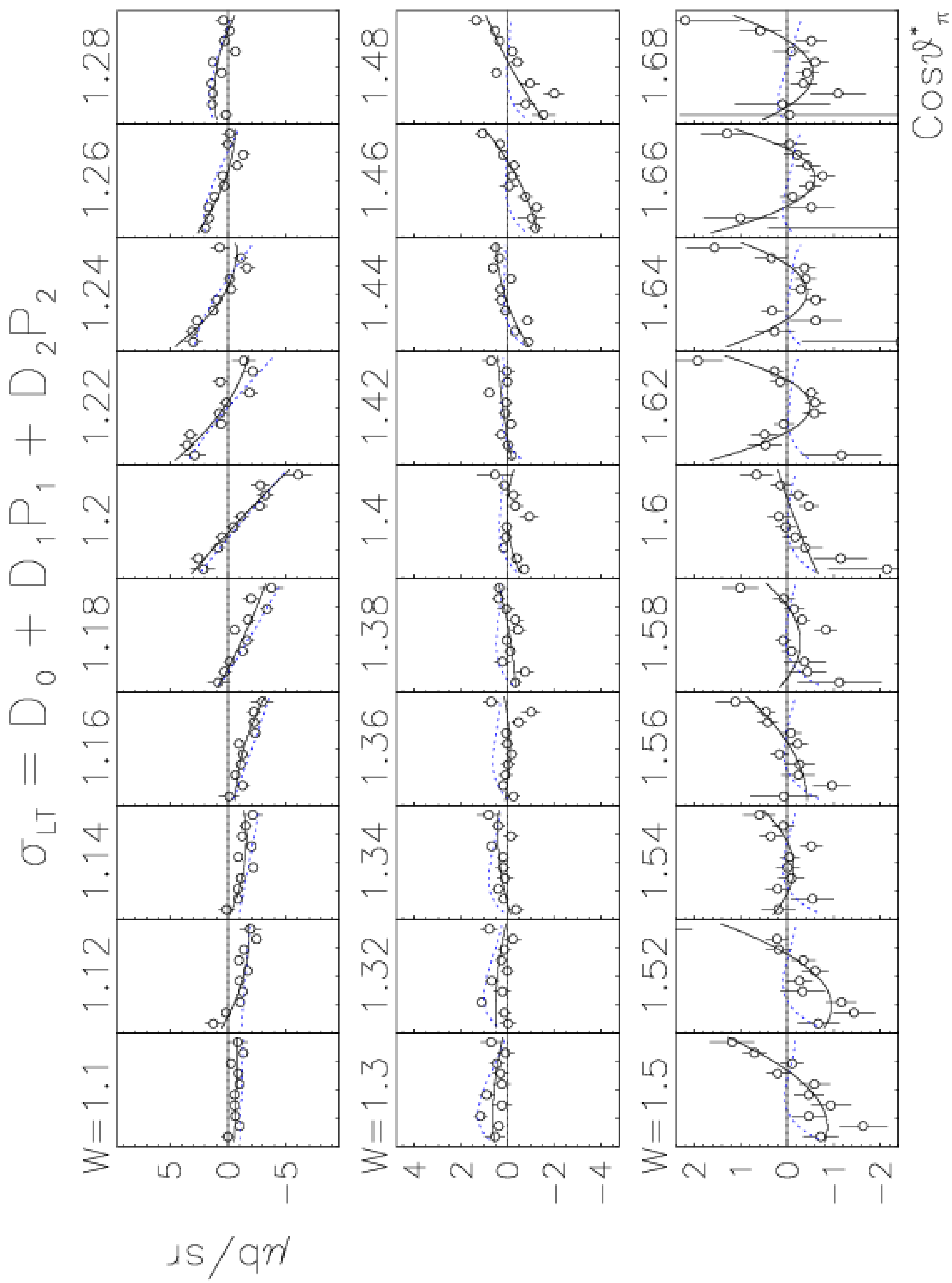

Figure 7.25: A plot of the fitted partial-wave series for the structure function σ_{LT} from [37]. The solid line is a fit to the data, the dashed line shows the MAID-98 theoretical calculations.

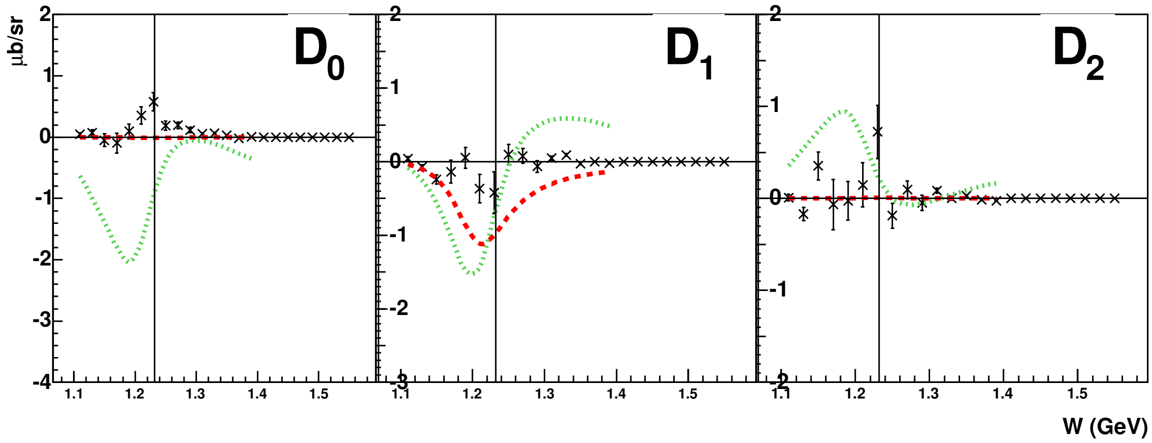

Figure 7.26: The set of partial-wave coefficients $D_0..D_2$ plotted against W for Q^2=0.35$(GeV/c)^2$. The red dashed line is a fit to theoretical calculations of the P33 resonance using MAID2003 and the green dotted line is the fit to theoretical calculations of the P33 + Born contributions. The black vertical line is the free-Δ mass (1232 GeV/c^2).

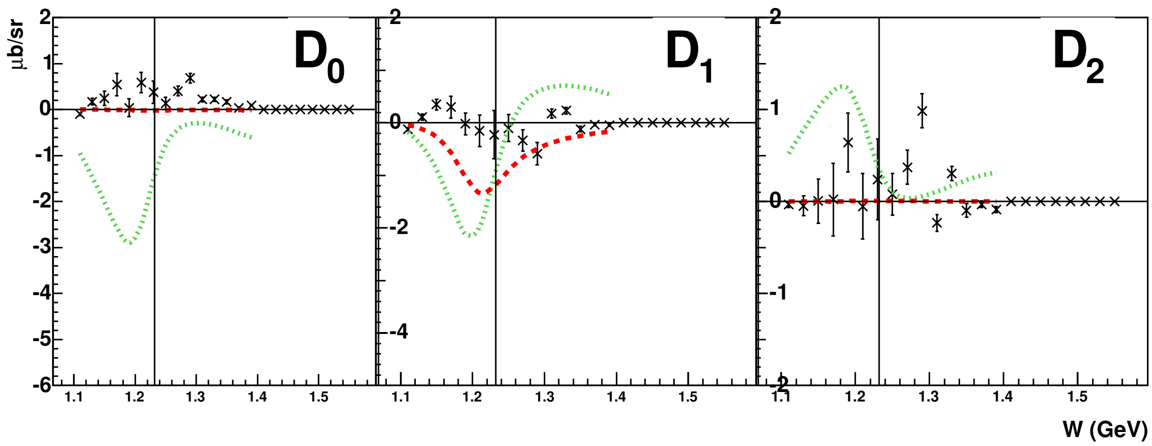

Figure 7.27: The set of partial-wave coefficients $D_0..D_2$ plotted against W for Q^2=0.25$(GeV/c)^2$. The red dashed line is a fit to theoretical calculations of the P33 resonance using MAID2003 and the green dotted line is the fit to theoretical calculations of the P33 + Born contributions. The black vertical line is the free-Δ mass (1232 GeV/c^2).

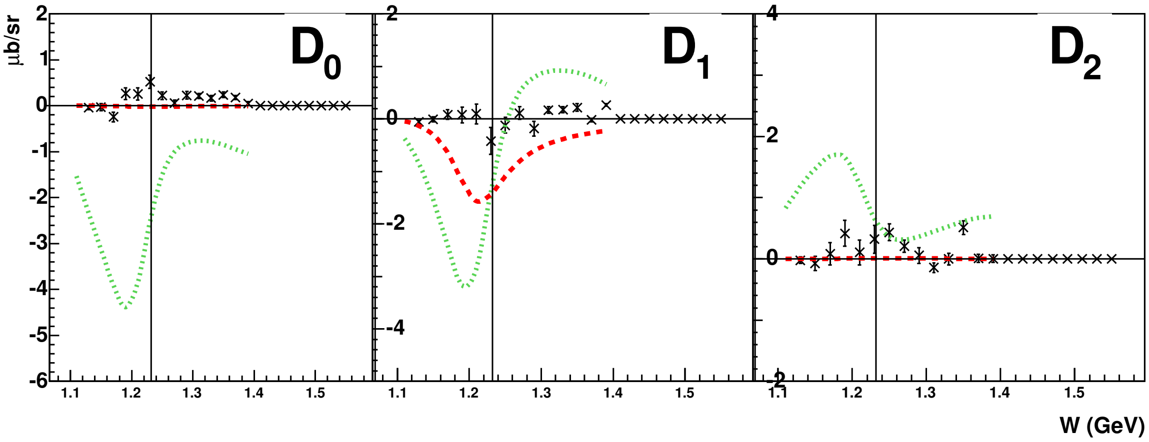

Figure 7.28: The set of partial-wave coefficients $D_0..D_2$ plotted against W for Q^2=$0.15(GeV/c)^2$. The red dashed line is a fit to theoretical calculations of the P33 resonance using MAID2003 and the green dotted line is the fit to theoretical calculations of the P33 + Born contributions. The black vertical line is the free-Δ mass (1232 GeV/c^2).

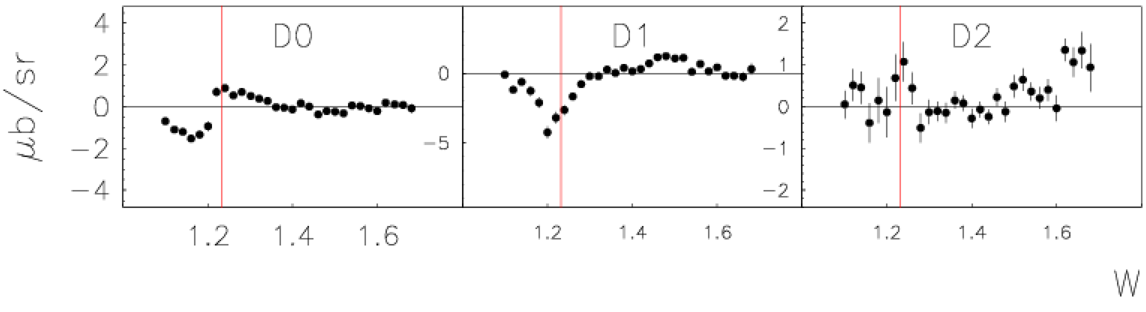

Figure 7.29: The set of partial-wave coefficients $D_0..D_2$ plotted against W from [37].

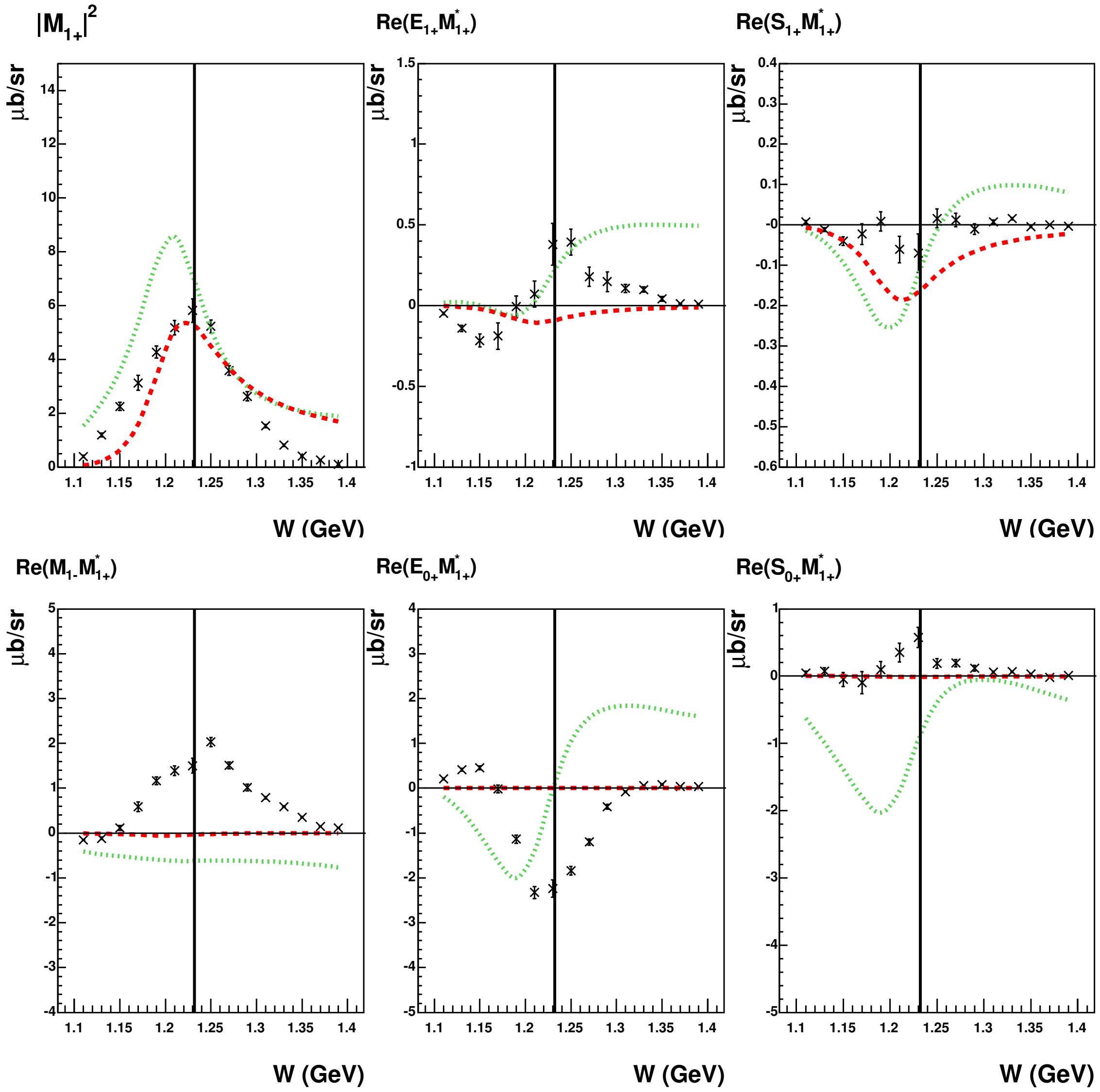

Figure 7.30: The dominant magnetic multipole and the interference terms for the $p\pi^-$ reaction at Q^2=0.35 $(GeV/c)^2$. The red dashed line is a fit to theoretical calculations of the P33 resonance using MAID2003 and the green dotted line is the fit to theoretical calculations of the P33 + Born contributions. The black vertical line is the free-Δ mass (1232 GeV/c^2).

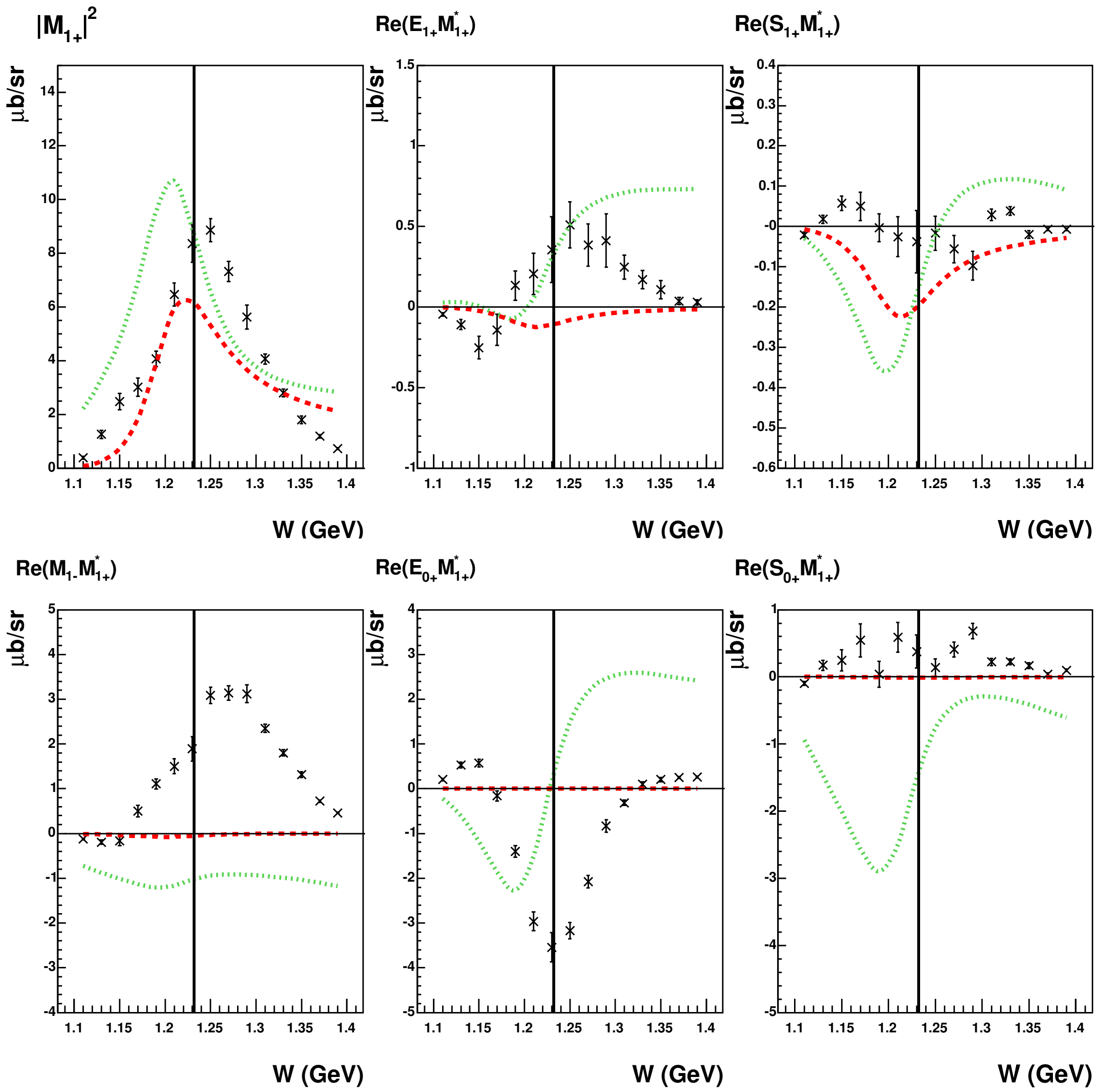

Figure 7.31: The dominant magnetic multipole and the interference terms for the $p\pi^-$ reaction at Q^2=0.25 $(GeV/c)^2$. The red dashed line is a fit to theoretical calculations of the P33 resonance using MAID2003 and the green dotted line is the fit to theoretical calculations of the P33 + Born contributions. The black vertical line is the free-Δ mass (1232 GeV/c^2).

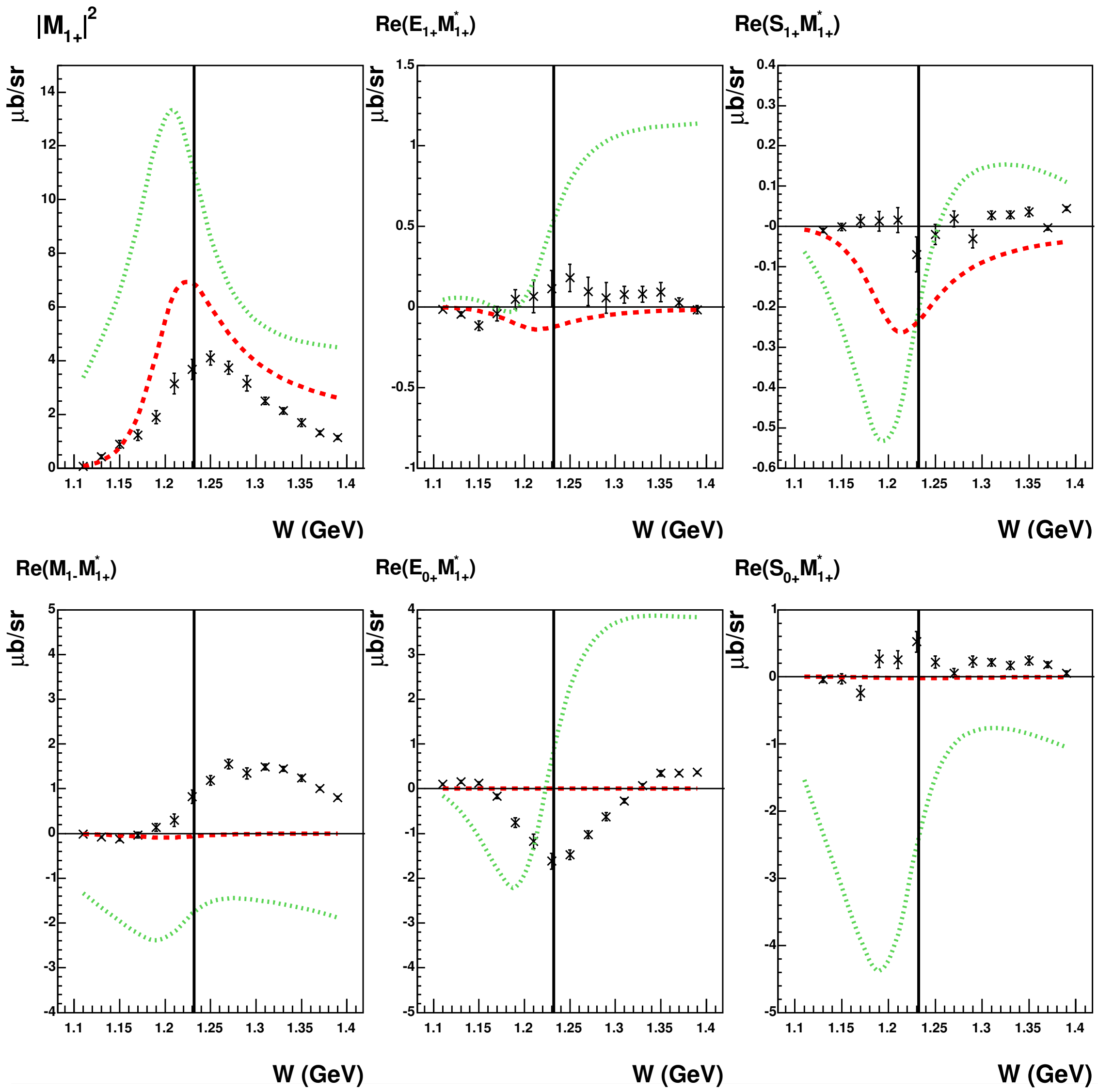

Figure 7.32: The dominant magnetic multipole and the interference terms for the $p\pi^-$ reaction at Q^2=0.15 $(GeV/c)^2$. The red dashed line is a fit to theoretical calculations of the P33 resonance using MAID2003 and the green dotted line is the fit to theoretical calculations of the P33 + Born contributions. The black vertical line is the free-Δ mass (1232 GeV/c^2).

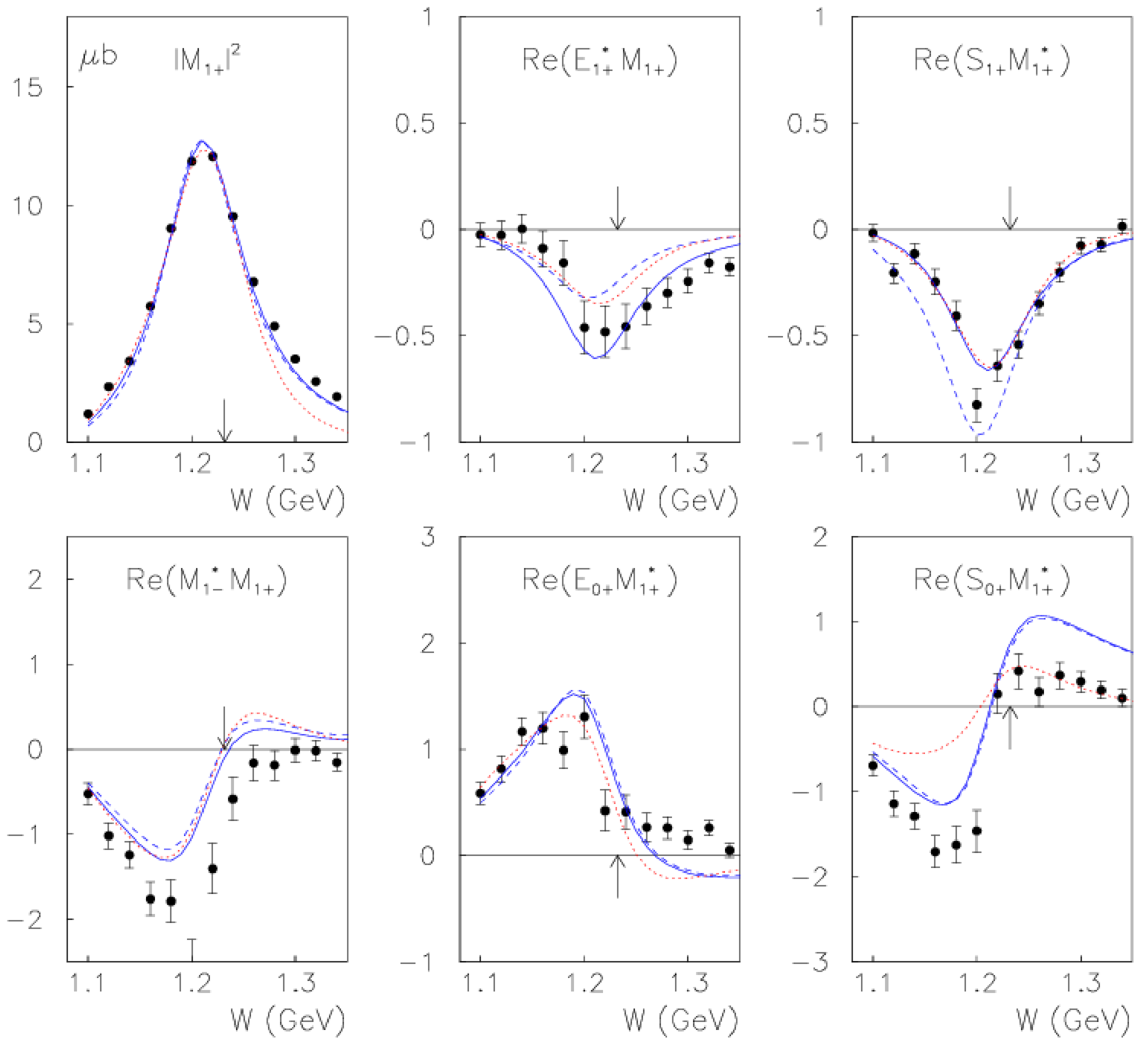

Figure 7.33: Taken from [37]. The dominant magnetic multipole and the interference terms for the $p\pi^0$ reaction at Q^2 0.4 $(GeV/c)^2$. The solid line shows the model predictions from MAID98, the dashed line MAID2000 and the dotted line dynamical pion scattering model of Sato and Lee.

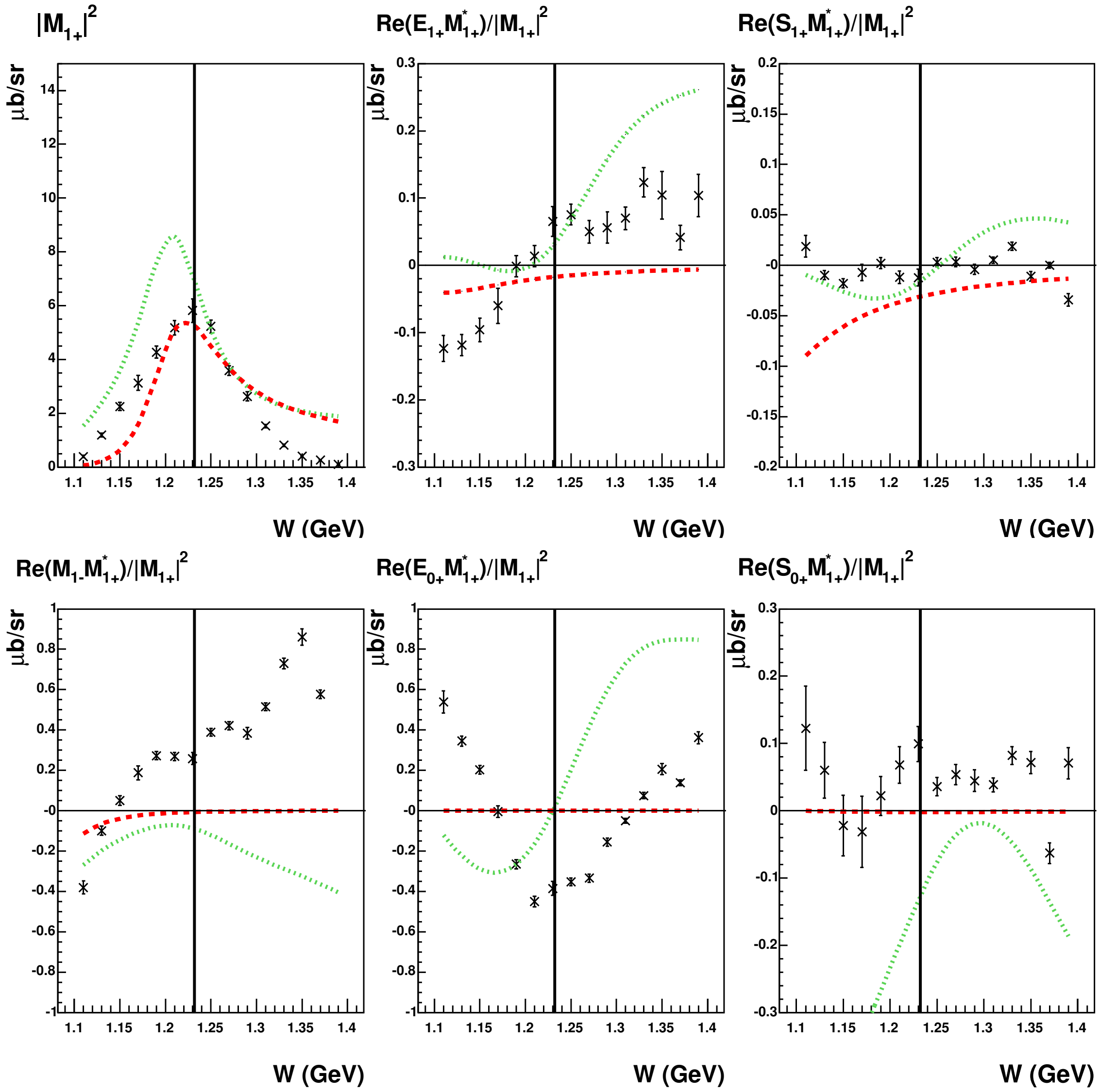

Figure 7.34: The dominant magnetic multipole and the interference terms taken as a ratio to the magnetic multipole transition. The red dashed line is a fit to theoretical calculations of the P33 resonance using MAID2003 and the green dotted line is the fit to theoretical calculations of the P33 + Born contributions. The black vertical line is the free-Δ mass (1232 GeV/c^2). The top centre plot and top right hand side plot correspond to the desired R_{EM} and R_{SM} values. These are for the $p\pi^-$ reaction at Q^2=0.35 $(GeV/c)^2$.

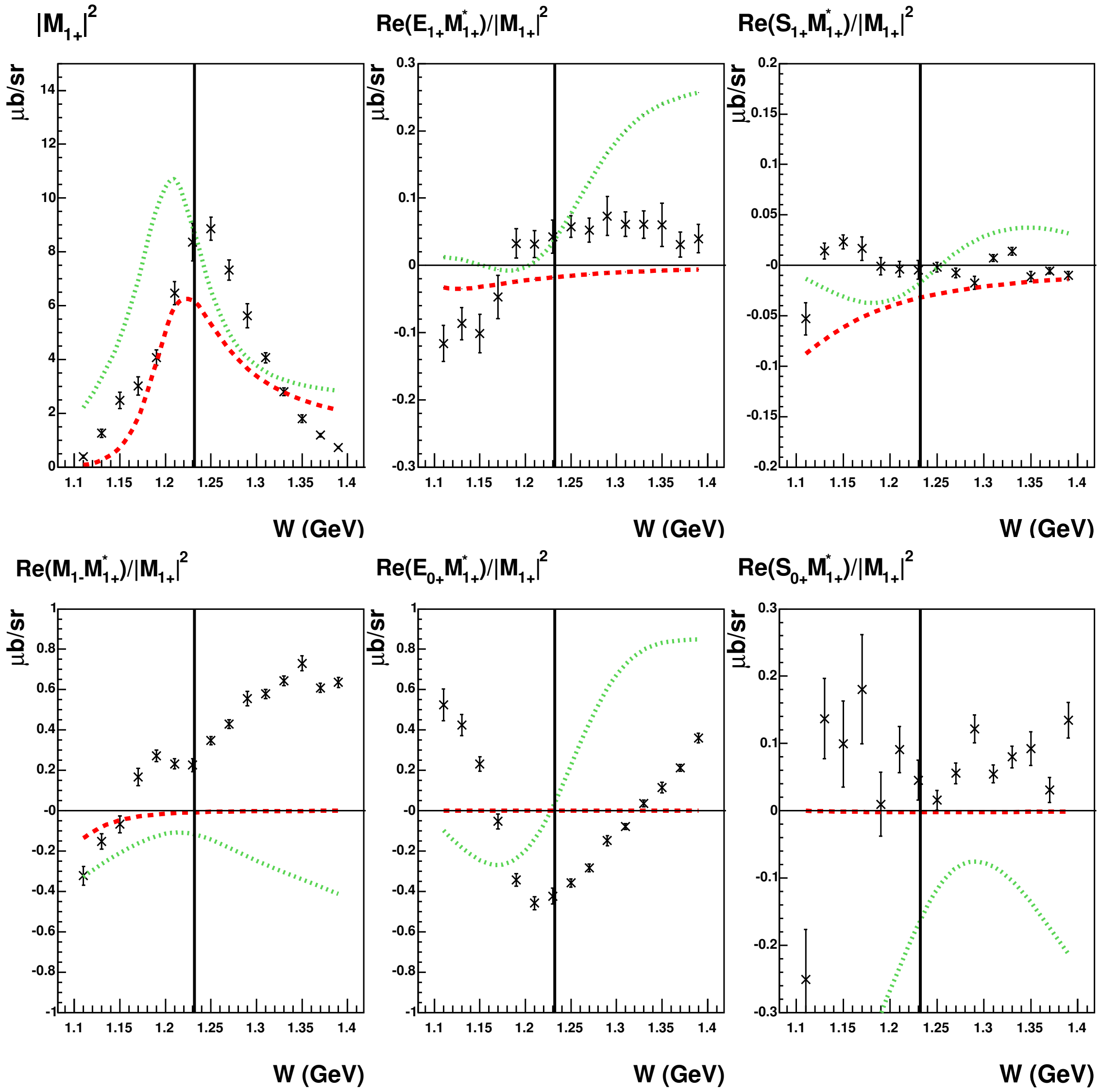

Figure 7.35: The dominant magnetic multipole and the interference terms taken as a ratio to the magnetic multipole transition. The red dashed line is a fit to theoretical calculations of the P33 resonance using MAID2003 and the green dotted line is the fit to theoretical calculations of the P33 + Born contributions. The black vertical line is the free-Δ mass (1232 GeV/c^2). The top centre plot and top right hand side plot correspond to the desired R_{EM} and R_{SM} values. These are for the $p\pi^-$ reaction at Q^2=0.25 $(GeV/c)^2$.

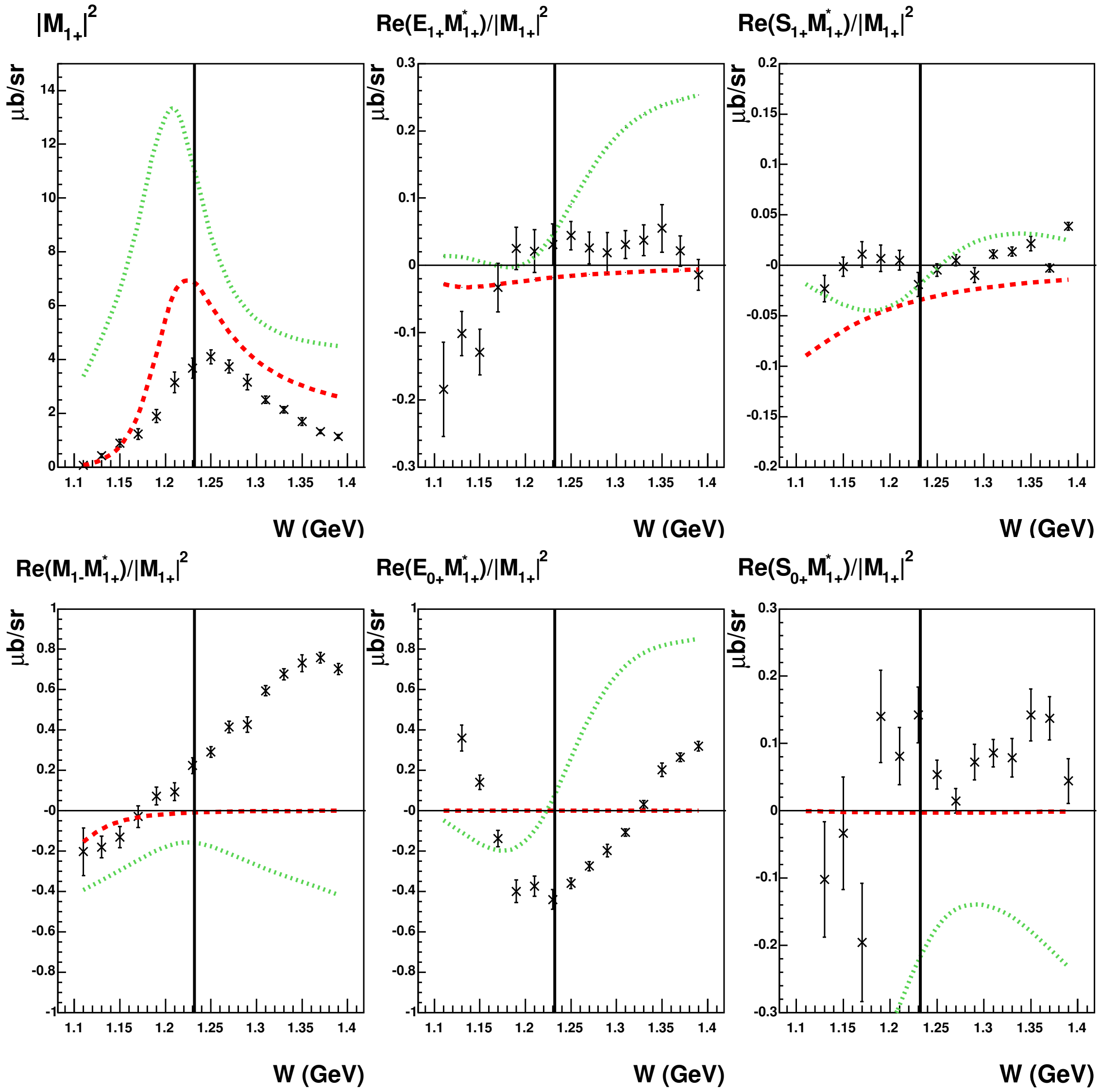

Figure 7.36: The dominant magnetic multipole and the interference terms taken as a ratio to the magnetic multipole transition. The red dashed line is a fit to theoretical calculations of the P33 resonance using MAID2003 and the green dotted line is the fit to theoretical calculations of the P33 + Born contributions. The black vertical line is the free-Δ mass (1232 GeV/c^2). The top centre plot and top right hand side plot correspond to the desired R_{EM} and R_{SM} values. These are for the $p\pi^-$ reaction at Q^2=0.15 $(GeV/c)^2$.

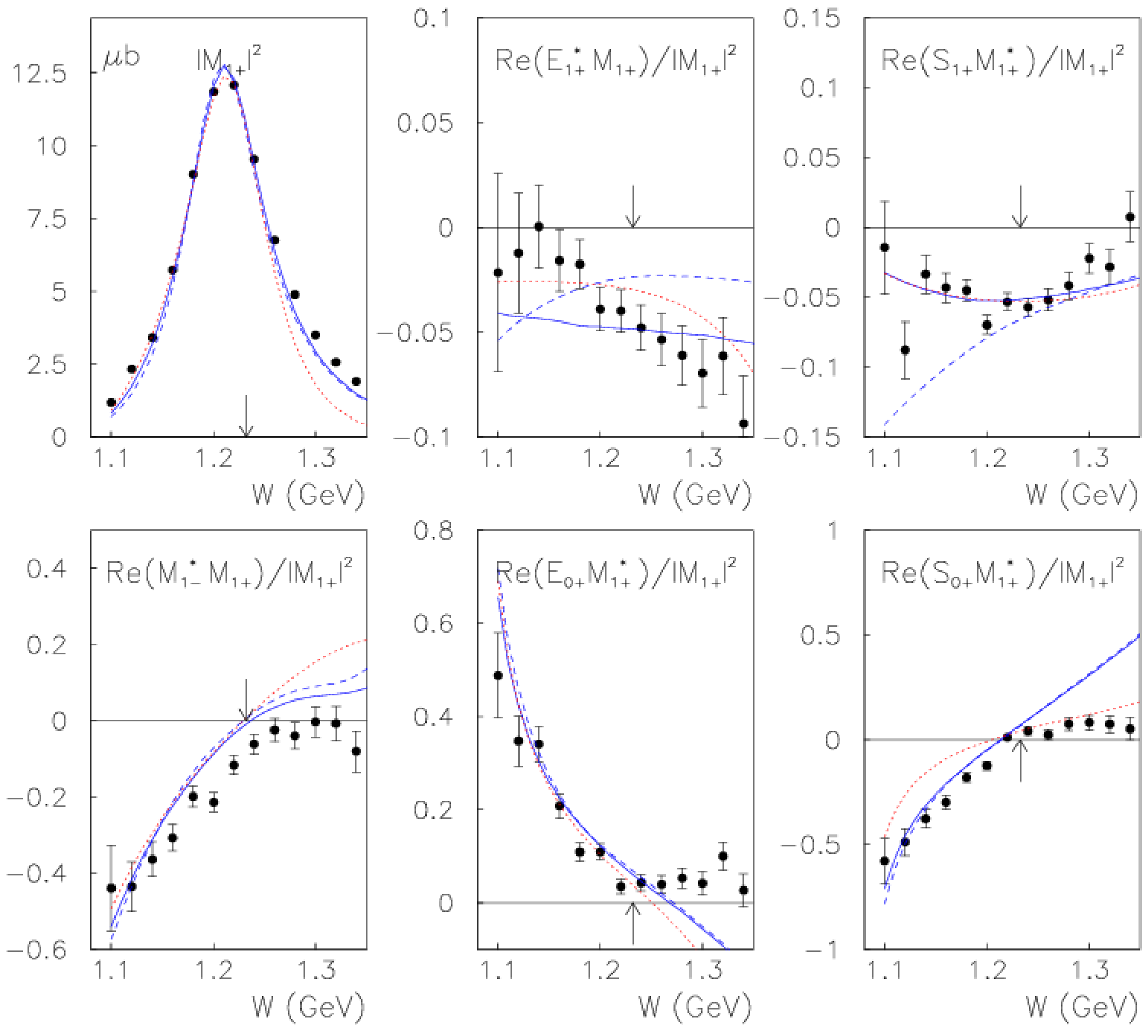

Figure 7.37: Taken from [37]. The dominant magnetic multipole and the interference terms taken as a ratio to the magnetic multipole transition. The solid line shows the model predictions from MAID98, the dashed line MAID2000 and the dotted line dynamical pion scattering model of Sato and Lee. The top centre plot and top right hand side plot correspond to the desired R_{EM} and R_{SM} values. These are for the $p\pi^0$ reaction at Q^2 0.4 $(GeV/c)^2$.

CHAPTER VIII
CONCLUSIONS

The object of our study was to look at the properties of the Δ^0 through electron scattering from a quasi-free neutron target in ^{3}He. Large amounts of previous data exists for the Δ^+, where it can be studied using a free proton target through the $p\pi^0$ or $n\pi^+$ reaction channels. We used the $p\pi^-$ channel to study the Δ^0 since detecting two charged particles in the final state is much easier and provides far greater statistics than the $n\pi^0$ channel.

We studied the reaction using an exclusive measurement selecting on the $p\pi^-$ channel. In order to study the exclusive reaction $^3\text{He}(e, e'p\pi^-)\,X$ it was necessary to have the near 4π acceptance that CLAS possesses. This allowed us to perform a study of the complete angular distribution of these final-state particles. By selecting on the reaction using the measured kinematics of the out-going particles, we were able to identify the specific channel and be confident that all particles came from the desired reaction vertex. A series of detector cuts and corrections relating to different aspects of CLAS were applied to ensure accurate measurements of the momenta, accurate particle identification and removal of any event with particles outside the flat acceptance region of the detector system.

By using simulations of CLAS to determine the acceptance in our kinematic bins, we were able to calculate the differential cross-sections and extract the relevant information from their distributions, including the various structure functions, the dominant magnetic dipole and its interference terms. More specifically we wished to measure the multipole ratios R_{EM} and R_{SM} for the interference terms of the E_{1+} and S_{1+} transitions, as these provide information on the shape of the Δ^0. We found values of $+3.5\% < R_{EM} < +6.5\%$ for the electric quadrupole transition. This is quite different from the more recent Δ^+ measurements (section 1.1) whose ratios were all measured to be negative values (figure 1.1). This could imply the Δ^0 has a different shape from the Δ^+ though further work has to be performed to account for the Born contributions and see how much effect they have on the multipole ratio measurements. We measured the Coulomb quadrupole ratio to be $-0.5\% < R_{SM} < -1.9\%$, smaller than any Δ^+ values from previous measurements at similar Q^2 values. We plot our results in figure 8.1 along with the results from Joo et al. [37] to illustrate the differences.

By studying the distributions of the purely transverse and longitudinal structure functions (σ_T and σ_L) we observed no Q^2 dependence on the Δ resonance peak position as previously reported. We did however find large differences between our determined structure functions and multipole measurements from those predicted by the MAID theoretical models. We had expected this given that little data existed for measurements of the Δ^0, and none published to date for a ^{3}He target. The results we have obtained here will be very useful in helping in refining the models and theoretical calculations.

Even though we see no indication of the Q^2 dependence due to medium modification, our study of the shape of the Δ^0 may provide information that will show medium effects. The prior results plotted in figure 1.1 showed that even in the case of the free-Δ, a distortion from the spherical was observed through the non-zero values of the ratios R_{EM} and R_{SM}. By comparing the shape of the bound-Δ and free-Δ, any modifications due to the nuclear environments could be studied. A study of the $p\pi^0$ channel would allow comparison of the bound and free cases of the Δ^+. Also a comparison between production of the Δ^0 from the quasi-free neutron and Δ^+ from the quasi-free proton would allow study of any differences the proton and neutron experience in the nuclear environment. This will allow a complete picture where data for the free-Δ^+, bound Δ^+ and bound Δ^0 can be used to look for medium effects.

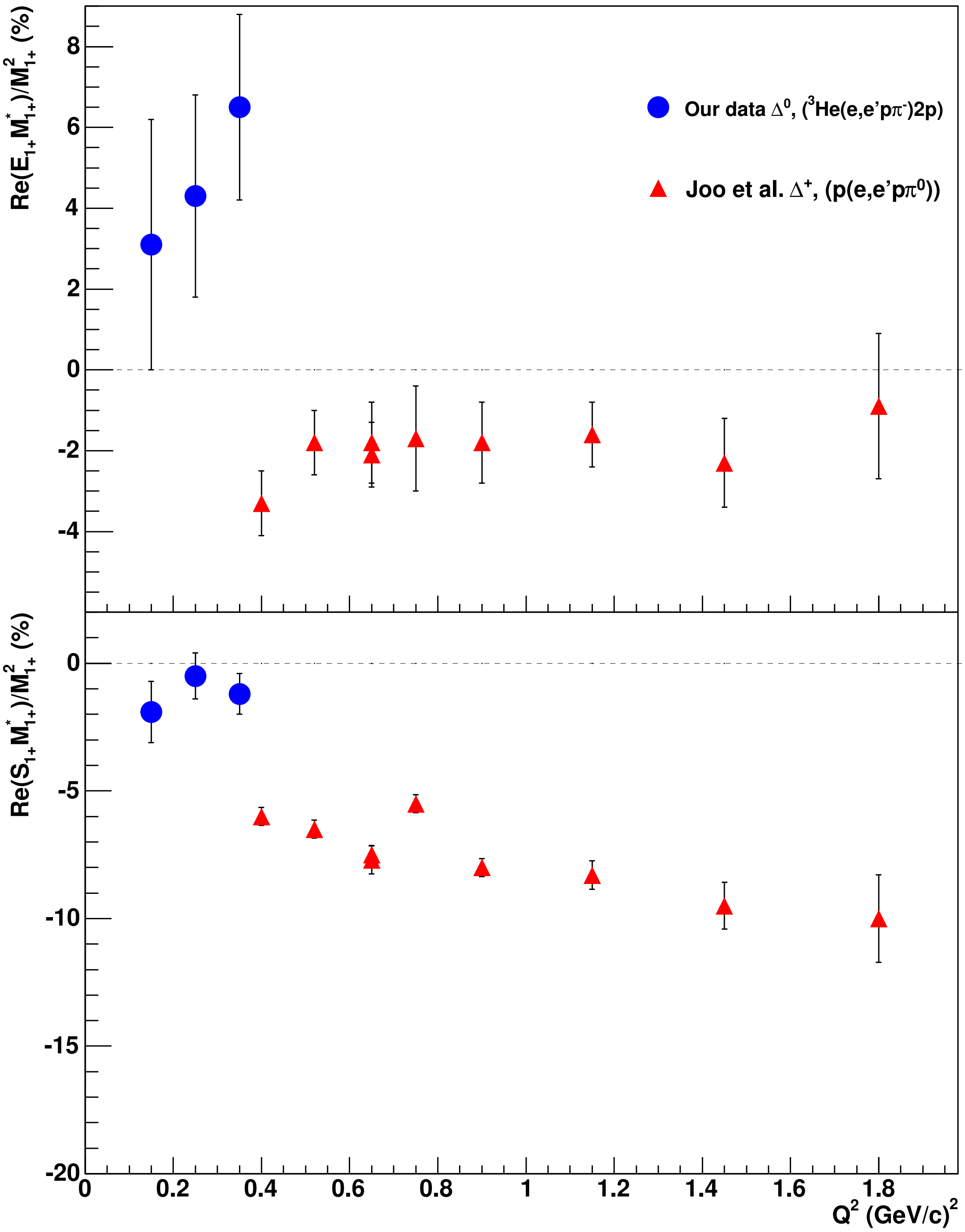

Figure 8.1: Our measurement of multipole ratios R_{EM} and R_{SM} plotted with those from [37].

APPENDIX I

APPENDIX A

Jacobian Calculation

In order to apply the study of the cross-section described in section 2.3.2 we must relate the measured experimental quantities to the calculated quantities. This is achieved by applying a Jacobian factor to the experimental cross-section (section 6.4.3) relating the experimental variables e' and $\cos(\theta_e)$ to the calculated quantities W and Q^2. To determine the Jacobian we have to derive W and Q^2 in terms of the experimental quantities.

Calculating Q^2

From figure A.1 it can be seen that,

$$q^2 = e^2 + e'^2 - 2ee' cos\Theta_e \tag{A.1}$$

and using,

$$\omega = e - e' \tag{A.2}$$

we have,

$$\omega^2 = e^2 + e'^2 - 2ee' \tag{A.3}$$

It then follows with,

$$\begin{aligned} Q^2 &= q^2 - \omega^2 \\ &= 2ee' - 2ee' cos\Theta_e \\ &= 2ee' (1 - cos\Theta_e) \end{aligned} \tag{A.4}$$

Calculating W

The reaction of the beam electron incident on the nucleon target can be written in terms of the four vectors as follows,

$$e^\mu + N^\mu = e'^\mu + \pi^\mu + p^\mu \tag{A.5}$$

Where e, N, e', π and p are the beam electron, struck nucleon, scattered electron, decay pion and decay proton respectively. Given the virtual photon 4-vector $q^\mu = e^\mu$ - e'^μ, the invariant mass (W) of the resonant system can be written as,

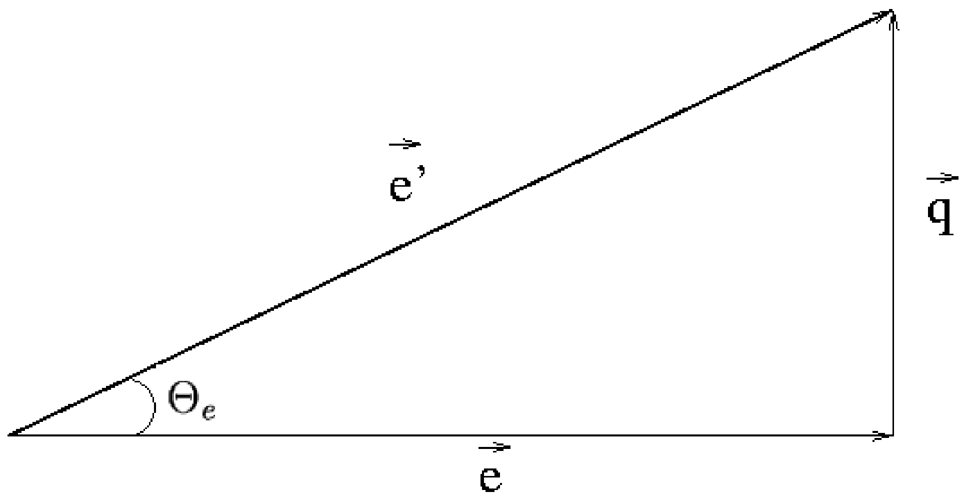

Figure A.1: Simple vector diagram for electron scattering.

$$W^2 \;=\; (\pi^\mu \;+\; p^\mu)^2 \;=\; (q^\mu \;+\; N^\mu)^2 \tag{A.6}$$

with,

$$\begin{aligned} q^\mu &= (\omega, \mathbf{q}) \\ N^\mu &= (m_N, 0, 0, 0) \end{aligned} \tag{A.7}$$

thus,

$$\begin{aligned} W^2 &= (\omega \;+\; m_N)^2 \;-\; q^2 \\ &= \omega^2 \;+\; 2m_N\omega \;+\; m_N^2 \;-\; q^2 \\ &= 2m_N\omega \;+\; m_N^2 \;-\; Q^2 \end{aligned} \tag{A.8}$$

Calculating J

$$|J| \;=\; \frac{\partial\left(Q^2, W\right)}{\partial\left(e', cos\left(\Theta_e\right)\right)} \;=\; \begin{vmatrix} \frac{\partial Q^2}{\partial e'} & \frac{\partial Q^2}{\partial cos(\Theta_e)} \\ \frac{\partial W}{\partial e'} & \frac{\partial W}{\partial cos(\Theta_e)} \end{vmatrix} \tag{A.9}$$

$$\frac{\partial W^2}{\partial x}\frac{\partial W}{\partial W^2} \;=\; \frac{1}{2W}\frac{\partial W^2}{\partial x} \tag{A.10}$$

$$\frac{\partial Q^2}{\partial e'} \;=\; 2e\left(1 \;-\; cos\Theta_e\right) \tag{A.11}$$

$$\frac{\partial Q^2}{\partial cos\Theta_e} \;=\; -2ee' \tag{A.12}$$

$$\frac{\partial W}{\partial e'} = \frac{1}{2W}\frac{\partial W^2}{\partial e'} = \frac{1}{2W}\left(-2m_N - 2e\left(1 - cos\Theta_e\right)\right)$$

$$\frac{\partial W}{\partial cos\Theta_e} = \frac{1}{2W}\frac{\partial W^2}{\partial cos\Theta_e} = \frac{1}{2W}.2ee' \tag{A.13}$$

$$\begin{aligned} |J| &= \left|\frac{\partial Q^2}{\partial e'}\frac{\partial W}{\partial cos\Theta_e} - \frac{\partial Q^2}{\partial cos\Theta_e}\frac{\partial W}{\partial e'}\right| \\ &= 2e\left(1 - cos\Theta_e\right)\frac{ee'}{W} + \frac{ee'}{W}\left(-2m_N - 2e\left(1 - cos\Theta_e\right)\right) \\ &= \left| -\frac{2m_N ee'}{W}\right| \end{aligned} \tag{A.14}$$

Now finally we have to factor in the azimuthal angle we are dealing with which introduces a factor of 2π to the equation. So we have,

$$|J| = \frac{m_N ee'}{\pi W} \tag{A.15}$$

Cross-section Calculation

Elastic Scattering

A full treatment of the derivation of the scattering cross-sections can be found in [100] and additional background information in [101,102]. We can start by expressing the differential cross-section with the relevant kinematic factors for this process as,

$$d\sigma = \frac{\overline{|T_{fi}|^2}}{J}\frac{d^3P_{e'}}{2E_{e'}\left(2\pi\right)^3}\frac{d^3P_{p'}}{2E_{p'}\left(2\pi\right)^3}\left(2\pi\right)^4\delta^4\left(P_e - P_{e'} + P_p - P_{p'}\right) \tag{A.16}$$

Where the flux factor J=4$\mathbf{P_p}.\mathbf{P_e}$ reduces to 4ME_e in the lab-frame. The factors $\left(2E_{e'}\right)^{-1}$ and $\left(2E_{p'}\right)^{-1}$ are related to the normalisation of the lepton and nucleon wave functions in the final state.

For unpolarised scattering, the spin average over the squared T-matrix gives

$$\overline{|T_{fi}|^2} = \frac{e^4}{q^4}L_{\mu\nu}N^{\mu\nu} \tag{A.17}$$

Since QED is well understood the leptonic tensor is known. This is not the case with the nucleon where the hadronic currents aren't well understood. However, in the case of scattering from a point-like particle we use a tensor similar to that of the lepton. So we have,

$$L_{\mu\nu} = 2\left[P_{\mu_e}P_{\nu_{e'}} + P_{\mu_{e'}}P_{\nu_e} - g_{\mu\nu}\mathbf{P_e}.\mathbf{P_{e'}}\right] \tag{A.18}$$

and

$$N_{\mu\nu} = 2\left[P_{\mu_p}P_{\nu_{p'}} + P_{\mu_{p'}}P_{\nu_p} - g_{\mu\nu}\left(\mathbf{P_p}.\mathbf{P_{p'}} - M^2\right)\right] \tag{A.19}$$

where the lepton mass has been neglected. Using the relationship $P_{p'} = P_p + P_e - P_{e'}$ we find in the lab frame,

$$L_{\mu\nu}N^{\mu\nu} = 16M^2E_eE_{e'}\left(cos^2\frac{\theta}{2} - \frac{q^2}{2M^2}sin^2\frac{\theta}{2}\right) \tag{A.20}$$

Integrating over $d^3P_{p'}$ and using $d^3P_{e'} = P_{e'}^2dP_{e'}d\Omega \approx E_{e'}^2dE_{e'}d\Omega$. The differential cross-section becomes

$$\frac{d^2\sigma}{d\Omega dE_{e'}} = \frac{\alpha}{4E_e^2sin^4\frac{\theta}{2}}\left(cos\frac{\theta}{2} - \frac{q^2}{2M^2}sin^2\frac{\theta}{2}\right)\delta\left(\omega + \frac{q^2}{2M}\right) \tag{A.21}$$

with $\alpha = e^2/4\pi$ and using the fact that in this elastic scattering process, energy and momentum conservation require $\omega = E_e - E_{e'} = E_{p'} - E_p = Q^2/2M$.

Inelastic Scattering

Now that we have established the form of the cross-section for the simplest case, we would like to extend it to a more realistic case. Firstly we must address the fact that our reaction isn't going to be elastic. We modify the above procedure for a charged lepton incident on nucleons but without detection of the hadronic final state. We also include the possibility of initial polarised states for the leptons and nucleons. To do this, we replace the lepton tensor in equation A.18 with

$$L_{\mu\nu} = 2\left[P_{\mu_e}P_{\nu_{e'}} + P_{\mu_{e'}}P_{\nu_e} - g_{\mu\nu}\mathbf{P_e}.\mathbf{P_{e'}} + i\epsilon_{\mu\nu\alpha\beta}s^\alpha q^\beta\right] \tag{A.22}$$

where $s^\alpha = \overline{u}\gamma^\alpha\gamma^5u$ is the lepton spin vector. We have neglected again the small lepton mass. The tensor $\epsilon_{\mu\nu\alpha\beta}$ is the Levi-Civita tensor and we use the convention $\epsilon_{0123} = +1$.

For the case of inelastic scattering we have to include all possible transitions of the nucleon from the ground state, $\langle N(P_p)|$, to any excited state, $\langle X(P_{p'})|$. In equation A.16 and A.19, the term $\int d^3P_{p'}\left(\pi/E_{p'}\right)\delta^4\left(P_e - P_{e'} + P_p - P_{p'}\right)N_{\mu\nu}$ is now replaced by the hadronic current tensor

$$W_{\mu\nu}(P_p, q) = \tfrac{1}{2M}\sum_X \langle N_s(P_p)|\, J_\mu(0)\, |X(P_{p'})\rangle \langle X(P_{p'})|\, J_\nu(0)\, |N_s(P_p)\rangle \\ .\,(2\pi)^3\,\delta^4(q + P_p - P_{p'}) \tag{A.23}$$

The initial nucleon spin state is denoted by s $= \pm\frac{1}{2}$. The summation over unobserved final states X is understood to include the integration $\int d^3P_{p'}/2E_{p'}\,(2\pi)^3$ over their total momenta. The hadron tensor can be split into symmetric and antisymmetric parts

$$W_{\mu\nu} = W^S_{\mu\nu} + W^A_{\mu\nu} \tag{A.24}$$

Now using Lorentz and gauge invariance along with parity conservation, the symmetric part can be written in the most general form as

$$W^S_{\mu\nu} = W_1\left(\omega, Q^2\right)\left(\frac{q_\mu q_\nu}{q^2} - g_{\mu\nu}\right) + \frac{W_2(\omega, Q^2)}{M^2}\left(P_{\mu_p} - \frac{\mathbf{P_p.q}}{q^2}q_\mu\right)\left(P_{\nu_p} - \frac{\mathbf{P_p.q}}{q^2}q_\nu\right) \tag{A.25}$$

Since we are not using a polarised beam or target, the antisymmetric component isn't required. We only need the response functions $W_{1,2}(\omega, Q^2)$. In the lab frame the cross-section is now given by

$$\frac{d^2\sigma}{d\Omega dE_{e'}} = \frac{\alpha^2}{q^4}\frac{E_{e'}}{E_e}L_{\mu\nu}W^{\mu\nu} \tag{A.26}$$

If we average over all the spins if the incident lepton and target nucleon, the unpolarised differential cross-section in the laboratory frame is as follows (compare to equation A.21).

$$\frac{d^2\sigma}{d\Omega dE_{e'}} = \frac{\alpha^2}{4E_e^2 sin^4\frac{\theta}{2}}\left(W_2\left(\omega, Q^2\right)cos^2\frac{\theta}{2} + 2W_1\left(\omega, Q^2\right)sin^2\frac{\theta}{2}\right) \tag{A.27}$$

Virtual Photon Cross-Sections

We now take the cross-section in A.27 and express it in terms of the cross-section for absorption of transverse and longitudinal virtual photons on a nucleon. These cross-sections are detoned as σ_T and σ_L respectively. So

$$\frac{d^2\sigma}{d\Omega dE_{e'}} = \Gamma\left[\sigma_T\left(\omega, Q^2\right) + \epsilon\sigma_L\left(\omega, Q^2\right)\right] \tag{A.28}$$

where ϵ is the transverse polarization of the virtual photon,

$$\epsilon = \left[1 + 2\left(1 + \frac{\omega}{Q^2}\right) tan^2\frac{\theta}{2}\right]^{-1} \tag{A.29}$$

and Γ is a kinematic factor associated with the choice for the flux of virtual photons,

$$\Gamma = \frac{\alpha}{2\pi^2 Q^2}\frac{E_{e'}}{E_e}\frac{k_\gamma}{1-\epsilon} \tag{A.30}$$

with k_γ being the equivalent real-photon energy exciting the nucleon of mass M to a hadronic system of invariant mass W.

$$k_\gamma = \frac{W^2 - M^2}{2M} \tag{A.31}$$

As well as the tranverse polarization of the virtual photon, the longitudinal polarisation contributes to the differential cross-section.

$$\epsilon_L \;=\; \frac{Q^2}{|k^*|^2}\epsilon \tag{A.32}$$

Where k^* is the equivalent real-photon energy in the c.m. frame. The equation A.28 only considered the transverse and longitudinal structure functions σ_T and σ_L. We must also consider any contributions from the transverse-longitudinal interference terms. In the case of our reaction where we have pion electroproduction, equation A.28 can be cast into the form [73, 103].

$$\frac{d\sigma}{d\Omega dE_{e'} d\Omega_\pi} \;=\; \Gamma\frac{d\sigma_\nu}{d\Omega_\pi} \tag{A.33}$$

$$\frac{d\sigma_\nu}{d\Omega_\pi} \;=\; \frac{d\sigma_T}{d\Omega_\pi} \;+\; \epsilon_L\frac{d\sigma_L}{d\Omega_\pi} \;+\; \epsilon\frac{d\sigma_{TT}}{d\Omega_\pi}cos\left(2\phi_\pi\right) \;+\; \left[2\epsilon_L\left(1+\epsilon\right)\right]^{\frac{1}{2}}\frac{d\sigma_{LT}}{d\Omega_\pi}cos\left(\phi_\pi\right) \tag{A.34}$$

Any helicity terms are not included as they do not contribute in our experiment. The first two terms of equation A.34 are the transverse and longitudinal structure functions and do not depend on the azimuthal angle. They can be decomposed into a partial-wave series in $\cos\theta_\pi$. The last two terms are as mentioned the transverse-longitudinal interferences. Since these have a dependence on $\cos\phi_\pi$ they have to contain an explicit factor in $\sin\theta_\pi$ (for σ_{LT}) and $\sin^2\theta_\pi$ (for σ_{TT}) i.e. they vanish along the axis of momentum transfer.

Additionally, for a multipole decomposition, it is useful to express the angular distribution of the emitted particles in the hadronic centre-of-mass frame. Therefore equation A.34 must be multiplied by a factor P^*_π/k^*_γ where P is the c.m. momentum and k the photon equivalent energy in the c.m. frame.

APPENDIX II

APPENDIX B

Table of Multipole Values

W(GeV/c^2)	$\|M_{1+}\|^2$	$Re(E_{1+}M^*_{1+})$	$Re(S_{1+}M^*_{1+})$
Q^2 = 0.15 (figure 7.32)	($\mu b/sr$)	($\mu b/sr$)	($\mu b/sr$)
1.11	0.07± 0.03	-0.01± 0.01	-1.39± 0.23
1.13	0.43± 0.07	-0.04± 0.01	-0.01± 0.01
1.15	0.90± 0.14	-0.12± 0.03	-0.00± 0.01
1.17	1.24± 0.20	-0.04± 0.04	0.01± 0.02
1.19	1.90± 0.24	0.05± 0.06	0.01± 0.02
1.21	3.15± 0.38	0.07± 0.10	0.02± 0.03
1.23	3.68± 0.38	0.11± 0.11	-0.07± 0.04
1.25	4.10± 0.26	0.18± 0.09	-0.02± 0.03
1.27	3.74± 0.24	0.10± 0.09	0.02± 0.02
1.29	3.15± 0.29	0.06± 0.10	-0.03± 0.02
1.31	2.51± 0.14	0.08± 0.05	0.03± 0.01
1.33	2.13± 0.12	0.08± 0.05	0.03± 0.01
1.35	1.69± 0.15	0.09± 0.06	0.04± 0.01
1.37	1.32± 0.07	0.03± 0.03	-0.00± 0.01
1.39	1.14± 0.06	-0.02± 0.03	0.04± 0.00

Table B.1: Table of values for the the multipole intereference terms $Re(E_{1+}M^*_{1+})$ and $Re(S_{1+}M^*_{1+})$ and the dominant magnetic dipole $|M_{1+}|^2$ where Q^2=0.15 $(GeV/c)^2$.

W(GeV/c^2)	$Re(M_{1-}M^*_{1+})$	$Re(E_{0+}M^*_{1+})$	$Re(S_{0+}M^*_{1+})$
Q^2 = 0.15 (figure 7.32)	($\mu b/sr$)	($\mu b/sr$)	($\mu b/sr$)
1.11	-0.01± 0.01	0.10± 0.02	13.40± 2.26
1.13	-0.08± 0.02	0.15± 0.03	-0.04± 0.04
1.15	-0.12± 0.05	0.13± 0.03	-0.03± 0.07
1.17	-0.04± 0.07	-0.17± 0.05	-0.24± 0.11
1.19	0.14± 0.08	-0.76± 0.11	0.27± 0.13
1.21	0.30± 0.14	-1.18± 0.16	0.25± 0.13
1.23	0.82± 0.15	-1.62± 0.18	0.52± 0.15
1.25	1.19± 0.11	-1.47± 0.11	0.22± 0.09
1.27	1.56± 0.11	-1.03± 0.08	0.05± 0.07
1.29	1.34± 0.12	-0.62± 0.10	0.23± 0.08
1.31	1.49± 0.06	-0.27± 0.04	0.21± 0.05
1.33	1.44± 0.06	0.07± 0.04	0.17± 0.06
1.35	1.24± 0.07	0.34± 0.06	0.24± 0.07
1.37	1.00± 0.03	0.35± 0.03	0.18± 0.04
1.39	0.80± 0.03	0.36± 0.03	0.05± 0.04

Table B.2: Table of values for the the multipole intereference terms $Re(M_{1-}M^*_{1+})$, $Re(E_{0+}M^*_{1+})$ and $Re(S_{0+}M^*_{1+})$ where Q^2=0.15 $(GeV/c)^2$.

W(GeV/c^2)	$\|M_{1+}\|^2$	$Re(E_{1+}M^*_{1+})$	$Re(S_{1+}M^*_{1+})$
Q^2 = 0.25 (figure 7.31)	($\mu b/sr$)	($\mu b/sr$)	($\mu b/sr$)
1.11	0.39± 0.06	-0.05± 0.01	-0.02± 0.01
1.13	1.26± 0.15	-0.11± 0.03	0.02± 0.01
1.15	2.48± 0.31	-0.25± 0.07	0.06± 0.02
1.17	3.01± 0.34	-0.14± 0.10	0.05± 0.04
1.19	4.07± 0.28	0.13± 0.09	-0.00± 0.03
1.21	6.46± 0.43	0.21± 0.13	-0.03± 0.05
1.23	8.36± 0.70	0.36± 0.20	-0.04± 0.08
1.25	8.86± 0.43	0.51± 0.14	-0.02± 0.04
1.27	7.33± 0.37	0.38± 0.13	-0.06± 0.03
1.29	5.63± 0.44	0.41± 0.16	-0.10± 0.04
1.31	4.06± 0.19	0.25± 0.07	0.03± 0.01
1.33	2.80± 0.15	0.17± 0.06	0.04± 0.01
1.35	1.80± 0.14	0.11± 0.06	-0.02± 0.01
1.37	1.19± 0.06	0.04± 0.02	-0.01± 0.00
1.39	0.73± 0.04	0.03± 0.02	-0.01± 0.00

Table B.3: Table of values for the the multipole intereference terms $Re(E_{1+}M^*_{1+})$ and $Re(S_{1+}M^*_{1+})$ and the dominant magnetic dipole $|M_{1+}|^2$ where Q^2=0.25 $(GeV/c)^2$.

W(GeV/c^2)	$Re(M_{1-}M_{1+}^*)$	$Re(E_{0+}M_{1+}^*)$	$Re(S_{0+}M_{1+}^*)$
Q^2 = 0.25 (figure 7.31)	($\mu b/sr$)	($\mu b/sr$)	($\mu b/sr$)
1.11	-0.13± 0.02	0.20± 0.03	-0.10± 0.03
1.13	-0.19± 0.05	0.53± 0.07	0.17± 0.08
1.15	-0.17± 0.10	0.57± 0.09	0.25± 0.16
1.17	0.50± 0.13	-0.16± 0.11	0.54± 0.25
1.19	1.11± 0.11	-1.40± 0.13	0.04± 0.19
1.21	1.50± 0.17	-2.96± 0.21	0.59± 0.22
1.23	1.89± 0.27	-3.54± 0.33	0.38± 0.25
1.25	3.09± 0.18	-3.17± 0.18	0.14± 0.13
1.27	3.14± 0.16	-2.08± 0.14	0.41± 0.11
1.29	3.12± 0.20	-0.83± 0.14	0.68± 0.12
1.31	2.35± 0.09	-0.32± 0.06	0.22± 0.05
1.33	1.80± 0.07	0.10± 0.05	0.22± 0.05
1.35	1.31± 0.07	0.21± 0.05	0.17± 0.05
1.37	0.72± 0.03	0.25± 0.02	0.04± 0.02
1.39	0.46± 0.02	0.26± 0.02	0.10± 0.02

Table B.4: Table of values for the the multipole intereference terms $Re(M_{1-}M_{1+}^*)$, $Re(E_{0+}M_{1+}^*)$ and $Re(S_{0+}M_{1+}^*)$ where Q^2=0.25 $(GeV/c)^2$.

W(GeV/c^2)	$\|M_{1+}\|^2$	$Re(E_{1+}M_{1+}^*)$	$Re(S_{1+}M_{1+}^*)$
Q^2 = 0.35 (figure 7.30)	($\mu b/sr$)	($\mu b/sr$)	($\mu b/sr$)
1.11	0.39± 0.04	-0.05± 0.01	0.01± 0.00
1.13	1.19± 0.08	-0.14± 0.02	-0.01± 0.01
1.15	2.25± 0.15	-0.22± 0.04	-0.04± 0.01
1.17	3.13± 0.28	-0.19± 0.08	-0.02± 0.03
1.19	4.28± 0.22	-0.01± 0.07	0.01± 0.02
1.21	5.17± 0.27	0.07± 0.08	-0.06± 0.03
1.23	5.82± 0.44	0.38± 0.13	-0.07± 0.05
1.25	5.23± 0.23	0.39± 0.08	0.02± 0.02
1.27	3.59± 0.18	0.18± 0.06	0.01± 0.02
1.29	2.63± 0.18	0.15± 0.06	-0.01± 0.01
1.31	1.52± 0.07	0.11± 0.03	0.01± 0.00
1.33	0.81± 0.04	0.10± 0.02	0.02± 0.00
1.35	0.41± 0.03	0.04± 0.01	-0.00± 0.00
1.37	0.26± 0.01	0.01± 0.00	0.00± 0.00
1.39	0.10± 0.01	0.01± 0.00	-0.00± 0.00

Table B.5: Table of values for the the multipole intereference terms $Re(E_{1+}M_{1+}^*)$ and $Re(S_{1+}M_{1+}^*)$ and the dominant magnetic dipole $|M_{1+}|^2$ where Q^2=0.35 $(GeV/c)^2$.

W(GeV/c^2)	$Re(M_{1-}M^*_{1+})$	$Re(E_{0+}M^*_{1+})$	$Re(S_{0+}M^*_{1+})$
Q^2 = 0.35 (figure 7.30)	($\mu b/sr$)	($\mu b/sr$)	($\mu b/sr$)
1.11	-0.15± 0.01	0.21± 0.02	0.05± 0.02
1.13	-0.12± 0.03	0.41± 0.03	0.07± 0.05
1.15	0.11± 0.05	0.46± 0.05	-0.05± 0.10
1.17	0.59± 0.11	-0.02± 0.09	-0.10± 0.17
1.19	1.17± 0.09	-1.14± 0.09	0.09± 0.12
1.21	1.39± 0.11	-2.33± 0.14	0.35± 0.14
1.23	1.50± 0.17	-2.24± 0.19	0.58± 0.15
1.25	2.03± 0.10	-1.84± 0.10	0.19± 0.07
1.27	1.51± 0.08	-1.20± 0.07	0.19± 0.05
1.29	1.01± 0.08	-0.41± 0.05	0.12± 0.04
1.31	0.79± 0.03	-0.08± 0.02	0.06± 0.02
1.33	0.59± 0.02	0.06± 0.01	0.07± 0.01
1.35	0.36± 0.02	0.08± 0.01	0.03± 0.01
1.37	0.15± 0.01	0.04± 0.00	-0.02± 0.00
1.39	0.11± 0.00	0.04± 0.00	0.01± 0.00

Table B.6: Table of values for the the multipole intereference terms $Re(M_{1-}M^*_{1+})$, $Re(E_{0+}M^*_{1+})$ and $Re(S_{0+}M^*_{1+})$ where Q^2=0.35 $(GeV/c)^2$.

Table of Multipole Ratios

W(GeV/c^2)	$Re(E_{1+}M^*_{1+})$	$Re(S_{1+}M^*_{1+})$
Q^2 = 0.15 (figure 7.36)	(%)	(%)
1.11	-18.4±7.0	-1930.5±325.0
1.13	-10.1±3.3	-2.3±1.3
1.15	-12.9±3.4	-0.1±1.0
1.17	-3.3±3.6	1.1±1.3
1.19	2.5±3.1	0.7±1.3
1.21	2.1±3.2	0.5±1.0
1.23	3.1±3.1	-1.9±1.2
1.25	4.4±2.1	-0.5±0.6
1.27	2.6±2.4	0.5±0.5
1.29	1.8±3.0	-1.0±0.7
1.31	3.1±2.1	1.1±0.4
1.33	3.8±2.3	1.4±0.4
1.35	5.5±3.5	2.2±0.7
1.37	2.1±2.2	-0.3±0.4
1.39	-1.4±2.3	3.9±0.4

Table B.7: Table of R_{EM} and R_{SM} values for Q^2=0.15 $(GeV/c)^2$. All values in this table are the ratio of the multipole to the interference term $|M_{1+}|^2$.

W(GeV/c^2)	$Re(M_{1-}M_{1+}^*)$	$Re(E_{0+}M_{1+}^*)$	$Re(S_{0+}M_{1+}^*)$
$Q^2 = 0.15$ (figure 7.36)	(%)	(%)	(%)
1.11	-20.3±11.8	141.4±29.9	18606.2±3132.7
1.13	-18.1±5.4	36.0±6.4	-10.2±8.6
1.15	-13.0±5.2	14.1±3.6	-3.3±8.4
1.17	-2.9±5.4	-13.8±4.0	-19.6±8.8
1.19	7.2±4.4	-39.9±5.5	14.0±6.9
1.21	9.4±4.4	-37.4±5.0	8.1±4.3
1.23	22.3±4.0	-44.0±4.8	14.2±4.2
1.25	29.0±2.6	-36.0±2.6	5.4±2.1
1.27	41.6±2.8	-27.4±2.2	1.5±1.8
1.29	42.6±3.8	-19.8±3.0	7.2±2.7
1.31	59.5±2.5	-10.8±1.8	8.6±2.0
1.33	67.6±2.7	3.2±1.9	7.9±2.9
1.35	73.2±4.1	20.4±3.4	14.2±3.9
1.37	75.9±2.6	26.4±2.2	13.7±3.2
1.39	70.3±2.7	32.0±2.3	4.4±3.3

Table B.8: Table of other multipole ratios for Q^2=0.15 $(GeV/c)^2$. All values in this table are the ratio of the multipole to the interference term $|M_{1+}|^2$.

W(GeV/c^2)	$Re(E_{1+}M_{1+}^*)$	$Re(S_{1+}M_{1+}^*)$
$Q^2 = 0.25$ (figure 7.35)	(%)	(%)
1.11	-11.6±2.7	-5.3±1.6
1.13	-8.7±2.4	1.4±0.8
1.15	-10.2±2.8	2.3±0.7
1.17	-4.7±3.2	1.7±1.2
1.19	3.3±2.2	-0.1±0.8
1.21	3.2±2.0	-0.4±0.8
1.23	4.3±2.5	-0.5±0.9
1.25	5.8±1.6	-0.2±0.5
1.27	5.2±1.8	-0.8±0.5
1.29	7.3±2.9	-1.7±0.6
1.31	6.1±1.8	0.7±0.4
1.33	6.1±2.1	1.4±0.4
1.35	6.0±3.2	-1.1±0.5
1.37	3.1±1.9	-0.5±0.3
1.39	4.0±2.1	-1.0±0.4

Table B.9: Table of R_{EM} and R_{SM} values for Q^2=0.25 $(GeV/c)^2$. All values in this table are the ratio of the multipole to the interference term $|M_{1+}|^2$.

W(GeV/c^2)	$Re(M_{1-}M^*_{1+})$	$Re(E_{0+}M^*_{1+})$	$Re(S_{0+}M^*_{1+})$
Q^2 = 0.25 (figure 7.35)	(%)	(%)	(%)
1.11	-32.3±4.6	52.4±7.9	-25.1±7.4
1.13	-15.2±3.9	42.4±5.2	13.7±6.0
1.15	-6.8±4.2	23.1±3.5	9.9±6.4
1.17	16.6±4.3	-5.3±3.7	18.1±8.1
1.19	27.2±2.8	-34.3±3.1	1.0±4.7
1.21	23.2±2.6	-45.8±3.3	9.1±3.4
1.23	22.6±3.2	-42.4±3.9	4.5±3.0
1.25	34.8±2.0	-35.8±2.0	1.6±1.5
1.27	42.9±2.2	-28.4±1.9	5.6±1.5
1.29	55.5±3.5	-14.8±2.5	12.2±2.1
1.31	57.8±2.2	-7.8±1.5	5.5±1.3
1.33	64.4±2.4	3.7±1.7	8.0±1.6
1.35	73.0±3.7	11.4±2.6	9.3±2.5
1.37	60.9±2.2	21.3±1.7	3.1±1.9
1.39	63.6±2.5	36.0±2.3	13.4±2.6

Table B.10: Table of other multipole ratios for Q^2=0.25 $(GeV/c)^2$. All values in this table are the ratio of the multipole to the interference term $|M_{1+}|^2$.

W(GeV/c^2)	$Re(E_{1+}M^*_{1+})$	$Re(S_{1+}M^*_{1+})$
Q^2 = 0.35 (figure 7.34)	(%)	(%)
1.11	-12.4±1.9	1.9±1.1
1.13	-11.8±1.6	-1.0±0.4
1.15	-9.6±1.8	-1.8±0.5
1.17	-6.0±2.6	-0.7±0.8
1.19	-0.1±1.6	0.2±0.6
1.21	1.4±1.6	-1.2±0.6
1.23	6.5±2.2	-1.2±0.8
1.25	7.5±1.5	0.3±0.4
1.27	5.0±1.7	0.4±0.5
1.29	5.6±2.3	-0.4±0.5
1.31	7.0±1.7	0.5±0.3
1.33	12.3±2.2	1.9±0.4
1.35	10.4±3.5	-1.1±0.5
1.37	4.1±1.8	0.0±0.3
1.39	10.4±3.2	-3.4±0.6

Table B.11: Table of R_{EM} and R_{SM} values for Q^2=0.35 $(GeV/c)^2$. All values in this table are the ratio of the multipole to the interference term $|M_{1+}|^2$.

W(GeV/c^2)	$Re(M_{1-}M^*_{1+})$	$Re(E_{0+}M^*_{1+})$	$Re(S_{0+}M^*_{1+})$
Q^2 = 0.35 (figure 7.34)	(%)	(%)	(%)
1.11	-38.1±3.2	54.0±5.5	12.3±6.3
1.13	-10.0±2.3	34.5±2.6	6.0±4.2
1.15	5.1±2.4	20.2±2.1	-2.2±4.5
1.17	18.8±3.4	-0.5±2.9	-3.1±5.3
1.19	27.2±2.1	-26.6±2.2	2.2±2.9
1.21	26.9±2.0	-44.9±2.6	6.8±2.7
1.23	25.8±2.9	-38.5±3.3	9.9±2.6
1.25	38.8±1.9	-35.2±1.9	3.6±1.4
1.27	42.1±2.1	-33.4±2.0	5.4±1.5
1.29	38.5±2.9	-15.6±2.0	4.5±1.6
1.31	51.5±2.0	-5.1±1.2	3.8±1.0
1.33	72.9±2.5	7.5±1.6	8.2±1.3
1.35	86.1±4.0	20.6±2.7	7.2±1.6
1.37	57.6±2.1	13.8±1.4	-6.3±1.6
1.39	115.2±3.6	36.2±3.0	7.1±2.3

Table B.12: Table of other multipole ratios for Q^2=0.35 $(GeV/c)^2$. All values in this table are the ratio of the multipole to the interference term $|M_{1+}|^2$.

Q^2	R_{EM}	R_{SM}	Lab	Reference
$(GeV/c)^2$	(%)	(%)		
0.0	-2.5±0.2	-	MAMI(DAPHNE)/Mainz	[20]
0.0	-2.7±0.2	-	MAMI(TAPS)/Mainz	[21]
0.121	-	-6.4±0.7±0.8	MAMI/Mainz	[22]
0.0	-3.1±0.2	-	LEGS/BNL	[23]
0.127	-	-12.7±1.5	ELSA/Bonn	[24]
0.126	0	-7.6±0.8	BATES/MIT	[10]
0.126	+0.9±1.4	-8.5±1.2	BATES/MIT	[10]
0.126	+0.8±0.8	-9.1±0.8	BATES/MIT	[10]
0.126	-2.2±0.2	-6.7±0.2	BATES/MIT	[10]
0.126	-3.3	-4.3	BATES/MIT	[10]
0.4	-3.3±0.4±0.4	-5.6±0.4±0.6	JLAB	[37]
0.52	-1.8±0.4±0.4	-6.4±0.4±0.5	JLAB	[37]
0.65	-1.8±0.5±0.5	-6.9±0.6±0.5	JLAB	[37]
0.75	-2.4±0.6±0.7	-7.4±0.8±0.5	JLAB	[37]
0.90	-1.8±0.6±0.4	-8.4±0.9±0.4	JLAB	[37]
0.65	-2.1±0.4±0.4	-6.6±0.4±0.2	JLAB	[37]
0.75	-1.7±0.5±0.5	-6.0±0.4±0.2	JLAB	[37]
0.90	-1.8±0.4±0.3	-7.2±0.4±0.1	JLAB	[37]
1.15	-1.6±0.5±0.3	-7.9±0.5±0.4	JLAB	[37]
1.45	-2.3±0.7±0.4	-8.1±0.9±0.7	JLAB	[37]
1.80	-0.9±1.1±0.7	-10.7±1.6±1.5	JLAB	[37]
Pre-1990				
0.0463	-9.0±2.4	-	CEA/Harvard	[28]
0.130	+6.0±3.0	-	CEA/Harvard	[28]
0.247	-4.0±2.0	-	CEA/Harvard	[28]
0.404	-10.0±4.0	-	CEA/Harvard	[28]
0.6	-7.1±3.8	-16.9±3.5	DESY	[29]
1.0	+7.8±4.4	-15.2±2.6	DESY	[29]
0.6	-2.6±1.4	-6.0±1.3	DESY	[30]
1.0	+5.6±2.2	-8.1±1.7	DESY	[30]
1.0	-4.8±2.1	-	DESY	[31]
0.46	+4.6±1.1	-29±7	NINA/Daresbury	[32]
0.30	+2.7±1.1	-6.5±2.1	NINA/Daresbury	[33]
0.45	+1.1±1.4	-7.5±1.5	NINA/Daresbury	[33]
0.60	+1.9±1.5	-6.5±2.3	NINA/Daresbury	[33]
0.75	+2.9±1.6	-3.0±2.0	NINA/Daresbury	[33]
0.573	+0.64±1.1	-6.5±0.56	NINA/Daresbury	[34]
1.153	+0.5±1.6	-4.1±1.1	NINA/Daresbury	[35]
0.3	-1.8±2.5	-4.1±2.1	Bonn	[36]

Table B.13: Table of R_{EM} and R_{SM} values from previous of experiments.

APPENDIX III

APPENDIX C

Table of Cross-sections

Q^2	W	Cos(θ^*_π)	ϕ^*_π	cross-section	error
$(GeV/c)^2$	(GeV/c^2)		^{o}	$(\mu b/sr)$	$(\mu b/sr)$
0.15	1.23	-0.9	15	5.15852	5.15852
0.15	1.23	-0.9	45	7.17105	1.03506
0.15	1.23	-0.9	75	4.98462	0.346456
0.15	1.23	-0.9	105	3.84125	0.250575
0.15	1.23	-0.9	135	6.39954	0.369478
0.15	1.23	-0.9	165	5.28299	0.513129
0.15	1.23	-0.9	195	5.2297	0.536558
0.15	1.23	-0.9	225	5.67207	0.345192
0.15	1.23	-0.9	255	4.21913	0.256295
0.15	1.23	-0.9	285	3.79706	0.263277
0.15	1.23	-0.9	315	6.03572	0.754464
0.15	1.23	-0.9	345	16.8121	11.8879
0.15	1.23	-0.7	15	5.28104	5.28104
0.15	1.23	-0.7	45	15.9912	4.1289
0.15	1.23	-0.7	75	7.95428	0.80764
0.15	1.23	-0.7	105	8.49366	0.744946
0.15	1.23	-0.7	135	10.9203	0.961477
0.15	1.23	-0.7	165	4.35258	0.609483
0.15	1.23	-0.7	195	4.59121	0.700156
0.15	1.23	-0.7	225	9.50801	0.853847
0.15	1.23	-0.7	255	9.79052	0.969407
0.15	1.23	-0.7	285	7.40134	0.76748
0.15	1.23	-0.7	315	11.3667	2.48042
0.15	1.23	-0.7	345	3.63904	3.63904
0.15	1.23	-0.5	15	12.3597	12.3597
0.15	1.23	-0.5	45	18.7763	5.42028
0.15	1.23	-0.5	75	12.8729	1.57268
0.15	1.23	-0.5	105	9.82672	0.987623

Table C.1: Experimental results data plotted in figures 7.2, 7.3 and 7.4.

Q^2	W	Cos(θ^*_π)	ϕ^*_π	cross-section	error
$(GeV/c)^2$	(GeV/c^2)		^{o}	$(\mu b/sr)$	$(\mu b/sr)$
0.15	1.23	-0.5	135	8.2583	0.770092
0.15	1.23	-0.5	165	5.00206	0.822335
0.15	1.23	-0.5	195	4.23457	0.748579
0.15	1.23	-0.5	225	9.33845	0.995475
0.15	1.23	-0.5	255	12.4555	1.36716
0.15	1.23	-0.5	285	9.87179	0.972696
0.15	1.23	-0.5	315	9.84577	2.09913
0.15	1.23	-0.5	345	3.46565	3.46565
0.15	1.23	-0.3	15	3.08888	3.08888
0.15	1.23	-0.3	45	9.73636	3.0789
0.15	1.23	-0.3	75	12.9261	1.60328
0.15	1.23	-0.3	105	13.1795	1.40493
0.15	1.23	-0.3	135	7.81235	0.823491
0.15	1.23	-0.3	165	2.71313	0.495349
0.15	1.23	-0.3	195	2.31219	0.380122
0.15	1.23	-0.3	225	8.61758	0.923897
0.15	1.23	-0.3	255	12.4721	1.27961
0.15	1.23	-0.3	285	12.2571	1.29201
0.15	1.23	-0.3	315	10.2146	2.47741
0.15	1.23	-0.3	345	2.41108	2.41108
0.15	1.23	-0.1	15	2.53618	2.53618
0.15	1.23	-0.1	45	9.55296	2.88033
0.15	1.23	-0.1	75	17.4992	2.18739
0.15	1.23	-0.1	105	15.2393	1.78363
0.15	1.23	-0.1	135	8.10015	0.935323
0.15	1.23	-0.1	165	1.77533	0.324129
0.15	1.23	-0.1	195	3.20477	0.801193
0.15	1.23	-0.1	225	6.54772	0.654772
0.15	1.23	-0.1	255	18.7274	2.20704
0.15	1.23	-0.1	285	18.3735	2.372
0.15	1.23	-0.1	315	7.78825	1.74151
0.15	1.23	-0.1	345	1.41174	0.99825
0.15	1.23	0.1	15	2.54299	1.79817
0.15	1.23	0.1	45	4.87778	1.21945
0.15	1.23	0.1	75	16.5127	1.95969
0.15	1.23	0.1	105	16.9259	1.99474
0.15	1.23	0.1	135	5.37434	0.582931
0.15	1.23	0.1	165	1.06583	0.217562
0.15	1.23	0.1	195	1.34106	0.244843
0.15	1.23	0.1	225	5.22263	0.583906
0.15	1.23	0.1	255	17.3182	1.90091

Table C.2: Experimental results data plotted in figures 7.2, 7.3 and 7.4.

Q^2	W	$\mathrm{Cos}(\theta^*_\pi)$	ϕ^*_π	cross-section	error
$(GeV/c)^2$	(GeV/c^2)		^{o}	$(\mu b/sr)$	$(\mu b/sr)$
0.15	1.23	0.1	285	15.4351	1.7823
0.15	1.23	0.1	315	6.60701	1.60243
0.15	1.23	0.1	345	1.22219	1.22219
0.15	1.23	0.3	15	0.947599	0.547096
0.15	1.23	0.3	45	6.61604	1.99481
0.15	1.23	0.3	75	14.0119	1.56658
0.15	1.23	0.3	105	15.2088	1.72207
0.15	1.23	0.3	135	4.62707	0.479804
0.15	1.23	0.3	165	0.939269	0.171486
0.15	1.23	0.3	195	1.22091	0.244182
0.15	1.23	0.3	225	4.99586	0.5517
0.15	1.23	0.3	255	13.1635	1.32298
0.15	1.23	0.3	285	18.0345	2.09647
0.15	1.23	0.3	315	6.30705	1.44694
0.15	1.23	0.3	345	1.74057	1.23077
0.15	1.23	0.5	15	1.44415	1.44415
0.15	1.23	0.5	45	6.96688	2.01116
0.15	1.23	0.5	75	10.8395	1.25164
0.15	1.23	0.5	105	9.3678	0.998608
0.15	1.23	0.5	135	4.24536	0.420353
0.15	1.23	0.5	165	1.12944	0.190911
0.15	1.23	0.5	195	1.17963	0.22293
0.15	1.23	0.5	225	5.68131	0.612632
0.15	1.23	0.5	255	9.26224	0.908239
0.15	1.23	0.5	285	8.93827	0.917049
0.15	1.23	0.5	315	6.18408	1.26232
0.15	1.23	0.5	345	1.09247	0.77249
0.15	1.23	0.7	15	1.5921	1.5921
0.15	1.23	0.7	45	4.42038	0.758088
0.15	1.23	0.7	75	3.80604	0.386444
0.15	1.23	0.7	105	3.43378	0.300011
0.15	1.23	0.7	135	4.34952	0.409166
0.15	1.23	0.7	165	1.14181	0.190302
0.15	1.23	0.7	195	1.54566	0.238501
0.15	1.23	0.7	225	4.40523	0.429906
0.15	1.23	0.7	255	4.02139	0.402139
0.15	1.23	0.7	285	3.4555	0.349058
0.15	1.23	0.7	315	4.42779	0.82222
0.15	1.23	0.7	345	2.34899	2.34899
0.15	1.23	0.9	15	16.1445	16.1445

Table C.3: Experimental results data plotted in figures 7.2, 7.3 and 7.4.

Q^2	W	$\text{Cos}(\theta^*_\pi)$	ϕ^*_π	cross-section	error
$(GeV/c)^2$	(GeV/c^2)		^{o}	$(\mu b/sr)$	$(\mu b/sr)$
0.15	1.23	0.9	45	2.48703	0.348254
0.15	1.23	0.9	75	1.52457	0.104955
0.15	1.23	0.9	105	1.13229	0.0719003
0.15	1.23	0.9	135	1.88428	0.114886
0.15	1.23	0.9	165	1.57714	0.165329
0.15	1.23	0.9	195	2.93533	0.298039
0.15	1.23	0.9	225	1.66927	0.103724
0.15	1.23	0.9	255	0.970823	0.0586494
0.15	1.23	0.9	285	1.03801	0.0680021
0.15	1.23	0.9	315	2.51489	0.336067
0.15	1.23	0.9	345	8.62818	8.62818
0.25	1.23	-0.9	15	14.8783	3.71956
0.25	1.23	-0.9	45	14.8552	1.35047
0.25	1.23	-0.9	75	8.87274	0.578793
0.25	1.23	-0.9	105	8.98218	0.533937
0.25	1.23	-0.9	135	14.9816	0.901787
0.25	1.23	-0.9	165	10.1591	1.08296
0.25	1.23	-0.9	195	12.4783	1.35346
0.25	1.23	-0.9	225	11.8461	0.730458
0.25	1.23	-0.9	255	8.49427	0.51599
0.25	1.23	-0.9	285	9.54478	0.572457
0.25	1.23	-0.9	315	13.3653	1.08406
0.25	1.23	-0.9	345	11.2234	2.39283
0.25	1.23	-0.7	15	20.2557	7.65592
0.25	1.23	-0.7	45	25.3636	2.9094
0.25	1.23	-0.7	75	23.3387	2.1217
0.25	1.23	-0.7	105	23.7066	2.19167
0.25	1.23	-0.7	135	27.4507	2.69176
0.25	1.23	-0.7	165	12.5046	1.80489
0.25	1.23	-0.7	195	16.238	2.8705
0.25	1.23	-0.7	225	26.3686	2.50279
0.25	1.23	-0.7	255	22.078	1.93637
0.25	1.23	-0.7	285	22.7648	2.08685
0.25	1.23	-0.7	315	28.0877	3.59627
0.25	1.23	-0.7	345	9.25396	2.92636
0.25	1.23	-0.5	15	22.339	8.44334
0.25	1.23	-0.5	45	21.9717	2.88502
0.25	1.23	-0.5	75	31.7429	3.14301
0.25	1.23	-0.5	105	32.8801	3.37343
0.25	1.23	-0.5	135	25.8218	2.51995

Table C.4: Experimental results data plotted in figures 7.2, 7.3 and 7.4.

Q^2	W	$\mathrm{Cos}(\theta^*_\pi)$	ϕ^*_π	cross-section	error
$(GeV/c)^2$	(GeV/c^2)		^{o}	$(\mu b/sr)$	$(\mu b/sr)$
0.25	1.23	-0.5	165	13.5911	2.40259
0.25	1.23	-0.5	195	10.4699	1.85084
0.25	1.23	-0.5	225	25.6388	2.56388
0.25	1.23	-0.5	255	36.7032	3.80593
0.25	1.23	-0.5	285	34.8314	3.73433
0.25	1.23	-0.5	315	32.9959	4.97435
0.25	1.23	-0.5	345	13.8325	3.9931
0.25	1.23	-0.3	15	13.1594	6.5797
0.25	1.23	-0.3	45	23.8283	4.21229
0.25	1.23	-0.3	75	44.4701	4.71381
0.25	1.23	-0.3	105	43.6777	4.79424
0.25	1.23	-0.3	135	17.5098	1.82552
0.25	1.23	-0.3	165	7.87116	1.4137
0.25	1.23	-0.3	195	9.42045	1.88409
0.25	1.23	-0.3	225	21.61	2.372
0.25	1.23	-0.3	255	41.3414	4.38217
0.25	1.23	-0.3	285	40.6773	4.28775
0.25	1.23	-0.3	315	19.2166	2.86463
0.25	1.23	-0.3	345	9.349	3.30536
0.25	1.23	-0.1	15	18.0222	10.4051
0.25	1.23	-0.1	45	18.324	2.86173
0.25	1.23	-0.1	75	43.9064	5.03641
0.25	1.23	-0.1	105	45.4151	4.86901
0.25	1.23	-0.1	135	17.4649	2.07269
0.25	1.23	-0.1	165	7.28251	1.55264
0.25	1.23	-0.1	195	4.37272	0.798347
0.25	1.23	-0.1	225	13.6596	1.53683
0.25	1.23	-0.1	255	41.9091	4.57267
0.25	1.23	-0.1	285	41.7486	4.72709
0.25	1.23	-0.1	315	15.7056	2.39509
0.25	1.23	-0.1	345	6.5403	2.1801
0.25	1.23	0.1	15	7.76394	3.88199
0.25	1.23	0.1	45	16.0824	2.6804
0.25	1.23	0.1	75	47.805	5.75504
0.25	1.23	0.1	105	38.1993	3.81993
0.25	1.23	0.1	135	12.6022	1.30679
0.25	1.23	0.1	165	3.63765	0.74253
0.25	1.23	0.1	195	3.50728	0.784252
0.25	1.23	0.1	225	11.9558	1.26732
0.25	1.23	0.1	255	46.5725	5.52715

Table C.5: Experimental results data plotted in figures 7.2, 7.3 and 7.4.

Q^2	W	$\text{Cos}(\theta^*_\pi)$	ϕ^*_π	cross-section	error
$(GeV/c)^2$	(GeV/c^2)		^{o}	$(\mu b/sr)$	$(\mu b/sr)$
0.25	1.23	0.1	285	46.3731	5.58266
0.25	1.23	0.1	315	11.8156	1.63852
0.25	1.23	0.1	345	4.03642	1.42709
0.25	1.23	0.3	15	8.33917	3.72942
0.25	1.23	0.3	45	13.3141	2.15983
0.25	1.23	0.3	75	39.2545	4.56325
0.25	1.23	0.3	105	31.5544	3.32612
0.25	1.23	0.3	135	12.978	1.51896
0.25	1.23	0.3	165	2.21367	0.411066
0.25	1.23	0.3	195	3.08522	0.545398
0.25	1.23	0.3	225	11.6787	1.2897
0.25	1.23	0.3	255	35.7605	3.99813
0.25	1.23	0.3	285	29.0991	2.95458
0.25	1.23	0.3	315	16.622	2.56483
0.25	1.23	0.3	345	2.79296	0.930988
0.25	1.23	0.5	15	5.84967	2.21097
0.25	1.23	0.5	45	16.4075	2.47353
0.25	1.23	0.5	75	23.4447	2.29894
0.25	1.23	0.5	105	21.9452	2.10196
0.25	1.23	0.5	135	13.6708	1.39527
0.25	1.23	0.5	165	3.87579	0.637176
0.25	1.23	0.5	195	4.19979	0.731093
0.25	1.23	0.5	225	15.6596	1.72932
0.25	1.23	0.5	255	22.4876	2.34449
0.25	1.23	0.5	285	22.7465	2.43868
0.25	1.23	0.5	315	15.1427	2.20878
0.25	1.23	0.5	345	4.48865	1.58698
0.25	1.23	0.7	15	7.94464	3.24339
0.25	1.23	0.7	45	15.747	1.96837
0.25	1.23	0.7	75	11.7659	1.12184
0.25	1.23	0.7	105	8.75478	0.830968
0.25	1.23	0.7	135	13.3018	1.19938
0.25	1.23	0.7	165	4.67652	0.768813
0.25	1.23	0.7	195	3.71861	0.554335
0.25	1.23	0.7	225	13.1971	1.22008
0.25	1.23	0.7	255	11.6327	1.05317
0.25	1.23	0.7	285	9.64513	0.91963
0.25	1.23	0.7	315	16.0555	2.16493
0.25	1.23	0.7	345	5.88085	1.96028
0.25	1.23	0.9	15	13.4737	2.7503

Table C.6: Experimental results data plotted in figures 7.2, 7.3 and 7.4.

Q^2	W	$\mathrm{Cos}(\theta^*_\pi)$	ϕ^*_π	cross-section	error
$(GeV/c)^2$	(GeV/c^2)		^{o}	$(\mu b/sr)$	$(\mu b/sr)$
0.25	1.23	0.9	45	8.04131	0.654392
0.25	1.23	0.9	75	4.05775	0.261382
0.25	1.23	0.9	105	3.47829	0.198517
0.25	1.23	0.9	135	5.85118	0.360115
0.25	1.23	0.9	165	7.17738	0.802453
0.25	1.23	0.9	195	8.28392	0.888128
0.25	1.23	0.9	225	7.1693	0.429213
0.25	1.23	0.9	255	3.58858	0.200295
0.25	1.23	0.9	285	3.47411	0.209879
0.25	1.23	0.9	315	5.62343	0.454628
0.25	1.23	0.9	345	10.0546	2.30668
0.35	1.23	-0.9	15	10.9187	1.38668
0.35	1.23	-0.9	45	10.199	0.70047
0.35	1.23	-0.9	75	7.11851	0.452025
0.35	1.23	-0.9	105	7.9939	0.482929
0.35	1.23	-0.9	135	10.3098	0.734544
0.35	1.23	-0.9	165	7.0725	0.693515
0.35	1.23	-0.9	195	5.92128	0.583445
0.35	1.23	-0.9	225	11.1427	0.736332
0.35	1.23	-0.9	255	7.05553	0.433416
0.35	1.23	-0.9	285	5.62492	0.330878
0.35	1.23	-0.9	315	11.1853	0.790922
0.35	1.23	-0.9	345	9.35566	1.13454
0.35	1.23	-0.7	15	11.4243	2.15899
0.35	1.23	-0.7	45	28.7597	3.25641
0.35	1.23	-0.7	75	19.4279	1.7172
0.35	1.23	-0.7	105	17.9028	1.64115
0.35	1.23	-0.7	135	24.5939	2.76704
0.35	1.23	-0.7	165	9.94507	1.57246
0.35	1.23	-0.7	195	11.7897	1.86412
0.35	1.23	-0.7	225	20.7408	2.04365
0.35	1.23	-0.7	255	20.6809	1.94549
0.35	1.23	-0.7	285	19.9017	1.90623
0.35	1.23	-0.7	315	25.3305	2.54582
0.35	1.23	-0.7	345	13.4595	2.49935
0.35	1.23	-0.5	15	14.632	3.11956
0.35	1.23	-0.5	45	27.8483	3.78966
0.35	1.23	-0.5	75	26.2511	2.52601
0.35	1.23	-0.5	105	23.8357	2.17589
0.35	1.23	-0.5	135	23.1904	2.39191

Table C.7: Experimental results data plotted in figures 7.2, 7.3 and 7.4.

Q^2	W	$\mathrm{Cos}(\theta^*_\pi)$	ϕ^*_π	cross-section	error
$(GeV/c)^2$	(GeV/c^2)		^{o}	$(\mu b/sr)$	$(\mu b/sr)$
0.35	1.23	-0.5	165	9.85836	1.71612
0.35	1.23	-0.5	195	12.1085	2.10783
0.35	1.23	-0.5	225	20.7266	2.26146
0.35	1.23	-0.5	255	25.4649	2.65489
0.35	1.23	-0.5	285	26.6026	2.44897
0.35	1.23	-0.5	315	27.6309	3.19054
0.35	1.23	-0.5	345	9.74894	2.03279
0.35	1.23	-0.3	15	13.4535	3.17101
0.35	1.23	-0.3	45	20.9143	2.61428
0.35	1.23	-0.3	75	36.7899	4.0141
0.35	1.23	-0.3	105	33.9152	3.81577
0.35	1.23	-0.3	135	20.5975	2.46188
0.35	1.23	-0.3	165	5.13866	0.812495
0.35	1.23	-0.3	195	4.18227	0.687565
0.35	1.23	-0.3	225	18.4426	2.25311
0.35	1.23	-0.3	255	33.4611	3.38007
0.35	1.23	-0.3	285	39.3514	4.29361
0.35	1.23	-0.3	315	16.3985	2.034
0.35	1.23	-0.3	345	6.89391	1.67202
0.35	1.23	-0.1	15	3.62703	0.791483
0.35	1.23	-0.1	45	16.4052	2.1541
0.35	1.23	-0.1	75	35.5578	3.92673
0.35	1.23	-0.1	105	31.5944	3.14376
0.35	1.23	-0.1	135	14.7276	1.84094
0.35	1.23	-0.1	165	6.54006	1.54151
0.35	1.23	-0.1	195	4.55666	0.84615
0.35	1.23	-0.1	225	15.4158	2.04186
0.35	1.23	-0.1	255	39.6972	4.03064
0.35	1.23	-0.1	285	28.1633	3.03693
0.35	1.23	-0.1	315	14.2251	1.91811
0.35	1.23	-0.1	345	2.6248	0.656199
0.35	1.23	0.1	15	7.8306	2.02185
0.35	1.23	0.1	45	11.7708	1.58718
0.35	1.23	0.1	75	36.2378	3.86296
0.35	1.23	0.1	105	30.4421	3.22686
0.35	1.23	0.1	135	10.1017	1.23411
0.35	1.23	0.1	165	2.68482	0.467368
0.35	1.23	0.1	195	4.03747	0.749737
0.35	1.23	0.1	225	8.53071	0.942065
0.35	1.23	0.1	255	25.1695	2.58234

Table C.8: Experimental results data plotted in figures 7.2, 7.3 and 7.4.

Q^2	W	$\mathrm{Cos}(\theta^*_\pi)$	ϕ^*_π	cross-section	error
$(GeV/c)^2$	(GeV/c^2)		^{o}	$(\mu b/sr)$	$(\mu b/sr)$
0.35	1.23	0.1	285	34.2809	4.01228
0.35	1.23	0.1	315	11.7984	1.35337
0.35	1.23	0.1	345	4.67769	0.997288
0.35	1.23	0.3	15	4.54353	1.04236
0.35	1.23	0.3	45	9.47995	1.08035
0.35	1.23	0.3	75	27.3616	3.05911
0.35	1.23	0.3	105	23.8005	2.56648
0.35	1.23	0.3	135	11.8179	1.51313
0.35	1.23	0.3	165	3.07695	0.512828
0.35	1.23	0.3	195	5.71528	1.19171
0.35	1.23	0.3	225	12.4466	1.59362
0.35	1.23	0.3	255	22.7922	2.3142
0.35	1.23	0.3	285	25.1473	2.55333
0.35	1.23	0.3	315	13.4054	1.65008
0.35	1.23	0.3	345	3.65165	0.816534
0.35	1.23	0.5	15	4.18159	0.820076
0.35	1.23	0.5	45	11.7414	1.45635
0.35	1.23	0.5	75	18.485	1.85782
0.35	1.23	0.5	105	14.5364	1.46097
0.35	1.23	0.5	135	12.1158	1.33798
0.35	1.23	0.5	165	4.19166	0.740989
0.35	1.23	0.5	195	3.24603	0.533645
0.35	1.23	0.5	225	10.5515	1.25223
0.35	1.23	0.5	255	18.5184	1.79867
0.35	1.23	0.5	285	15.0317	1.51075
0.35	1.23	0.5	315	10.9107	1.1976
0.35	1.23	0.5	345	3.53001	0.720561
0.35	1.23	0.7	15	6.37219	1.39053
0.35	1.23	0.7	45	12.6953	1.43746
0.35	1.23	0.7	75	8.33078	0.766912
0.35	1.23	0.7	105	8.8478	0.847465
0.35	1.23	0.7	135	10.1636	0.987175
0.35	1.23	0.7	165	4.62244	0.704916
0.35	1.23	0.7	195	4.15472	0.692455
0.35	1.23	0.7	225	13.7592	1.37592
0.35	1.23	0.7	255	8.35381	0.762596
0.35	1.23	0.7	285	8.70051	0.80436
0.35	1.23	0.7	315	13.8104	1.43983
0.35	1.23	0.7	345	5.11752	0.984868
0.35	1.23	0.9	15	8.12051	1.04835

Table C.9: Experimental results data plotted in figures 7.2, 7.3 and 7.4.

Q^2	W	$\mathrm{Cos}(\theta^*_\pi)$	ϕ^*_π	cross-section	error
$(GeV/c)^2$	(GeV/c^2)		^{o}	$(\mu b/sr)$	$(\mu b/sr)$
0.35	1.23	0.9	45	5.28247	0.354535
0.35	1.23	0.9	75	4.28559	0.265273
0.35	1.23	0.9	105	3.17518	0.190093
0.35	1.23	0.9	135	6.38749	0.413171
0.35	1.23	0.9	165	6.88252	0.650339
0.35	1.23	0.9	195	6.99186	0.772125
0.35	1.23	0.9	225	6.75045	0.455115
0.35	1.23	0.9	255	3.29355	0.193071
0.35	1.23	0.9	285	3.5796	0.211297
0.35	1.23	0.9	315	5.47582	0.376079
0.35	1.23	0.9	345	8.05745	1.03165

Table C.10: Experimental results data plotted in figures 7.2, 7.3 and 7.4.

BIBLIOGRAPHY

[1] S. A. Moszkowski and B. L. Scott. *Ann. Phys.*, 11:65, 1960.

[2] S. Scherer. Introduction to Chiral Perturbation Theory. *Adv. Nucl. Phys., hep-ph/0210398*, 27:277–538, 2002.

[3] B. Svetitsky. The flux-tube model of particle creation in nuclear collisions. *hep-ph/9907278*, 1999.

[4] G. Cattapan and L. S. Ferreira. The role of the Δ in nuclear physics. *Physics Reports*, 362:303–407, 2002.

[5] G. Karl N. Isgur and R. Koniuk. *Phys. Rev.*, D 25:2394, 1982.

[6] G. Kalbermann and J. Eisenberb. *Phys. Rev.*, D 28:71, 1983.

[7] K. Bermuth et al. *Phys. Rev.*, D 37:89, 1988.

[8] A. J. Buchmann and E. M. Henley. *Phys. Rev.*, C 63:015202, 2001.

[9] H. Georgi A. De Rujula and S. L. Glashaw. *Phys. Rev.*, D 12:147, 1975.

[10] C. Mertz et al. *Phys. Rev. Lett.*, 86:2963–2966, 2001.

[11] K. Joo et al. *Phys. Rev. Lett.*, 88:122001, 2002.

[12] R. Koniuk and N. Isgur. *Phys. Rev.*, D 21:1868, 1980.

[13] S. S. Gersteyn and G. V. Dzhikiya. *Sov. J. Nucl. Phys.*, 34:870, 1981.

[14] D. Drechsel and M. M. Giannini. *Phys. Lett.*, B 143:329, 1984.

[15] E. Hernandez A. J. Buchmann and A. Faessler. *Phys. Rev.*, C 55:448, 1997.

[16] S. Capstick and G. Karl. *Phys. Rev.*, D 41:2767, 1990.

[17] S. Capstick. *Phys. Rev.*, D 46:2864, 1992.

[18] A. Wirzba and W. Weise. *Phys. Lett.*, B 188:6, 1987.

[19] T. Draper D. B. Leinweber and R. M. Woloshyn. *Phys. Rev.*, D 48:2230, 1993.

[20] R. Beck et al. *Phys. Rev. C*, 61:035204, 2000.

[21] R. Beck et al. NSTR2000. 2000.

[22] Th. Pospischil et al. *Phys. Rev. Lett.*, 86:2959–2962, 2001.

[23] G. Planpied et al. *Phys. Rev. Lett.*, 79:4337, 1997.

[24] F. Kalleicher et al. *Z. Phys.*, A 359:201, 1997.

[25] V. V. Frolov et al. *Phys. Rev. Lett.*, 82:45, 1999.

[26] S. S. Kamalov et al. *Phys. Rev.*, C64:032201, 2001.

[27] L. Tiator et al. *Nucl. Phys.*, A689:205–214, 2001.

[28] C. Mistrettaet al. *Phys. Rev.*, 184:1487, 1969.

[29] W. Albrecht et al. *Nucl. Phys.*, B25:1, 1970.

[30] J. C. Alder et al. *Nucl. Phys.*, B46:573, 1972.

[31] S. Galster et al. *Phys. Rev.*, D 5:519, 1972.

[32] R. D. Hellings et al. *Nucl. Phys.*, B32:179, 1971.

[33] R. Siddle et al. *Nucl. Phys.*, B35:93, 1971.

[34] A. Latham et al. *Nucl. Phys.*, B156:58, 1979.

[35] A. Latham et al. *Nucl. Phys.*, B189:1, 1981.

[36] K. Batzner et al. *Nucl. Phys.*, B76:1, 1974.

[37] K. Joo and L. C. Smith. Single π^0 electroproduction in the $\Delta(1232)$ resonance from e1a data. *Data Analysis Document*, CLAS-ANALYSIS 2001-008, 2001.

[38] K. Kossert et al. *Eur. Phys. J.*, A19:391–399, 2004.

[39] J. J. Aubert et al. *Phys. Lett.*, B123:275, 1983.

[40] A. Bodek et al. *Phys. Rev. Lett.*, 50:1431, 1983.

[41] R. G. Arnold et al. *Phys. Rev. Lett.*, 52:727, 1984.

[42] G. Bari et al. *Phys. Lett.*, B163:282, 1985.

[43] S. Dietrich et al. *Phys. Lett.*, B500(nucl-ex/0011008):47, 2001.

[44] S. Dietrich et al. *Nucl. Phys.*, A690:231, 2001.

[45] S. Strauch et al. *Phys. Rev. Lett.*, 91(nucl-ex/0211022):052301, 2003.

[46] R. D. Ransome. *Nucl. Phys.*, A699:360, 2002.

[47] J. S. O'Connell et al. Electromagnetic excitation of the delta resonance in nuclei. *Physical Review C*, 35(3), 1987.

[48] R. M. Sealock et al. Electroexcitation of the Δ (1232) in Nuclei. *Physical Review Letters*, 62(12), 1989.

[49] J. S. O'Connel and R. M. Sealock. Phenomenologial Δ-nucleus potential from inclusive electron-nucleus scattering data. *Physical Review C*, 42(6), 1990.

[50] Byckling & Kajantie. *Particle Kinematics.* Wiley, 1973.

[51] Kenneth S. Krane. Introductory Nuclear Physics. *John Wiley and Sons*, 1988.

[52] J. S. O'Connell et al. *Phys. Rev. Lett.*, 53:1627, 1984.

[53] J. S. O'Connell et al. *Phys. Rev.*, C35:1063, 1987.

[54] P. Barreau et al. *Nucl. Phys.*, A402:515, 1983.

[55] Z. E. Meziani et al. *Phys. Rev. Lett.*, 54:1238, 1985.

[56] F. H. Heimlich et al. *Nucl. Phys.*, A231:509, 1974.

[57] U. Glawe et al. *Phys. Lett.*, 89B:44, 1979.

[58] S. McLauchlan. Δ *Electroproduction in* ^{12}C. PhD thesis, University of Glasgow, 2003.

[59] W. Ingram. *Semi-Exclusive studies of* $\Delta(1232)$ *electroproduction in* ^{3}He. PhD thesis, University of Glasgow, 2002.

[60] D. Protopopescu. Private communication.

[61] M. Ichimura & M. Ishihara H. Toki. *RIKEN International Workshop on Delta Excitation in Nuclei.* World Scientific, 1994.

[62] Donald H. Perkins. *Introduction to High Energy Physics.* Addison-Wesley, 1987.

[63] K. W. Ford. *Classical and Modern Physics*, volume Vol. 3. John Wiley and Sons, 1972.

[64] B. Krushe. *Single pion production and the P33(1232) resonance,*. `http://jazz.physik.unibas.ch/~krusche/delta_Npi.html`.

[65] E. P. Wigner. *Group Theory and its Applications to the Quantum Mechanics of Atomic Spectra.* New York: Academic Press, 1959.

[66] Particle physics booklet. Extracted from the Review of particle physics.

[67] B. Krusche. Photoproduction of mesons from nuclei, Lecture at International School of Nuclear Physics, 26th Course, Lepton Scattering and the Structure of Hadrons and Nuclei, Erice-Sicily, Italy 16. - 24. September 2004.

[68] M. Hirata et al. *Ann. Phys.*, 120:205, 1979.

[69] J. H. Koch and N. Ohtsuka. Inclusive electron scattering from light neclei at intermediate energies. *Nuclear Physics A*, 435:765–790, 1984.

[70] V. D. Burkert and L. Elouadrhiri. *Phys. Rev. Lett.*, 75:20, 1995.

[71] B. Krusche. and S. Schadmand. Study of Non-Strange Baryon Resonances with Meson Photoproduction., 2003.

[72] M. N. Rosenbluth. *Phys. Rev.*, 79:615, 1950.

[73] Amaldi et al. Pion-Electroproduction. *Springer Tracts of Modern Physics*, vol. 83, 1979.

[74] A. S. Raskin and T. W. Donnelly. *Ann. Phys.*, 191:78, 1989.

[75] K. M. Watson. *Phys. Rev.*, 95:228, 1954.

[76] M. D. Mestayer et al. The CLAS drift chamber system. *Nuclear Instruments and Methods in Physics Research A*, 449:81–111, 2000.

[77] Jefferson lab web link. *Drift Chamber construction,*. `http://www.physics.odu.edu/htmlstuf/docs/dccon.html`.

[78] G. Adams et al. The CLAS Čerenkov detector. *Nuclear Instruments and Methods in Physics Research A*, 465:414–427, 2001.

[79] B. Zhang. *Searching for Short Range Correlations Using* $(e, e'NN)$ *Reactions.* PhD thesis, Massachusetts Institute of Technology, 2003.

[80] E. S. Smith et al. The time-of-flight system for CLAS. *Nuclear Instruments and Methods in Physics Research A*, 432:265–298, 1999.

[81] M. Amarian et al. The CLAS forward electromagnetic calorimeter. *Nuclear Instruments and Methods in Physics Research A*, 460:239–265, 2000.

[82] Vardan Gyurjyan. Jefferson lab. *CLAS archives,*.

[83] S. McAleer & S. Barrow J. J. Manak, E. S. Smits. Jlab CLAS-NOTE 1999-016.

[84] D. Protopopescu. *A Survey of Beam Asymmetries in Semi-Esclusive Electron Scattering on* ^4He *and* ^{12}C*.* PhD thesis, University of New Hampshire, 2002.

[85] R. Niyazov. *PhD Thesis.* PhD thesis, Old Dominion University, 2002.

[86] D. Lawrence et al. CLAS Drift Chamber Calibration: Software and Procedures. *Jefferson Laboratory*, CLAS-NOTE 1999-018.

[87] E. S. Smith et al. Calibration of the CLAS TOF System. *Jefferson Laboratory*, CLAS-NOTE 1999-011.

[88] A. V. Vlassov. *CC Calibration.* `http://www.jlab.org/~vlassov/cc/index.html`.

[89] A. Klimenko. `http://www.physics.odu.edu/~klim/checkelectron.html`.

[90] D. Protopopescu et al. Electron momentum corrections for clas at 4.4GeV. *Jefferson Laboratory*, CLAS-NOTE 2001-008.

[91] D. Protopopescu et al. Fiducial Cuts for Electrons in CLAS/E2 Data at 4.4GeV. *Jefferson Laboratory*, CLAS-NOTE 2001-007.

[92] D. Jenkins. A Comparison of Simple and Full Acceptance. *Jefferson Laboratory*, CLAS-NOTE 2004-043.

[93] W. Brooks et al. *Jefferson Laboratory*, CLAS-NOTE, to be published.

[94] O. Skjeggestad A. G. Frodesen and H. Tofte. Probability and Statistics in Particle Physics. *Universitetsforlaget*, 1979, Eq 4.12.

[95] D. Protopopescu. `http://nuclear.gla.ac.uk/clas-secure/protopop/e2_delta/Acceptance/Gener%ators/PhysGen/`.

[96] M. Holtrop. `GSIM-http://www.physics.unh.edu/$\~$maurik/gsim_info.shtml`.

[97] N. Dashyan. `e2btarget-http://www.jlab.org/Hall-B/secure/e2/natasha/target/e2b/`.

[98] MAID2003. `http://www.kph.uni-mainz.de/MAID/maid2003/`.

[99] D. Drechsel et al. A unitary isobar model for pion photo- and electroproduction on the proton up to 1 GeV. *Nuc. Phys.*, A 645, 1999.

[100] A. W. Thomas and W. Weise. *The Structure of the Nucleon.* WILEY-VCH.

[101] S. Boffi, C. Giusti, F. D. Pacati and M. Radici. *Electromagnetic Response of Atomic Nuclei.* Oxford Science Publications, 1996.

[102] J. D. Bjorken and S. D. Drell. *Relativistic Quantum Mechanics.* McGraw-Hill, 1964.

[103] A. Donnachie and G. Shaw. Electromagnetic Interactions of Hadrons. *New York: Plenum Press*, 1978.